DISSERTATION

PROCESSING AND PROPERTIES OF METAL OPEN-CELL FOAMS WITH PERIODIC TOPOLOGY

Submitted by

Peter Thompson Nivala

Department of Mechanical Engineering

In partial fulfillment of the requirements

For the Degree of Doctor of Philosophy

Colorado State University

Fort Collins, Colorado

Fall 2018

Doctoral Committee:

Advisor: Susan P. James

Christian M. Puttlitz
Ketul Popat
Paul R. Heyliger

ABSTRACT

PROCESSING AND PROPERTIES OF METAL OPEN-CELL FOAMS WITH PERIODIC TOPOLOGY

Metal open-cell foams are competitively poised to meet the demands of next generation applications due to the ability to tailor their properties to achieve multifunctionality through material selection and control of the pore structure. The topological design of metal foams must consider many factors including pore size, shape, spatial distribution, and interconnectivity; however, the current manufacturing techniques limit the degree to which the tailored pore structures can be realized.

In the current research, a novel manufacturing approach to tailoring the pore structure of metal open-cell foams has been conceptually demonstrated based on a structured assembly of porogens. A process integrating space-holder replication and spark plasma sintering (SPS) was developed to fabricate metal open-cell foams exhibiting increased control over the pore size, shape, and position. The pore structure consisted of spherical copper porogens arranged into a hexagonal close-packed pattern. This sacrificial template was co-sintered with nickel-titanium (NiTi) powder using SPS and subsequently leached using nitric acid. The resultant NiTi open-cell foams were characterized for their spatial and mechanical properties, which exhibit uniform, well-replicated pore structures with a high-degree of interconnectivity. During compression testing the open-cell foams displayed unexpected brittle behavior, which was traced to the initiation and inter-particulate propagation of cracks through the NiTi matrix leading to sudden specimen failure.

Additionally, the Master Sintering Curve (MSC) concept was utilized to investigate the effect of copper porogens on the densification behavior of NiTi during the fabrication of open-cell foams. Typically, the MSC is used to determine the *apparent activation energy* (Q_{MSC}) for sintering densification of powder materials and to predict the final specimen density under arbitrary time-temperature sintering profiles. The MSC predicted the areal matrix density of the NiTi open-cell foams to within 1.2%. Comparisons of the densification behavior between NiTi and NiTi with copper specimens suggests the porogens have little to no effect on the densification behavior of NiTi powders within the current experimental setup.

The manufacturing approach demonstrated within the current research will be extended to leverage advanced manufacturing techniques, such as additive manufacturing, to realize optimum pore structures for multifunctional applications to enable the next generation of open-cell foams exhibiting higher performance at lower cost and less weight.

ACKNOWLEDGEMENTS

I would like to thank the committee members Dr. Popat, Dr. Puttlitz, and Dr. Heyliger for your time and feedback. To my advisor, Dr. James, thank you for your precious time, support, advice, determination, and mentorship. I sincerely appreciate the opportunities you have provided for me to finish my doctoral studies; I hope I have repaid your kindness by being an advisee you are proud of.

Thank you to Trevor Aguirre for all his dependable assistance with any and everything I needed to support my weekly lab trips up to Fort Collins. I could not have progressed through my research without the support and flexibility of my manager at Lockheed Martin Space (LMS), Gil Braun. The machining work required of this project was influenced by David Oberle of LMS; thank you Dave for every time you went out of your way to keep me moving forward. The spectacular scanning electron microscopy images were captured with assistance from Dr. Pat McCurdy of the Colorado State University Central Instrumentation Facility, thank you Pat for always being accommodating. Thank you to Dr. Kirk McGilvray, Associate Director of the Orthopaedic and Bioengineering Research Laboratory (OBRL), for donating time on the X-ray micro-computed tomography scanner and thank you to Lucas Nakamura, Associate Research Engineer OBRL, for assistance post-processing the data.

Behind every notable accomplishment in my life is a great support system anchored by my friends and family, who always believed in me, even when I didn't. I would like to thank my friends Nick Gruber and Austin Dvorak. I would like to sincerely thank my great family, including my dad, Bill, and my mom, Jan, for all your love and support. A special thanks to my

best friend, my wife Angela, who has supported me unconditionally through the past ten-plus years of my life; I have unfairly burdened you with my stress and yet you are always there for me, I love you. Last, but not least, thank you to my three wonderful children: Lily, Logan, and Eva. You truly have taught me about life and what's important, I am so proud of you and love you all so much!

TABLE OF CONTENTS

LIST OF TABLES

LIST OF FIGURES

LIST OF SYMBOLS

A	Interfacial Area
a	Sigmoid Function Curve Fit Parameter
b	Sigmoid Function Curve Fit Parameter
c	Sigmoid Function Curve Fit Parameter
C_1	Gibson-Ashby Scaling Parameter
D_0	Diffusion Coefficient
dA	Area Differential
D_b	Grain Boundary Diffusion Coefficient
D_{foam}	Foam Diameter
dL	Linear Shrinkage Differential
dr	Sphere Radius Differential
dt	Time Differential
dV	Volume Differential
D_v	Volume Diffusion Coefficient
$d\rho$	Density Differential
E^*	Elastic Modulus of Foam Material
E_S	Elastic Modulus of Solid Material
G	Mean Grain Diameter
H	Numerical Constant
IQR	Interquartile Range
k	Boltzmann Constant
L	Linear Shrinkage
L_{foam}	Foam Length/Height
$\ln(\Theta_0)$	Sigmoid Function Curve Fit Parameter
m	Stress Exponent
m_{foam}	Foam Mass
m_{s+s}	Mass of Specimen with Sealant

n	Grain Size Exponent
p_a	Uniaxial Applied Stress
Q_1	Lower Quartile
Q_3	Upper Quartile
Q_{MSC}	Apparent Activation Energy
r	Sphere Radius
R	Gas Constant
T	Absolute Temperature
γ	Specific Interfacial Energy / Surface Energy
Γ_b	Grain Boundary Diffusion Lumped Scaling Parameter
Γ_v	Volume Diffusion Lumped Scaling Parameter
δ	Grain Boundary Width
$\Theta(t, T(t))$	Work of Sintering
ρ	Density
ρ^*	Density of Foam Material
ρ_0	Green Density
ρ_{foam}	Foam Density
ρ_{NiTi}	Theoretical Density of NiTi
$\rho_{relative}$	Relative Density
ρ_S	Theoretical Density of Solid Material
σ	Sintering Stress
ϕ	Stress Intensification Factor
ϕ_{foam}	Foam Porosity
Ω	Atomic Volume

1. INTRODUCTION TO METAL OPEN-CELL FOAMS

The purpose of the introduction to metal open-cell foams is to establish the baseline knowledge necessary to understand the research presented in Chapter 4, NITI OPEN-CELL FOAMS WITH PERIODIC TOPOLOGY. Terminology related to the field of cellular solids will be defined, and specific applications of metal open-cell foams will be presented to convey their importance as future multifunctional materials. The two variations in cellular topologies will be introduced and their current fabrication methods reviewed. Finally, the research opportunity will be presented based on the argument that current fabrication methods limit the tailorability of cellular topologies for multifunctional applications of metal open-cell foams. Existing solutions and their main limitations will be briefly considered.

1.1 Cellular Solids

Cellular solids are a class of materials exhibiting novel properties derived from their cell-based architecture [1, 2]. The cell is the basic unit of a cellular solid and can be defined geometrically as a polygon (2D) or polyhedral (3D), which are repeatedly nested together to form the cellular structure [1]. Cellular solids can be thought of as a 2-phase composite [3] whose behavior is a result of the solid material properties, cellular structure, and the relative density of the overall cellular solid [3-12]. The engineering of cellular solids from metallic, ceramic, and polymeric materials, are undoubtedly inspired by the strong, stiff, and lightweight structures found in nature, such as wood, bone, cork, sponge, and coral [13].

Specifically, cellular metals offer a unique combination of low weight, excellent mechanical properties (high strength, high stiffness, ductility), thermal and chemical stability, as

well as high electrical and thermal conductivity [2, 4, 14, 15]. Cellular metals refer to a metal possessing repeating unit cells whose internal volume is filled with air; such unit cells are commonly referred to as voids or pores [15]. Cellular metals with a three-dimensional spatial arrangement of unit cells are classified as foams [1].

Metal foams can be sub-divided based on the existence of cell faces and edges, those with both are closed-cell foams, and those with only cell edges are open-cell foams. Furthermore, the cell walls characteristic of closed-cell foams isolates each cell, while the absence of cell walls in open-cell foams allows a high degree of interconnectivity between adjacent cells. Closed-cell foams are mainly used for structural applications, where the cell walls and edges both carry load, whereas open-cell foams are primarily used for functional applications leveraging the permeability of the interconnected cellular network [13]. Open-cell foams are often referred to as, “sponges” due to their similarity with the naturally occurring organisms [14, 16-19]. Herein, sponges shall be considered a special class of open-cell foams capable of absorbing liquids and thus shall defer to the terminology, “open-cell foam” to describe a foam with interconnected cells.

Additionally, metal foams can be characterized by the variability in their cell topology, stochastic or periodic, and by their relative density. Stochastic topologies cannot be characterized by a single unit cell [20]. Periodic topologies are characterized by a single unit cell, which repeats spatially in two-dimensions (prismatic) or in three-dimensions [20].

The term *porous metal* is also present in the lexicon. Herein, metals with relative densities less than 0.3 shall be considered, “foams”, while those with relative densities greater than 0.3 shall be, “porous metals”. Porous metals characteristically contain isolated, often

rounded pores that are not cellular in nature as in, for example, the structure derived from the incomplete sintering of a powdered material [1, 3, 15].

1.2 Applications

Manipulation of the cellular structure, density, and/or alloy composition allows the properties of metal open-cell foams to be tailored for non-structural, functional applications such as energy absorption and thermal management [14].

1.2.1 Energy Absorption, Attenuation, and Damping

The stress-strain behavior of metal open-cell foams subjected to compression loading is illustrated in Figure 1.1. The energy absorption potential arises due to the large area under the curve generated by a characteristic constant *plateau stress* (σ_{pl}) [7]. This energy is not stored, but rather absorbed through the plastic deformation of the cellular structure by buckling of the cell edges, which can be tailored through control of foam density [15, 21]. The strain at which the compression loading has achieved densification of the foam is referred to as the *densification strain* (ε_D), occurring at approximately 50 to 70% strain, at which point the stress begins to rise sharply and the collapsed foam behaves more like a monolithic solid [21].

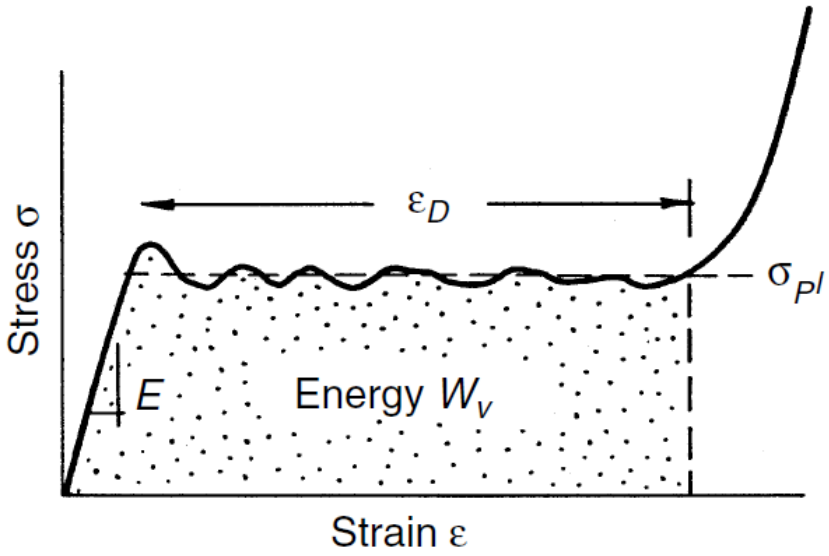

Figure 1.1. Stress (σ) vs. strain (ε) plotted for an ideal energy absorber illustrating the characteristic plateau stress (σ_{pl}) and absorbed energy up to the densification strain (ε_D) resulting from a large plastic deformation. [4]

The energy absorption potential of metal open-cell foams has resulted in applications as impact attenuators, crash structures, projectile defense, packaging, and blast mitigation [4, 7, 22-25]. Commercially, metal open-cell foams have been used in bolt capture mechanisms, emergency landing systems, and micrometeoroid debris shields [21].

Metal open-cell foams have been considered for acoustic absorption due to their increased damping capacity compared to full dense monoliths [2, 14, 20, 26, 27]; however, cell size plays a critical role as relatively large (> 1 mm) and small (< 0.1 mm) cells perform poorly as acoustic absorbers across a wide range of frequencies [23, 28]. Additionally, metal open-cell foams have been used to dampen pressure pulses and mechanical vibrations [16]. In a very specialized case, aluminum open-cell foam filled with various secondary phases was used for radiation shielding by attenuating gamma rays and thermal neutrons [29].

1.2.2 Thermal Management

Metal open-cell foams show promise in thermal management applications due to their large surface areas, high thermal conductivities, and permeability, as shown in Figure 1.2. These properties enable high heat transfer rates due to the mixing of internally circulated cooling fluids, with twice the heat transfer effectiveness of conventional finned heat exchangers [10, 14, 21, 22, 30-32].

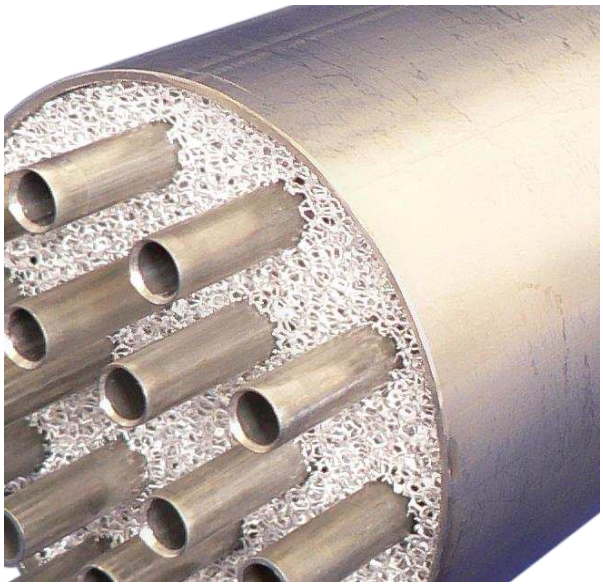

Figure 1.2. Metal open-cell foams are used for thermal management, with such applications as heat exchangers. [21]

Heat exchangers, heat sinks, and heat pipes have been constructed based on copper and aluminum open-cell foams to provide thermal management of aeronautical equipment, power electronics, medical products, defense systems, industrial power generation plants, process intensification reactors, cryogenics, condenser towers and regenerators [4, 10, 14, 16, 21, 22, 33-36]. Specifically, metal open-cell foams have been used as fluid-fluid heat exchangers for the Space Shuttle atmospheric control system [4]. Elevated temperature

capable heat exchangers have been fabricated from tungsten open-cell foams for application as nuclear reactor components [37]. Extensive research has been carried out to investigate the heat transfer capabilities of metal open-cell foams in different configurations subject to various boundary conditions, with both air and liquids as the heat transfer fluid medium [36, 38-48]. Not surprisingly, the heat transfer performance of metal open-cell foams is largely dependent on the porosity, pore size, and heat transfer paths to the container walls (if internal) and that optimization of the cellular structure could lead to increased heat transfer performance [10, 32, 38-41, 49].

1.2.3 Additional Applications

Nickel-based electrodes for nickel-metal hydride (NiMH) and nickel-cadmium (NiCd) rechargeable batteries was the largest commercial consumption of stochastic metal open-cell foams based on weight savings and higher energy densities [14, 16, 20, 50, 51]. Similarly, stochastic lead foams have been investigated as current collectors for lead-acid batteries due to their high specific surface areas [52-54]. Additionally, metal open-cell foams have found usage in fuel cells due to their high surface areas, as well as usage in fuel cell stacks for thermal management, flow distribution, membrane support, and current collection [16, 55].

Metal open-cell foams have found usage as catalyst support structures for catalytic reactions due to their high surface areas, enhanced heat and mass transfer rates, and thermal capabilities [16, 56-59]. Applications include diesel particulate filters [60] and catalytic degradation of pollutants [10, 61, 62], such as removing nitrogen oxides from power plant exhaust fumes [16].

Furthermore, metal open-cell foams are used to control the motion of fluids, such as air-oil separators for use in aircraft engine gearboxes [21], internal anti-slosh baffles within pressure tanks [4, 21], flame arresters [21], fluid pressure control within submarine-launched ballistic missiles [21], and as gas distribution media [55] shown in Figure 1.3. Metal open-cell foams have been used for elevated temperature fluid filtration within corrosive environments, such as diesel particulate filters [4, 14, 50]. Additionally, refractory metal open-cell foams show potential as liquid fuel injectors within the combustion zones of rocket engines due to their high fluid mixing performance, low pressure drop, and elevated temperature material properties [37].

Figure 1.3. Metal open-cell foams are used to control the motion of fluids, with such applications as air-oil separators (LEFT), and flame arresters (RIGHT). [21]

Aluminum open-cell foams have been used as the core material in lightweight composite mirror structures with both flat and curved optical surfaces due to the high specific

stiffness requirements of advanced mirror systems [4, 37]. Reactive, ultra-light metal foams, such as those made from Mg-Li-Al alloys, have been considered for space applications [63].

1.2.4 Multifunctionality

Metal open-cell foams are strong candidates for multifunctional materials, where two or more applications can be realized simultaneously, for example, lightweight, load-carrying structures with additional functionality such as fluid flow, energy absorption, filtration, vibration control, thermal management, or power storage capabilities [4, 6, 7, 20, 64].

One example of metal open-cell foams utilized for multiple applications is a gas-permeable catalyst support structure which also functions as a heat exchanger, shown in Figure 1.4. Embedded tubes are sintered within the foam to create a structural reinforcement and thermal pathway resulting in excellent heat transfer, improved stiffness along the tube axis, and a uniform catalyst support structure with controlled permeability [55].

Another example of a multifunctional application is a liquid fuel injector used within the combustion zones of rocket engines [37]. Based on refractory metal open-cell foams, the liquid rocket fuel injectors combine excellent elevated temperature properties, such as strength, oxidation resistance, and thermal shock resistance, with high performance mixing characteristics at low-pressure drops [37].

Figure 1.4. A metal open-cell foam demonstrating multifunctionality by functioning as both a catalyst support structure and as a heat exchanger. [55]

Multifunctional applications will predominately require the metal foam serve as a load-bearing structure. Most structural applications of stochastic metal foams are as the core material within a sandwich structure and closed-cell foams are preferred due to their stiffness-to-weight ratio when loaded in bending, as well as their superior shear strength [2, 23, 65-69].

Stochastic metal open-cell foams have been evaluated for structural applications [70, 71]. Specifically, titanium open-cell foams have been considered for orthopedic implants due to titanium's biocompatibility, bone-like stiffness, and the foam's pore structure promoting osteointegration and vascularization for biologic fixation between the implant and tissue [72-76]. Demonstrated applications include an acetabular cup for hip replacement [73], a lumbar spine implant shown in Figure 1.5 [72, 77], a mandibular condyle scaffold [75], dental implants [78], and a knee prosthesis fixation [79]. Although these implants are structural, they are designed to prevent stress-shielding by matching the bone's stiffness through a combination of

titanium's lower modulus and the low intrinsic stiffness of the foam structure. Stress-shielding occurs when the implant has higher stiffness than the surrounding bone, which preferentially loads the implant due to the stiffness mismatch and could lead to bone resorption and loosening of the implant [80-86].

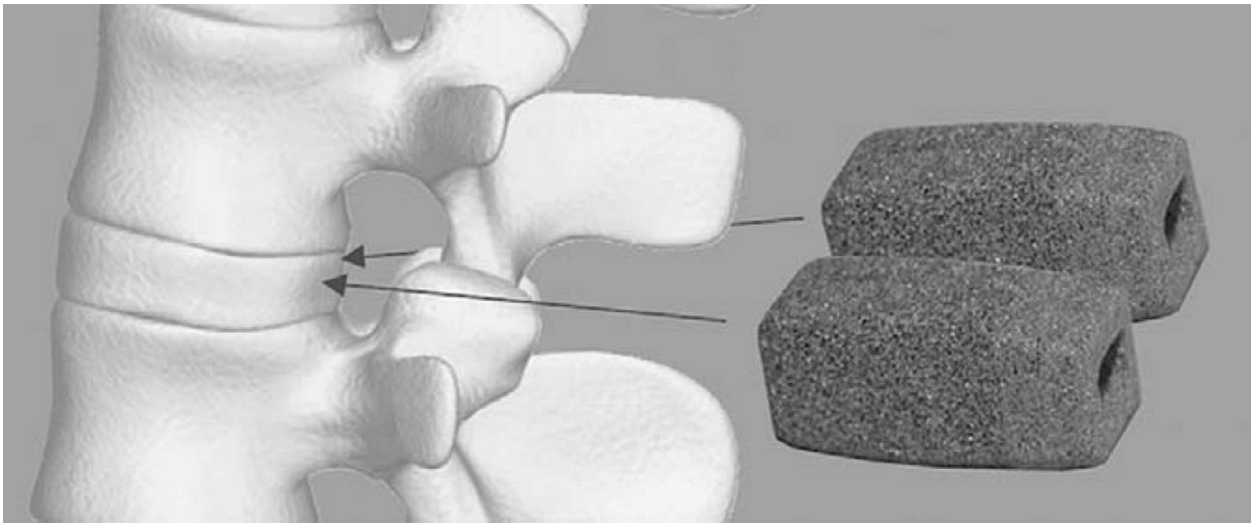

Figure 1.5. A lumbar spine implant fabricated from a titanium foam having a porosity of 65%. [87]

Although orthopedic applications prefer stochastic topologies due to their reduced mechanical properties, most structural applications seek cellular materials with periodic topologies to achieve optimized mechanical performance, as discussed in section 1.4.

1.3 Stochastic Topologies

1.3.1 Fabrication Methods

Fabrication of stochastic cellular metals can be segregated by the methods which produce porous metals and by those which produce metal foams [3]. Porous metals can be produced by entrapped gas expansion [88-91], by gas-metal eutectic solidification (aka.

GASARS) [3, 92-98], by partial, pressureless sintering (aka. *free sintering*) of metal powders [99-105], or by freeze casting of aqueous powder slurries [106-110].

Fabrication methods of stochastic metal foams can be separated into those which produce closed-cells and those which produce open-cells. Closed-cell metal foams have been produced in the liquid state using direct gas injection [2, 111] and gas expansion by foaming agents [2, 112], as well as in the solid-state using gas expansion by foaming agents [2, 113-115] and sintering of hollow spheres [116-120]. Open-cell metal foams are produced using reticulated foam templating and space-holder replication techniques, detailed in the following sections.

1.3.1.1 Reticulated Foam Templating

Reticulated foam templating utilizes a stochastic open-cell polymer foam as either a template upon which the metal is deposited, or as the basis for a mold for which liquid metal is cast into. The variations between reticulated foam templating techniques are due to the way the metal is deposited, or the specific casting technique used.

Deposition methods involve the solid state (powder slurry), ion transfer (electrodeposition), or the vapor phase (CVD, PVD). After the metal is deposited, the polymer template, and any organic binders used to facilitate the deposition process, is pyrolyzed through an elevated temperature heat treatment. Further thermal exposure sinters the metal coating into a densified structure possessing characteristic hollow cell edges once occupied by the polymer template [13, 20, 22].

The polymer foam template can also be carbonized prior to the deposition process to create a vitreous, reticulated amorphous carbon foam template to allow higher sintering temperatures required of the more thermally stable metal alloys [37, 121, 122].

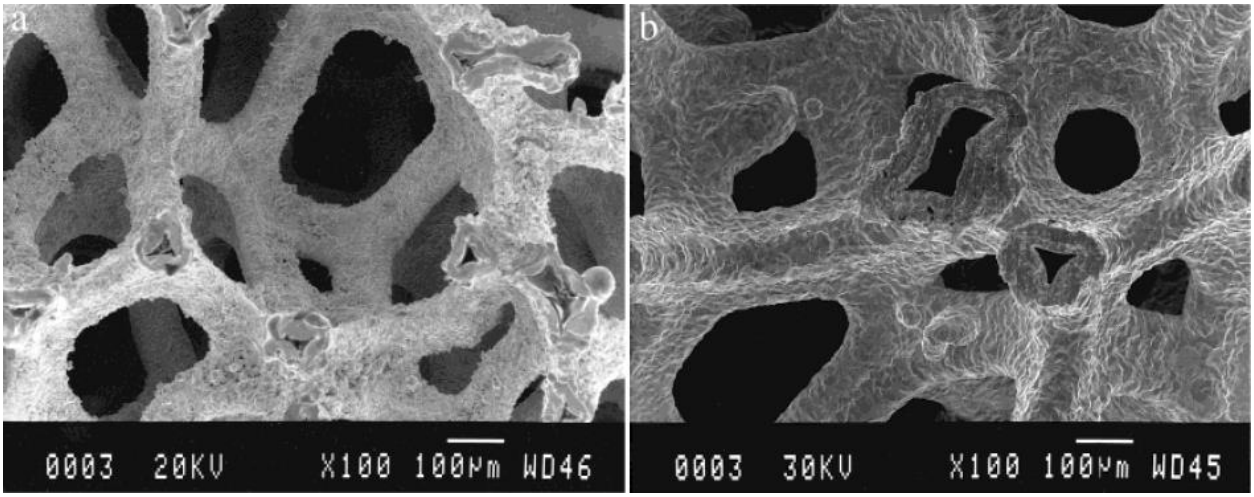

Figure 1.6. Tantalum open-cell foam fabricated using CVD deposition technique. [123]

In the solid-state deposition process, a slurry containing the metal powder and various organic binders is immersion- or spray-coated onto a reticulated polyurethane foam prior to sintering. Titanium [124-126], stainless steel [127], tantalum [122], and Inconel [121] metal open-cell foams created using the powder slurry deposition technique have been reported in the literature.

Ion transfer deposition uses electrolytic methods to layer metal ions onto a polymer template (cathode), which is made electrically conductive through sputtering or ionic deposition of a conductive layer [16, 128]. The metal ions are generated from the dissolution of a metal electrode (anode) within an electrolyte solution [16, 128]. Ion deposition via electrolytic methods is limited to a few metallic elements with alloys proving difficult [128]. The deposition rates are low and often result in non-uniform coatings on the polymer

templates [128]. The lack of alloying and variation in deposition thickness restricts the foam properties [128]. Nickel [129] and lead [52, 54] foams formed from ion transfer deposition have been reported.

Illustrated in Figure 1.7, chemical vapor deposition (CVD) uses the decomposition of a feed gas, such as a metal carbonyl, to coat heated reticulated foam templates with metal vapor [4]. CVD allows high deposition rates of elemental metals and some of their alloys and is not restricted to line-of-sight deposition [128]. While the initial capital investment to obtain a CVD system is relatively low, the use of toxic, thermally decomposable gases results in a costly process with environmental concerns [128]. Nickel [4], zirconium [128], hafnium [128], and the refractory metals [37, 128] (i.e. niobium, molybdenum, tantalum [123, 130], tungsten, and rhenium) have been reported in the literature.

Similarly, physical vapor deposition (PVD) uses metal spray, thermal evaporation, reactive sputtering, arc-vapor, and electron beam techniques to deposit metal vapor on reticulated foam templates with Inconel-alloy metal foams reported [128]. PVD is capable of depositing most elemental metals and their alloys, including in multilayered or functionally graded arrangements, but the high-vacuum environment causes stoichiometry variations in alloys with vastly different vapor pressures [128]. Furthermore, the high-vacuum environment restricts deposition to line-of-sight to the vapor source resulting in low deposition rates and uneven coating of the polymer template [128].

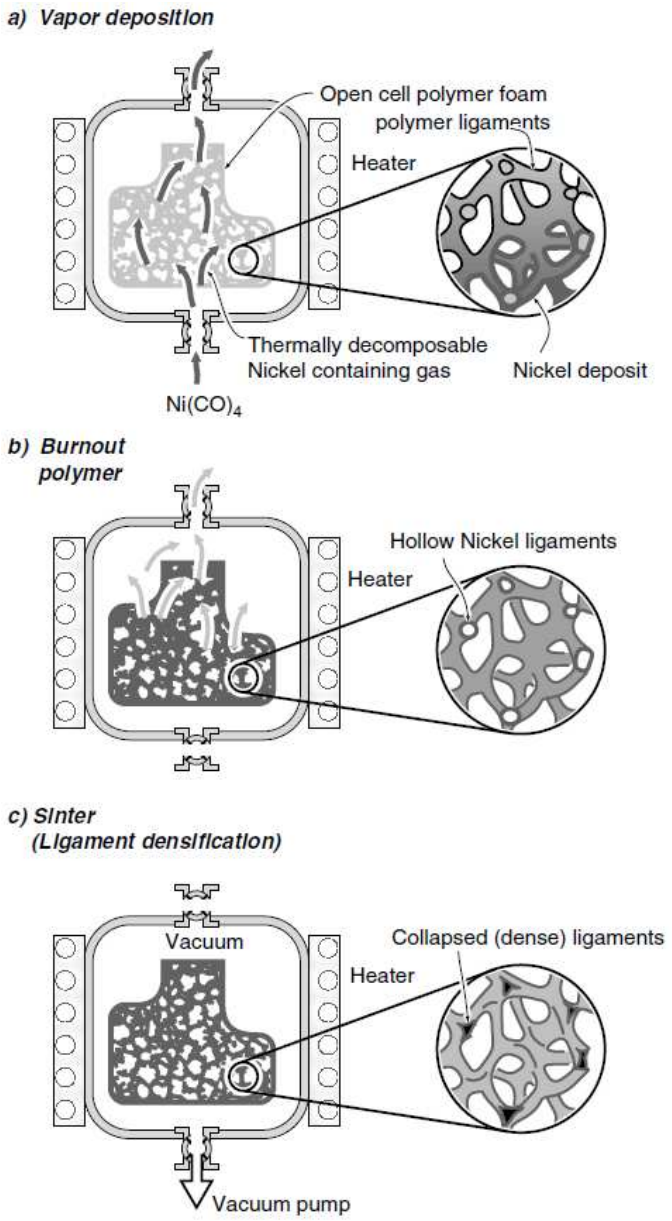

Figure 1.7. Chemical vapor deposition coats heated reticulated foam templates with a metal vapor obtained from the thermal decomposition of a feed gas to achieve highly porous metal open-cell foams. [4]

Reticulated polymer foams can also be used to generate molds for the casting of liquid metals. As illustrated in Figure 1.8, one technique involves coating the polymer foam with plaster or casting sand and then pyrolyzing the polymer. Liquid metal can then be poured into the plaster mold, which is typically evacuated under vacuum to facilitate filling of the complex

and restrictive channels [2]. The metal is solidified, and the mold material removed. Any metal that can be investment cast is a candidate material, but easily castable, low-melting point alloys are preferred [121]. The investment casting approach struggles to produce metal open-cell foams with pores smaller than approximately 500 μm [131]. Aluminum [16, 132-136], copper [16, 132-134], iron [134], magnesium [16, 133, 135-139], nickel [134], lead [53, 132], tin [132], and zinc [16, 132-134] metal open-cell foams have been reported in the literature.

A variation of investment casting is the lost-foam or evaporative pattern casting technique where the template is not pyrolyzed prior to pouring of the liquid metal, instead the liquid metal directly pyrolyzes the polymer template as it comes into contact during the pour [18]. Additionally, reticulated open-cell foam templates are not confined to polymer foams as silicon carbide (SiC) ceramic foundry filters have been used as templates to cast steel foams [17, 140-142]. The SiC templates are subsequently removed by leaching in hydrofluoric acid [17, 140-142].

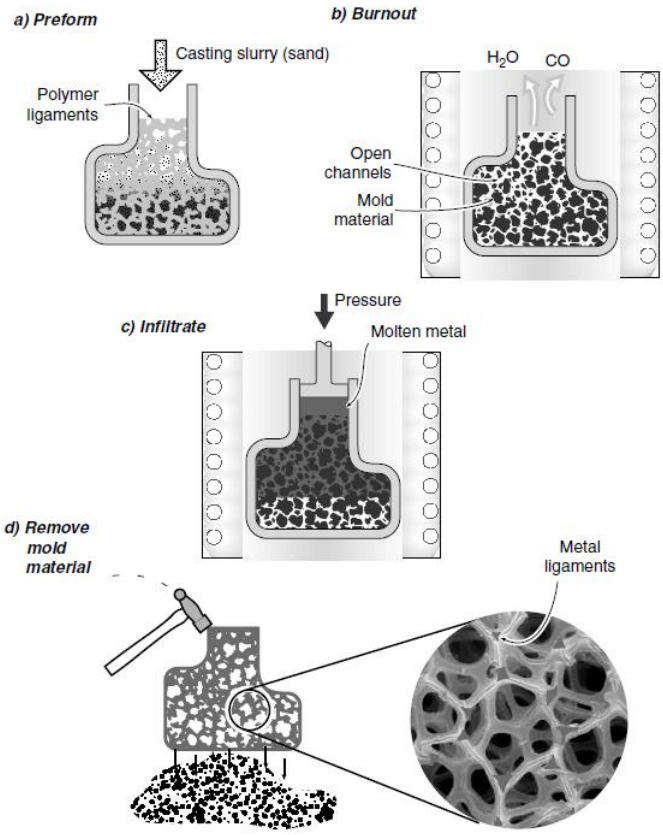

Figure 1.8. Investment casting involves mold creation through the coating and pyrolysis of a reticulated polymer foam template, infiltration of the mold with liquid metal, solidification of the molten metal, and removal of the mold to achieve metal open-cell foams. [4]

1.3.1.2 Space-Holder Replication

In the space-holder replication technique, an interconnected network of leachable porogens (aka. space holders) are assembled into a template. Powder metallurgy or liquid infiltration techniques are used to infiltrate the porogen template, which is subsequently leached from a densified or solidified metal matrix. The resulting open-cell foam possesses a pore structure which replicates the initial template, as shown in Figure 1.9. The first published use of space-holder replication was in 1961 using liquid aluminum infiltration of sodium chloride porogens by the Pittman-Dunn Laboratories in Philadelphia [143].

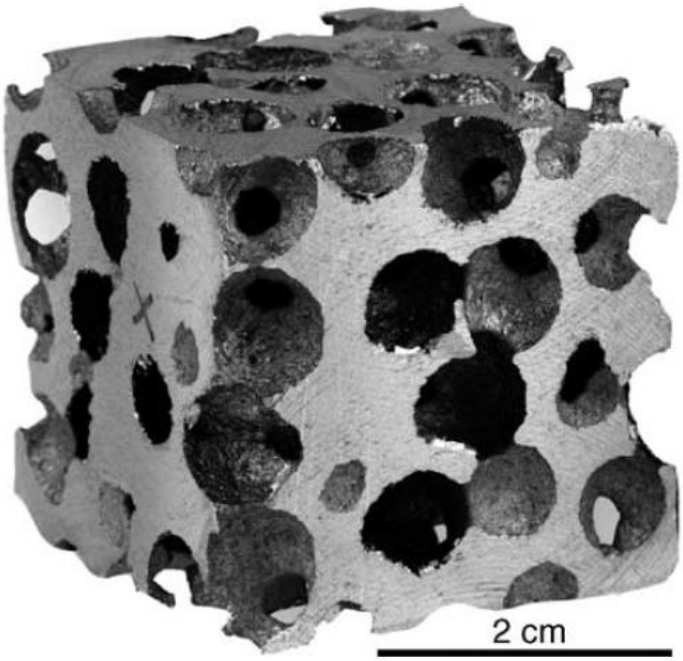

Figure 1.9. Aluminum open-cell foam produced by the space-holder method. [144]

Also known as the sintering and dissolution process [145], space-holder replication has many variations, primarily classified into either powder metallurgy [72, 73, 81, 82, 131, 145-188], liquid infiltration [5, 70, 153, 189-207], or metal injection molding [208-214].

Illustrated in Figure 1.10, the powder metallurgy technique involves mixing the porogens with metal powder, compacting the mixture into a die, followed by sintering and porogen leaching. Foams of aluminum [145, 148, 151, 160, 161, 172, 173, 175, 180, 181, 185, 186], copper [149, 150, 155, 156, 177-179], iron [169], nickel [147, 162, 168], lead [153], magnesium [163, 182, 183], steel [162, 171], and titanium [72, 73, 81, 82, 131, 146, 152, 154, 157-159, 162-167, 170, 174, 176, 184, 187, 188] have all be fabricated using powder metallurgy-based space-holder replication.

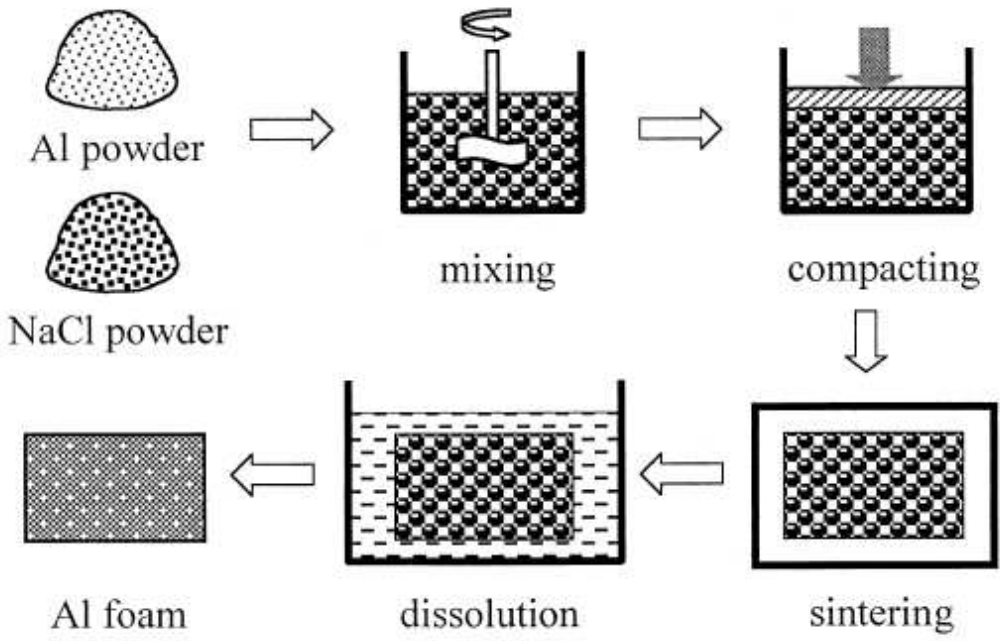

Figure 1.10. Powder metallurgy-based space-holder replication involves the mixing of a sacrificial porogen with a metal powder, compacting the mixture into a green-body, densifying the metal powder by sintering, and leaching the porogen material to achieve a metal open-cell foam. [145]

As depicted in Figure 1.11, the liquid infiltration technique involves assembling the porogens into a template, which can be sintered to bind the particles for strength, infiltrating the template with the liquid metal, directional solidification, followed by machining, porogen leaching, and post-processing [18]. Various infiltration techniques have been used including unassisted [199, 202, 206], vacuum-assisted [197, 205], gas pressure-assisted [5, 70, 189, 192-196, 198, 200, 201, 203, 204, 207], and mechanical-assisted [153, 190, 191]. Metal foams produced through liquid infiltration have been reported for aluminum [5, 70, 189, 192, 193, 197, 198, 200-206], brass [190], lead [153, 199], shape memory (Cu-Zn-Al) [191], and zirconium bulk metallic glass (BMG) [194-196, 207].

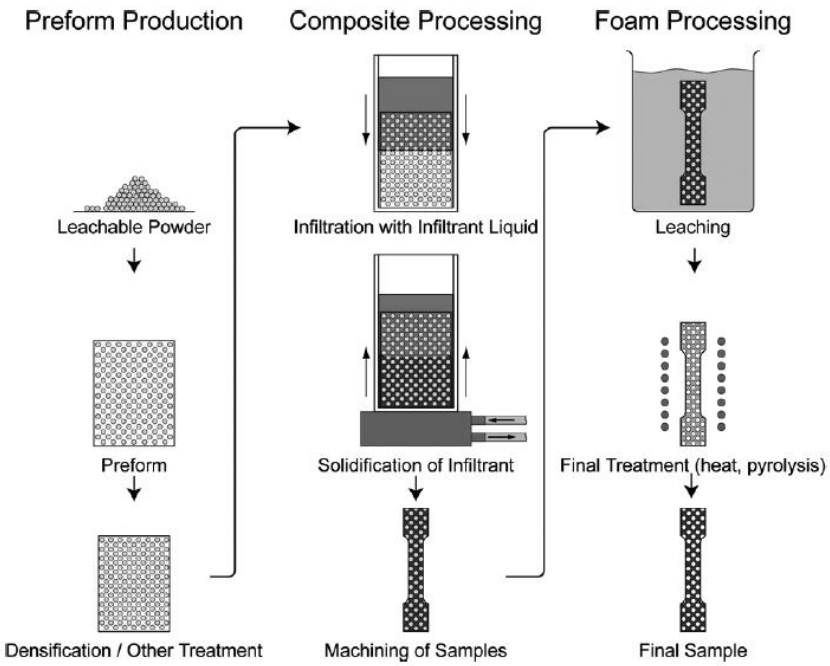

Figure 1.11. Liquid infiltration-based space-holder replication involves assembling the porogens into a template, which can be sintered to bind the particles for strength, infiltrating the template with the liquid metal, directional solidification, followed by machining, porogen leaching, and post-processing to achieve a metal open-cell foam. [18]

The metal injection molding (MIM) technique is a loose combination of the powder metallurgy and infiltration techniques. Illustrated in Figure 1.12, MIM injects a feedstock containing a mixture of metal powder, porogens, and binders, into a die. The binder and porogens are removed and the remaining metal powders are sintered. Both stainless steel (316L) [209-211] and titanium [208, 212-214] foams manufactured by MIM have been reported in the literature.

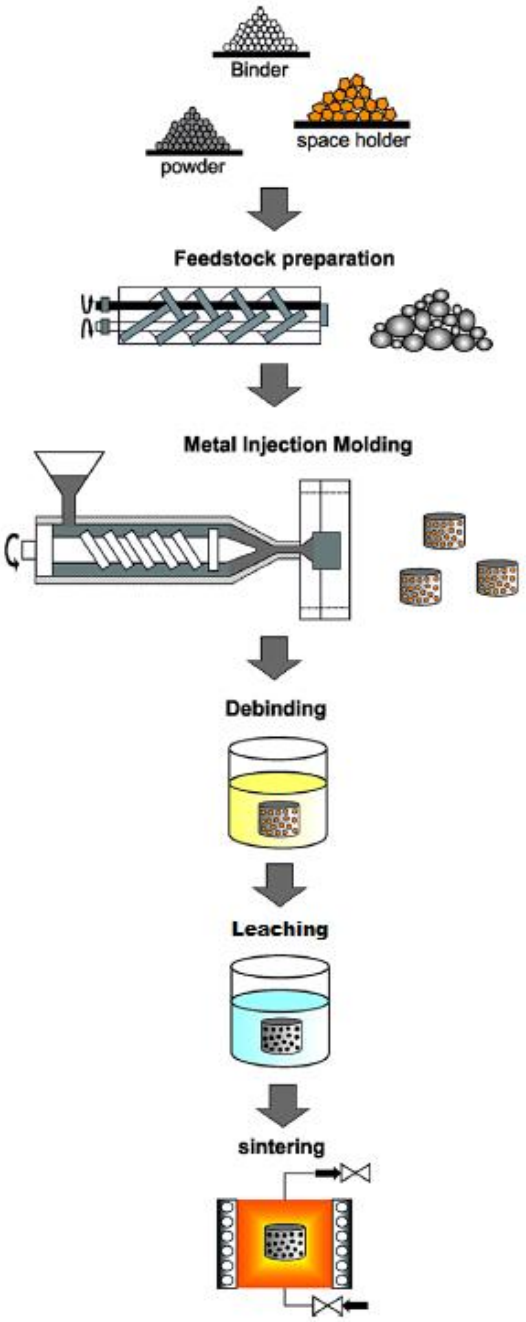

Figure 1.12. Metal injection molding involves the injection a feedstock containing a mixture of metal powder, porogens, and binders, into a die, the removal of the binder and porogens, and the densification of the metal powder by sintering to achieve metal open-cell foams. [213]

Space-holder replication enables the use of assorted porogens summarized in Table 1.1.

Porogens are distinguished by their thermal stability, size, shape, cost, and leaching method.

Porogens are initially selected based on their compatibility with the processing technique, for instance, only porogens with high melting temperatures and chemical inertness are used in the liquid infiltration routes [18]. Porogens are further down selected by their cost and geometry based on the desired pore shape and size distribution.

Porogens are leached through thermal decomposition [72, 73, 106, 131, 146, 153-157, 159, 162-165, 168, 175-179, 182, 187, 188, 209-211] or chemical dissolution, enabled through aqueous reactions with water [5, 70, 81, 82, 145, 147-153, 160, 161, 169-174, 177, 180, 181, 184-186, 189, 192, 193, 197-199, 201-204, 206, 208, 212-216], acids [153, 158, 190, 191, 194-196, 207], or bases [183]. By far, the most widely used porogen is sodium chloride due to its availability, low cost, thermal stability, and high solubility in water.

Table 1.1. Summary of porogens used in the space-holder replication technique.

Space Holder	Melt Temperature (°C)	Processing Technique	Leaching Agent / Method	Refs.
Ammonium Bicarbonate [$(NH_4)HCO_3$]	41.9	Powder Metallurgy	Thermal Decomposition	72, 73, 131, 146, 153, 154, 164, 165, 176, 182
Barium Fluoride [BaF_2]	1,368	Liquid Infiltration	Nitric Acid	194, 195, 207
Carbamide [$CO(NH_2)_2$]	135	Powder Metallurgy	Thermal Decomposition Water Sodium Hydroxide	152, 157, 160, 171, 172, 180, 181, 183, 187
Lanthanum Oxide [La_2O_3]	2,315	Liquid Infiltration	Nitric Acid	196
Magnesium [Mg]	650	Powder Metallurgy	Thermal Decomposition Hydrochloric Acid	158, 159
Poly(methyl methacrylate) [$C_5O_2H_8]_n$	160	MIM Powder Metallurgy	Thermal Decomposition	175, 178, 179, 209-211,
Polyoxymethylene [$CH_2O]_n$	175	Powder Metallurgy	Thermal Decomposition	168
Polypropylene Carbonate [$CH(CH_3)CH_2OCO_2]_n$	150 – 180 (decomposition)	Powder Metallurgy	Thermal Decomposition	188
Potassium Carbonate [K_2CO_3]	891	MIM Powder Metallurgy	Thermal Decomposition Water	155, 156, 177, 208
Potassium Chloride [KCl]	770	MIM Powder Metallurgy	Water	184, 213, 214
Silica Gel [SiO_2]	1,713	Liquid Infiltration	Hydrofluoric Acid	153, 190, 191
Sodium Chloride [NaCl]	801	Liquid Infiltration MIM Powder Metallurgy	Water	5, 70, 81, 82, 145, 147-151, 153, 161, 169, 170, 184-186, 189, 192, 193, 198-203, 206, 212, 215
Sodium Fluoride [NaF]	993	Powder Metallurgy	Water	216
Sucrose [$C_{12}H_{22}O_{11}$]	186 (decomposition)	Powder Metallurgy	Water	173, 174

1.3.1.3 Templating versus Replication

Reticulated foam templating is the only metal open-cell fabrication technique that can produce very high porosities up to 98% [4, 217]. Therefore, reticulated foam templating can

produce foams with higher interconnectivities than space-holder replication, which is limited to 90% porosity [147, 192, 201, 203, 217]. Due to the pyrolysis of the polymer template, the resultant foam possesses characteristic hollow cell edges which degrades the mechanical properties, including the fatigue strength [217, 218]. The mechanical properties can also be affected due the potential solubility of the polymeric template within the metal matrix [159] and from the lack of densification during pressureless sintering.

Additionally, reticulated foam templating struggles to produce metal open-cell foams with pore sizes below 500 μm [217]. The resultant foam pore structure is also limited to the available polymer templates, which appear to be highly stochastic in nature without the ability to tailor the pore structure. Furthermore, the metal matrix is not a replica of the reticulated template, but more appropriately a negative mold since the metal is deposited on top of the template.

In contrast, space-holder replication offers precise replication of the porogen template [148] with a wide range of pore shapes and sizes [217], ranging from 5 mm [160, 172] down to 20 μm [175]. Space-holder replication is a simple, yet mature, process offering uniform control over the volume fraction, shape, and size of the pores as a direct result of the porogen used [5, 18, 81, 156, 217]. This control offers a potential path toward tailoring of the foam properties, which are determined in part by the cellular structure [5, 156].

Additional advantages of space-holder replication include the ability to leave the porogen in place during sintering to facilitate pressure-assisted densification of the metal matrix, with a concomitant increase in mechanical properties [81], and the potential to use water as a simple leaching agent for water soluble porogens such as salts [18]. Porogen

templates tend to be more economical than investment casting compounds used in reticulated foam templating [18].

Space-holder replication is limited by available porogens, which must be thermally and chemically compatible with the chosen metal [217]. Contamination issues are often addressed by leaching the porogens prior to sintering or sintering at a lower temperature to avoid impurities in the metal matrix [162]. Leaching the porogens prior to densification necessitates both pressureless sintering and a reduction in the sintering temperature to maintain geometric integrity of the foam structure due to the risk of pore collapse from the weight and softening of the matrix [18]. Both pressureless sintering and a reduction in the sintering temperature result in a partially-sintered structure containing micro-porosity in the cell edges and a reduction in material properties [81]. The mechanical properties can also be affected by the rough internal cell walls, which not always reflect the surface finish of the porogens [148, 219], while non-spherical porogens can produce undesirable anisotropy in the pore structure leading to directional mechanical property variations [72].

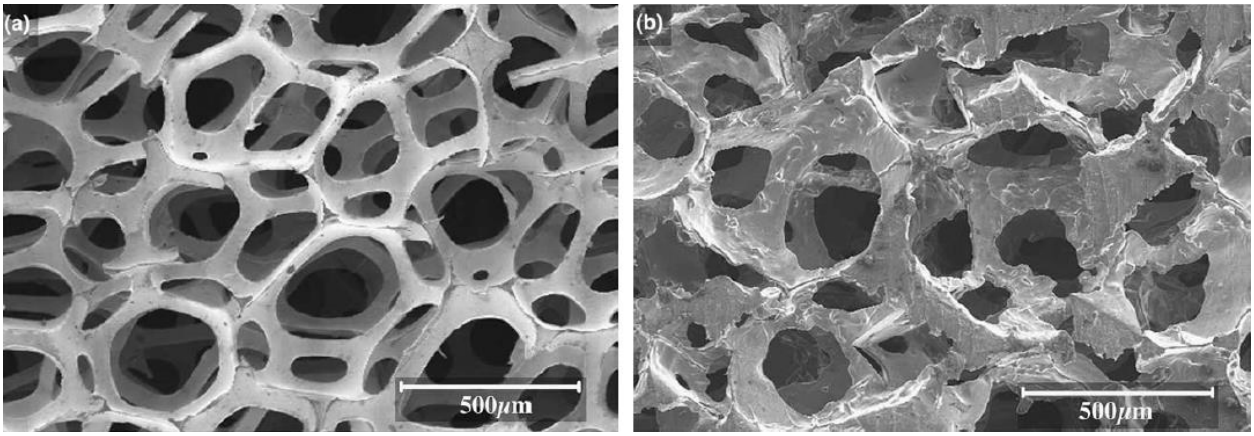

Figure 1.13. Examples of highly porous metal open-cell foams with nearly spherical pores manufactured using reticulated foam templating (LEFT) and space-holder replication (RIGHT). [198]

1.3.1.4 Additive Manufacturing

Stochastic metal open-cell foams have been fabricated without the use of porogens or templates through electron beam melting (EBM) [220-225], laser engineered net shaping (LENS) [226, 227], and selective laser sintering (SLS) [228] additive manufacturing (AM) techniques. Titanium [226-228], titanium alloy [220, 222, 223, 225], copper [221], and cobalt alloy [224] foams have been reported with porosities upwards of 92% [221, 224, 225].

The typical *direct* fabrication route is to import a foam model, developed from computed tomography (CT) scans of stochastic aluminum open-cell foams, into a computer aided design (CAD) software package to manipulate the foam model into the proper geometric configuration. The digitized model is then sliced into sequential layers by a computer aided manufacturing (CAM) software for the AM machine to consume [220-225]. A single digitized model can produce varying degrees of porosities as illustrated in Figure 1.14.

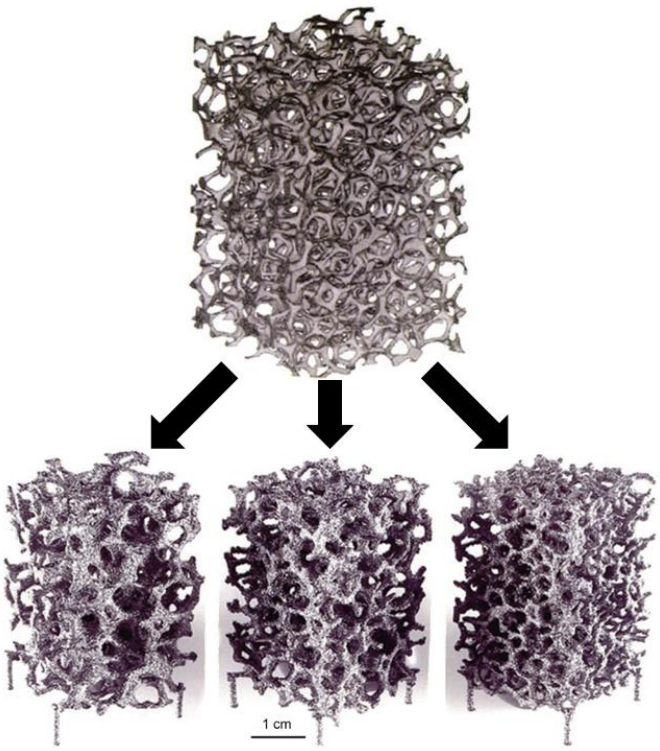

Figure 1.14. (TOP): Three-dimensional model of a stochastic open-cell foam generated by X-ray micro-computed tomography. (BOTTOM): Three titanium alloy foam structures with densities of (left to right) 0.58, 0.68, and 0.83 gcc fabricated from the model using Electron Beam Melting. [220]

The typical *indirect* fabrication route involves restricting the AM machine energy source (laser or electron beam) to prevent full melting of the metal powder resulting in interparticle voids, although this technically results in a porous metal and not a metal foam due to the limited porosities generated: 27% [226], 40% [227], and 65% [228], reported.

1.3.2 Limitations

The main limitation of stochastic metal open-cell foam fabrication methods is the lack of control of the cellular structure over size, shape, spatial distribution, and interconnectivity of the individual pores, the consequences of which are detrimental variations in the foam properties [229]. While space-holder replication offers increased control of the cellular

structure over reticulated foam templating, it does not provide *absolute* control of individual pores [230], as evidenced by the random packing arrangements of the porogens leading to variations in the pore interconnectivity and cell edge thickness [217]. Additive manufacturing techniques provide an opportunity to increase the control and open avenues to tailorability of the cellular structure, but as will be discussed in section 1.4.2.3, direct AM techniques have prohibitive manufacturing-related barriers to realizing fully functional metal open-cell foams.

Moreover, to position metal open-cell foams as multifunctional materials, their cellular structure must be optimized for load-bearing applications through the implementation of periodic topologies, which will require the precise control of individual pores during both the design and manufacturing phases.

1.4 Periodic Topologies

It has been established that the mechanical properties of stochastic metal open-cell foams are limited due to the variability of the individual cells [20]. Periodic topologies offer the potential to obtain repeatable, near-theoretical properties based on a single, repeating unit cell [16, 20], while demonstrating superior performance compared to stochastic topologies at the same relative density [6, 8, 20, 231-233]. Examples of periodic core materials used in sandwich panel constructions are shown in Figure 1.15 for two-dimensional topologies and Figure 1.16 for three-dimensional topologies [231]. Two-dimensional periodic topologies (aka. prismatic) are constructed of honeycomb and corrugated geometries, while three-dimensional periodic topologies are constructed of lattice-truss architectures. Of the periodic topologies, the three-dimensional geometries have shown the most promise for multifunctionality due to their structural capabilities and open architectures.

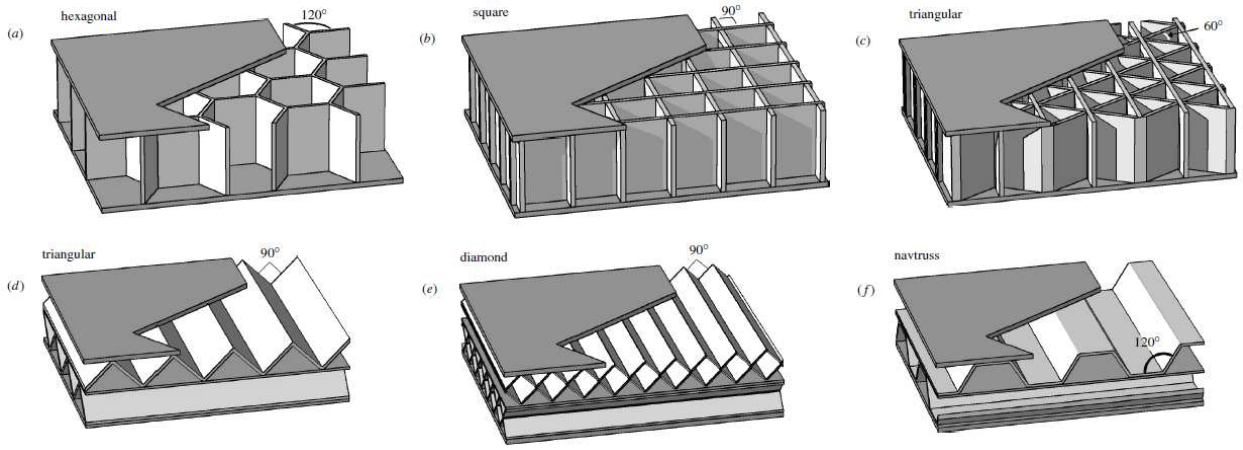

Figure 1.15. Various periodic/prismatic core materials used in sandwich panel constructions based on two-dimensional honeycomb (top) and corrugated (bottom) geometries. [231]

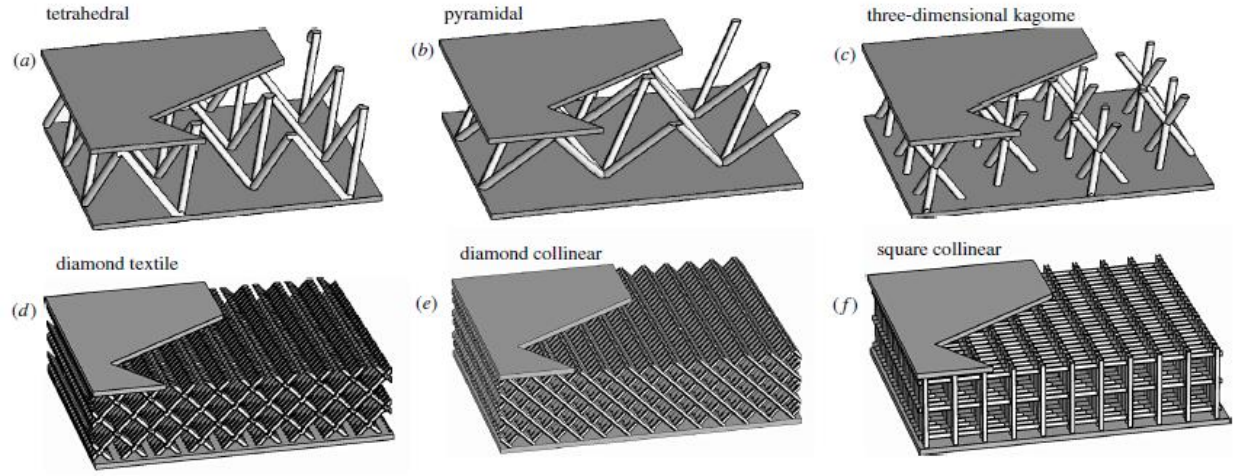

Figure 1.16. Various periodic core materials used in sandwich panel constructions based on three-dimensional lattice-truss architectures. [231]

1.4.1 Lattice-Truss Architectures

Lattice-truss architectures are designed to carry load using minimal mass by stressing the individual member struts in tension or compression without bending [6, 234]. As shown in Figure 1.16, lattice-truss architectures consist of tetrahedra [234-240, 253], pyramidal [241-250], kagomé [245, 251-256], diamond textile [8, 240], diamond collinear [257-260], and square

collinear [259, 260] topologies with circular [8, 234, 235, 240-244, 246-249, 251-256, 259, 261, 262], square [236, 238, 240, 245, 249, 250] or rectangular [239] strut cross-sections. Additionally, the octet-truss unit cell shown in Figure 1.17, is another lattice-truss architecture reported in the literature [261].

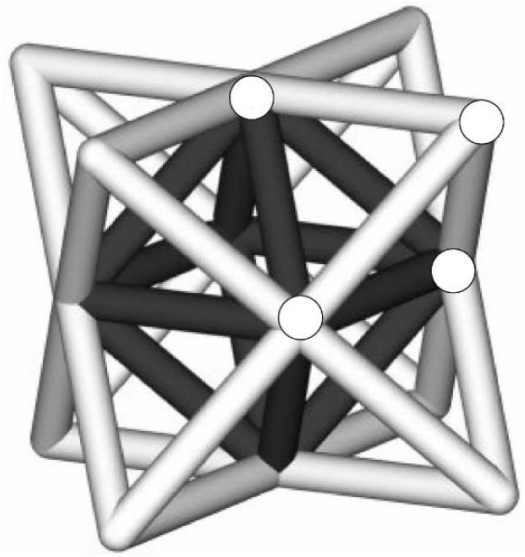

Figure 1.17. Octet-truss unit cell consisting of an internal octahedral cell (dark) surrounded by multiple tetrahedral cells (light). [261]

The sandwich panel constructions illustrated in Figure 1.16 are shown with lattice-truss cores and solid face sheets. A specialized geometric variation is called a *lattice block material* (LBM), a three-dimensional space frame consisting of a pyramidal lattice-truss core with triangulated face sheets as shown in Figure 1.18 and Figure 1.19 [231, 235, 242, 244, 246, 263]. This structural architecture exhibits characteristically high specific strength and stiffness [244, 246]. LBMs are available commercially from JAM Corporation [263], who has patented a low-cost casting process to produce LBMs constructed from a variety of materials [244, 246].

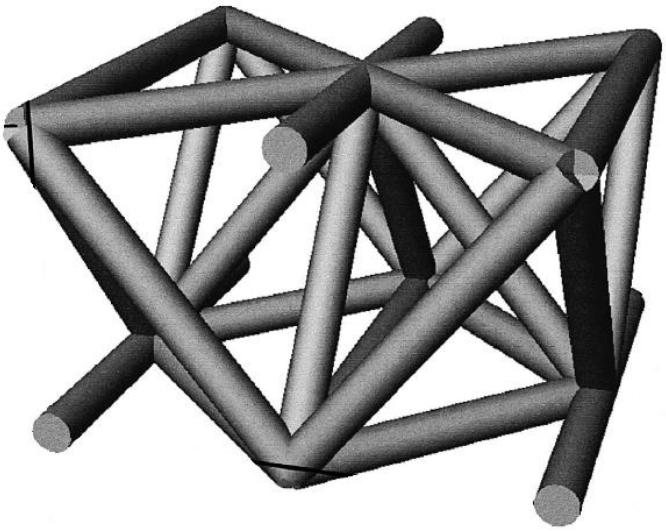

Figure 1.18. Unit cell of the Lattice Block Material consisting of a pyramidal core with triangulated face sheets. [242]

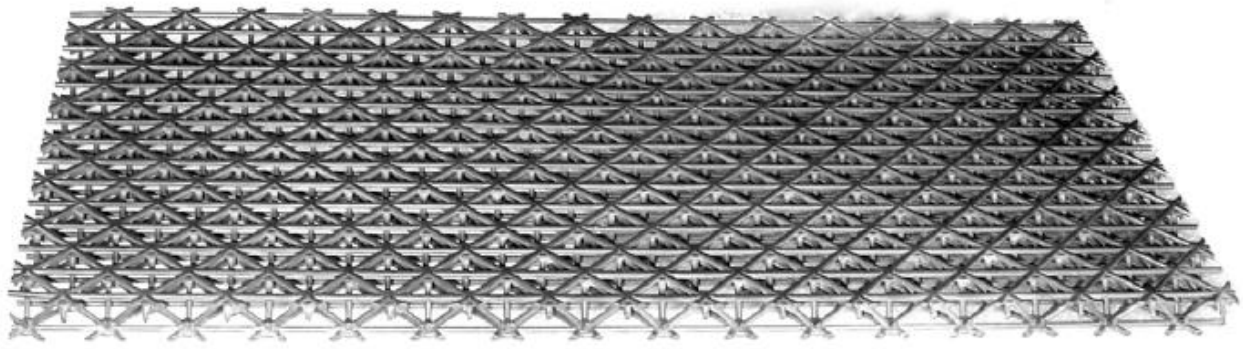

Figure 1.19. Inconel 718 Lattice Block Material produced through a low-cost casting process. [244]

1.4.2 Fabrication Methods

1.4.2.1 Lattice-Truss Architectures

Lattice-truss architectures have been fabricated from aluminum alloys [235, 237, 238, 240-242, 248, 252, 261], copper alloys [234, 235, 248, 251, 253], cobalt alloys [248], iron alloys [236, 239, 245, 248-250, 253-256, 259, 260], nickel alloys [8, 243, 244, 246, 248], and titanium alloys [247, 257, 258]. Fabrication techniques include collinear metal layup [259, 260],

investment casting [234, 235, 244, 246, 247, 251, 261], lithography + electrodeposition [243], perforated metal sheet forming [236-240, 245, 249, 250], additive manufacturing (Selective Electron Beam Melting) [257, 258], and woven metal textile layup [8, 240, 252-256]. Examples of collinear metal layup, perforated metal sheet forming, and woven metal textile layup are illustrated in Figure 1.20, Figure 1.21, and Figure 1.22, respectively.

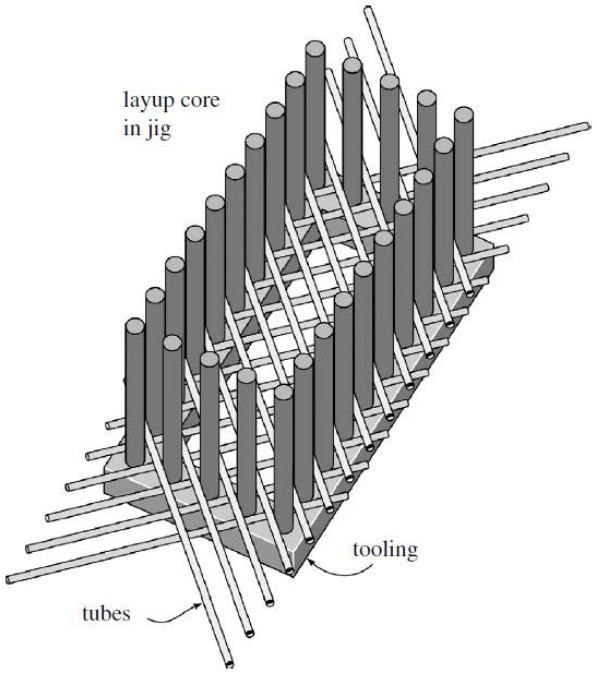

Figure 1.20. Collinear metal layup technique to fabricate lattice-truss architectures. Wires or tubes are laid up in a jig to control spacing and orientation, followed by bonding or welding at the points of contact. Once the proper thickness is built-up, the square/diamond collinear lattice-truss core is machined to sized and bonded to face sheets. [231]

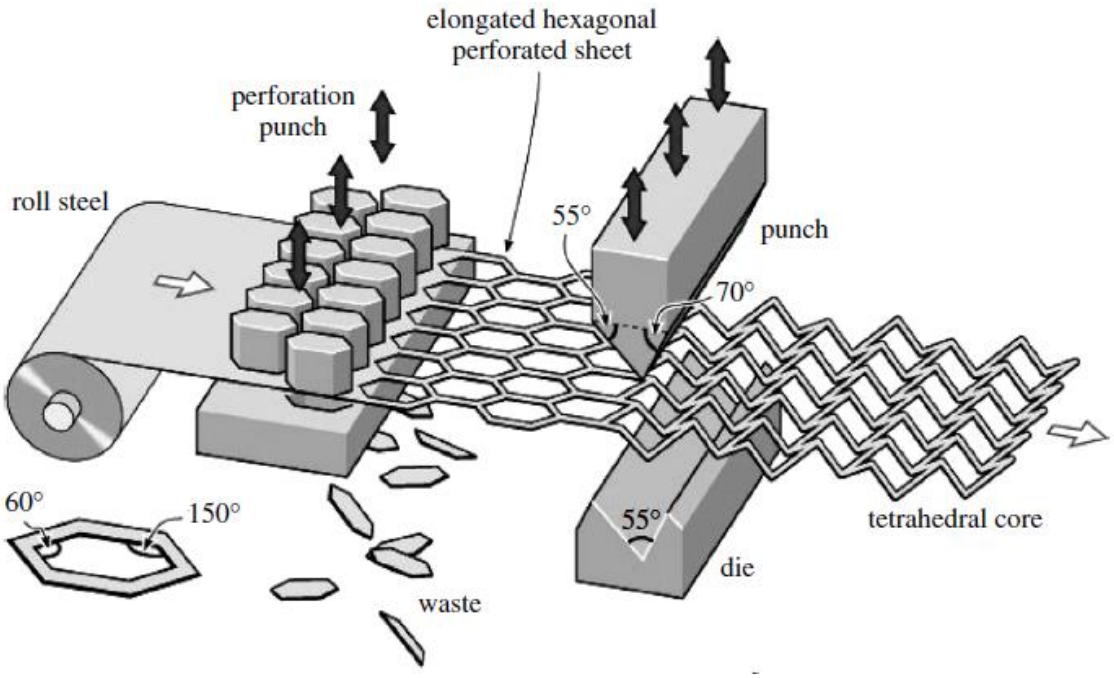

Figure 1.21. Perforated metal sheet forming technique to fabricate lattice-truss architectures. A roll of sheet metal is perforated with a nested pattern of hexagonal-shaped dies and fed into a punch that bends the sheet into a three-dimensional tetrahedral lattice-truss core. [231]

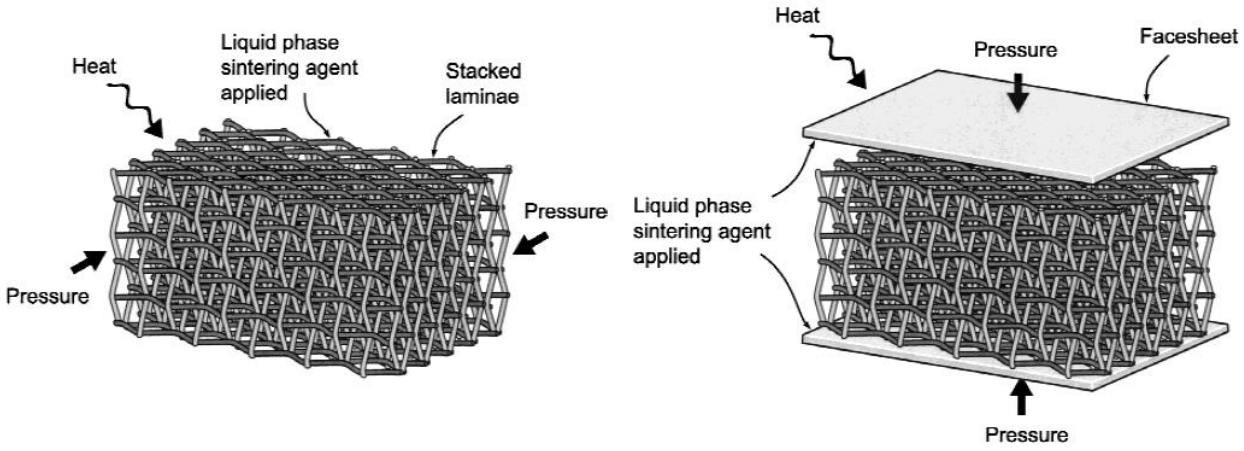

Figure 1.22. Woven metal textile layup technique to fabricate lattice-truss architectures. Circular wires are woven into a plain square pattern to form individual lamina. The laminae are stacked together in an aligned arrangement and bonded at the points of contact to form a diamond textile lattice-truss core, to which face sheets are subsequently bonded. [8]

1.4.2.2 Additive Manufacturing

Periodic topologies can be fabricated through direct or indirect additive manufacturing (AM) routes by consuming digital models. Direct routes "print" the periodic structure layer-by-layer directly from the digital data and either melt or sinter metal powders into the desired geometry. Direct AM routes include three-dimensional fiber deposition (3DF) [264-266], direct laser forming (DLF) [267], electron beam melting (EBM) [220-222, 224, 258, 268-275], laser engineered net shaping (LENS) [226, 227, 276,], and selective laser melting (SLM) [277-279]. An example of a directly printed periodic foam structure and its digital representation is shown in Figure 1.23. Periodic foam structures have been additively manufactured with porosities as high as 96.2% [273].

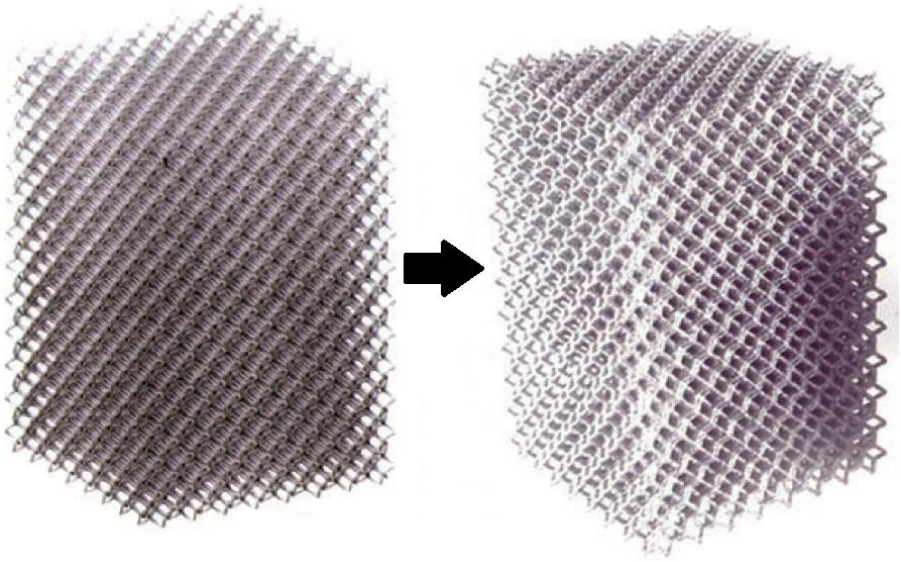

Figure 1.23. (LEFT): Three-dimensional CAD model of a mesh-type periodic open-cell foam. (RIGHT): A titanium alloy foam structure with a density of 0.86 gcc fabricated from the CAD model using Electron Beam Melting. [220]

Indirect routes to periodic structures leverage additive manufacturing to create sacrificial templates for investment casting [280, 281] or for powder metallurgy [282, 283]. A

zinc open-cell foam fabricated using an additively manufactured template and powder metallurgy is shown in Figure 1.24.

An active area of research is attempting to hybridize space-holder replication with current digital fabrication methods. The aim is to integrate *drop-on-demand* concepts into existing additive manufacturing techniques to insert sacrificial porogens into well controlled locations within the powder layer to create and control porosity in final part [284-286]. Porogen insertion techniques include vacuum insertion [287], electrostatics insertion [288-290], acoustic levitation [291], laser-induced forward transfer (LIFT) [292-294], micro-punching [284, 295], and sacrificial material dispensing [285, 296, 297]. A micro-punching technique is illustrated in Figure 1.25.

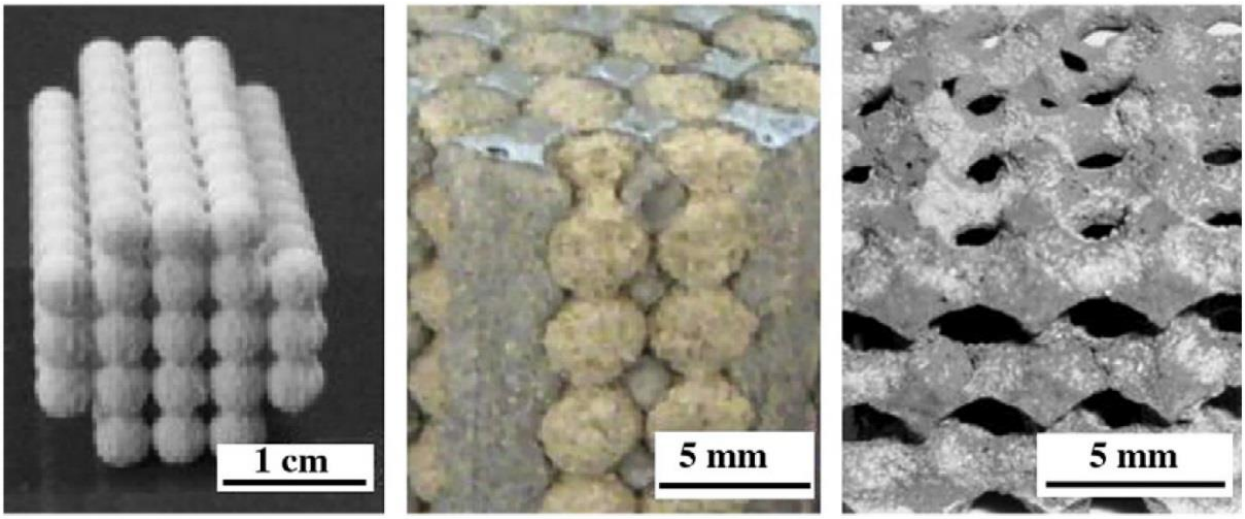

Figure 1.24. Metal open-cell foam fabricated using a sacrificial template consisting of 3.5 mm spheres additively manufactured from calcium sulfate ($CaSO_4$). The sacrificial template was constructed, infiltrated with liquid metal, and leached to realize an open-cell foam with a periodic structure. [282]

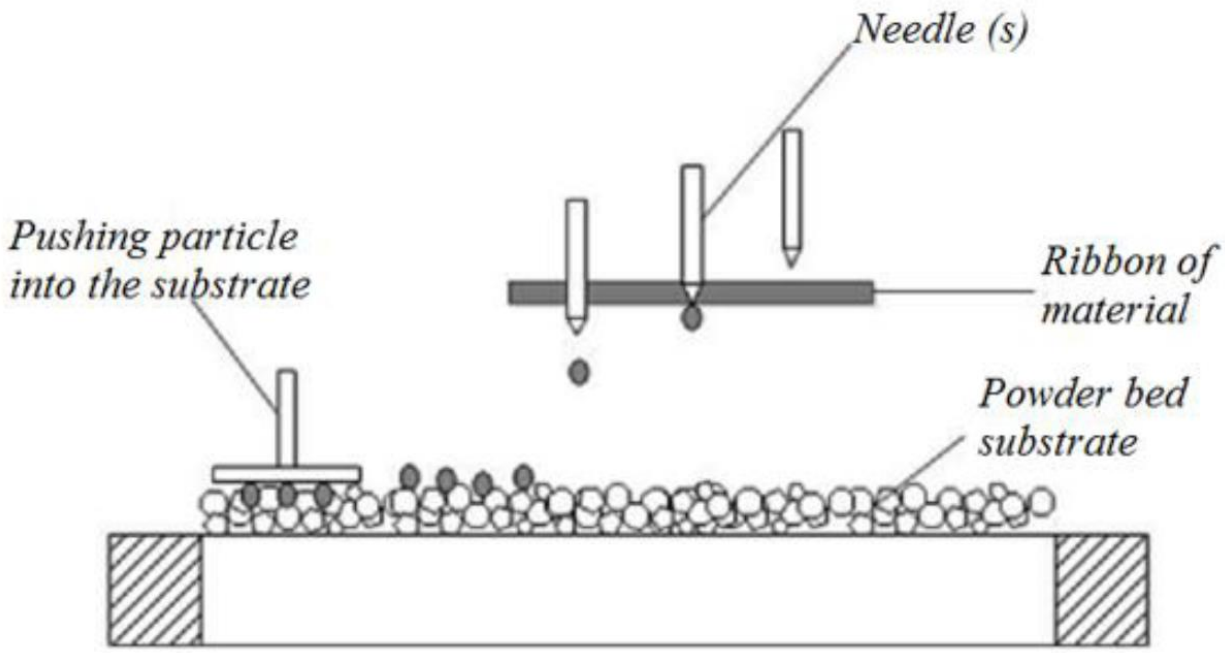

Figure 1.25. Illustration of a micro-punching drop-on-demand technique to insert sacrificial porogens at select locations within a powder bed during additive manufacturing processes. [284]

1.4.2.3 Other Techniques

Related to the lattice-truss architectures is the ultralight micro-lattice formed by electroless nickel deposition onto a sacrificial photopolymer-based template, which is subsequently leached to reveal a periodic structure assembled of hollow-tubes with a density as low as 0.001 gram-per-cubic centimeter (gcc) [298].

Additionally, “regular” foams based on Kelvin unit cells have been fabricated through metal liquid casting into printed sand- or salt-based preforms to create porosities upwards of 90% as shown in Figure 1.26 [299-303].

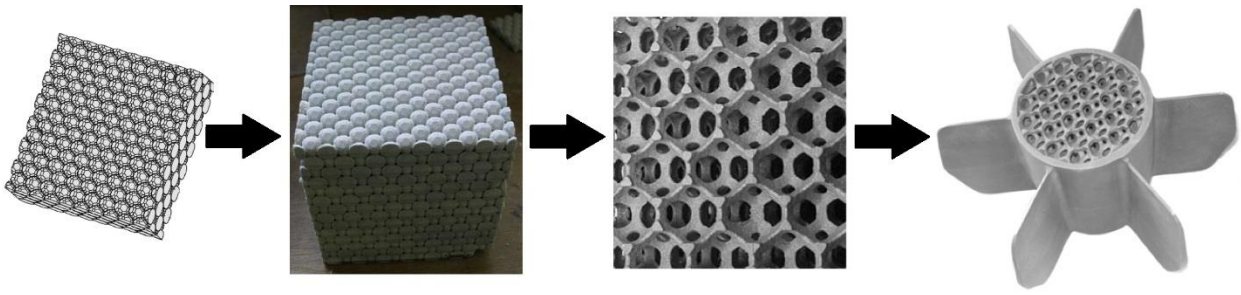

Figure 1.26. Liquid metal casting process to fabricate *regular* foams. A three-dimensional preform based on the ordered arrangement of repeating Kelvin unit cells was designed using CAD software. A sand-based mold was created and infiltrated by liquid metal in a casting process. After metal solidification and sand removal, a highly porous, periodic structure remains. This process was demonstrated on a functional copper thermal exchanger. [299, 301, 303]

1.4.3 Limitations

Periodic architectures have demonstrated superior mechanical properties over stochastic structures and have shown promise for multifunctional applications [6, 8, 20, 236, 304, 305]; however, the full potential of periodic architectures has yet to be realized due to limitations of the current fabrication methods.

Investment casting is relatively expensive, and the intricate molds required of complex periodic topologies necessitates a high fluidity metal be used, limiting material options [8, 20, 234, 236, 251, 304]. The mechanical performance of cast structures is typically reduced due to the significant porosity and casting defects present in the final part [8, 20, 234, 236, 245, 246], which drives the mold design toward facilitating the casting process and away from optimizing the periodic topology [244]. While additive manufacturing of the complex molds can reduce costs, the intrinsic casting challenges are still present, including the limitation on cell size [251, 306].

Fabrication techniques of lattice-truss architectures are limited to a single repeating unit cell throughout the structure; the collinear metal layup, lithography + electrodeposition, perforated metal sheet forming, and woven metal textile layup don't lend themselves to graded structures, the likely result from the tailored design of multifunctional cellular materials [306]. Lattice-truss architectures are also limited to planar geometry, such as sandwich panels, and the fabrication techniques have been demonstrated across only a narrow selection of metal alloys [306]. Lithography + electrodeposition appears to result in hollow replications with limited material build up during deposition creating possible material property concerns to accompany a limited material selection.

Direct fabrication of metal periodic structures using additive manufacturing is faced with challenges related to resolution, surface finish, and material properties [306]. The current powder-based techniques cannot reproduce geometric details below 500 μm [285, 307]. Poor surface finish arises from staircase effects between layers and the inability to fully fuse powder particles into a smooth, homogenous surface [217, 308]. The elevated temperatures required of metal additive manufacturing induces thermal gradients within the part leading to build up of residual stresses and dimensional variations due to flow of material [271, 306]. Metal additive manufacturing techniques are relatively expensive with slow build rates [306]. Support structures are often required to stabilize the part geometry but are potentially an obstacle due to the difficulties removing them from complex internal features typical of periodic structures [285]. Additive manufactured parts often require post-fabrication processing to improve the mechanical properties, including heat treatments and hot isostatic pressing, which can result in

deformation of the pore structure and loss of geometric control without support structures in place [274, 309].

Integrating drop-on-demand concepts into existing additive manufacturing techniques presents an opportunity to enable post-fabrication processing without deformation of the pore structure and loss of geometric control due to the presence of sacrificial porogens; however, this technology is still in the initial development phase with a potential for prohibitive costs due to the complexity of the equipment required and the integration into existing metal additive manufacturing machines [284]. The drop-on-demand concept lacks absolute control of the porogen size, shape and location within the powder bed due to using liquid "drops" which fall into place causing part deformation, poor resolution, and lack of repeatability [284, 297]. Additionally, current drop-on-demand developments appear to be focused on placing polymeric materials at discrete locations within the powder bed and not creating an interconnected network [295]. The insertion of polymeric materials will limit the processing temperature of the part and will require the porogen to be removed prior to post-fabrication processing [284, 285].

2. INTRODUCTION TO SOLID-STATE SINTERING

The purpose of the introduction to solid-state sintering is to establish the baseline knowledge necessary to understand the research presented in Chapter 5, EFFECT OF COPPER POROGENS ON THE DENSIFICATION OF NITI POWDER DURING SPARK PLASMA SINTERING USING MASTER SINTERING CURVES. A brief overview of solid-state sintering, electric current assisted sintering, and the master sintering curve is presented. The electric current assisted sintering process is based on solid-state sintering theory and was chosen to fabricate tailored pore structures discussed in chapter 1, *Introduction to Metal Open-Cell Foams*. The master sintering curve was used to understand the effects on densification of co-sintering metal powders and metal porogens.

2.1 Solid-State Sintering Fundamentals

Powder materials densify through sintering, particle rearrangement, or plastic deformation mechanisms [310]. Sintering is a solid-state process involving the thermally-activated transportation of matter at the atomic scale, which serves to bond the powder particles together to obtain physical properties and remove porosity [311]. The thermodynamic driving force for sintering is the reduction in total interfacial (aka. surface) energy (γA) through a reduction in specific interface energy (γ) and/or interfacial area (A) [310-314]:

$$\Delta(\gamma A) = \Delta\gamma A + \gamma\Delta A$$

A reduction in specific interface energy $(\Delta\gamma)$ occurs through *densification*, whereby solid-vapor interfaces are replaced by lower energy solid-solid interfaces [312]. A reduction in

interfacial area (ΔA) occurs through *grain growth*, whereby two or more particles coalesce into a single, larger particle [312]. These basic phenomena of sintering are illustrated in Figure 2.1.

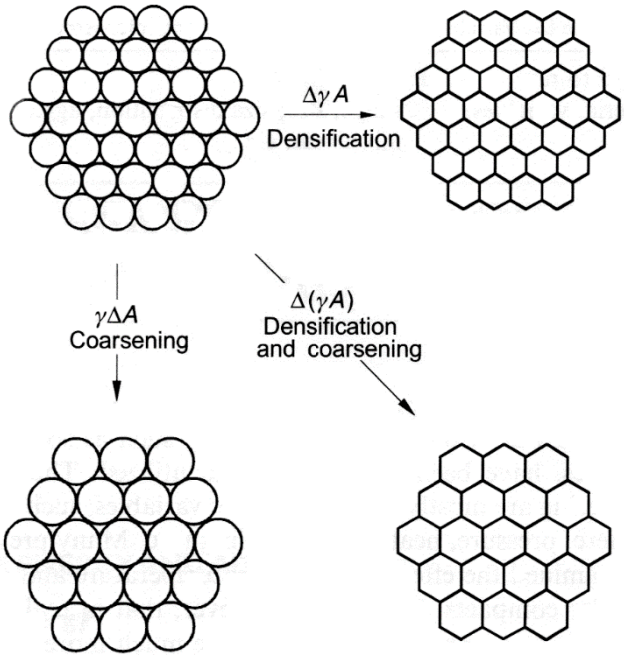

Figure 2.1. Densification and grain growth (aka. coarsening) phenomena of sintering. [312]

Interfacial energy acting over a curved surface generates a *sintering stress*, determined by equating the mechanical work (σdV) required to create surface area to the increase in total interfacial energy (γdA) for a sphere (assumed that powder particles are well represented by sphere geometries) [311, 312]:

$$\sigma dV = \gamma dA$$

$$dV = 4\pi r^2 dr, dA = 8\pi r dr$$

$$\sigma = \frac{\gamma(8\pi r dr)}{4\pi r^2 dr} = \frac{2\gamma}{r}$$

This is the *Young-Laplace equation* and suggests that smaller diameter particles have higher sintering stress, flat surfaces ($r = \infty$) are stress free, and that curved surfaces will

flatten ($r \to \infty$) during sintering [311]. The sintering stress will direct the local flow of matter to eliminate particle curvature provided sufficient atomic mobility exists [311, 313, 314]. The local flow of matter is determined by one of several temperature-dependent mass transport mechanisms, classified into those which originate at a surface or within the bulk [311].

2.1.1 Mass Transport Mechanisms

Surface mass transport mechanisms describe the flow of mass originating from, and terminating at, the particle surface. Mass moves along the particle free surface (surface diffusion), across the open pore space (vapor transport or evaporation-condensation), or through the bulk (lattice or volume diffusion) [311, 313, 314]. Surface diffusion has a low activation energy barrier due to the high atomic mobility along the particle free surface, while vapor transport is active at high material vapor pressures [314]. Surface mass transport mechanisms contribute to particle bonding and coarsening without densification since the origin and destination of mass is the particle surface [311, 313, 314].

However, bulk mass transport mechanisms do contribute to densification by moving mass from the particle bulk to the particle contact neck along the grain boundary (grain boundary diffusion) or through the bulk (lattice or volume diffusion) [311, 313, 314]. Grain boundary diffusion has a higher activation energy barrier than surface diffusion due to the greater disorder of the grain boundary compared to the particle surface [314]. Similarly, volume diffusion has the highest activation energy barrier due to the low atomic mobility within the bulk [314]. Additionally, metal atoms can *plastically* flow from the bulk to the neck through dislocation motions [311, 314].

Surface and bulk mass transport mechanisms are illustrated in Figure 2.2 for a two-sphere model of sintering. Both mechanisms contribute to particle bonding, but only bulk mechanisms promote densification. Multiple mass transport mechanisms can be active during a single sintering process and dominate different temperature regimes relative to the material melting point: surface diffusion is most active at lower temperatures, volume diffusion is most active at higher temperatures, while grain boundary diffusion is most active in between [311, 314]. Elevated temperatures allow for higher activation energy barriers to be overcome by creating more vacancies and providing higher atomic mobility [311, 314]. The relative activations of the diffusion-based mass transport mechanisms are captured by the classical three-stage sintering model, which helps to describe the microstructural evolution resulting from the mass flow during sintering.

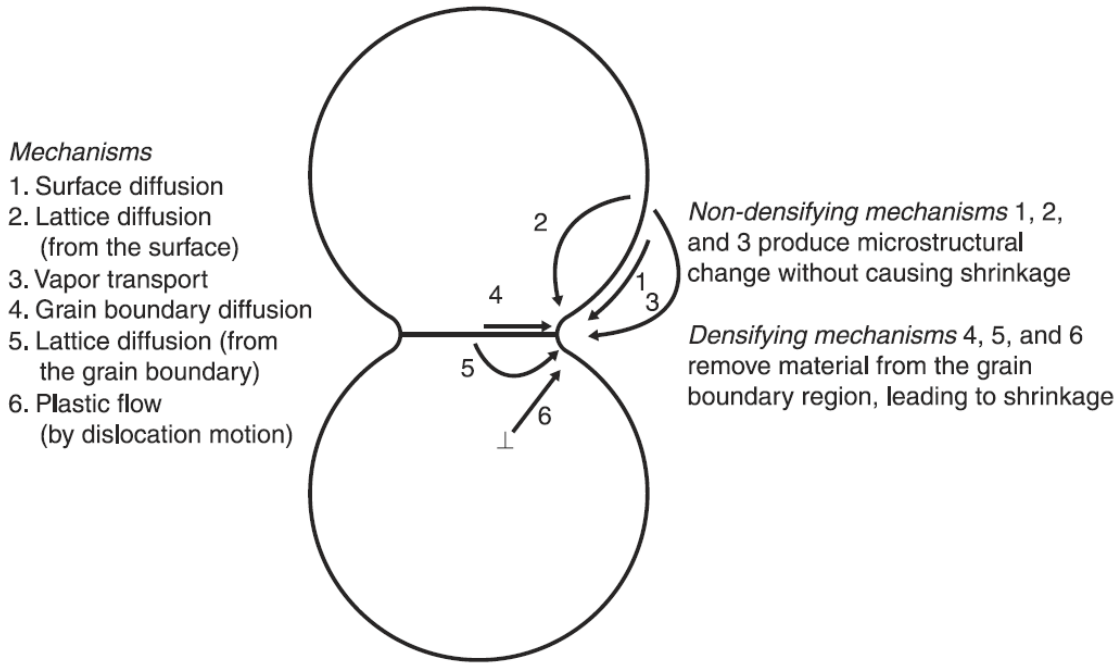

Figure 2.2. Two sphere model of sintering illustrating mass flow paths for surface and bulk transportation mechanisms to the particle contact neck. [314]

2.1.2 Stages of Sintering

As illustrated in Figure 2.3, the initial, intermediate, and final stages of sintering describe the evolution of a *green-body* powder compact through full densification. During the initial stage of sintering, inter-particle bonds develop through the formation of a neck region. Surface diffusion is active during initial stage sintering and serves to grow the neck region, thus, densification is minimal, but surface area loss can be significant. The intermediate stage of sintering is characterized by the rounding, elongation, and eventual isolation of the pore network. The majority of densification occurs during the intermediate stage due to the thermal activation of grain boundary and volume diffusion mechanisms. The isolation of the pore network on grain boundaries occurs between approximately 85% and 93% relative density signifying the end of the intermediate stage [311, 312]. Final stage sintering is characterized by rapid grain growth at the expense of densification. Isolated pores can coarsen and/or detach from grain boundaries and in doing so become extremely stable and nearly impossible to eliminate from the bulk.

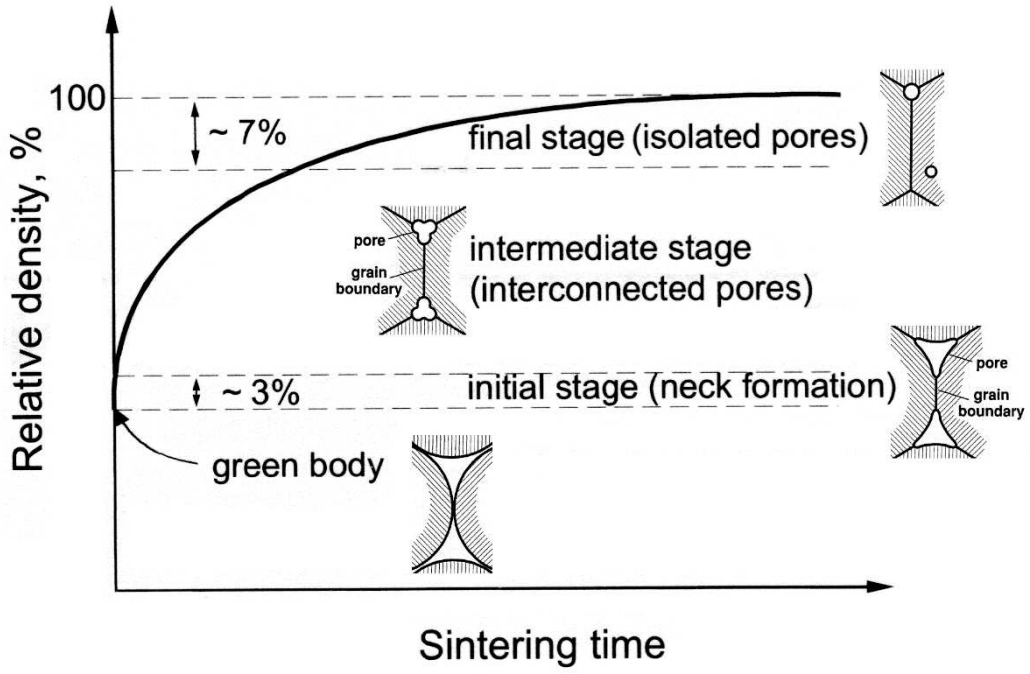

Figure 2.3. Typical densification behavior of a powder compact during the classical three stages of sintering illustrating the pore formation, spheriodization, isolation, and elimination. As the powder compact densifies, the pores are replaced by grain boundaries. Adapted from [311, 312].

2.1.3 Manufacturing Techniques

Densification of powder materials occurs through conventional sintering (pressureless sintering, hot-pressing, etc.) [315-318], self-propagating high temperature synthesis (SHS) [315, 319-325], hot isostatic pressing (HIP) [326-334], electric current assisted sintering (ECAS) [317, 335-347], and metal injection molding (MIM) [184, 208-213, 348-353, 355] techniques.

Although the equipment requires a large capital investment and the present technique is limited to relatively simple part geometries [335, 356], ECAS has demonstrated the ability to fabricate advanced materials with enhanced properties for next generation applications [316, 341, 342, 357-371]. Compared to the other sintering techniques, ECAS can rapidly densify a

wide range of powder materials at lower temperatures with precision control of processing parameters and ease of operation [335, 356].

2.2 Electric Current Assisted Sintering

Electric Current Assisted Sintering (ECAS) is a manufacturing technique which simultaneously applies uniaxial mechanical pressure and Joule heating to densify powder materials under atmospheric control (vacuum, inert, etc.). More than 60 designations exist in the literature for ECAS [372], the most prevalent are summarized in Table 2.1. Spark Plasma Sintering (SPS) is by-far the most popular designation having been coined during the early years of the technology based on anecdotal evidence for the existence of electric sparks and formation of plasma during processing [373].

It appears the first patents related to ECAS were issued to Bloxam in 1906 for pure direct current resistance sintering [375], followed by Hoyt in 1927 for simultaneous application of uniaxial mechanical pressure and an electric current to sinter metal powders [381]. Inoue was issued patents in 1966 [382, 383] and 1967 [384] for his pioneering work to modernize the ECAS technique and equipment. Commercialization of ECAS systems based on Inoue's work began once his patents expired, circa 1990, spearheaded by Japanese companies such as the Sumitomo Coal Mining Co. Ltd. [346, 372, 375]. Today, commercial ECAS systems are manufactured by companies in Japan, Germany, Korea, China, and the United States [374]. The need for increased throughput has driven process automation developments for modern ECAS systems and has resulted in several patented solutions: multi-head [385], tunnel [386], rotary table [387] and shuttle [388] systems [375].

Table 2.1. Various Electric Current Assisted Sintering process designations, abbreviations, and usage [146, 310, 313, 314, 316, 357, 374-380].

Designation	Abbreviation	Usage (%)
Spark Plasma Sintering	SPS	66.2
Pulsed Electric Current Sintering	PECS	7.43
Pulse Discharge Sintering	PDS	3.96
Plasma Activated Sintering	PAS	3.05
Resistance Sintering	RS	1.95
Pulse Current Sintering	PCS	1.83
Plasma Pressure Compaction	P^2C	1.65
Field Activated Sintering Technique	FAST	1.58
Electrical Discharge Compaction	EDC	< 1.5%
Current Activated & Pressure Assisted Densification	CAPAD	< 1.5%
Electric Field Assisted Sintering	EFAS	< 1.5%
Electric Pulse Assisted Consolidation	EPAC	< 1.5%
Electric Current Activated/Assisted Sintering	ECAS	< 1.5%

ECAS has enjoyed wide-scale adoption due to the process efficiencies and the unique assortment of materials it can sinter: metals (elemental, alloys, intermetallic, refractory, etc.), metal matrix composites (MMCs), ceramics (oxide, non-oxide, ultra-high temperature, transparent), ceramic matrix composites (CMCs), glasses, polymers, nanostructured materials, functionally-graded materials (FGMs), cellular and porous materials, shape memory materials, and metastable materials [310, 316, 357, 358, 372]. Patents have been filed for production of magnetic, thermoelectric, electronic, bio-, nano-composite, FGM, and optical materials produced by ECAS techniques [374]. Furthermore, ECAS techniques have been used to generate near-net-shape parts for nozzles, hollow parts, FGMs, annular magnets, automotive pistons, complex parts, and disc brake friction elements [375, 389-393].

2.2.1 Process Details

The key differentiator of the ECAS process is the ability to rapidly densify a powder compact through resistive heating of the powder die and simultaneous application of uniaxial pressure [146, 310, 313]. The ECAS process, illustrated in Figure 2.4, imposes pulsed DC electric current to the powder die to achieve extremely high heating rates upwards of 1000 °C/min [313, 314, 316]. Maximum applied uniaxial loads range from 50 to 250 kN [372], and cylindrical samples with diameters up to 75 mm have been produced [394]. Typical atmospheres include rough vacuum, ranging from approximately 10 to 2 Pa [339, 340], inert gas, such as argon or nitrogen pressurized up to 130 kPa, or a reducing (i.e. hydrogen) environment [358, 372, 394]. Process temperature measurements involve either a non-contact optical pyrometer or thermocouple probes embedded in the graphite tooling.

ECAS tooling (aka. punches and dies) are typically fabricated from high-density graphite due to its low cost, machinability, electrical conductivity, and high elevated use temperature within vacuum environments [314, 394]; however, graphite tooling possesses limited mechanical strength and is generally limited to 125 MPa of applied uniaxial pressure during sintering. Carbon fiber reinforcements have been used to increase the mechanical strength of graphite [372]. For higher strength applications, metal or cemented carbide tooling has been used but are limited to 600 °C; higher temperature capable double-acting tooling with silicon carbide or tungsten carbide internals have been demonstrated, but do not retain the good electrical conductivity properties of graphite [314].

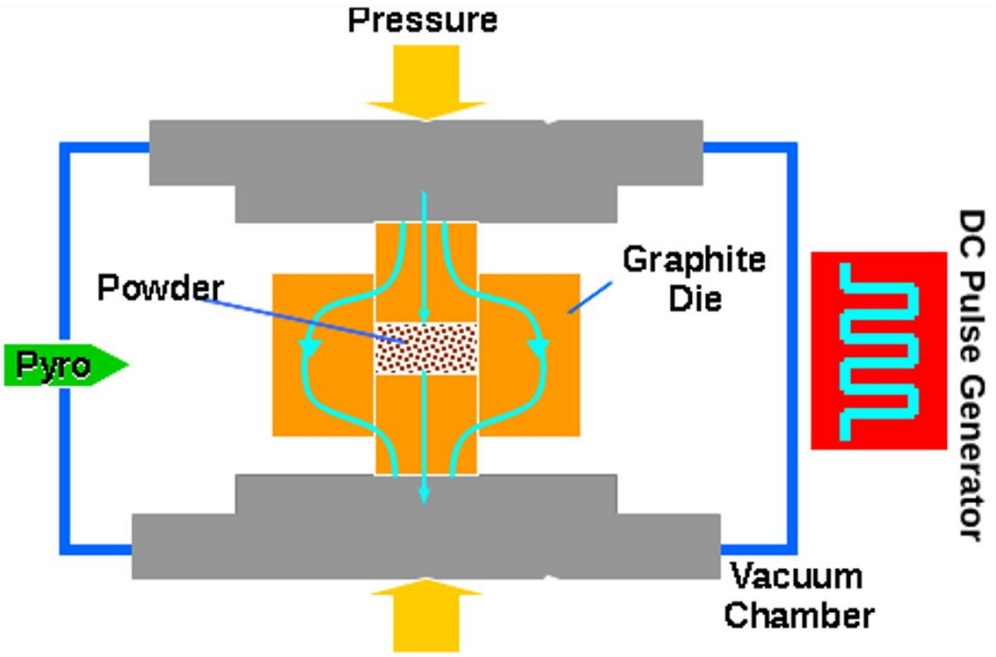

Figure 2.4. Schematic of the Electric Current Assisted Sintering technique. [395]

2.2.2 Processing Benefits & Material Property Enhancements

Compared to conventional sintering techniques (pressureless sintering, hot-pressing, etc.), ECAS can reduce densification times [310, 313, 316, 357, 396-398], lower sintering temperatures [357, 310, 316, 314, 396-398], achieve higher densities [314, 316, 399, 400], and exhibit improved control of material properties and microstructures [384, 401-404]. Reduced sintering temperatures and durations can minimize material vaporization [405-408], inhibit adverse phase transformations [343, 357, 409], and suppress grain growth [313, 410-413].

Furthermore, ECAS has shown its utility in densifying materials, without additives, that are traditionally difficult, if not impossible, to sinter [310, 314, 345, 357, 375, 414-416]. Reduced sintering temperatures and durations has particularly benefited the densification of nano-materials [310, 314], refractory metals [314], and metastable (aka. non-equilibrium)

materials, such as amorphous metals [417-420], cubic boron nitride [421], and silicon nitride [422].

The ability of the ECAS process to sinter specimens with higher density and smaller grain sizes leads to a discernible enhancement of material properties [316, 357, 358, 370]. Improvements in microstructure [341, 361, 362, 371], environmental resistance [359, 360], mechanical properties [341, 359, 364, 368], magnetic properties [365], optical properties [342, 369], thermoelectric properties [366, 367], and electrical properties [341, 363] have been reported in the literature.

2.2.3 Effects of Heating Rate, Applied Pressure, and Electric Current

The processing benefits and material property enhancements due to ECAS sintering are attributed to effects of heating rate, applied pressure, and electric current [313, 316]. High heating rates are used to quickly circumvent the low-temperature, non-densifying surface mass transport mechanisms to minimize grain coarsening, while concomitantly activating grain and volume diffusion to enhance densification [310, 311, 316, 372, 423-426]. Additionally, high heating rates can induce large thermal gradients in the ECAS tooling creating additional driving force for densification [311].

Conventional sintering techniques rely on the intrinsic sintering stress, generated by the interfacial energy of curved surfaces, for densification [311]. Application of uniaxial mechanical pressure during ECAS augments the relatively small sintering stress with a large secondary stress to enhance densification [311, 314]. Pressure has also been applied to break up powder agglomerates prevalent in nanopowders and enables additional densification mechanisms such as particle rearrangement and sliding [310, 314, 374]. Applied pressure has been observed to

reduce thermal gradients within the powder sample by minimizing local concentrations of current and thermal energies through a reduction in contact resistance across the graphite tooling interfaces [427-429]. Densification of metal powders is sensitive to the application of pressure due to the activation of the plastic flow mass transport mechanism [310, 312, 314].

The importance of electric current in generating high heating rates is well established, but the intrinsic effects of the electric field on densification has been debated despite the experimental evidence suggesting enhanced densification [313, 430-432]. It was prominently suggested that the electric current could discharge sparks between particles leading to formation of plasma [433, 434]. The resultant increase in temperature would produce localized melting, vaporization, or sputtering events could increase rates of mass flow to the particle necks [373]. Furthermore, the plasma formation could enhance surface diffusion through a removal of surface impurities and oxide layers [18, 146, 313]; however, experimental investigations into the existence of electric sparks and formation of plasma during ECAS has yielded little supportive evidence [435-438]. Modern theories suggest the electric current stimulates mass flow through electromigration, electroplasticity, interaction with the grain boundary, increase in vacancy concentration, higher vacancy mobility, and Joule heating [313, 316, 375, 430, 439-449].

2.2.4 Limitations

The ECAS process has several notable limitations. The temperature measurement of the graphite tooling, either by optical pyrometer or by thermocouple probe, does not directly indicate the temperature of the powder sample; significant temperature differences can occur between an optical pyrometer focused on the outside surface of graphite die and a

thermocouple probe embedded within graphite die for the same sintering cycle [372]. Furthermore, high heating rates can induce thermal gradients that are not readily detected by the standard single point-source temperature measurement technique typical of the ECAS process equipment. Thermal gradients can persist over the relatively short dwell times common to ECAS resulting in microstructural inhomogeneities in fully dense samples [450, 451]. Additionally, the graphite tooling can contaminate the sintered specimen, although the contamination is typically limited to the surface and is easily removed through light grinding [314].

The biggest challenge facing the ECAS process is the scale up for commercial applications, specifically net-shape forming of large, complex parts, and process throughput [310, 358]. The current obstacles include design of ECAS systems to provide sufficient current and pressure, and the design of tooling to minimize the often-severe temperature and pressure gradients present during ECAS sintering of large parts, which will require the predictive capabilities of mature finite element modelling [310, 372].

2.3 Master Sintering Curve

The master sintering curve (MSC) is an empirical tool to predict the densification behavior of a given green-body powder material subjected to an arbitrary time-temperature sintering profile. The MSC is based on the combined-stage sintering model, which describes the contribution of grain boundary and volume diffusion to densification under pressureless sintering conditions without consideration of surface diffusion [452]. The model defines instantaneous linear shrinkage rate as [452]:

$$-\frac{dL}{Ldt} = \frac{\gamma\Omega}{kT}\left(\frac{\Gamma_v D_v}{G^3} + \frac{\Gamma_b \delta D_b}{G^4}\right)$$

Assuming isotropic shrinkage, the linear shrinkage rate can be equated to the densification rate as [453]:

$$-\frac{dL}{Ldt} \cong \frac{d\rho}{3\rho dt}$$

Assuming a single, dominate diffusion mechanism, the model equation can be simplified to [453]:

$$\frac{d\rho}{3\rho dt} = \frac{\gamma\Omega[\Gamma(\rho)]}{kT[G(\rho)]^n}\left[D_0 e^{\left(-\frac{Q}{RT}\right)}\right]$$

Assuming $\Gamma(\rho)$ and $G(\rho)$ are only functions of powder material, density, and green-body preparation, and the atomic diffusion processes $\left[D_0 e^{\left(-\frac{Q}{RT}\right)}\right]$ are independent of the powder microstructure and material, the model equation can be rearranged such that the parameters related to the microstructural evolution (grain size and geometry) and material properties are isolated on the left-hand side (except for the activation energy), while the parameters associated with the atomic diffusion process are grouped on the right-hand side [453]:

$$\frac{k}{\gamma\Omega D_0}\int_{\rho_0}^{\rho}\frac{[G(\rho)]^n}{3\rho\Gamma(\rho)}d\rho = \int_0^t \frac{1}{T}e^{\left(-\frac{Q}{RT}\right)}dt$$

The assumption that $\Gamma(\rho)$ and $G(\rho)$ are functions of only density is based on negligible differences in the mass transportation mechanisms of densification and grain growth and holds true unless significant surface diffusion or exaggerated grain growth occurs [453, 454]. The average grain size has been shown experimentally to depend on density, while being independent of temperature and heating rate [455]. Deviations in powder material and green-

body preparation can affect densification behavior through variations in particle size, particle size distribution, initial pore size distribution, and green density [456].

Two functions can be defined such that [453]:

$$\Phi(\rho) \equiv \frac{k}{\gamma \Omega D_0} \int_{\rho_0}^{\rho} \frac{[G(\rho)]^n}{3\rho\Gamma(\rho)} d\rho$$

$$\Theta\big(t, T(t)\big) \equiv \int_0^t \frac{1}{T} e^{\left(-\frac{Q_{MSC}}{RT}\right)} dt$$

Where $\Theta\big(t, T(t)\big)$ is termed, *work of sintering* [457]. The MSC is constructed from the specimen relative density $[\rho(t)]$ and temperature $[T(t)]$ data generated through a series of constant heating rate sintering experiments. Plotting the instantaneous specimen relative density on the ordinate versus the natural logarithm of theta $[\ln(\Theta)]$ on the abscissa forms the MSC as illustrated in Figure 2.5. Originally, the MSC was fitted with a polynomial function [453], but modern techniques use a sigmoid function [458, 459] of the form:

$$\rho = \rho_0 + \frac{1 - \rho_0}{1 + e^{\left(-\frac{\log(\Theta) + a}{b}\right)}}$$

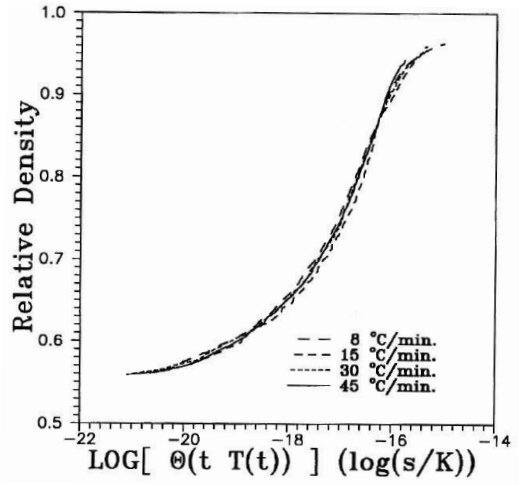

Figure 2.5. Master Sintering Curve (MSC) for alumina with an activation energy of 487.6 kJ/mol. [453]

The MSC can be used to estimate a constant value of activation energy, which can be used to infer the dominate diffusion mechanism responsible for densification during sintering since the sintering rate is proportional to the diffusion coefficient [460, 461]; however, several diffusion mechanisms can be active concurrently and therefore, the constant value determined through the MSC is termed the *apparent activation energy* (Q_{MSC}) [462]. The MSC can also be used to predict densification behavior due to arbitrary time-temperature sintering profiles assuming the prediction sample is constructed from the same powder material, green-body preparation, and green density as the specimens used during the constant heating rate experiments [453].

The experiments necessary to obtain the raw data for generation of an MSC are most often performed on a precision laboratory dilatometer, which measures dimensional variations of materials as a function of temperature [454, 458, 460, 462-477]. Additional methods include a hot press equipped with a linear variable differential transformer (LVDT) to measure displacement of the driven ram [478, 479], and an ECAS machine [317, 480-487].

The MSC has been generated to study the densification of a variety of ceramic and metallic materials including alumina (Al_2O_3) [317, 453, 471, 474, 475, 478, 479], zirconia (ZrO_2) [470, 473, 477, 488], zinc oxide (ZnO) [376, 453, 468], titanium dioxide (TiO_2) [467, 469], thoria (ThO_2) [460, 466], barium titanate ($BaTiO_3$) [476], cerium oxide (CeO_2) [472], stainless steel (17-4PH) [458, 462, 464, 465], tungsten [454, 462-464], molybdenum [462, 464, 489], nickel [464], and niobium [464].

Typically, the MSC is generated through a series of constant heating rate experiments and validated by subjecting additional samples to arbitrary time-temperature profiles with

isothermal dwells [463, 465-469, 474, 478, 479, 488], as shown in Figure 2.6. In certain cases, the accuracy of MSC-based density predictions has been verified to 1-percent or less [465, 478, 479].

Since the MSC approach is a quantitative description of the sintering behavior, it can be used to study the effect of dopants [317, 466, 473, 474], green-shaping [475], and particle size [468] on densification through the comparison of two or more MSC profiles (and/or apparent activation energies), as demonstrated in Figure 2.7. The effect of various phases on diffusivities [465] and the evaluation of assorted powder material vendors [489] have also been studied in this manner.

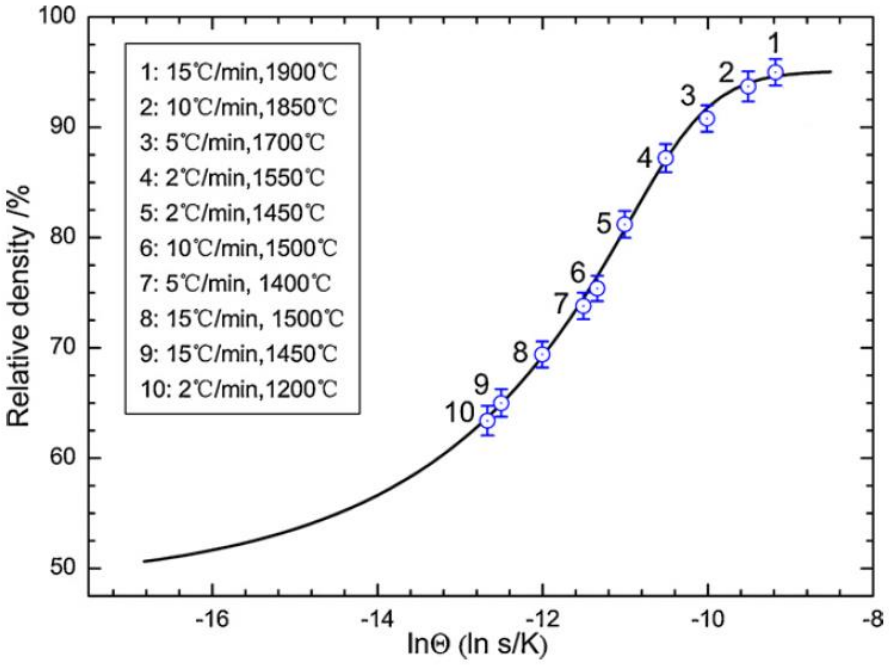

Figure 2.6. Master Sintering Curve (MSC) from sintering experiments on tungsten carbide-magnesium oxide nanocomposites exhibiting a good agreement between the model predictions and the validation specimens. [463]

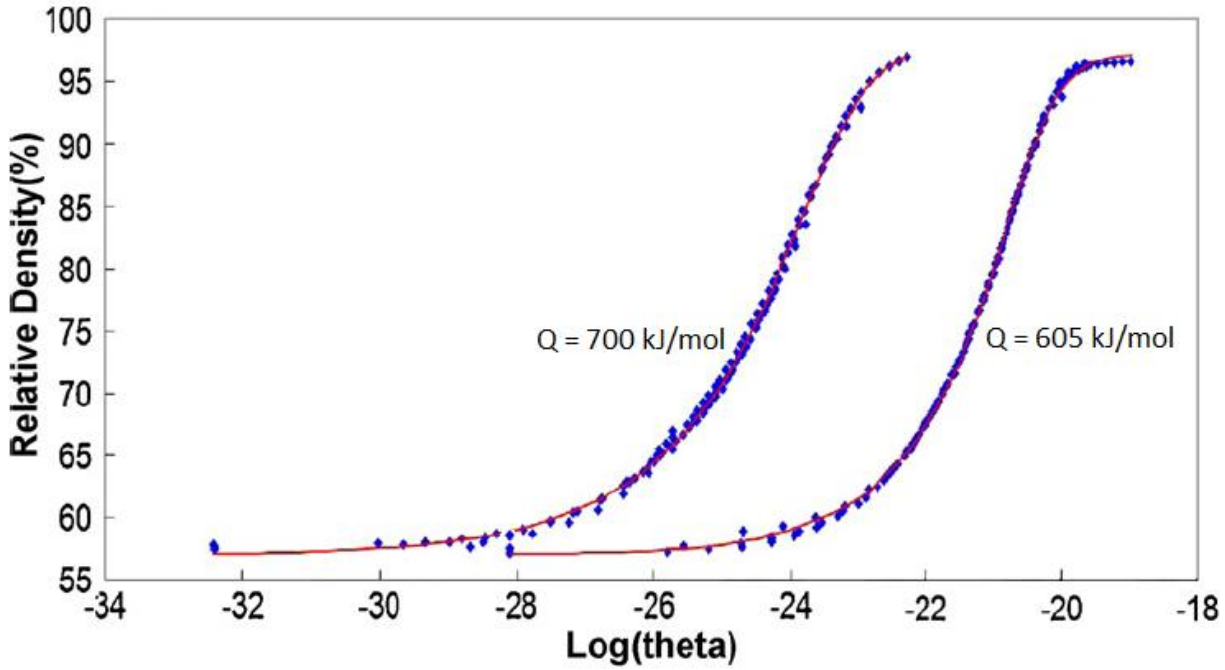

Figure 2.7. Master Sintering Curve (MSC) from sintering experiments on alumina green-bodies prepared by dry pressing (700 kJ/mol) or by pressure filtration (605 kJ/mol) showing the ability of the MSC to quantify effects on densification due to green-shaping. [475]

Although the combined-stage sintering model does not consider plastic flow mechanisms, the MSC methodology has been successfully applied to the pressure-assisted sintering of alumina [478-480]. Consideration of pressure, or another material property such as green density, allows a three-dimensional master sintering surface to be constructed and used to predict sintering results [314, 478, 479]. Furthermore, a two-phase MSC has been used to model the densification behavior of materials which experience a phase change during sintering [458, 465, 473]. The phase transformation is indicated by an abrupt change in activation energy and is modeled by dividing the MSC into multiple segments [473]; finite element shape functions have also been used to determine varying activation energies [490]. The MSC

methodology has also been extended to model and predict the microstructural development associated with grain growth during sintering, demonstrated in Figure 2.8 [454, 488].

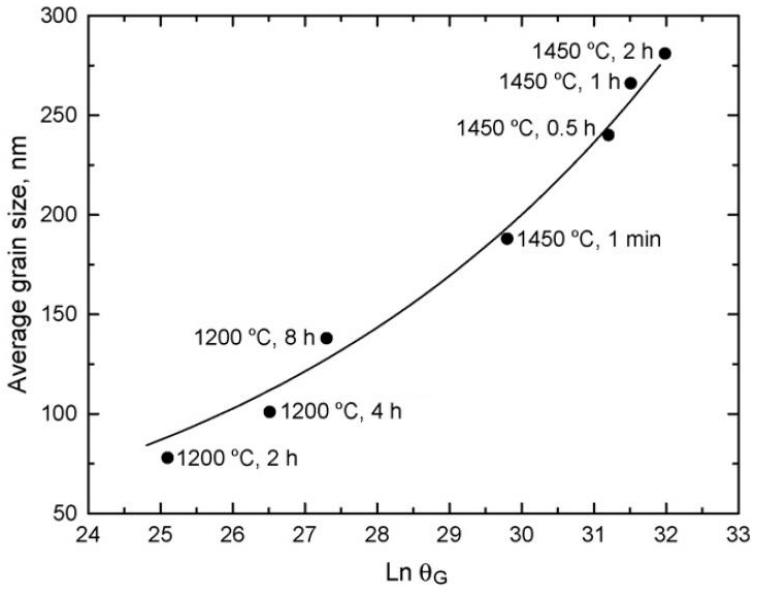

Figure 2.8. Master Grain Growth Curve from sintering experiments on yttria stabilized zirconia (3Y-TZP) exhibiting a maximum error of ±4% between the model predictions and the validation specimens. [488]

2.3.1 Application to Electric Current Assisted Sintering

The MSC methodology has also been successfully applied to the ECAS technique based on the following equation relating densification rate to axial strain rate (powder shrinkage during ECAS occurs primarily in the axial direction; lateral shrinkage is negligible) [480, 491]:

$$\frac{1}{\rho}\frac{d\rho}{dt} = \frac{HD}{G^m kT}(\varphi p_a)^n$$

Rearrangement and substitution yields:

$$\frac{kG^m}{\rho H D_0 p_a^n \varphi^n} d\rho = \frac{1}{T} e^{\left(-\frac{Q}{RT}\right)} dt$$

Which forms the familiar MSC construction provided the uniaxial applied stress p_a^n is constant:

$$\Phi(\rho) \equiv \frac{k}{HD_0 p_a^n} \int_{\rho_0}^{\rho} \frac{G^m}{\rho \varphi^n} d\rho$$

$$\Theta\big(t, T(t)\big) \equiv \int_0^t \frac{1}{T} e^{\left(-\frac{Q_{MSC}}{RT}\right)} dt$$

The applicability of the MSC for ECAS processes has been experimentally validated on alumina [317, 480, 484,], uranium dioxide (UO_2) and uranium dioxide composites (UO_2-SiC) [483], zinc oxide (ZnO) [482], and hafnium diboride (HfB_2) [481]. The densification mechanisms of alumina nanopowders have been shown to be the same between conventional dilatometry and ECAS [317].

The specimen relative density $[\rho(t)]$ is calculated from the axial shrinkage of the powder compact measured by the displacement of the ECAS electrodes during the constant heating rate experiments; however, the displacement data also includes the thermal expansion of the graphite tooling, which can be significant considering the elevated sintering temperatures typical of ECAS processes. To eliminate the thermal expansion of the graphite tooling from the displacement data, a second process cycle must be performed on a fully densified sample. Subtraction of the measured displacement data between the two process cycles isolates the axial shrinkage of the powder compact due to densification and is known as the *background subtraction technique*, illustrated in Figure 2.9 [480, 483, 486, 487].

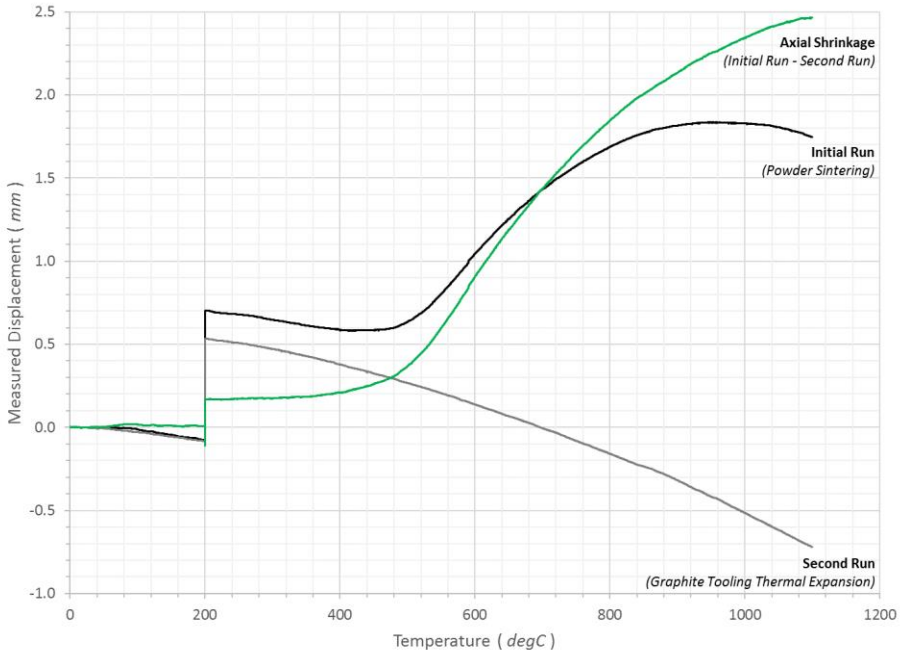

Figure 2.9. Example of background subtraction technique to isolate the axial shrinkage of a powder compact during ECAS sintering.

3. RESEARCH OBJECTIVES

The purpose of this chapter is to detail the research objectives. Context will be provided by discussing the research opportunity to establish the uniqueness and novelty of the scholarly contributions. The materials, experimental procedures, results, and discussion associated with the current research effort are communicated in chapters 4 and 5. Note that, while the author feels the ECAS terminology is most appropriate to describe the sintering technique employed with the current research effort, the chapter titles will use, “Spark Plasma Sintering” due to its popularity within the literature. The conclusions are presented in Chapter 6, where the significant findings and contributions are discussed within the framework of the research objectives and future work is suggested to build upon the current research accomplishments.

3.1 Research Opportunity

To meet the demands of next generation applications, advanced materials will require higher performance at lower cost and less weight. Metal open-cell foams are competitively poised to meet these requirements due to their intrinsic low weight, combination of thermal and mechanical properties, and relative cost; however, the real utility of metal open-cell foams will be the ability to tailor their properties through material selection and control of the pore structure to achieve multifunctionality.

While material selection is typically well constrained, the topological design of metal foams must consider many factors including pore size, shape, spatial distribution, and interconnectivity. Although topological design principles have advanced in recent years to allow for optimization of foam properties, the current manufacturing techniques limit the

degree to which the tailored pore structures can be realized. Historical manufacturing processes developed for stochastic foams lack the ability to control the pore size, shape, and position. Furthermore, the advanced manufacturing techniques associated with periodic structures have limited material options, reduced mechanical properties, and ultimately lack the fine geometric control required of tailored pore structures.

Based on the current research, an opportunity exists to combine space-holder replication, additive manufacturing, and powder metallurgy to fill complementary roles for the manufacture of tailored pore structures. While the space-holder method provides precision replication, the spatial arrangement of individual porogens is not well controlled. Computer aided design can construct a well-controlled, geometrically complex digital model and additive manufacturing provides a pathway to translate the digital data into a three-dimensionally printed sacrificial template. Unlike additive manufacturing, powder metallurgy is compatible with a wide selection of materials and offers realization of full mechanical properties through complete sintering densification of the matrix.

3.1.1 Existing Solutions

In the work by Ryan et al. [283], a sacrificial wax template was additively manufactured, coated with a titanium slurry, and compacted within a mold. The wax template was leached, and the remaining titanium structure was pressureless sintered under a high vacuum environment between 1100 and 1300 °C for 1 hour. Deformation of the titanium matrix was observed, likely due to the significant shrinkage reported, and the measured matrix porosity would certainly degrade the mechanical properties.

Similarly, Covaciu et al. [282], additively manufactured a cubic arrangement of spherical porogens from calcium sulfate ($CaSO_4$), as shown in Figure 1.24. The template was filled with zinc powder and sintered at 380 °C under nitrogen gas pressure for 2 hours. Although calcium sulfate melts at 1460 °C, the organic additives used to print the sacrificial template pyrolyze during sintering of the zinc powder, reducing the strength of the template such that it can be subsequently removed by blowing compressed air through the sintered zinc foam. The resultant open-cell foam specimens appear to have fully dense matrices, aided by the pressure applied during sintering.

Research by both Ryan et al. [283] and Covaciu et al. [282] demonstrate the feasibility of combining space-holder replication, additive manufacturing, and powder metallurgy to fabricate metal open-cell foams. Contrasting both research efforts highlights the necessity for using a porogen material capable of the temperatures required during sintering to control the pore geometry and accelerate densification by allowing pressure application; however, the calcium sulfate material used by Covaciu et al. thermally decomposes at approximately 400 °C. To support a proper sintering process of aluminum or magnesium, the lowest melting temperature metals which might be considered for structural applications, the sacrificial template material would need to be thermally stable to at least 500 °C.

3.2 Detailed Research Objectives

The current research effort seeks to achieve the following objectives:

1. Identify a leachable porogen material compatible with pressure-assisted sintering that extends the working temperature range of the space-holder replication technique beyond the commonly used salt porogens.
2. Develop a manufacturing process based on the integration of the space-holder replication technique and electric current assisted sintering to fabricate tailored metal open-cell foams exhibiting control over the pore size, shape, and position.
3. Apply the Master Sintering Curve concept to determine the time-temperature parameters required to achieve complete densification of metal powders during electric current assisted sintering.
4. Extend the Master Sintering Curve concept to quantify the effects on densification behavior of metal powders during electric current assisted sintering due to the addition of porogens.

These objectives are structured to build upon the current metal open-cell foam knowledge base and drive toward next generation application of foams requiring higher performance at lower cost and less weight.

4. NITI OPEN-CELL FOAMS WITH PERIODIC TOPOLOGY FABRICATED BY SPARK PLASMA SINTERING

One of the original objectives of this research was to investigate the structure-property relationships of shape memory alloy foams for the application of self-healing energy absorbers. Open-cell foams were based on an intermetallic nickel-titanium (NiTi) shape memory alloy matrix with silica gel (SiO_2) particles as sacrificial porogens. Although the original research objectives evolved into those listed in section 3.2, the usage of NiTi as the matrix material was carried forward due to the availability of raw powder stock. The intrinsic shape memory and superelasticity properties of NiTi has no particularity to the objectives of the current research effort to fabricate open-cell foams with periodic topologies, thus these properties will not be explicitly quantified.

Originally, silica gel particles were selected as the sacrificial porogens due to their low-cost, availability, spherical geometry, high melting temperature (>1600 °C) [492], and ease of dissolution in hydrofluoric acid (HF) based on published literature [191, 354, 493-497]. Unfortunately, it was discovered during leaching experimentation that HF reacts with NiTi and SiO_2 at similar rates, breaking down the metal matrix quite readily. Potassium hydroxide (KOH) was then investigated as an alternate leaching agent. KOH was capable of dissolving as-received SiO_2 within a few hours while proving unreactive with NiTi at similar exposure conditions; however, leaching attempts on sintered NiTi-SiO_2 composite specimens failed to leach the porogen from the matrix. Experimental investigations revealed that the sintering temperature caused a phase change in the SiO_2 porogens which rendered them unreactive with KOH.

While looking for alternate porogens to SiO_2, the research team discovered commercially available metal balls available in steel, stainless steel, aluminum, tungsten carbide, brass, copper, titanium, and lead alloys. Metal balls are an ideal porogen as spherical porosity was highly desirable to eliminate stress concentrations and to achieve a high packing factor of porogens. Ultimately, the copper balls were selected as sacrificial porogens based upon cost, sphericity, use temperature, and known reactivity with nitric acid (HNO_3). Preliminary experimentation confirmed the copper porogen's high reactivity with $HN0_3$, while also demonstrating NiTi's relative inertness to the aqueous acid at the same concentration and exposure time.

4.1 Materials and Methods

4.1.1 Raw Materials and SPS Tooling

Pre-alloyed NiTi powder supplied from Special Metals Corporation with a particle size range of 10 to 44 μm (Figure 4.1) was utilized for both the NiTi and NiTi with copper porogens (abbreviated as NiTi+Cu hereafter). Porogens were low-cost copper spheres (102, H04 temper, 99.95% purity) commercially available from McMaster-Carr with a nominal diameter of 0.09375 ± 0.001-inch.

The as-received NiTi powder was subjected to direct current plasma emission spectroscopy to determine its elemental composition per ASTM E1097-12 [498]; characterization was performed by Luvak Inc., of Massachusetts. The phase constituents of the as-received NiTi powder were investigated using a Bruker D8 Discover X-ray diffractometer. Using CuK_α radiation at 40 kV and 40 mA, the X-ray diffractogram was captured between diffraction angles of 35° to 80° (2Θ) at a 0.02° step size and a 0.2 second preset time. The

powder sample was dynamically rotated during characterization. The phase analysis was performed by hand using the methods detailed by Cullity [499] and the parameters listed in Table 4.1.

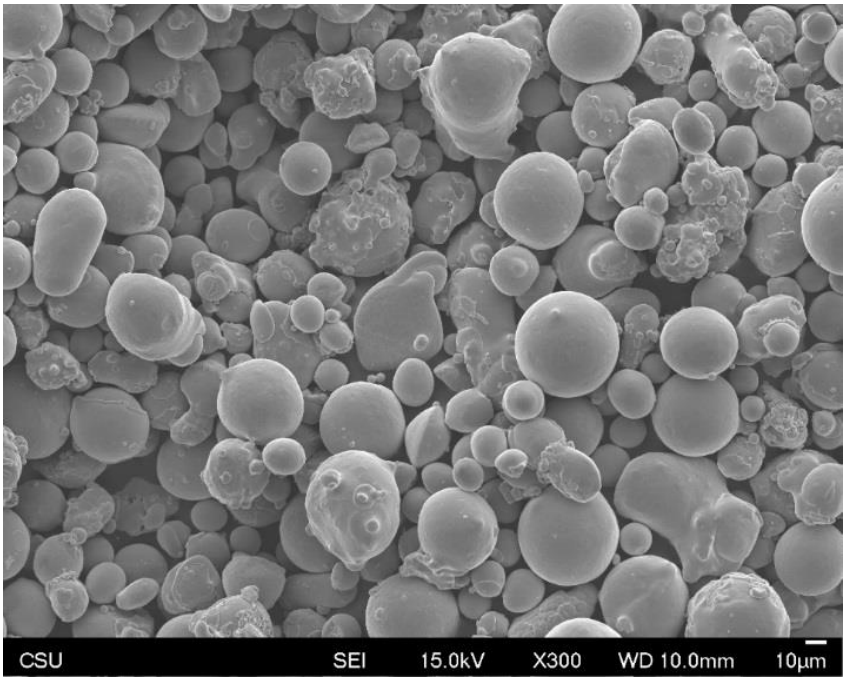

Figure 4.1. SEM micrograph of NiTi powder used for all sintering experiments obtained from Special Metals Corporation.

Table 4.1. Parameters used to perform phase analysis of X-ray diffractogram data obtained from as-received NiTi powder.

NiTi Phase	Lattice System	a (Å)	b (Å)	c (Å)	β (°)	λ (Å)
Austenite	Cubic	3.010	-	-	-	1.5405
Martensite	Monoclinic	4.646	4.108	2.898	97.78	

Both the as-received NiTi powder and a sintered NiTi specimen were subjected to differential scanning calorimetry (DSC) to determine the austenite-martensite phase transformation temperatures. The NiTi specimen was prepared for DSC by grinding and

polishing a small sheet of dense NiTi sectioned from a sintered disc. The mass of NiTi powder dispensed for DSC evaluation was matched to that of the sintered specimen to avoid potential scaling complications. The experimental procedure was loosely based on ASTM F2004-05 [500] and consisted of thermal cycling the specimens from -130 °C to +425 °C and back at 10 °C/min with 5-minute dwells at the temperature extrema. Dry nitrogen was used as a cover gas with a flow rate of 30 mL/min at 5 psi. The DSC instrument was calibrated using indium and tin samples; a baseline correction was also applied.

All sintering runs were conducted using a die and two punches fabricated from ultra-fine graphite round stock (AR-14 material name) sourced from Ohio Carbon Blank. Geometrically, the die was an annular cylinder of dimensions 38 mm (outer diameter) by 62 mm (height) with a 12.5 mm axial hole, while the punches were cylinders of dimensions 12.2 mm (diameter) by 27 mm (height). The punch diameter was slightly undersized to accommodate the thickness of a graphite liner, which primarily facilitated the post-sintering extraction of the punches and specimen from the die. Additionally, two graphite discs were placed on the internal face of both punches in contact with the NiTi powder to separate the punches from the sintered specimen. An example of a graphite die, graphite punches, graphite discs, and a graphite liner used to sinter the NiTi open-cell foam specimens is shown in Figure 4.2.

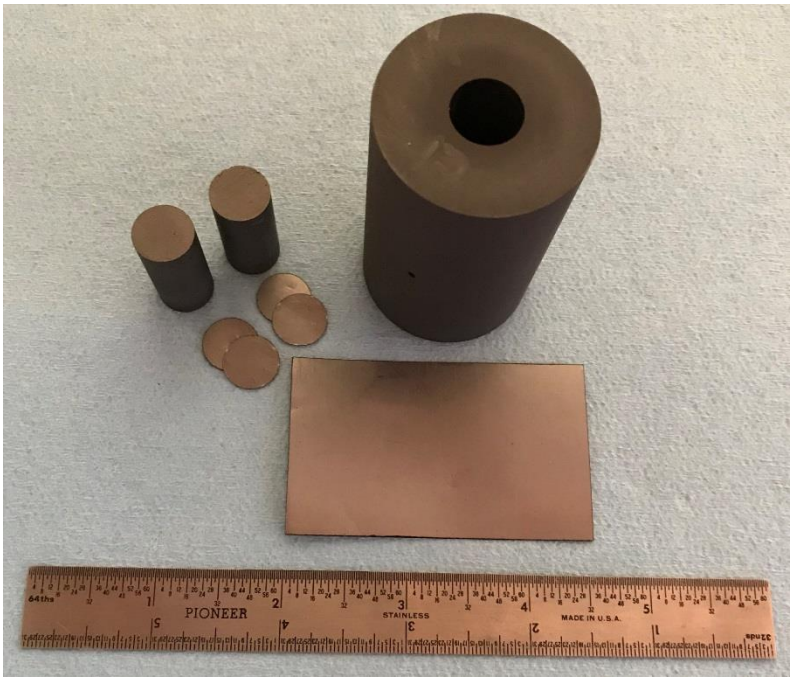

Figure 4.2. Graphite die (x1), graphite punches (x2), graphite discs (x4) and graphite liner (x1) used to sinter the NiTi open-cell foam specimens.

4.1.2 CAD Design of Open-Cell Foam Specimens

To realize a high porosity using spherical porogens, the pore structure of the NiTi open-cell foams was designed in CAD for maximum packing factor following a hexagonal close-packed (HCP) arrangement (ABAB…). The design process balanced practical considerations for tooling size, effort required to assemble the porogen template, and usage of raw materials, including the constraint of using only whole spheres. Ultimately, an as-sintered cylindrical geometry of 12.5 mm (diameter) x 19 mm (length) was selected to achieve a length-to-diameter ratio greater than 1.5 for mechanical compression testing. The complete porogen template totaled nine layers as shown in Figure 4.3.

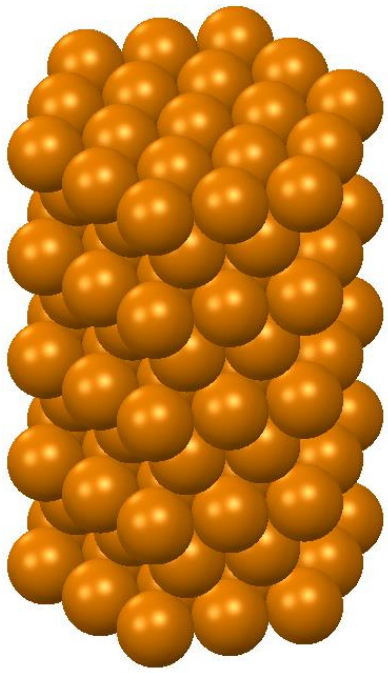

Figure 4.3. The CAD designed copper porogen template assembly showing the full nine-layer HCP stacking sequence.

Furthermore, it was anticipated that the as-sintered foam specimens would require machining to expose each copper porogen layer to facilitate leaching. A final specimen geometry of 9.2 mm (diameter) x 16.5 mm (length) was selected and resulted in a designed NiTi open-cell foam density of 1.77 gcc at 72.6% porosity. The theoretical packing factor of HCP is 74%; this discrepancy is due to the constraint of using full spheres, which results in empty pockets of space within both A and B layers normally occupied by partial spheres that are being filled by matrix material instead, thus slightly decreasing the porosity. The CAD designed NiTi open-cell foam after sintering, machining, and leaching of the copper porogens is shown in Figure 4.4, along with the metal matrix unit cell based on the HCP arrangement of porogens.

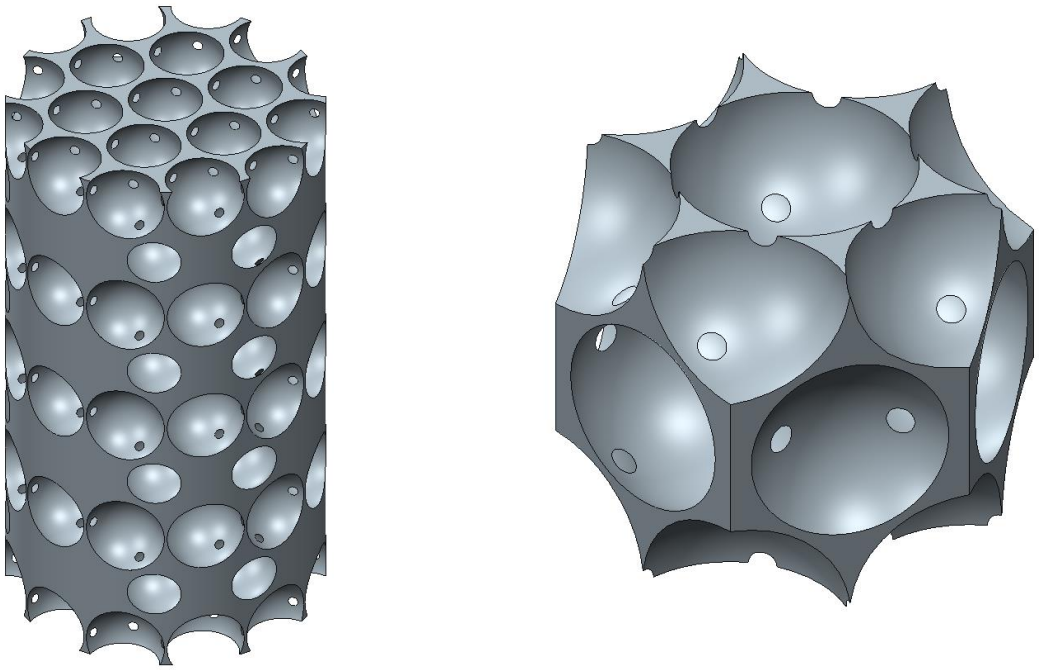

Figure 4.4. (LEFT): The CAD designed NiTi open-cell foam after sintering, machining, and leaching of the copper porogens having a density of 1.77 gcc at 72.6% porosity; (RIGHT): The CAD designed metal matrix unit cell based on the HCP arrangement of porogens after leaching illustrating the interconnectivity of the pores.

4.1.3 Assembly of Copper Porogen Templates

To facilitate the sintering of the open-cell foam specimens, porogen templates were constructed in two different layers as illustrated in Figure 4.5. Layer A contained 19 individual copper spheres, while layer B contained 12 spheres. The individual copper spheres were placed in a jig according to their layer pattern and glued by hand according to the glue points identified in Figure 4.5. Loctite Ultra Gel Control Super Glue (P/N: 1363589) was dispensed in discrete droplets from a 3 mL plastic syringe equipped with a 304 stainless steel needle having an 0.012-inch inner diameter and a 0.25-inch length. Each layer was fully cured for 24 hours before being subjected to the sintering process.

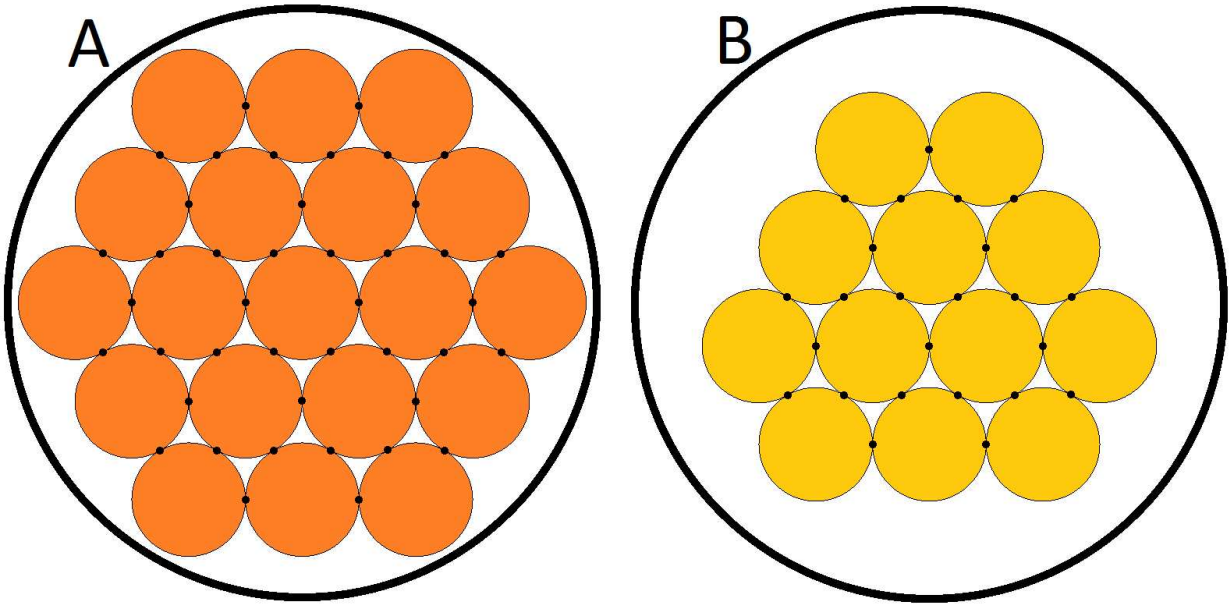

Figure 4.5. Layer A and layer B porogen templates constructed from copper spheres. Glue points are indicated as black dots. The inner wall of the graphite die is shown to illustrate the relative packing factor of each layer.

4.1.4 Fabrication of Foam Specimens

Seven open-cell foam specimens (labeled as: pNiTi 31 – 37) were fabricated in total, starting with sintering of the NiTi powder and copper porogens, followed by machining of the composite, and finishing with leaching of the copper porogens from the NiTi matrix.

Foam specimens were sintered by inserting a graphite liner into the die and assembling both over the lower punch. Two discs of graphite were placed inside the die covering the top surface of the lower punch. A 2 mm thick layer of fully dense NiTi was required on the top and bottom of each specimen to facilitate post-sintering machining of the foams. The bottom layer was created by weighing out 1.5 grams of NiTi powder based on a full density of 6.45 gram/cm^3 (gcc). The dispensed NiTi powder was poured into the die and slightly agitated to distribute the powder evenly. A slightly undersized punch was inserted into the die to compact the powder

by hand, then slowly removed with a slight twisting motion to minimize disturbance of the powder.

Approximately 10 grams of NiTi powder was weighed and loaded into a 6 mL plastic syringe equipped with a 304 stainless steel needle having an 0.054-inch inner diameter and a 0.25-inch length. The first A layer of copper spheres was carefully placed on top of the compacted powder. NiTi powder was dispensed from the syringe to fill in the small gaps between the copper porogens and around the perimeter of the A layer. The first B layer of copper spheres was then nested on top of the A layer as indicated in Figure 4.6, and filled with powder. In total nine layers were assembled into the die in the sequence: ABABABABA, with NiTi powder dispensed from the syringe around each layer. Subsequently, an additional 1.5 grams of NiTi powder was added to form the top 2 mm layer as discussed earlier and the entire assembly was compacted using an undersized punch. Two more discs of graphite were carefully placed on top of the compacted assembly, followed by insertion of the upper punch.

The graphite tooling was loaded into a Dr. Sinter SPS machine (Fuji Electronic Industrial Co., LTD., Japan) between six circular graphite plates symmetrically arranged between the two SPS electrode platens. The graphite stack and tooling were positioned coaxial with the electrode platens to facilitate uniform current density distribution. A slight pre-load was applied across the assembly and a K-type thermocouple probe (Omega Engineering, P/N: TJ48-CAIN-116G-24) was installed into the die ensuring the probe was sufficiently sprung to avoid loss of contact during sintering operations. The SPS chamber was sealed and pumped down under vacuum pressure.

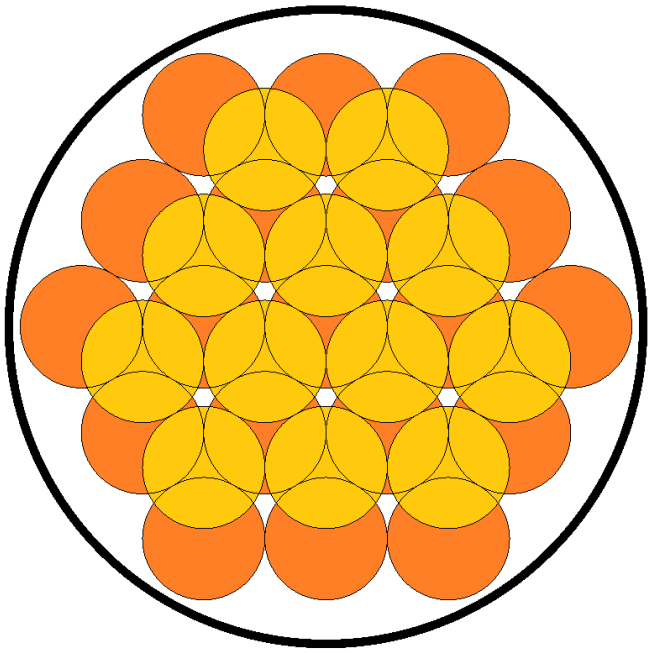

Figure 4.6. Nesting of the copper porogens, the A layer is on bottom (orange) and the B layer is on top (yellow). The circular outlines indicate the position of the next A layer, which forms a hexagonal close-packed (HCP) arrangement (ABAB…).

The SPS thermal controller was programmed based upon the experimental process parameters detailed in Table 4.2. The SPS thermal controller leveraged a PID strategy for temperature control with user-defined values of 10 (proportional), 20 (integral), and 5 (derivative). The pre-load across the graphite stack was initially set to 3.8 kN (32.5 MPa) and adjusted to 9.5 kN (81.4 MPa) during step two of the thermal profile (Table 4.2). The thermal profile was initiated on the SPS thermal controller and allowed to run to completion.

Once the graphite tooling had cooled to room temperature, the sintered foam specimens were ejected from the die using a hydraulic bench top press and ground by hand under flowing water using 120-grit SiC paper to remove all graphite contamination from the surface. The specimens were cleaned in an ultrasonic bath using a sequential progression of

acetone, ethanol, and isopropanol alcohol, followed by a rinse under pressurized deionized water. The specimens were dried on a hot plate at 150 °C for 15 minutes.

Table 4.2. SPS process parameters to sinter NiTi open-cell foams using copper porogen templates.

Step	Set Point Variable (°C)	Time (minutes)	Applied Load (kN)
S0	0	-	3.8
S1	200	2	3.8
S2	200	2	3.8 → 9.5
S3	900	7	9.5
S4	950	1	9.5
S5	950	5	9.5
S6	END		

Each specimen was machined on a lathe to nominal cylindrical dimensions of 9.2 mm (diameter) and 13.4 mm (length) to expose the copper porogens for leaching. The length of the as-sintered specimens had to be machined approximately 3.1 mm shorter than the CAD designed length (16.5mm, section 4.1.2) due to suspected deformation of the copper porogens during sintering. The copper porogens were subsequently leached from the NiTi matrices by exposing the foam specimens to a 10-molar concentration of nitric acid (HNO_3). The specimens were exposed to two aqueous baths of 10M nitric acid to ensure complete dissolution of the copper porogens. Afterwards, the foam specimens were placed in a beaker filled with deionized water and cleaned in an ultrasonic bath for 10 minutes, then dried on a hot plate at 150 °C for 15 minutes.

4.1.5 Characterization Techniques

The porosity (ϕ_{foam}) of each open-cell foam specimen was estimated according to the following equations:

$$\rho_{foam} = \frac{m_{foam}}{\frac{\pi}{4} D_{foam}^2 L_{foam}}$$

$$\phi_{foam}(\%) = 100\left(1 - \frac{\rho_{foam}}{\rho_{NiTi}}\right)$$

The mass (m_{foam}) was measured using an analytical balance, while the dimensions (D_{foam}, L_{foam}) were measured using a micrometer. Determination of porosity using this approach assumes the foam specimens conform to a cylindrical geometry; any deviation in the specimen shape from the ideal cylindrical geometry will introduce error into the porosity estimation. Each foam specimen was carefully machined into a cylindrical shape using the methods described in section 4.1.4 to minimize this potential error.

Like the porosity equation, the *relative density* equation relates the overall density of the foam to the density of the matrix material:

$$\rho_{relative} = \frac{\rho_{foam}}{\rho_{NiTi}}$$

The relative density is reported as either a decimal quotient (e.g. 0.971) or as a percentage (e.g. 97.1%); thus, the value of full density is defined as either 1.00 or 100%. The porosity and relative density equations are related such that:

$$\rho_{relative} + \phi_{foam} = 1$$

All seven NiTi open-cell foam specimens (pNiTi 31 – 37) were imaged in the axial direction using a Scanco µCT 80 X-ray micro-computed tomography scanner at 10 µm

resolution. Three-dimensional models were constructed from the scan data and were used to qualitatively assess the completeness of the leaching process in dissolving the copper porogens and the effectiveness of the fabrication technique in replicating the copper porogen templates to the pore structure of the NiTi open-cell foams.

One foam specimen (pNiTi 34) was sectioned transverse to its long axis by low-speed saw and mounted in acrylic casting resin. The mounted specimen was ground and polished on an 8-inch rotating wheel in accordance with the sequence and parameters detailed in Table 4.3. Energy-Dispersive X-ray spectroscopy (EDS) analysis was performed on the prepared specimen cross-section using a JEOL JSM-6500F Field Emission Scanning Electron Microscope and an Oxford Instruments X-Max detector to determine the extent of diffused copper in the NiTi matrix.

Table 4.3. Grinding and polishing sequence and parameters for the mounted NiTi open-cell foam specimen in preparation for EDS.

Step	SiC Paper Grit	Diamond Abrasive Media	Duration (minutes)	Wheel Speed (rpm)	Water Flow Rate
1	400	-	1	200	low
2	600	-	6		low
3	800	-	4		low
4	1200	-	4		low
5	-	6µ	3		-
6	-	3µ	6		-
7	-	1µ	12		-

The remaining six foam specimens (pNiTi 31 – 33, 35 – 37) were subjected to room temperature destructive mechanical compression tests to determine their stress-strain behavior under the guidance of the ASTM E9 standard [501]. Specimens were compressed to

failure using an Instron 1332 hydraulic load frame equipped with a non-contact laser extensometer and a specially designed compression test fixture with hardened steel platens (Figure 4.7). The first specimen (pNiTi 31) was compressed to failure at 0.076 mm/min without any hysteresis loops to understand the expected stress-strain behavior of the remaining foam specimens and, as such, the test data for pNiTi 31 will not be presented; the remaining specimens (pNiTi 32, 33, 35-37) were compressed to failure in accordance with the sequence and parameters detailed in Table 4.4. The reflective targets for the laser extensometer were located on the steel platens just above and below the foam specimen. Two hysteresis loops were included in the compression test sequence (Table 4.4) to assess the sensitivity of the foam specimen stiffness to loading and unloading cycles, both prior to and after the yield strength had been exceeded.

Table 4.4. Destructive mechanical compression test sequence and parameters used to determine the stress-strain behavior of NiTi open-cell foam specimens.

Step	**Step Type**	**Compression Load (N)**	**Displacement Rate (mm/min)**
1	Absolute Ramp	667	0.076
2		222	
3		1334	
4		222	
5		Failure	

Figure 4.7. Mechanical compression test setup to characterize the NiTi open-cell foam specimens to failure. (LEFT): Overall test setup showing the Instron 1332 hydraulic load frame, non-contact laser extensometer, and custom-designed compression loading fixture. (RIGHT): Close-up of the compression loading fixture showing a foam specimen installed prior to test initiation, laser extensometer reflective targets, and hardened steel platens.

The elastic modulus, yield strength, and ultimate strength were determined for each specimen from the stress-strain data to quantitatively assess the variability in mechanical properties across the batch of specimens. The elastic modulus was calculated during the second loading cycle (reference: Table 4.4, step 3) by the method of least squares per ASTM E111 [502] using the subset of compression load data between 75 and 125 lb_f. The yield strength was calculated using the 0.2% offset method per ASTM E9 [501]. Additionally, the elastic strain rate was calculated to determine conformance to the ASTM E9 standard for loading rate in the elastic portion of the stress-strain curve.

After the destructive mechanical compression tests, microscopy was performed on the NiTi open-cell foam fracture surfaces using a JEOL JSM-6500F Field Emission Scanning Electron Microscope at an accelerating voltage of 15 kV.

4.2 Results

4.2.1 NiTi Material Properties

The elemental composition of as-received NiTi powder determined by direct current plasma emission spectroscopy is reported in Table 4.5. The NiTi composition falls within the standard range for nickel atomic fraction range studied in the literature (48.6 to 51.0 at.% Ni).

Table 4.5. Elemental composition of as-received NiTi powder determined by direct current plasma emission spectroscopy.

Nickel Weight Fraction (%)	**Titanium Weight Fraction (%)**	**Nickel Atomic Fraction (%)**	**Titanium Atomic Fraction (%)**
55.2	44.3	50.4	49.6

The X-ray diffractogram of the as-received NiTi powder is shown in Figure 4.8. The peaks at 42.3° (110), 61.4° (200), and 77.5° (211) signify the presence of austenite and indicate the as-received NiTi powder is not fully martensitic at room temperature. The remaining peaks are all associated with various diffraction planes of the martensite phase.

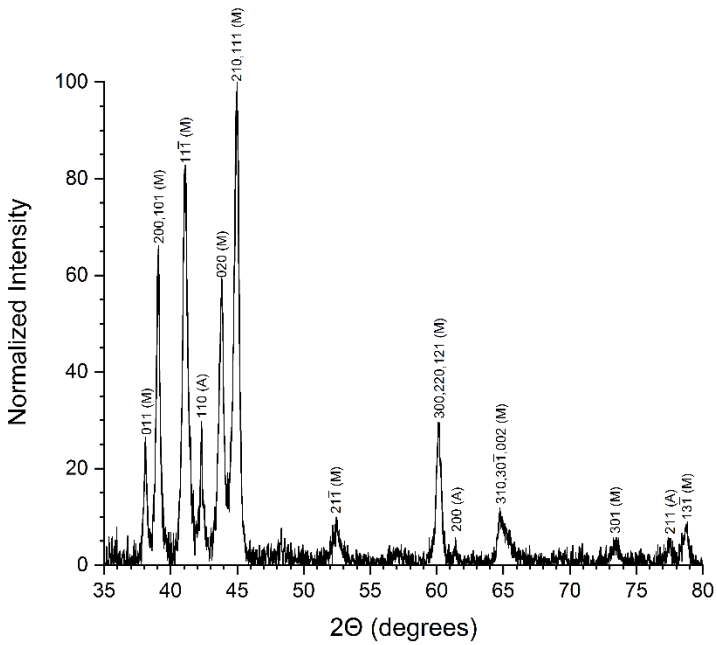

Figure 4.8. X-ray diffractogram of as-received NiTi powder with the background and $CuK_{\alpha 2}$ subtracted. The diffraction reflections from the martensite (M) and austenite (A) phases are identified.

The heat flow versus temperature profiles for the as-received NiTi powder and sintered NiTi specimen are shown in Figure 4.9; the extracted phase transformation temperatures are presented in Table 4.6. The DSC results indicate the as-received NiTi powder and sintered NiTi specimen should be predominantly martensitic at room temperature.

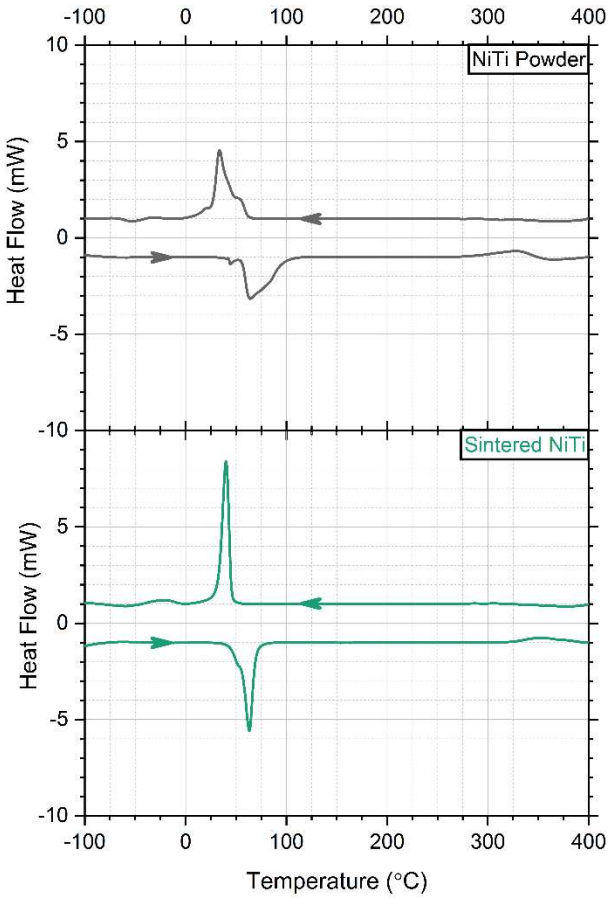

Figure 4.9. Heat flow versus temperature plotted from the differential scanning calorimetry data of as-received NiTi powder and a sintered NiTi specimen. The arrows indicate thermal ramp directions. Positive heat flow corresponds to exothermic events, while negative heat flow corresponds to endothermic events.

Table 4.6. Phase transformation temperatures of as-received NiTi powder and the sintered NiTi specimen determined through analysis of the DSC profiles from Figure 4.9.

Material	Martensitic Finish (°C)	Martensitic Start (°C)	Austenitic Start (°C)	Austenitic Finish (°C)
NiTi Power	26.9	49.6	54.9	98.4
Sintered NiTi	31.4	45.4	54.1	69.6

4.2.2 Density

The geometric measurements and calculated porosities for the NiTi open-cell foam specimens are tabulated in Table 4.7. The low coefficient of variation of the measured porosity (Table 4.7) indicates that any mechanical properties of the foam specimens extracted from the stress-strain profiles will not require normalization prior to comparison using the Gibson-Ashby scaling relations [1]. The difficulties in machining the NiTi+copper composites using conventional tooling and techniques resulted in a degree of variability in the geometric dimensions due the different thermal properties and machining characteristics of the constituent materials. The length of each specimen was judged subjectively based on the degree to which the upper and lower A layer porogens were exposed, a consequence of having to machine a 2 mm layer of NiTi from either end.

Table 4.7. Geometric measurements and calculated porosities for the NiTi open-cell foam specimens (note: pNiTi 34 was sectioned and mounted for EDS analysis, while the remaining specimens were subjected to mechanical testing).

Foam Specimen	**Mass (g)**	**Diameter (mm)**	**Length (mm)**	**L/D Ratio**	**Density (gcc)**	**Porosity (%)**
pNiTi 31	1.05689	9.11	13.67	1.50	1.19	81.6
pNiTi 32	1.09964	9.05	13.72	1.52	1.25	80.7
pNiTi 33	1.13417	9.30	13.42	1.44	1.24	80.7
pNiTi 34	1.12658	9.15	13.55	1.48	1.26	80.4
pNiTi 35	1.08613	9.20	13.11	1.43	1.25	80.7
pNiTi 36	1.06560	9.18	13.21	1.44	1.22	81.1
pNiTi 37	1.06079	9.15	13.18	1.44	1.22	81.0
					Average	80.9
					Standard Deviation	0.039
					Coefficient of Variation (%)	0.49

Additionally, a two-dimensional, cross-sectional SEM image of specimen pNiTi 34 was captured and the relative areal density was determined to be 0.975 by post-process analysis.

The Master Sintering Curve developed for NiTi+Cu specimens (section 5.2.3) predicted the relative density of the NiTi matrix to be 0.964 based on the SPS process parameters used to sinter the NiTi open-cell foams (Table 4.2). The Master Sintering Curve predicted the density of the NiTi matrix to within 1.2% of the areal density extracted from the SEM cross-section image.

4.2.3 Micro-CT

Three-dimensional models constructed from the micro-CT scan data on all seven NiTi open-cell foams after leaching of the copper porogens are shown in Figure 4.10. The variation in model height and skew is due to misalignment of the foam relative to the axis of the micro-CT scanner. The volumetric measurements and calculated porosities from the analysis of the micro-CT data are tabulated in Table 4.8. The porosities measured by the micro-CT scan correspond to those measured by hand (Table 4.7), but exhibit increased variability likely due to the resolution of the scan and the subjective masking required during post-processing to isolate the area of each slice over which to perform the analysis. A representative radiograph of the approximate mid-plane of specimen pNiTi 33 is presented in Figure 4.11. A qualitative review of the individual radiographs reveals uniform pore structure and high degree of replication of the copper porogen template throughout the specimens. Figure 4.11 also shows an unknown mass located in the center pore that is believed to be remnants of undissolved copper, which was also discovered in specimen pNiTi 35 during SEM imaging of the failure surfaces generated by mechanical compression testing (Figure 4.16).

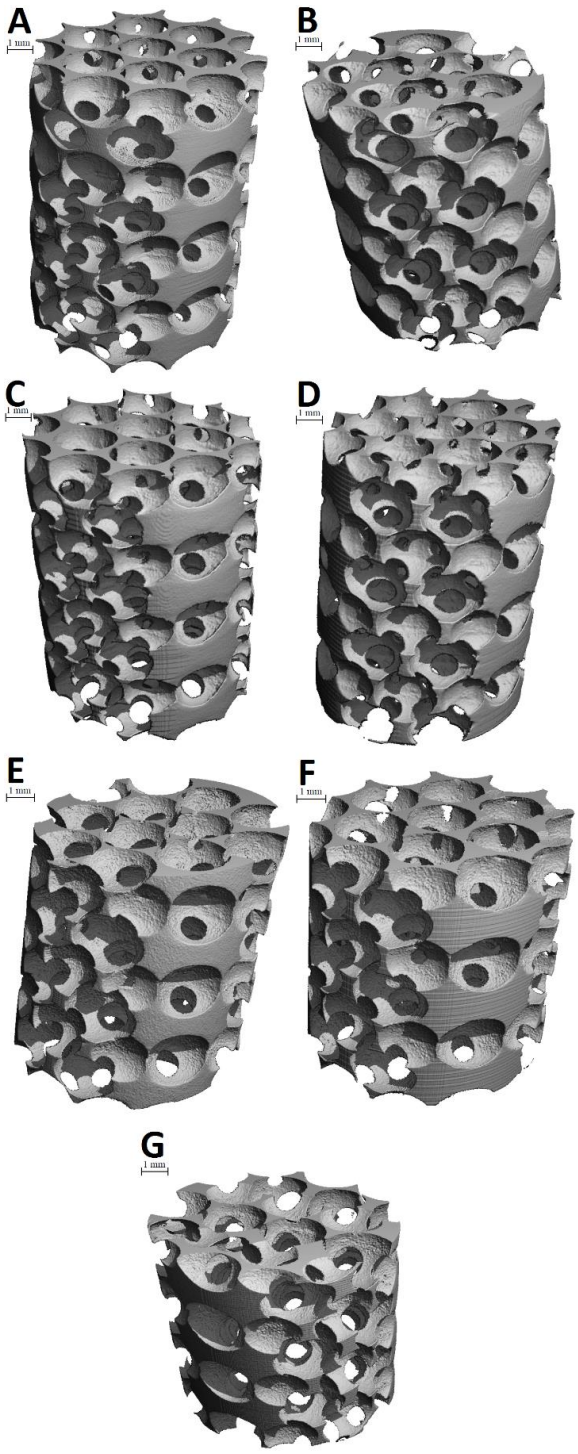

Figure 4.10. Three-dimensional models constructed from the micro-CT scan data on all seven NiTi open-cell foams after leaching of the copper porogens (note: some of the specimens were not well-aligned with the scan axis of the micro-CT and appear shorter due to the skew). (A): pNiTi 31, (B): pNiTi 32, (C): pNiTi 33, (D): pNiTi 34, (E): pNiTi 35, (F): pNiTi 36, (G): pNiTi 37.

Table 4.8. Volumetric measurements and calculated porosities for the NiTi open-cell foam specimens from micro-CT data analysis post-processing (note: pNiTi 34 was sectioned and mounted for EDS analysis, while the remaining specimens were subjected to mechanical testing).

Foam Specimen	Total Volume (mm^3)	Matrix Volume (mm^3)	Density (gcc)	Porosity (%)
pNiTi 31	860.7	178.7	1.34	79.2
pNiTi 32	727.7	143.6	1.27	80.3
pNiTi 33	850.4	159.7	1.21	81.2
pNiTi 34	748.3	143.5	1.24	80.8
pNiTi 35	623.0	128.7	1.33	79.3
pNiTi 36	579.5	119.3	1.33	79.4
pNiTi 37	615.3	122.0	1.28	80.2
			Average	80.1
			Standard Deviation	0.78
			Coefficient of Variation (%)	0.97

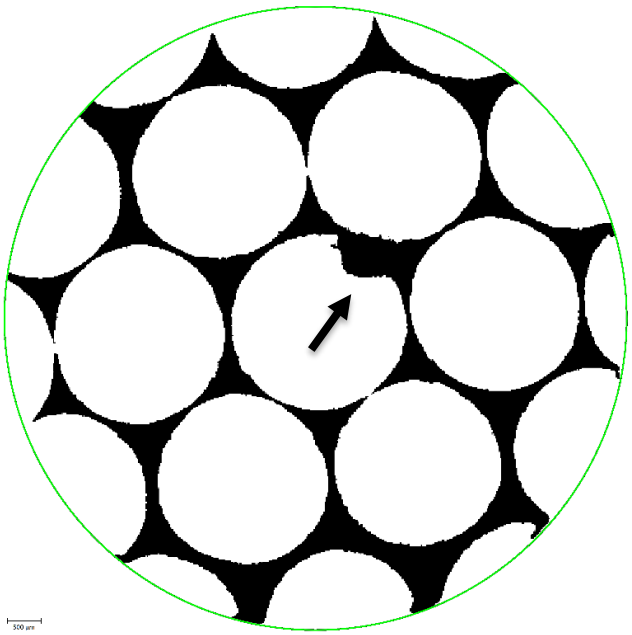

Figure 4.11. Radiograph at the approximate mid-plane of NiTi open-cell foam specimen pNiTi 33 exhibiting uniform pore structure and high degree of replication of the copper porogen template. Arrow indicates unknown mass in center pore believed to be remnants of undissolved copper (note: green circle represents the subjective mask applied to each slice during post-processing analysis to determine the specimen porosity listed in Table 4.8).

4.2.4 Energy-Dispersive X-Ray Spectroscopy

The location and quantitative results from the EDS line scans of NiTi open-cell foam specimen pNiTi 34 are shown in Figure 4.12 through Figure 4.14. Both line scans originated in the acrylic casting resin and transitioned into the NiTi matrix at varying distances. The acrylic casting resin filled an empty pore created by a copper porogen leached during fabrication.

Line scan 1 encounters the gap between the resin and the NiTi matrix from 5.5 µm to 7.5 µm, within which an increase in titanium is detected. There appears to be an edge effect between 7.5 µm and 10 µm where the detection of nickel and titanium is not immediate. Between 10 µm and 13 µm, the three traces plateau with detectable amounts of copper. At an approximate distance of 13 µm, the line scan crosses an apparent powder boundary which causes the nickel and copper traces to decrease sharply with a concomitant increase in titanium. By 15 µm, all three traces have reached steady state values. At approximately 31 µm, the scan appears to encounter another powder boundary.

Line scan 2 encounters the gap between the resin and the NiTi matrix from 7.5 µm to 9 µm. At an approximate distance of 10 µm, the line scan crosses an apparent powder boundary which causes the nickel and titanium traces to decrease sharply. By 12 µm, all three traces have reached steady state values. At approximately 30 µm, the scan appears to encounter another powder boundary, but this time the nickel trace appears mostly unaffected; copper appears to replace titanium across this 4 µm region.

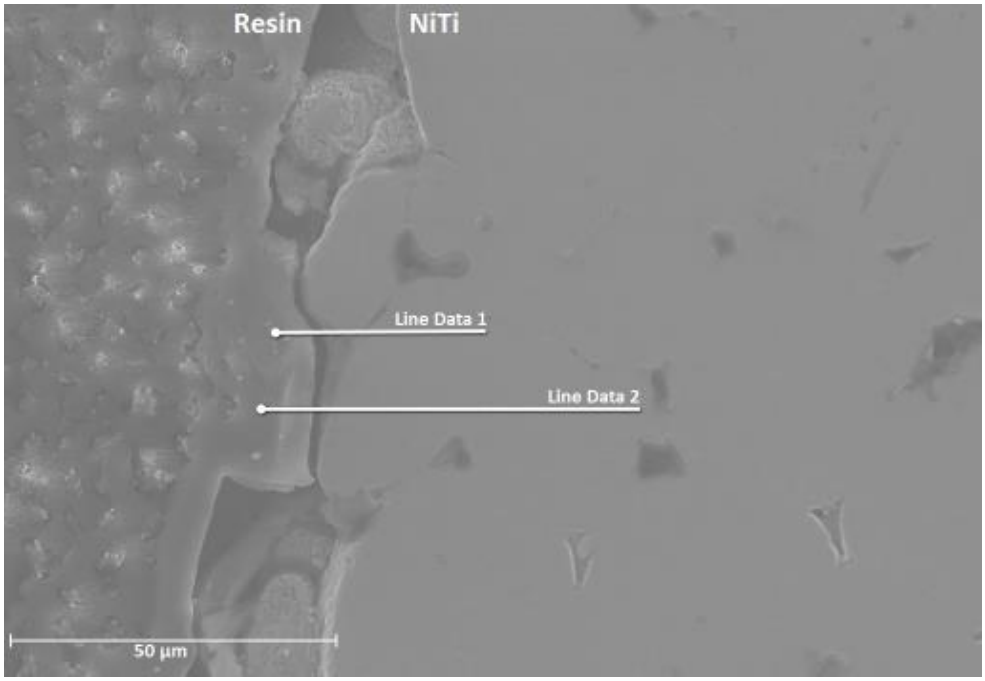

Figure 4.12. SEM image of the potted and polished surface of NiTi open-cell foam specimen pNiTi 34 identifying the location of line scans 1 and 2. The region shown is a cross-section of a triple junction between three pores, like that shown in Figure 4.17.

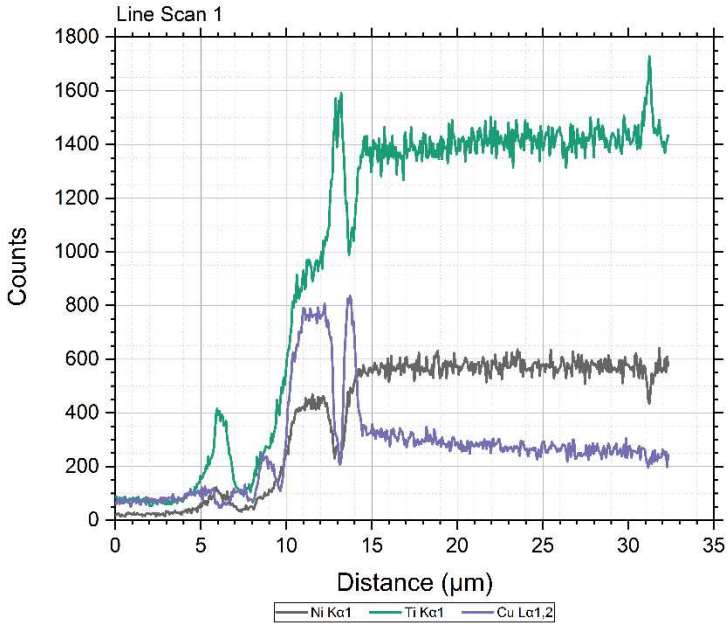

Figure 4.13. EDS data plotted versus distance from the line scan 1 indicating traces of nickel, titanium, and copper detected in NiTi open-cell foam specimen pNiTi 34.

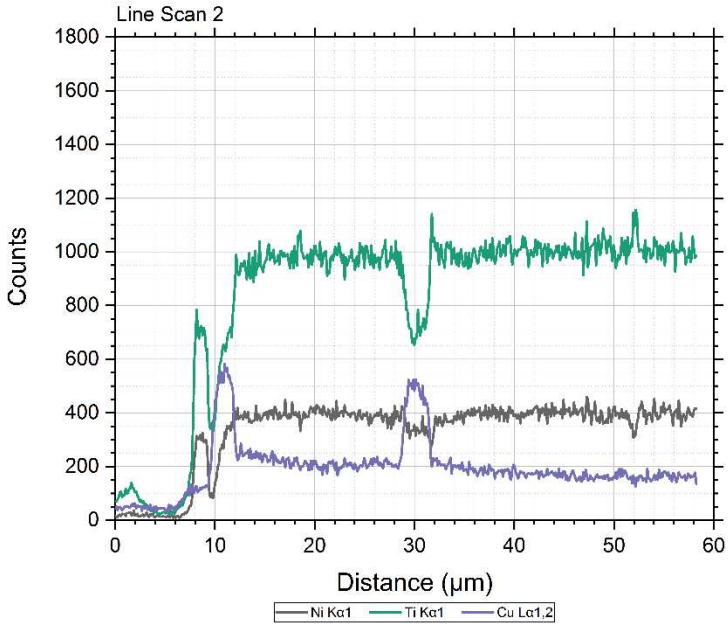

Figure 4.14. EDS data plotted versus distance from the line scan 2 indicating traces of nickel, titanium, and copper detected in NiTi open-cell foam specimen pNiTi 34.

4.2.5 Mechanical Behavior

The stress-strain profiles generated from the destructive mechanical compression tests on the NiTi open-cell foam specimens are plotted in Figure 4.15. The two hysteresis loops have been removed from the plots for clarity; preliminary analysis indicated that the stiffness of the foam specimens did not show a significant sensitivity to loading and unloading cycles prior to and after the yield strength. The stress-strain profiles are plotted starting with the second loading cycle (reference: Table 4.4, step 3), which was extended down to the abscissa using the calculated elastic modulus. The stress-strain profiles display classic elastic-plastic behavior with strain hardening, followed by a progressive failure pattern; however, the foam specimens do not exhibit the expected stress-strain behavior illustrated in Figure 1.1 for an ideal energy absorber: the characteristic plateau stress, large plastic deformation, and densification strain

are all absent. The stress-strain behavior of pNiTi 36 noticeably deviates from the other specimens potentially indicating out-of-family results. Furthermore, the foam specimens appear to cluster into two groups based on their ultimate strength, demarcated by those with strengths above 30 MPa (pNiTi 32, pNiTi 33) and those below (pNiTi 35, pNiTi 36, pNiTi 37).

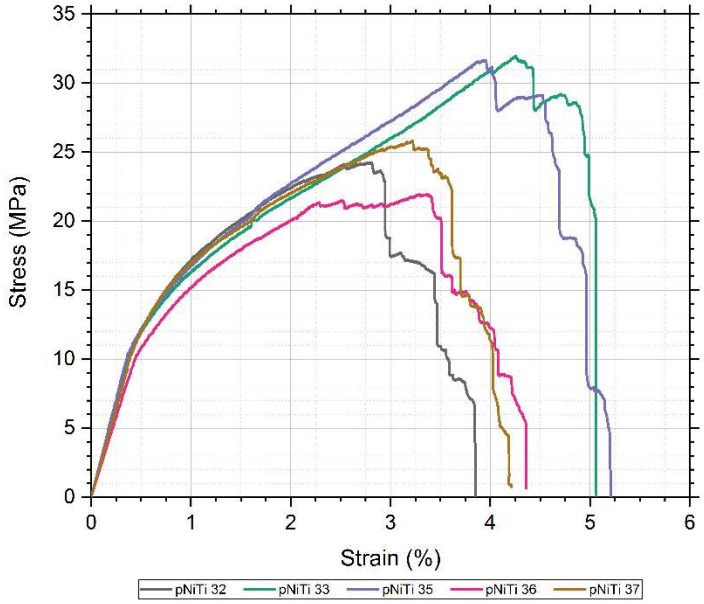

Figure 4.15. Stress versus strain plotted from the destructive mechanical compression tests on the NiTi open-cell foam specimens.

The loading-unloading moduli extracted from the stress-strain profiles (Figure 4.15) are tabulated in Table 4.9. The moduli from the first loading-unloading cycle and the second loading were generated before the yield strength had been exceeded, while the second unloading and third loading moduli values were generated afterwards. The modulus increases by an average of 53% during the initial loading-unloading hysteresis cycle but decreases by an average of 22% during the second cycle. The increased stiffness observed during the initial unloading was maintained during the second loading. The decreased stiffness associated with

the second unloading was temporary as the stiffness measured during the third loading matched that of the second loading, even though they occurred on either side of the yield point.

Table 4.9. The loading-unloading moduli extracted from the stress-strain profiles (Figure 4.15) for each NiTi open-cell foam specimen.

Foam Specimen	Load 1 Modulus (GPa)	Unload 1 Modulus (GPa)	Load 2 Modulus (GPa)	Unload 2 Modulus (GPa)	Load 3 Modulus (GPa)
pNiTi 32	1.89	2.62	2.65	2.04	2.45
pNiTi 33	1.83	2.82	2.77	2.19	2.64
pNiTi 35	1.97	2.93	2.86	2.36	2.76
pNiTi 36	1.35	2.29	2.34	1.97	2.35
pNiTi 37	1.69	2.61	2.49	2.19	2.67

The elastic modulus, elastic strain rate, yield strength, and ultimate strength properties extracted from the stress-strain profiles (Figure 4.15) are tabulated in Table 4.10, along with the average, standard deviation, and coefficient of variation (CV). The elastic strain rate for each specimen meets the requirement of 0.005 inch/inch/minute detailed in ASTM E9 [501], with a CV of 5.3%. The modulus and strength values of pNiTi 36 are clearly lower than the remaining specimens, reinforcing the earlier observation that the stress-strain behavior might be out-of-family; however, a simple statistical analysis based on Tukey Fences (see Appendix 8.4.1) suggests that the parameters associated with pNiTi 36 are not statistical outliers from the larger group. The ultimate strength exhibits the largest CV alluding to stochastic failure behavior, corroborated by the SEM images of the fracture surfaces shown in Figure 4.16 and Figure 4.21.

Table 4.10. The elastic modulus, elastic strain rate, yield strength, and ultimate strength properties extracted from the stress-strain profiles (Figure 4.15) for each NiTi open-cell foam specimen. The average, standard deviation, and coefficient of variation (CV) are calculated across the data set for each property.

Foam Specimen	Elastic Modulus (GPa)	Elastic Strain Rate (inch/inch/min)	Ultimate Strength (MPa)	Yield Strength (MPa)
pNiTi 32	2.65	0.005	24.2	15.3
pNiTi 33	2.77	0.005	32.0	14.0
pNiTi 35	2.86	0.005	31.7	14.4
pNiTi 36	2.34	0.005	21.9	13.6
pNiTi 37	2.49	0.006	25.8	15.5
Average (%)	2.62	0.005	27.1	14.5
Std. Dev. (%)	0.209	0.0003	4.49	0.83
CV (%)	8.0	5.3	16.6	5.7

4.2.5.1 Scanning Electron Microscopy

Select images from the microscopy of the NiTi open-cell foam fracture surfaces produced by the destructive mechanical compression tests are shown in Figure 4.16 through Figure 4.21. Additional microscopy images are available in Appendix 8.2.1. Figure 4.16 shows the remnants of undissolved copper within a pore of specimen pNiTi 35. Figure 4.17 shows a fracture surface from specimen pNiTi 32 located through the minimum cross-sectional area within a triple junction formed between three porogens. This minimum area lies in a plane that bisects the circular interconnect between pores formed by the contact deformation between two copper porogens. Figure 4.18 shows a point of the triple junction shown in Figure 4.17 at higher magnification. Figure 4.19 is a closeup of a fracture surface from specimen pNiTi 36 showing a high degree of sintering between NiTi particles and the intergranular nature of the failure mechanism. Figure 4.20 shows crack initiation at a stress concentration located along the edge of an interconnect between pores from specimen pNiTi 35 and the subsequent

intergranular crack propagation. Figure 4.21 is a closeup along the edge of an interconnect between pores of specimen pNiTi 33 showing the single NiTi particle packing that occurs at the contact point between copper porogens and the nature of an intergranular crack.

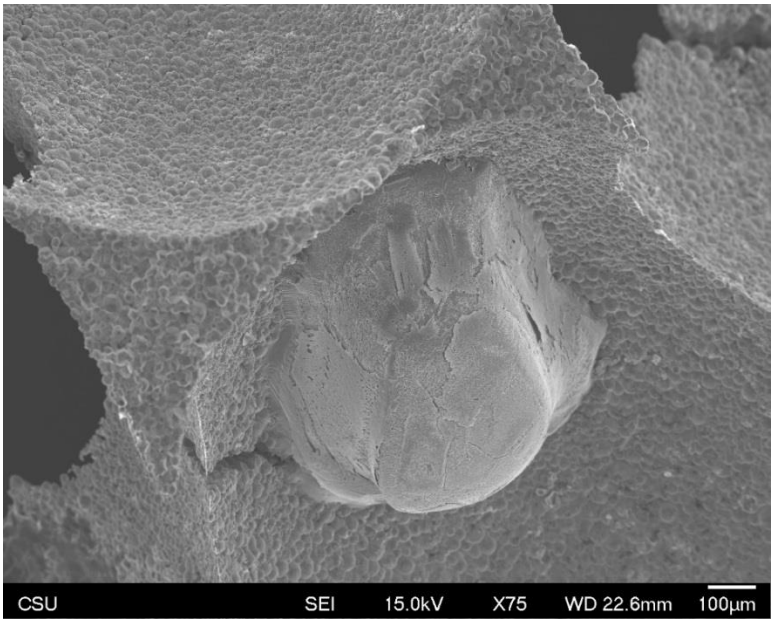

Figure 4.16. Scanning electron microscopy image from specimen pNiTi 35 showing remnants of undissolved copper.

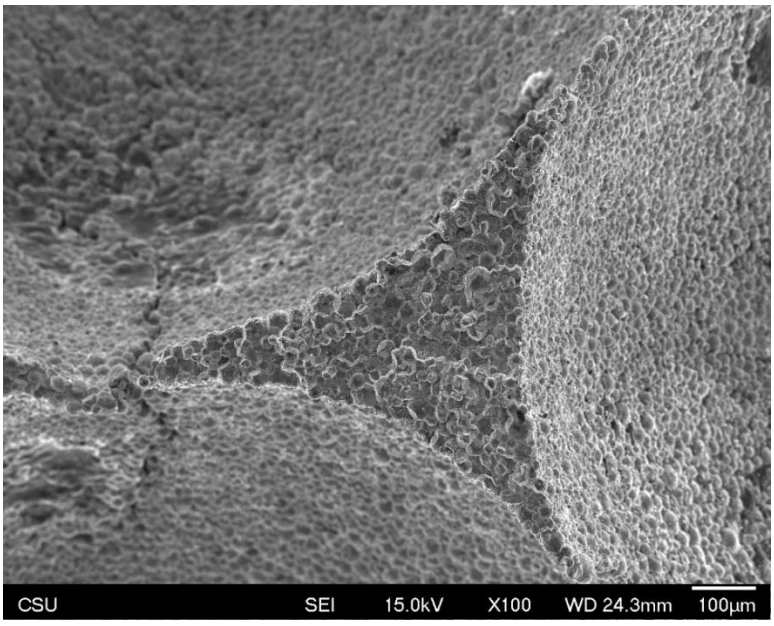

Figure 4.17. Scanning electron microscopy image from specimen pNiTi 32 of fracture surface across smallest cross-sectional area within triple junction between three pores.

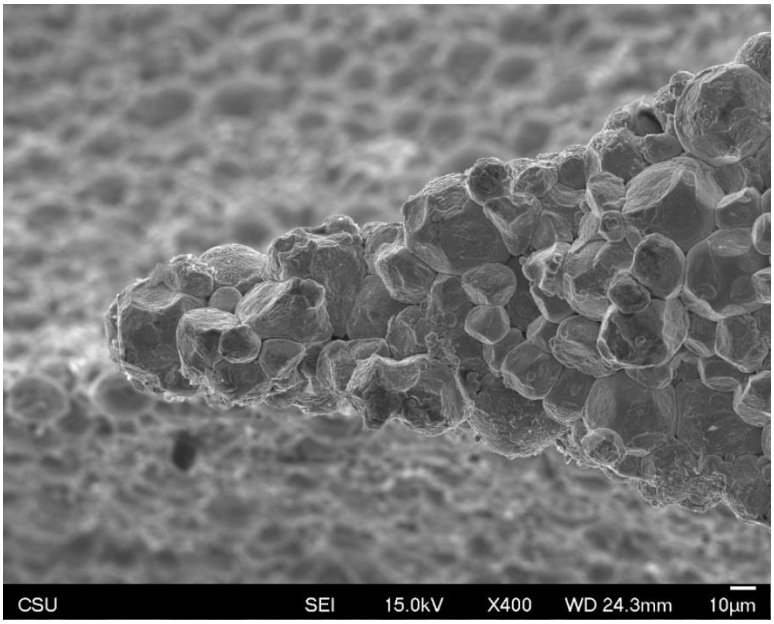

Figure 4.18. Scanning electron microscopy image from specimen pNiTi 32 of higher magnification of surface shown in Figure 4.17.

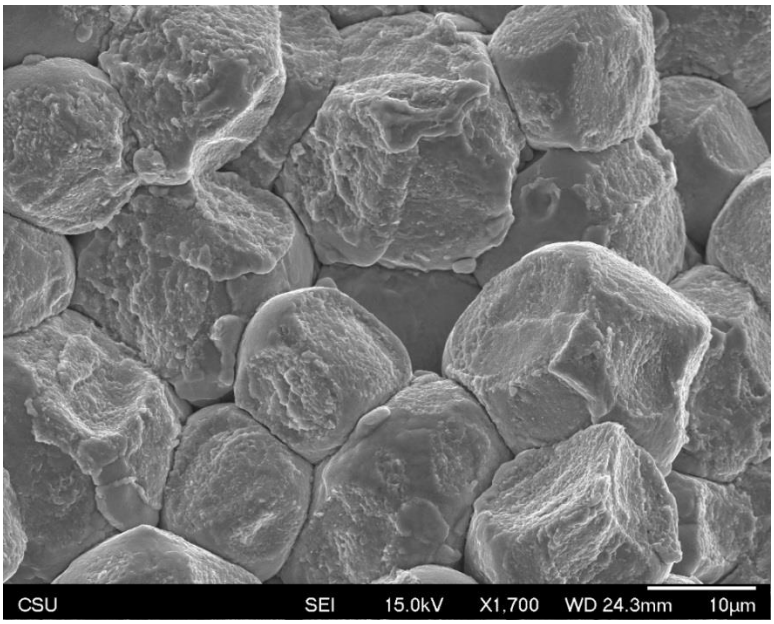

Figure 4.19. Scanning electron microscopy image from specimen pNiTi 36 of closeup of fracture surface showing degree of sintering and intergranular failure surface.

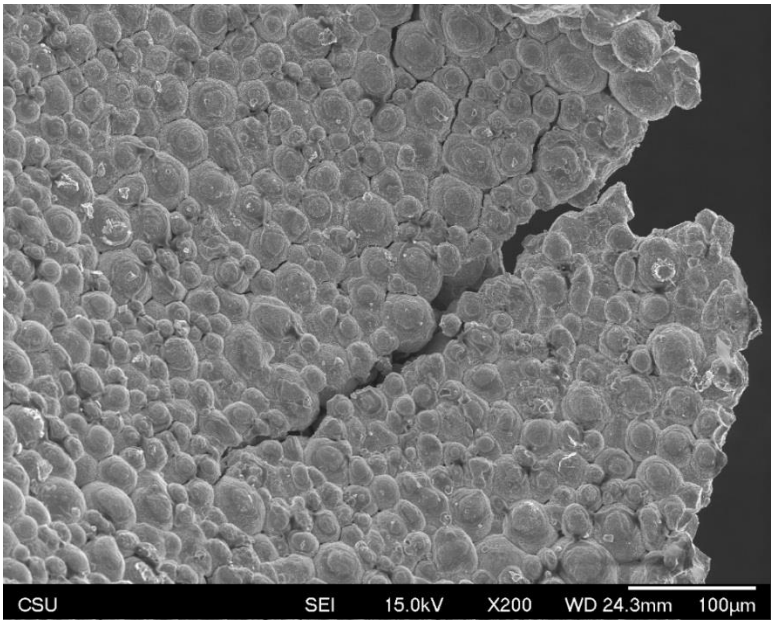

Figure 4.20. Scanning electron microscopy image from specimen pNiTi 35 of crack initiation at a stress concentration along edge of pore interconnect and intergranular crack propagation.

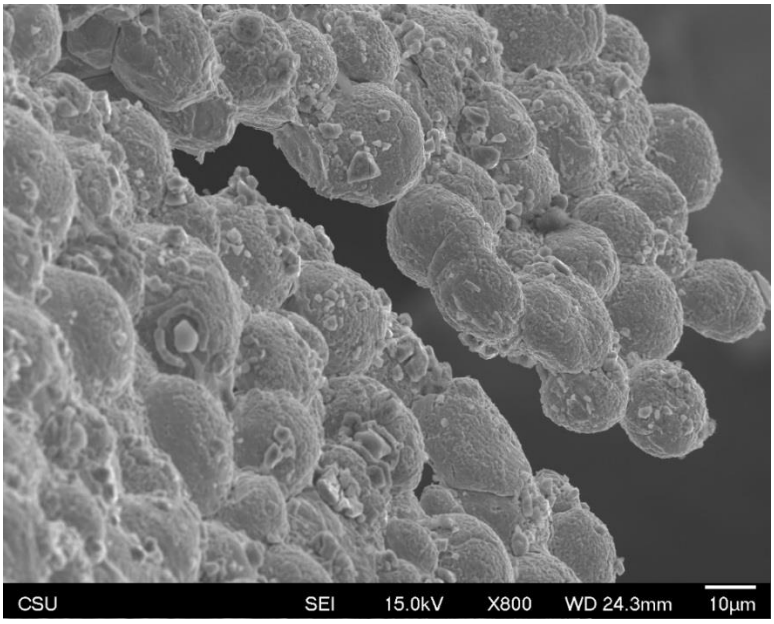

Figure 4.21. Scanning electron microscopy image from specimen pNiTi 33 of closeup of pore interconnect edge showing single particle packing and intergranular crack propagation.

4.3 Discussion

4.3.1 Copper Porogens

The usage of commercially available copper spheres as porogens to fabricate NiTi open-cell foams was driven by the need to achieve higher processing temperatures than the commonly used salt porogens, the need to apply pressure during sintering, and the need to realize spherical pores. Higher processing temperatures and applied pressure both enable faster densification rates during sintering. A porogen which can support the applied pressure at the given processing temperature will exhibit increased control over the pore geometry compared with a porogen that thermally decomposes prior to reaching the sintering temperature. The use of spherical porogens will reduce the internal stress concentrations within pores formed by cuboidal or otherwise irregular porogens.

The processing temperature during sintering (950 °C, Table 4.2) was selected with the intentions of staying well below the melting temperature of copper (1,085 °C). The micro-CT radiographs (Figure 4.11) and SEM images (Figure 4.16 through Figure 4.21) show well-replicated pores and do not suggest any flow of liquid copper; however, inspection of the three-dimensional models constructed from the micro-CT scan data (Figure 4.10) reveals deformation of the pores located on the perimeter of layer B, as highlighted in Figure 4.22. This deformation is not apparent from the individual micro-CT radiographs as they are captured along the axis of the foam specimen which coincides with the axis of pressure application during sintering. The deformation appears to be isolated to each of the B layer pores, the outer A layer pores appear to be spherical as expected. SEM micrographs shown in Figure 8.4 and Figure 8.5 also capture several elliptical pores, although the precise location of the pores within the foam structure is

unclear. The as-machined length (13.1 to 13.7 mm, Table 4.7) shows an approximate 20% decrease from the as-designed length (16.5 mm, section 4.1.2), which is likely caused by the deformation of the B layer pores. One possible explanation could be the increased amount of NiTi powder packed around the B layer providing enough compliance during pressure application to allow a greater deformation of the outer copper porogens, especially considering the likely reduction in copper modulus with increased temperature.

Another potential explanation is the temperature of the NiTi powder and copper porogen mixture exceeded the melting temperature of copper. Thermal gradients across the graphite die have been demonstrated indicating a higher internal temperature than on the surface of the die [428], suggesting the measurement of the die temperature for process control may not capture the true temperature of the powder specimen. A supplemental SPS experiment was conducted on NiTi powders with parameters consistent with those in Table 4.2. Thermocouples embedded in the upper graphite punch exhibited a maximum temperature delta of +179 °C compared to the thermocouple embedded in the graphite die. Furthermore, the punch temperature exceeded the melting temperature of copper (1,085 °C) at a die temperature of only 917 °C. The Master Sintering Curve developed for NiTi+Cu specimens (section 5.2.3) indicates the NiTi matrix relative density at 917 °C should be 0.913, indicating a high degree of pore isolation which would likely have contained any liquid copper formation. Finite element modeling [428, 503] has illustrated a localized peak temperature within the upper punch which suggests the punch temperature recorded during the supplemental SPS experiment was a measurement of this localized thermal gradient and not necessarily extensible to the powder specimen temperature within the graphite die. The inability to

directly measure the internal temperature of the powder specimen can neither confirm or deny the formation of liquid copper during NiTi open-cell foam sintering, but the evidence suggests it is a possibility.

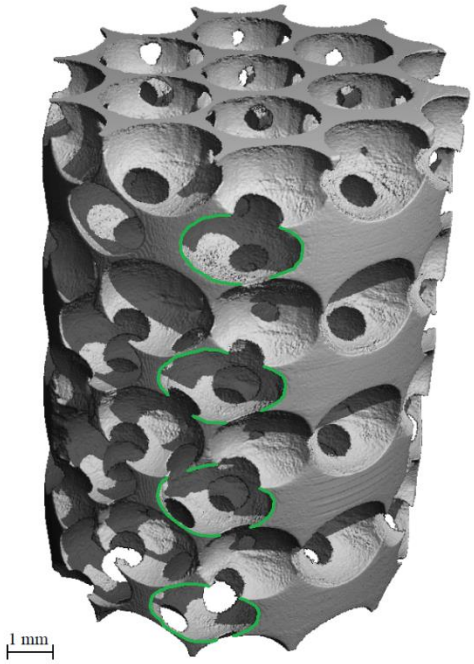

Figure 4.22. Deformation of the outer pores within each of the four B layers of specimen pNiTi 31 highlighted in green.

Another concern of using copper porogens is the potential of elemental copper to diffuse into the NiTi matrix resulting in inadvertent compositional variations. According to the EDS line scan data (Figure 4.13 and Figure 4.14) copper appears to have diffused up to 5 µm into the NiTi matrix. There is an additional peak in copper detection from line scan 2 at 30 µm, which appears to have substituted for titanium. It is unclear if this distance is located within a powder particle or within the particle boundary. Copper also exhibits a low-level threshold across most of the scan distance; follow up point measurements did not reveal any copper trace in the spectrum at greater distances. This low-level threshold could be due to the

proximity of the copper peaks relative to nickel within the spectrum, creating a possible false-positive detection of copper. Overall, there is insignificant copper diffusion into the matrix, and therefore the NiTi material properties are unlikely to have been compromised. The relatively short sintering time afforded by the SPS process has likely restricted this diffusion.

The use of nitric acid (HNO_3) was highly effective in leaching the copper porogens without reacting with the NiTi matrix. The micro-CT radiographs (Figure 4.11) and SEM images (Figure 4.16 through Figure 4.21) indicate complete dissolution of the porogens except in two isolated cases where a small copper remnant was detected in specimens pNiTi 33 (Figure 4.11) and pNiTi 35 (Figure 4.16).

4.3.2 Open-Cell Foam Structure

The average porosity of the NiTi open-cell foams fabricated during the current research was measured to be 80.9% (Table 4.7), which exceeds 91% of the published research summarized in Figure 4.23. Higher porosities were obtained in the literature through either reticulated foam templating (section 1.3.1.1) or the NiTi foams possessed significant amounts of matrix microporosity. The average porosity of 80.9% exceeds that predicted from the CAD design (72.6%, section 4.1.2) due to the copper sphere deformations mentioned previously (section 4.3.1) causing the specimen length to be approximately 20% shorter than predicted.

Examination of the SEM micrographs (Figure 4.19, Figure 8.2, and Figure 8.10) indicates the NiTi matrix achieved nearly full density, observable microporosity appears to be less than 10 µm in size. Indeed, the density predictions based on the master sintering curve concept (chapter 5) indicate the matrix density exceeds 97% for the given open-cell foam processing

parameters (Table 4.2). Unfortunately, the micro-CT radiographs cannot readily detect the matrix porosity due to the 10 µm resolution of the scans.

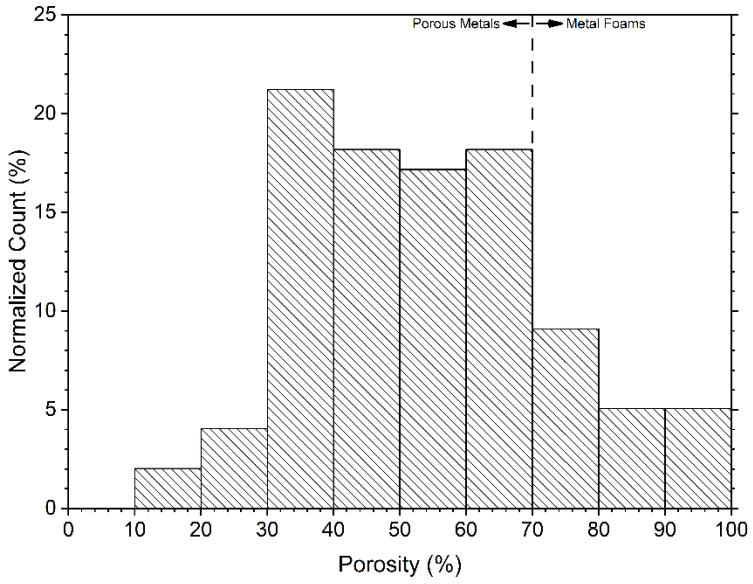

Figure 4.23. Histogram showing percentage of literature publications with respect to specimen porosity detailing research on porous NiTi metals (< 70% porosity) and NiTi metal foams (≥ 70% porosity). Research on porous NiTi metals comprises 81% of the total literature surveyed, while the remaining 19% details NiTi metal foams.

Examination of the SEM micrographs (Figure 4.19, Figure 8.2, and Figure 8.10) indicates the NiTi matrix achieved nearly full density, observable microporosity appears to be less than 10 µm in size. Indeed, the density predictions based on the master sintering curve concept (chapter 5) indicate the matrix density exceeds 97% for the given open-cell foam processing parameters (Table 4.2). Unfortunately, the micro-CT radiographs cannot readily detect the matrix porosity due to the 10 µm resolution of the scans.

The micro-CT radiographs (Figure 4.11) and SEM images (Figure 4.16 through Figure 4.21) show well-replicated pores arranged in an HCP structure. Analysis of the mid-plane

radiographs for specimens pNiTi 31, 33, 34, and 36 reveal an average circularity of 0.73, adjusted for the pixelation of a perfect circle. The circularity measures the two-dimensional shape and roughness, and as such the circularity of elongated pores, such as those shown in Figure 8.4, can exceed 0.90. The average circularity from the analysis of the mid-plane radiographs has most likely been lowered below expectations due to the roughness of the pores, whether artificial or real. For comparison, circularity measurements of pores formed from cuboidal salt porogens are as low as 0.39. Furthermore, the micro-CT radiographs indicate a high degree of interconnectivity between pores; however, there appear to be some pores which do not exhibit full in-plane coordination with their surrounding neighbors. This could be an artifact of the scan resolution, but more likely the copper porogens separated under applied load during sintering due to an insufficient bond formed from the superglue. It is unlikely that melting of the copper porogens would cause separation as this would require flow of the liquid copper away from the neighboring porogens and would be apparent due to collapse of the vacated pores. It is also unlikely that deformation of the copper porogens resulted in separation since the spheres would exhibit uniform outward in-plane deformation toward their neighbors.

4.3.3 Mechanical Behavior

The NiTi open-cell foams specimens were predominantly in the martensitic phase during room temperature mechanical compression testing, as indicated by the XRD (Figure 4.8) and DSC (Figure 4.9, Table 4.6) results.

The 53% difference in elastic modulus during the initial loading-unloading hysteresis cycle is attributed to a reduction of the initial loading modulus resulting from the occurrence of

localized plasticity at stress concentrations within the foam structure leading to detwinning of the martensitic phase. The 22% decrease in elastic modulus during the second unloading is likely due to the strain recovery characteristic of the small fraction of austenitic phase present within the NiTi microstructure. This superelastic effect also explains why the subsequent loading stiffness matches the loading stiffness from the second hysteresis cycle.

The specimens exhibit elastic modulus and yield strength values with no statistical outliers in part due to the small scatter in measured porosity values (Table 4.7). Theoretical elastic modulus values were established by applying the following Gibson-Ashby scaling equation [1, 4]:

$$\frac{E^*}{E_s} = C_1 \left(\frac{\rho^*}{\rho_s}\right)^2$$

where $C_1 = 1$ [1] and $E_s = 69\ GPa$ [504]. The comparison of the theoretical and experimental elastic moduli is presented in Table 4.11, with reasonably good agreement, noting that the elastic modulus of martensitic NiTi has a tolerance of ± 4 GPa [504] which might account for some of the difference. The apparent yield point exhibited by each specimen relates to the stress-induced detwinning of martensite; however, difficulties in assigning a consistent detwinning stress to martensitic NiTi precluded the application of the Gibson-Ashby scaling equation for compression stress.

The small scatter in measured porosity values (Table 4.7) suggests the significant variability in the measured failure stress is due to stochastic failure behavior, possibly controlled by fracture mechanisms such as crack initiation and propagation. Investigation of the fracture surfaces by scanning electron microscopy (Figure 4.16 through Figure 4.21) reveals

brittle failure behavior and an abundance of macro- and microscopic interparticle crack growth. Crack initiation generally appears to be highly concentrated around the perimeter of the pore interconnects at stress concentrations created by the decidedly irregular edge morphology formed by a single layer of NiTi particles. Closer examination of the fracture surfaces uncovers very little material transfer between particles during failure suggesting little-to-no ductility mechanisms were active.

Table 4.11. Comparison of the theoretical and experimental elastic moduli for the five-compression tested NiTi open-cell foam specimens which underwent loading-unloading hysteresis cycling. The theoretical elastic modulus was calculated using the Gibson-Ashby scaling equation [1, 4] and an elastic modulus of martensitic NiTi of 69 GPa [504].

Foam Specimen	Geometric Density (gcc)	Theoretical Elastic Modulus (GPa)	Experimental Elastic Modulus (GPa)	Difference (%)
pNiTi 32	1.25	2.58	2.65	2.6
pNiTi 33	1.24	2.57	2.77	7.1
pNiTi 35	1.25	2.57	2.86	10.0
pNiTi 36	1.22	2.46	2.34	5.0
pNiTi 37	1.22	2.49	2.49	0.1

The small scatter in measured porosity values (Table 4.7) suggests the significant variability in the measured failure stress is due to stochastic failure behavior, possibly controlled by fracture mechanisms such as crack initiation and propagation. Investigation of the fracture surfaces by scanning electron microscopy (Figure 4.16 through Figure 4.21) reveals brittle failure behavior and an abundance of macro- and microscopic interparticle crack growth. Crack initiation generally appears to be highly concentrated around the perimeter of the pore interconnects at stress concentrations created by the decidedly irregular edge morphology

formed by a single layer of NiTi particles. Closer examination of the fracture surfaces uncovers very little material transfer between particles during failure suggesting little-to-no ductility mechanisms were active.

The stress-strain behavior of the NiTi open-cell foam specimens (Figure 4.15) deviate from that of an ideal energy absorber (Figure 1.1) due to the fracture-dominate failure mechanisms resulting from the numerous microscopic stress concentrations. Additionally, the NiTi matrix was not designed to be a load-bearing structure, but rather to accommodate a high packing factor of spherical pores. Although the stress-strain profiles of Figure 4.15 appear to exhibit a yield stress expected of an ideal energy absorber, this behavior is associated with the stress-induced detwinning of the martensitic NiTi phase and not indicative of classical yielding. The crack initiation and propagation-induced brittle failure precedes the yield stress, plastic deformation-driven plateau stress, and eventual densification strain characteristic of an ideal energy absorber. Elimination of the microscopic stress concentrations, along with a more structurally-sound, load-bearing design of the foam matrix, would most certainly allow the NiTi open-cell foams to achieve the characteristics of an ideal energy absorber.

5. EFFECT OF COPPER POROGENS ON THE DENSIFICATION OF NITI POWDER DURING SPARK PLASMA SINTERING USING MASTER SINTERING CURVES

The principal goal during powder metallurgy is to achieve full specimen density such that the maximum properties available from the metal alloy are realized. The typical practice to determine the optimal process parameters is iterative: assume a set of values, sinter, and measure resultant specimen density. This is repeated to *map* the density-process parameter space, which requires dozens of specimens due to the number and range of variables. This practice is not conducive to determining optimal process parameters in an efficient manner from the perspective of time and material usage.

This research effort applies the master sintering curve (MSC) concept (see section 2.3) to determine the optimal time and temperature process parameters, at a fixed pressure, to achieve full density (≥ 0.97) of NiTi specimens by running a limited number of sintering experiments. Subsequently, several additional specimens are sintered isothermally to verify the accuracy of the generated MSC.

The MSC concept is extended to investigate the effect of copper porogens on the densification behavior of NiTi during the fabrication of open-cell foams discussed in chapter 4. To achieve maximum mechanical properties, the open-cell foams required fully dense matrices obtained through proper selection of the sintering parameters. Due to the exertion required to fabricate individual open-cell foam specimens, and the difficulties in accurately measuring their as-sintered matrix density, a detailed processing-density study that included the potential contributions of the copper porogens was not feasible. Based on the literature [317, 465, 466, 468, 473-475, 489], it was hypothesized that any densification-related effects from the copper

porogens would manifest as differences in the apparent activation energies between NiTi and NiTi with copper porogens (abbreviated as NiTi+Cu hereafter).

While MSCs are typically generated from dilatometry data, the current research effort utilizes the same spark plasma sintering (SPS) equipment by which all NiTi specimens, including the open-cell foams, were fabricated. This *in situ* approach aims to capture the influence of applied load and possible field effects afforded by the SPS technique which cannot be easily replicated in a standard dilatometer.

5.1 Materials and Methods

5.1.1 Raw Materials and SPS Tooling

Pre-alloyed NiTi powder supplied from Special Metals Corporation with a particle size range of 10 to 44 μm (Figure 5.1) was utilized for both the NiTi and NiTi+Cu specimens. Porogens were low-cost copper spheres (102, H04 temper, 99.95% purity) commercially available from McMaster-Carr with a diameter of 0.09375 ± 0.001-inch.

The as-received NiTi powder was subjected to direct current plasma emission spectroscopy to determine its elemental composition per ASTM E1097-12 [498]; characterization was performed by Luvak Inc., of Massachusetts. The phase constituents of the as-received NiTi powder were investigated using a Bruker D8 Discover X-ray diffractometer. Using CuK_α radiation at 40 kV and 40 mA, the X-ray diffractogram was captured between diffraction angles of 35° to 80° (2Θ) at a 0.02° step size and a 0.2 second preset time. The powder sample was dynamically rotated during characterization. The phase analysis was performed by hand using the methods detailed by Cullity [499] and the parameters listed in Table 5.1.

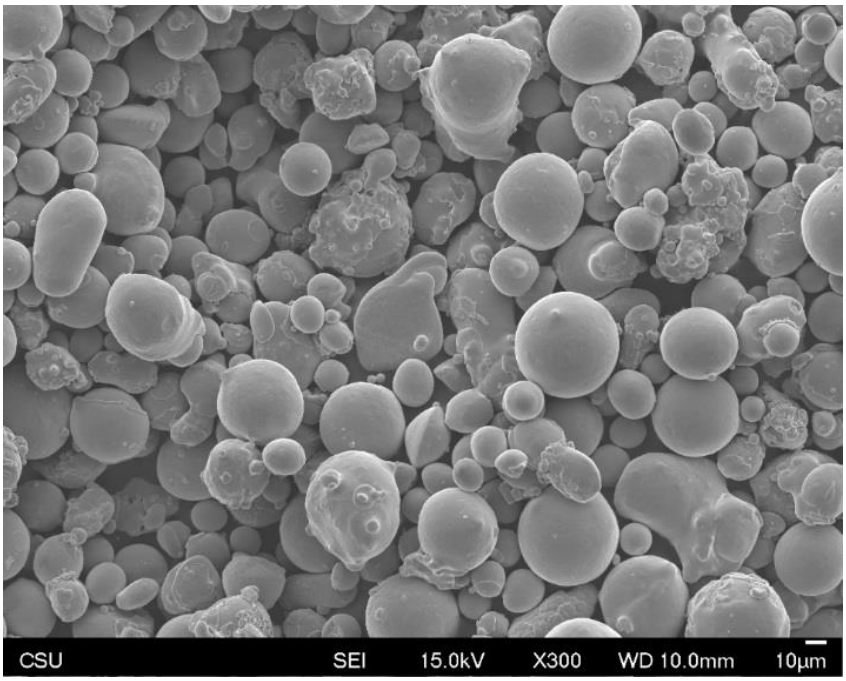

Figure 5.1. SEM micrograph of NiTi powder used for all sintering experiments obtained from Special Metals Corporation.

Table 5.1. Parameters used to perform phase analysis of X-ray diffractogram data obtained from as-received NiTi powder.

NiTi Phase	Lattice System	a (Å)	b (Å)	c (Å)	β (°)	λ (Å)
Austenite	Cubic	3.010	-	-	-	1.5405
Martensite	Monoclinic	4.646	4.108	2.898	97.78	

Both the as-received NiTi powder and a sintered NiTi specimen were subjected to differential scanning calorimetry (DSC) to determine the austenite-martensite phase transformation temperatures. The NiTi specimen was prepared for DSC by grinding and polishing a small sheet of dense NiTi sectioned from a sintered disc. The mass of NiTi powder dispensed for DSC evaluation was matched to that of the sintered specimen to avoid potential scaling complications. The experimental procedure was loosely based on ASTM F2004-05 [500] and consisted of thermal cycling the specimens from -130 °C to +425 °C and back at 10 °C/min

with 5-minute dwells at the temperature extrema. Dry nitrogen was used as a cover gas with a flow rate of 30 mL/min at 5 psi. The DSC instrument was calibrated using indium and tin samples; a baseline correction was also applied.

All sintering runs were conducted using a die and two punches fabricated from ultra-fine graphite round stock (AR-14 material name) sourced from Ohio Carbon Blank. Geometrically, the die was an annular cylinder of dimensions 50 mm (outer diameter) by 48 mm (height) with a 20 mm axial hole, while the punches were cylinders of dimensions 19.7 mm (diameter) by 27 mm (height). The punch diameter was slightly undersized to accommodate the thickness of a graphite liner, which primarily facilitated the post-sintering extraction of the punches and specimen from the die. Additionally, a graphite disc was placed on the internal face of both punches in contact with the NiTi powder to separate the punches from the sintered specimen. An example of a graphite die, graphite punches, graphite discs, and a graphite liner used to sinter MSC specimens is shown in Figure 5.2.

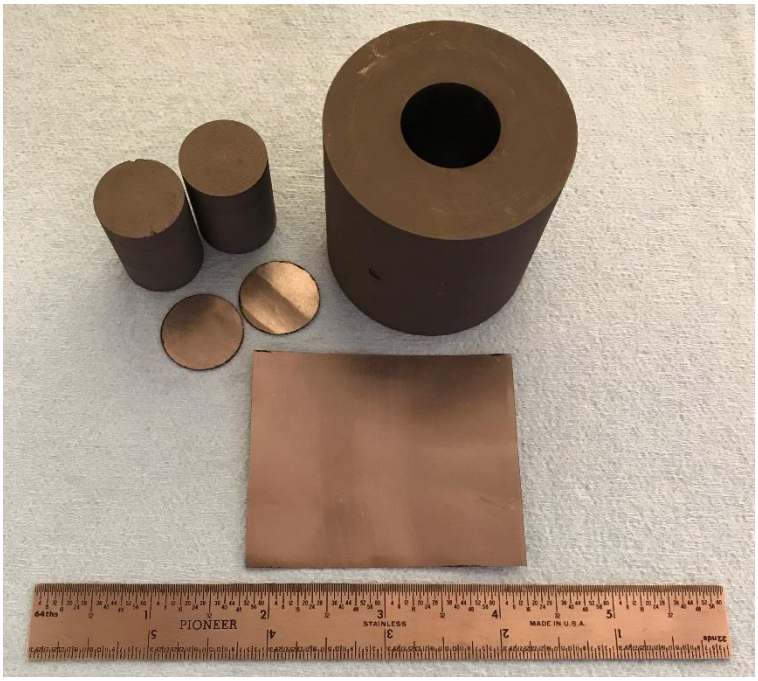

Figure 5.2. Graphite die (x1), graphite punches (x2), graphite discs (x2) and graphite liner (x1) used to sinter MSC specimens.

5.1.2 Sintering of NiTi

NiTi specimens were sintered by weighing out 9.82 grams of powder based on a full density of 6.45 gram/cm^3 (gcc) and a target specimen height of 5 mm. A graphite liner was inserted into the die and together they were assembled over the lower punch. A single disc of graphite was placed inside the die covering the top surface of the lower punch. The dispensed NiTi powder was poured into the die and slightly agitated to distribute the powder evenly. A slightly undersized punch was inserted into the die to compact the powder by hand, then slowly removed with a slight twisting motion to minimize disturbance of the powder. Another disc of graphite was carefully placed on top of the compacted powder, followed by insertion of the upper punch.

The graphite tooling was loaded into a Dr. Sinter SPS machine (Fuji Electronic Industrial Co., LTD., Japan) between six circular graphite plates symmetrically arranged between the two SPS electrode platens. The graphite stack and tooling were positioned coaxial with the electrode platens to facilitate uniform current density distribution. A slight pre-load was applied across the assembly and a K-type thermocouple probe (Omega Engineering, P/N: TJ48-CAIN-116G-24) was installed into the die ensuring the probe was sufficiently sprung to avoid loss of contact during sintering operations. The SPS chamber was sealed and pumped down under vacuum pressure.

The SPS thermal controller was programmed based upon the experimental process parameters detailed in Table 5.2. Three different constant heating rate experiments were chosen to generate the MSC: 50, 40, and 30 °C-per-minute. The SPS thermal controller leveraged a PID strategy for temperature control with user-defined values of 10 (proportional), 20 (integral), and 5 (derivative). The pre-load across the graphite stack was initially set to 10 kN (32.8 MPa) and adjusted to 25 kN (82.1 MPa) during step two of the thermal profile (Table 5.2). The thermal profile was initiated on the SPS thermal controller and allowed to run to completion; this constituted the initial sintering run. After allowing the graphite die to cool to room temperature, a background run was performed by re-executing the thermal and load profiles (Table 5.2) on the sintered NiTi specimen.

Table 5.2. SPS process parameters to determine the Master Sintering Curve for NiTi from individual constant heating rate experiments of 50, 40, and 30 °C/minute.

Step	Set Point Variable (°C)	Time (minutes)	Applied Load (kN)
S0	0	-	10
S1	200	2.0	10
S2	200	2.0	10 → 25
S3	1100	18.0 (50 °C/min) 22.5 (40 °C/min) 30.0 (30 °C/min)	25
S4	END		

5.1.3 Assembly of Copper Porogen Templates

To facilitate the sintering of the NiTi+Cu specimens, porogen templates were constructed in two different layers as illustrated in Figure 5.3. Layer A contained 48 individual copper spheres, while layer B contained 36 for a total of 84 copper spheres per specimen. The geometry and eventual nesting (Figure 5.4) of layers was designed for maximum packing factor following a hexagonal close-packed (HCP) arrangement consistent with the fabrication of open-cell foams discussed in chapter 4 [note: since only 2 layers are assembled for the MSC generation, the packing arrangement also can be considered face-centered cubic (FCC)]. The individual copper spheres were placed in a jig according to their layer pattern and glued by hand according to the glue points identified in Figure 5.3. Loctite Ultra Gel Control Super Glue (P/N: 1363589) was dispensed in discrete droplets from a 3 mL plastic syringe equipped with a 304 stainless steel needle having an 0.012-inch inner diameter and a 0.25-inch length. Each layer was fully cured for 24 hours before being subjected to the sintering process.

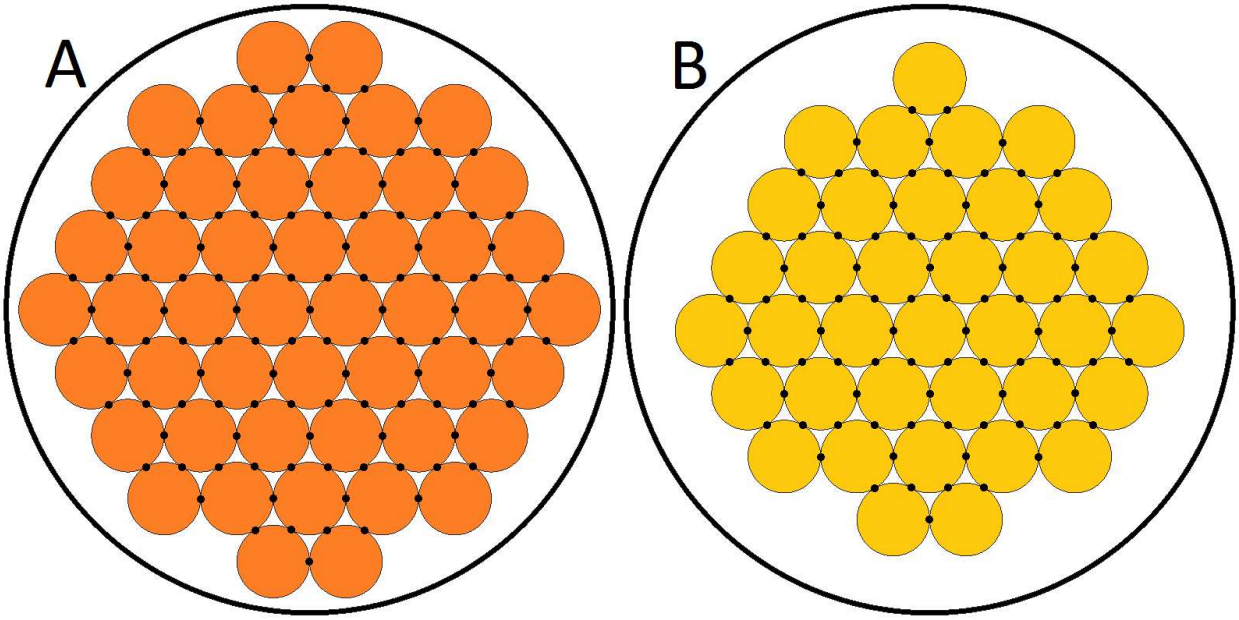

Figure 5.3. Layer A and layer B porogen templates constructed from copper spheres. Glue points are indicated as black dots. The inner wall of the graphite die is shown to illustrate the relative packing factor of each layer.

5.1.4 Sintering of NiTi+Copper

To isolate the potential influence of the copper porogens on the densification behavior of NiTi, the mass of NiTi powder and the applied load was kept constant across the two experimental groups (NiTi and NiTi+Cu). Enforcing a constant sintered specimen height was also considered, which would have reduced the mass of NiTi powder required for the NiTi+Cu specimens; however, this would have reduced the magnitude of the raw displacement data output by the SPS equipment relative to the NiTi specimens and would have potentially obscured the effects of the copper porogens on densification behavior. Considering the mass of NiTi (9.82 grams) combined with the number of copper spheres (84), the NiTi+Cu specimens possess a nominal composition of 71.9% NiTi to 28.1% copper by volume.

A graphite liner was inserted into the die and together they were assembled over the lower punch. A single disc of graphite was placed inside the die covering the top surface of the lower punch. One-half the total mass of NiTi (4.91 grams) was weighed, poured into the die, and slightly agitated to distribute the powder evenly. A slightly undersized punch was inserted into the die to compact the NiTi powder, then slowly removed with a slight twisting motion to minimize disturbance of the powder. The remaining NiTi powder (4.91 grams) was weighed and loaded into a 6 mL plastic syringe equipped with a 304 stainless steel needle having an 0.054-inch inner diameter and a 0.25-inch length. The A layer of copper spheres was carefully placed on top of the compacted powder. Additional NiTi powder was dispensed from the syringe to fill in the small gaps between the copper porogens and around the perimeter of the A layer. The B layer of copper spheres was then nested on top of the A layer as indicated in Figure 5.4. The remaining NiTi powder contained in the syringe was dispensed over the top of the B layer and compacted with an undersized punch as before. Another disc of graphite was carefully placed on top of the compacted powder, followed by insertion of the upper punch.

The graphite tooling was loaded into the SPS machine and sintered as described previously (see section 5.1.2). The SPS temperature controller was programmed based upon the experimental process parameters detailed in Table 5.3. Unlike the NiTi specimens, which can be sintered very close to the melting temperature of NiTi (1,310 °C), the copper porogens cannot exceed 1,085 °C. To generate a densification curve only using a constant heating rate would require a very low heating rate for the sintered specimen to reach full density, which might risk significant surface diffusion and invalidate the application of the MSC concept. Thus, combined constant heating rate and isothermal dwell experiments were conducted during the

generation of the MSC to allow the NiTi+Cu specimens to achieve full density. As detailed in Table 5.3, three different constant heating rate experiments were chosen to generate the MSC: 100, 75, and 50 °C-per-minute, each followed by a 10-minute dwell at 950 °C. A reduction in the heating rate at 900 °C was implemented to dampen the disturbance in the SPS electrode platen displacement data during the abrupt transition to the isothermal dwell; this disturbance will create an artificial perturbation in the MSC and should be minimized as much as possible. A cross-section of the final specimen configuration illustrating the location of the porogen layers within the sintered NiTi matrix, the relative volumetric portions of the constituents, and the contact points between individual porogens is shown in Figure 5.5.

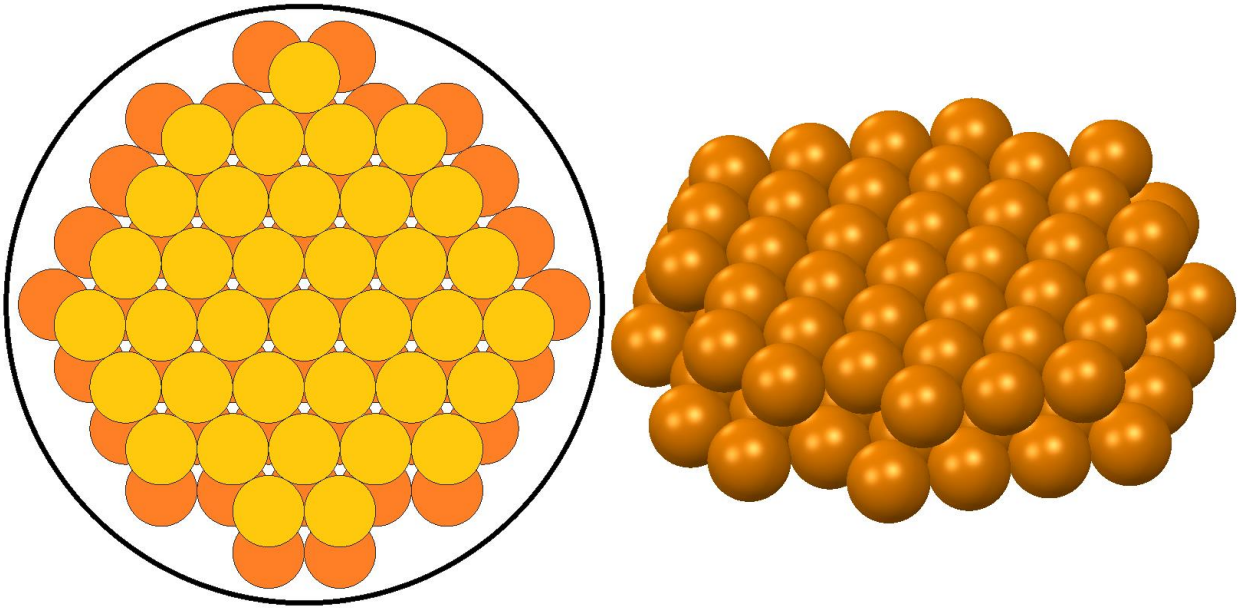

Figure 5.4. Nesting of the copper porogens: (left) A layer is on bottom (orange) and B layer is on top (yellow); (right) three-dimensional representation of copper porogen template used for the MSC studies.

Table 5.3. SPS process parameters to determine the Master Sintering Curve for NiTi+Cu from individual constant heating rate experiments of 100, 75, and 50 °C/minute, followed by a 10-minute dwell at 950 °C.

Step	Set Point Variable (°C)	Time (minutes)	Applied Load (kN)
S0	0	-	10
S1	200	2.0	10
S2	200	2.0	10 → 25
S3	900	7.0 (100 °C/min) 9.33 (75 °C/min) 14.0 (50 °C/min)	25
S4	950	1.0	25
S5	950	10.0	25
S6	END		

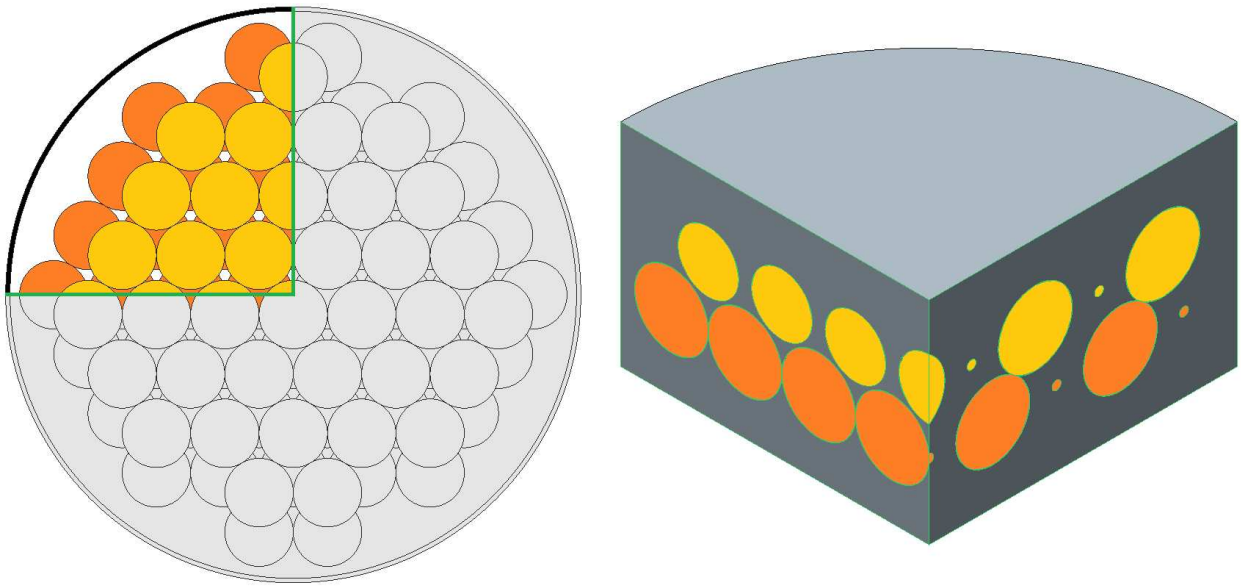

Figure 5.5. A cross-section of the final specimen configuration illustrating the location of the porogen layers within the sintered NiTi matrix, the relative volumetric portions of the constituents, and the contact points between individual porogens.

5.1.5 Archimedes' Principle for Determination of Density

Generation of the MSC requires either the initial or final specimen density to be known along with the density evolution as a function of time (or temperature). Additionally, it is

critical to the MSC generation that the powder compact be sintered to full density during the initial run to prevent densification from occurring during the background run and thus, artificially increasing the thermal expansion. To determine the final specimen density, an additional three specimens for both experimental groups (NiTi and NiTi+Cu) were sintered to the process parameters detailed in Table 5.2 (NiTi) or Table 5.3 (NiTi+Cu) without performing the secondary background run.

Once the graphite tooling had cooled to room temperature, the sintered specimens were ejected from the die using a hydraulic bench top press and ground by hand under flowing water using 120-grit SiC paper to remove all graphite contamination from the surface. The specimens were cleaned in an ultrasonic bath using a sequential progression of acetone, ethanol, and isopropanol alcohol, followed by a rinse under pressurized deionized water. The specimens were dried on a hot plate at 150 °C for 15 minutes.

Once cool, the mass of each specimen $(m_{specimen})$ was measured using an analytical balance and recorded. Half of each specimen was sealed with a layer of *Sally Hansen Hard as Nails Xtreme Wear* clear/invisible topcoat nail polish (a.k.a., sealant) and allowed to dry for a minimum of 45 minutes. Likewise, the other half of the specimen was sealed and allowed to dry. Then the mass of each sealed specimen (m_{s+s}) was measured using an analytical balance and recorded.

The analytical balance was reconfigured for density measurements based on Archimedes' Principle. Care was taken to fill a beaker with fresh deionized water to a volume sufficient to cover the entire specimen basket. The temperature of the deionized water bath was measured using a mercury thermometer and recorded. The thermometer was removed

from the water bath, the beaker was placed inside the analytical balance, and the specimen basket was inserted into the water bath. The specimen basket was agitated to remove any air bubbles attached to the surface. Each specimen was carefully inserted into the water bath using a pair of forceps at a slight angle to the horizontal. Prior to releasing the specimen onto the basket, the specimen was agitated to dislodge any air bubbles attached to its surface. The specimen was then carefully placed in the center of the basket and, after stabilizing, the mass reading ($m_{indicated}$) was recorded.

The density of each sintered NiTi specimen was calculated using the following equations:

$$\rho_{NiTi\ Specimen} = \frac{(\rho_{water})(m_{specimen})}{m_{s+s} - m_{indicated} - (\rho_{water})(V_{sealant})}$$

$$V_{sealant} = \frac{m_{sealant}}{\rho_{sealant}} = \frac{m_{s+s} - m_{specimen}}{\rho_{sealant}}$$

A sealant density ($\rho_{sealant}$) of 1.181 gcc was used and the density of the water bath (ρ_{water}) was corrected for temperature according to the following equation [505]:

$$\rho_{water}[gcc] = \frac{-0.0053(T_{water}[\text{°C}])^2 + 0.0071(T_{water}[\text{°C}]) + 1000.2}{1000}$$

Determination of the NiTi+Cu specimen matrix density required knowledge of the total mass and volume of the copper spheres. This realization occurred after the copper porogens were already glued into layers. Since the mass of glue could not be readily established, it was decided to weight 300 remaining copper spheres to determine an average porogen mass of 64.58 milligrams-per-copper sphere. The volume of a copper porogen was determined by assuming a perfectly spherical geometry with a manufacturer's listed diameter of 0.09375-inch,

which produced a volume of 7.06 mm^3-per-copper sphere. The matrix density of each sintered NiTi+Cu specimen was calculated using the following equations:

$$V_{specimen} = \frac{m_{s+s} - m_{indicated}}{\rho_{water}} - \frac{m_{s+s} - m_{specimen}}{\rho_{sealant}}$$

$$\rho_{NiTi\ Matrix} = \frac{m_{specimen} - \left(N_{Cu\ spheres}\right)(0.06458\ g)}{V_{specimen} - \left(N_{Cu\ spheres}\right)(7.06\ mm^3)}$$

The specimen density is reported as *relative density*, which relates the actual density of the specimen to the theoretical density of the parent material:

$$\rho_{NiTi\ relative} = \frac{\rho_{NiTi\ Specimen}}{\rho_{NiTi}}$$

$$\rho_{NiTi+Cu\ relative} = \frac{\rho_{NiTi\ Matrix}}{\rho_{NiTi}}$$

The relative density is reported as either a decimal quotient (e.g. 0.971) or as a percentage (e.g. 97.1%); thus, the value of full density is defined as either 1.00 or 100%. For clarity, the relative density of the NiTi+Cu specimens is reported as the density of the NiTi matrix relative to theoretical density of NiTi.

5.1.6 Construction of the Master Sintering Curve

The initial task in generating the master sintering curve was to calculate specimen density as a function of temperature $[\rho(T)]$ from the raw data output by the SPS equipment, noting that a positive displacement change corresponds to a negative height change on the powder compact. The displacement data used to construct the Master Sintering Curve started at a temperature of 225 °C to exclude the inconsequential isothermal dwell at 200 °C used to drive loosely bound water from the system (step S1 and S2 of Table 5.2 and Table 5.3).

First, the displacement measured during the background run $\left[\Delta s_{background}(T)\right]$ was subtracted from that measured during the sintering run $[\Delta s_{sinter}(T)]$ to isolate the displacement due to powder densification $\left[\Delta s_{powder}(T)\right]$ (reference: Figure 2.9):

$$\Delta s_{powder}(T) = s_{sinter}(T) - s_{background}(T)$$

This displacement curve was then inverted due to the sign convention previously noted:

$$\Delta s_{inverted}(T) = -\Delta s_{powder}(T)$$

The final specimen height $\left(h_f\right)$ was determined from post-sintering measurements of the distance across the punches $\left(\Delta l_{\substack{punches \\ post-sinter}}\right)$ prior to the ejection of the specimen from the die, which includes the thickness of two graphite discs $\left(2t_{graphoil}\right)$:

$$h_f = t_{\substack{sintered \\ specimen}} = \Delta l_{\substack{punches \\ post-sinter}} - h_{\substack{upper \\ punch}} - h_{\substack{lower \\ punch}} - 2t_{graphoil}$$

The final specimen height of the NiTi+Cu specimens was adjusted to exclude the contributions of the copper porogens. To construct the specimen height as a function of temperature $[h(T)]$ from the inverted displacement curve, the final displacement data point $\left(\Delta s_{inverted}\left(T_f\right)\right)$ was forcibly equated to the final specimen height $\left(h_f\right)$ using the following equation:

$$h(T) = \Delta s_{inverted}(T) + \left[h_f - \Delta s_{inverted}\left(T_f\right)\right]$$

A few simple math manipulations are required to arrive at specimen density as a function of temperature $[\rho(T)]$:

$$\rho_f = \frac{m}{\frac{\pi}{4}D^2 h_f} \rightarrow m = \rho_f \left(\frac{\pi}{4}D^2\right) h_f$$

$$\rho(T) = \frac{m}{\frac{\pi}{4}D^2 h(T)} = \frac{\rho_f \left(\frac{\pi}{4}D^2\right) h_f}{\frac{\pi}{4}D^2 h(T)} = \frac{\rho_f h_f}{h(T)}$$

The final specimen density (ρ_f) was determined by applying Archimedes' Principle to the additional specimens sintered for both experimental groups (NiTi and NiTi+Cu) without performing the secondary background run, as discussed in section 5.1.5.

After the specimen density as a function of temperature was determined for each specimen, the Master Sintering Curve was generated by estimating the unknown apparent activation energy (Q_{MSC}) through an iterative process involving evaluating theta for a single Q-value for each specimen:

$$\Theta\big(t, T(t)\big) \equiv \int_0^t \frac{1}{T} e^{\left(-\frac{Q_{MSC}}{RT}\right)} dt$$

For every assumed Q-value, a curve fit analysis was performed on the combined experimental data from all specimens using a sigmoid and/or polynomial function in the *relative density-log theta* space. Convergence was quantified through the root mean square error (RMSE) of the experimental data relative to the fitted curve, where the resulting minimum RMSE across the range of assumed Q-values yields the appropriate apparent activation energy. The iterative process and curve fit analysis lend themselves to computer code.

During the curve fit analysis, the sigmoid curve form was specified which, for the current research effort, takes a slightly modified form of Teng et al.'s [459] (note: Teng et al.'s "a" parameter has been replaced by $[1 - \rho_0]$):

$$\rho = \rho_0 + \frac{1 - \rho_0}{\left[1 + e^{\left(-\frac{\ln(\Theta) - \ln(\Theta_0)}{b}\right)}\right]^c}$$

Leveraging the Matlab environment, a Levenberg-Marquardt algorithm was used to generate the sigmoid curve fit to the experimental data, from which the RMSE was subsequently calculated. Similarly, the native Matlab curve fitting tool was also used to generate the coefficients to an eighth-degree polynomial fitted to the experimental data.

The NiTi MSC was validated using previously sintered specimens subjected to various processing temperatures. For each specimen the relative density was measured using Archimedes' Principle and the theta value was calculated using the apparent activation energy determined through the curve fit analysis. The measured relative density and the MSC predicted relative density using the calculated theta value are compared to establish the validity of the MSC.

5.1.7 Test Matrix Summary

The test matrix shown in Table 5.4 summarizes each specimen sintered during the generation and validation of the MSCs.

Table 5.4. Test matrix summary of all 20 specimens produced during this research effort to generate the MSCs of NiTi and NiTi+Cu. Specimens sintered to validate the MSC of NiTi are also listed, the specifics of which are detailed in Table 5.8.

Specimen Count	Specimen Label	Experimental Group	Specimen Purpose	Process Cycles	Heating Rate (°C/min)
1	NiTi-109	NiTi	Final Density	Sintering	50
2	NiTi-110				40
3	NiTi-111				30
4	NiTi-112		MSC	Sintering + Background	50
5	NiTi-113				40
6	NiTi-114				30
7	pNiTi-39	NiTi Matrix + Cu Spheres	MSC	Sintering + Background	100
8	pNiTi-40				75
9	pNiTi-41				50
10	pNiTi-42		Final Density	Sintering	100
11	pNiTi-43				75
12	pNiTi-44				50
13	NiTi-79	NiTi	MSC Validation	Isothermal Sintering	100
14	NiTi-80				
15	NiTi-81				
16	NiTi-82				
17	NiTi-83				
18	NiTi-84				
19	NiTi-85				
20	NiTi-86				

5.2 Results

5.2.1 NiTi Material Properties

The elemental composition of as-received NiTi powder determined by direct current plasma emission spectroscopy is reported in Table 5.5. The NiTi composition falls within the standard range for nickel atomic fraction range studied in the literature.

Table 5.5. Elemental composition of as-received NiTi powder determined by direct current plasma emission spectroscopy.

Nickel Weight Fraction (%)	Titanium Weight Fraction (%)	Nickel Atomic Fraction (%)	Titanium Atomic Fraction (%)
55.2	44.3	50.4	49.6

The X-ray diffractogram of the as-received NiTi powder is shown in Figure 5.6. The peaks at 42.3° (110), 61.4° (200), and 77.5° (211) signify the presence of austenite and indicate the as-received NiTi powder is not fully martensitic at room temperature. The remaining peaks are all associated with various diffraction planes of the martensite phase.

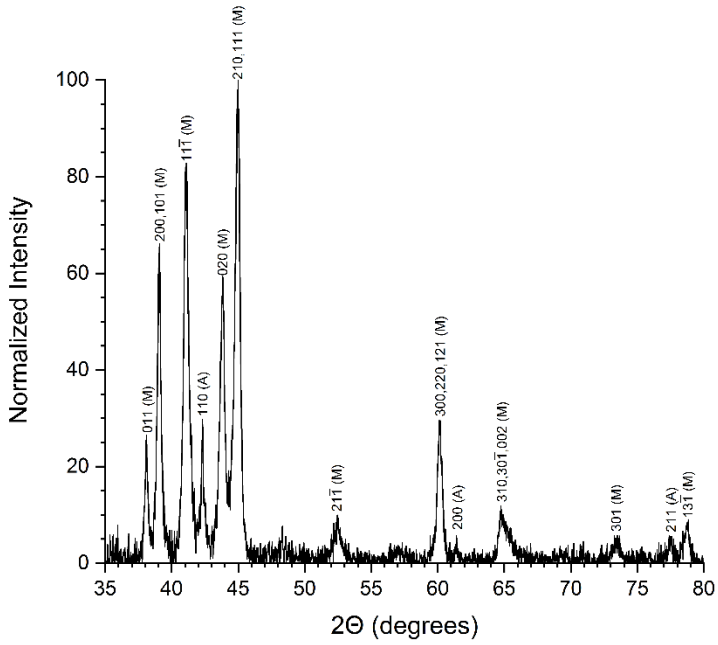

Figure 5.6. X-ray diffractogram of as-received NiTi powder with the background and $CuK_{\alpha 2}$ subtracted. The diffraction reflections from the martensite (M) and austenite (A) phases are identified.

The heat flow versus temperature profiles for the as-received NiTi powder and sintered NiTi specimen are shown in Figure 5.7; the extracted phase transformation temperatures are

presented in Table 5.6. The DSC results indicate the as-received NiTi powder and sintered NiTi specimen should be predominantly martensitic at room temperature.

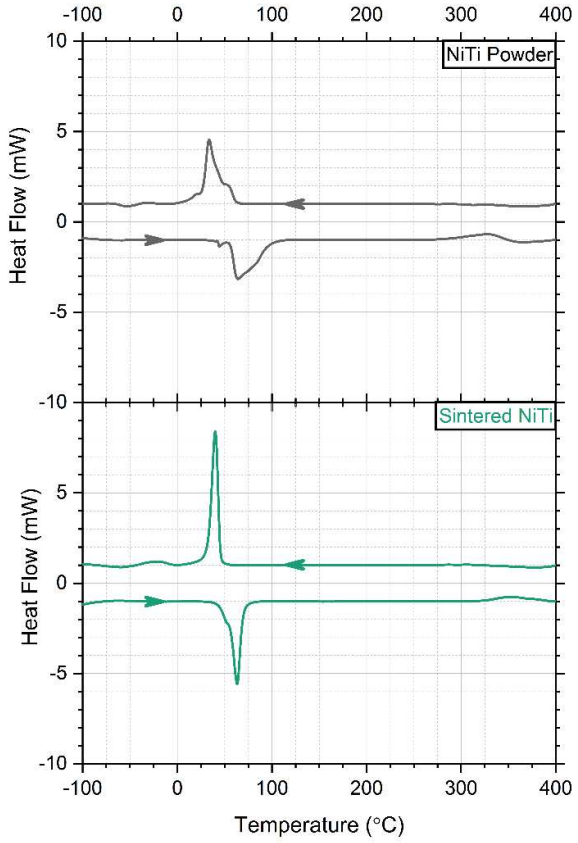

Figure 5.7. Heat flow versus temperature plotted from the differential scanning calorimetry data of as-received NiTi powder and a sintered NiTi specimen. The arrows indicate thermal ramp directions. Positive heat flow corresponds to exothermic events, while negative heat flow corresponds to endothermic events.

Table 5.6. Phase transformation temperatures of as-received NiTi powder and the sintered NiTi specimen determined through analysis of the DSC profiles from Figure 5.7.

Material	Martensitic Finish (°C)	Martensitic Start (°C)	Austenitic Start (°C)	Austenitic Finish (°C)
NiTi Power	26.9	49.6	54.9	98.4
Sintered NiTi	31.4	45.4	54.1	69.6

5.2.2 NiTi MSC

The relative densities of the three NiTi specimens sintered to determine the final density of the constant heating rate experiments are listed in Table 5.7. The relative densities indicate that the SPS process parameters (Table 5.2) were sufficient to achieve full density (≥ 0.97 relative density) of the powder compact during the initial sintering run. As expected, the specimen density was inversely proportional to heating rate due to the additional sintering time at temperature afforded by the slower heating rates; however, this observation is subject to scrutiny without a properly robust statistical data set.

Table 5.7. Relative densities, as determined by the Archimedes' Principle, of the NiTi specimens sintered to establish the final density for the MSC (reference Table 5.4).

Specimen Label	**Heating Rate (°C/min)**	**Relative Density**
NiTi-109	50	0.995
NiTi-110	40	0.997
NiTi-111	30	0.998

Relative density is plotted versus time in Figure 5.8 for the three constant heating rate experiments. The relative density profiles predict a typical green density of the NiTi powder compact of 0.665.

Initially, a sigmoid curve was fitted to the *relative density-log theta* data set generated from Figure 5.8 across a range of possible activation energies. The resultant RMSE versus activation energy, plotted in Figure 5.9, indicated a minimum RMSE value (aka. best curve fit) at an activation energy of 582 kJ/mol. Based on this apparent activation energy, the MSC was generated using the parameters determined during the sigmoid curve fit analysis; The MSC is plotted on top of the constant heating rate experimental data in Figure 5.10.

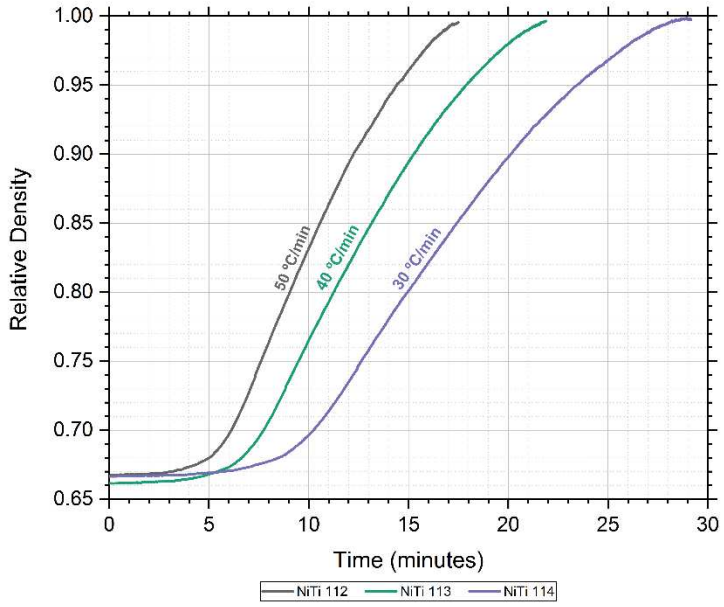

Figure 5.8. Relative density plotted versus time from the constant heating rate sintering runs of NiTi specimens 112 (50 °C/min), 113 (40 °C/min), and 114 (30 °C/min). Data is plotted from 225 °C through 1100 °C.

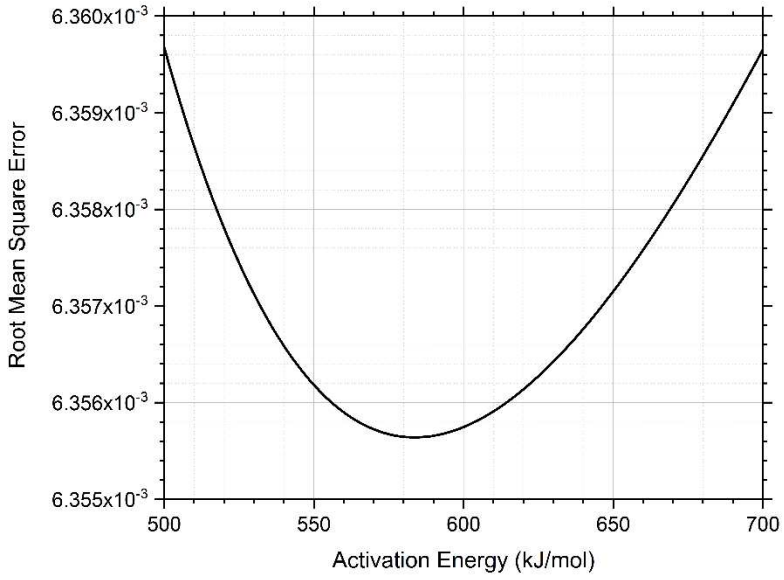

Figure 5.9. RMSE versus activation energy (Q) plotted from the sigmoid curve fitment to the NiTi experimental data collected from the three constant heating rate sintering runs. The RMSE minimum occurs at an apparent activation energy of 582 kJ/mol.

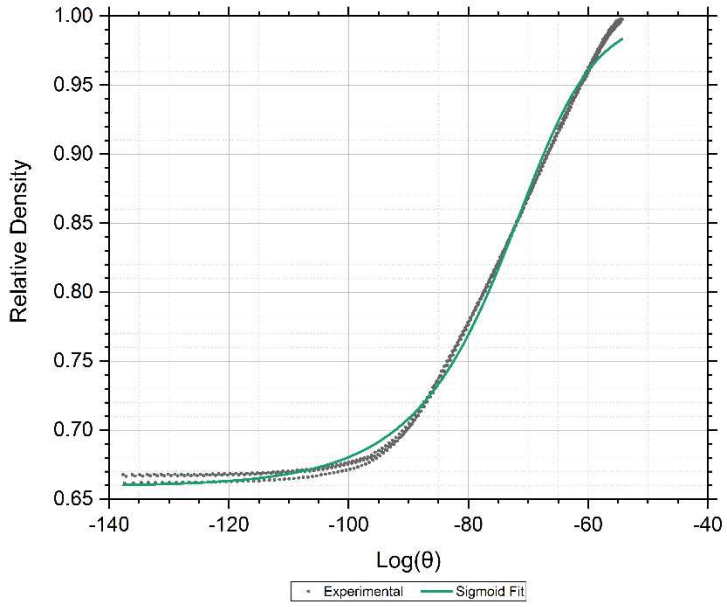

Figure 5.10. MSC for NiTi experimental data collected from the three constant heating rate sintering runs fitted with a sigmoid curve.

The experimental data is reasonably well represented by the sigmoid curve shown in Figure 5.10, with a coefficient of determination (R^2) of 0.9972; however, there are noticeable deviations at a log-theta value of -72, around the inflection point of the sigmoid curve, and especially above a relative density of 0.95.

To achieve a better curve fit, a polynomial function was explored based upon its application in the original MSC journal article [453]; thus the curve fit analysis was repeated on the *relative density-log theta* data set generated from Figure 5.8 with an eighth-degree polynomial function, which was found to provide the best fit. The resultant RMSE versus activation energy is plotted in Figure 5.11, indicating a minimum RMSE value at an activation energy of 576 kJ/mol. Based on this apparent activation energy, the MSC was generated using

the parameters determined during the polynomial curve fit analysis; The MSC is plotted on top of the constant heating rate experimental data in Figure 5.12.

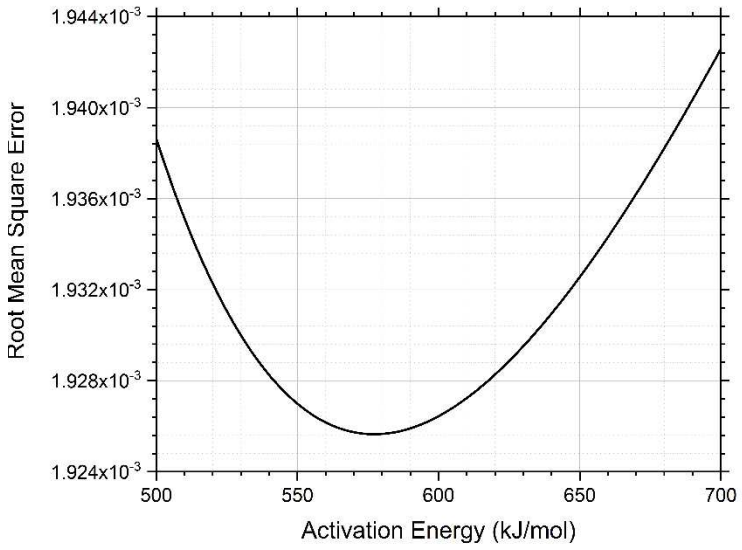

Figure 5.11. RMSE versus activation energy (Q) plotted from the eighth-degree polynomial curve fitment to the NiTi experimental data collected from the three constant heating rate sintering runs. The RMSE minimum occurs at an apparent activation energy of 576 kJ/mol.

The eighth-degree polynomial provides an improved fit to the experimental data, with a coefficient of determination (R^2) of 0.9997. Although there are noticeable undulations at the lower end of the curve (< 0.70 relative density), this will not impact the practical usage of the polynomial MSC since most sintering activities seek to attain full density.

The relative densities of the eight NiTi isothermal validations specimens are plotted on top of the polynomial-based MSC in Figure 5.13 and detailed in Table 5.8. Percent differences between the relative density measured by Archimedes' Principle and that predicted by the polynomial MSC are less than four-percent, indicating the MSC has a reasonable predictive capability.

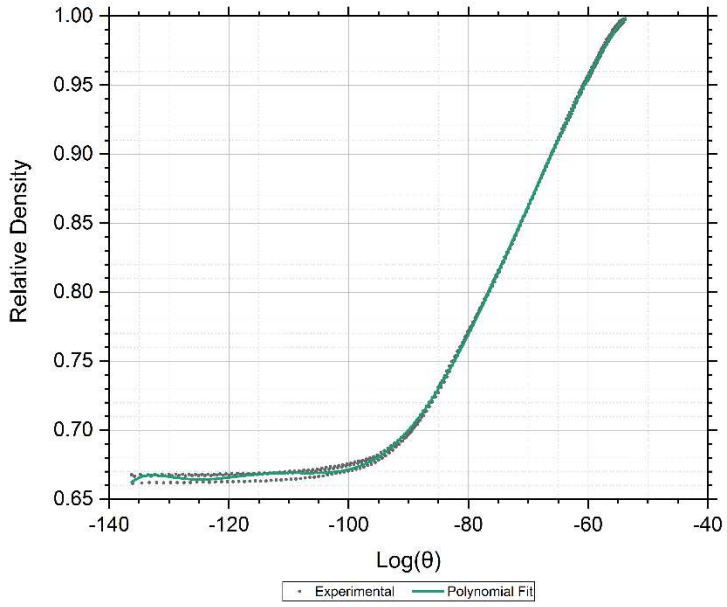

Figure 5.12. MSC for NiTi experimental data collected from the three constant heating rate sintering runs fitted with an eighth-degree polynomial curve.

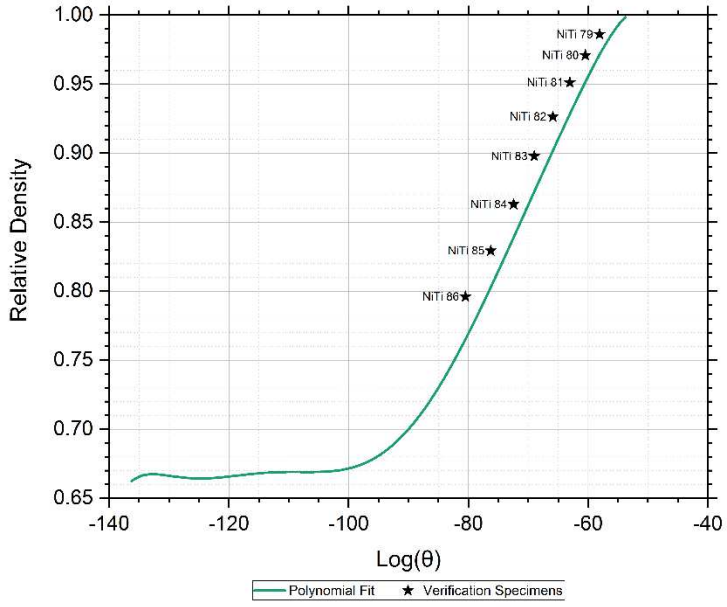

Figure 5.13. Relative densities, determined by Archimedes' Principle, of NiTi specimens sintered at various temperatures to validate the MSC plotted on top of the eighth-degree polynomial curve fit. The theta value for each validation specimen was calculated using the thermal profiles detailed in Table 5.8 and an apparent activation energy of 576 kJ/mol.

Table 5.8. Relative densities of NiTi specimens sintered at various temperatures to validate the MSC. All validation specimens were sintered at a heating rate of 100 °C-per-minute, an applied load of 25 kN, and an isothermal dwell time of 5 minutes. The specimen relative density is compared to that predicted by the MSC.

Specimen Label	Dwell Temperature (°C)	Relative Density (Archimedes')	Relative Density (MSC)	Percent Difference (%)
NiTi-79	950	0.986	0.971	1.5
NiTi-80	900	0.971	0.952	2.0
NiTi-81	850	0.951	0.928	2.4
NiTi-82	800	0.926	0.902	2.6
NiTi-83	750	0.898	0.872	2.9
NiTi-84	700	0.863	0.839	2.8
NiTi-85	650	0.829	0.803	3.2
NiTi-86	600	0.796	0.765	3.9

5.2.3 NiTi+Cu MSC

The relative densities of the three NiTi+Cu specimens sintered to determine the final density of the isothermal experiments are listed in Table 5.9. The relative densities indicate that the SPS process parameters (Table 5.3) were sufficient to achieve full density (≥ 0.97 relative density) of the powder matrix during the initial sintering run; however, preliminary exploratory experiments using the process parameters detailed in Table 5.3 to sinter NiTi specimens (without copper porogens) produced very consistent densities of 0.987. The final densities of the NiTi+Cu specimens all have the same value regardless of heating rate and are all below the expected value (0.987) by approximately 1%, and further below the NiTi densities (Table 5.7) by 2%.

Table 5.9. Relative densities, as determined by the Archimedes' Principle, of the NiTi+Cu specimens sintered to establish the final density for the MSC (reference Table 5.4).

Specimen Label	Heating Rate (°C/min)	Relative Density
pNiTi-42	100	0.979
pNiTi-43	75	0.979
pNiTi-44	50	0.979

Relative density is plotted versus time in Figure 5.14 for the three isothermal experiments. The relative density profiles predict a typical green density of the NiTi powder matrix of 0.655.

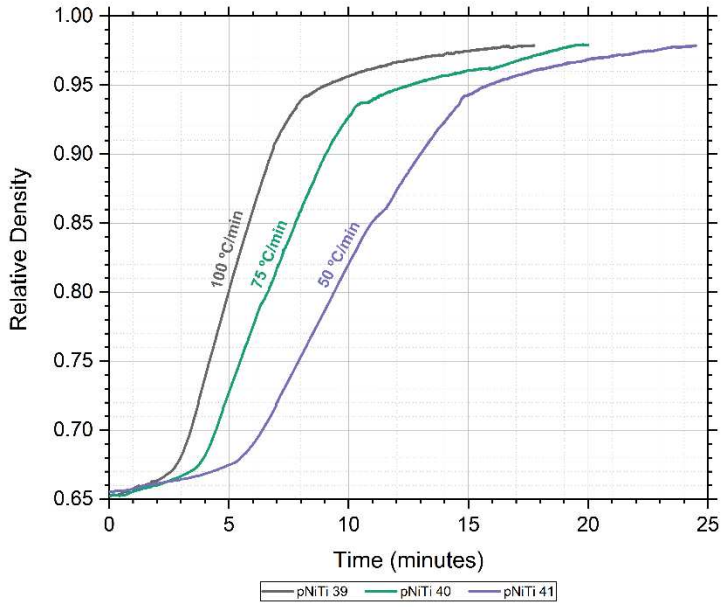

Figure 5.14. Relative density plotted versus time from the isothermal sintering runs of NiTi+Cu specimens 39 (100 °C/min), 40 (75 °C/min), and 41 (50 °C/min). Data is plotted from 225 °C through the end of the 10-minute isothermal dwell at 950 °C.

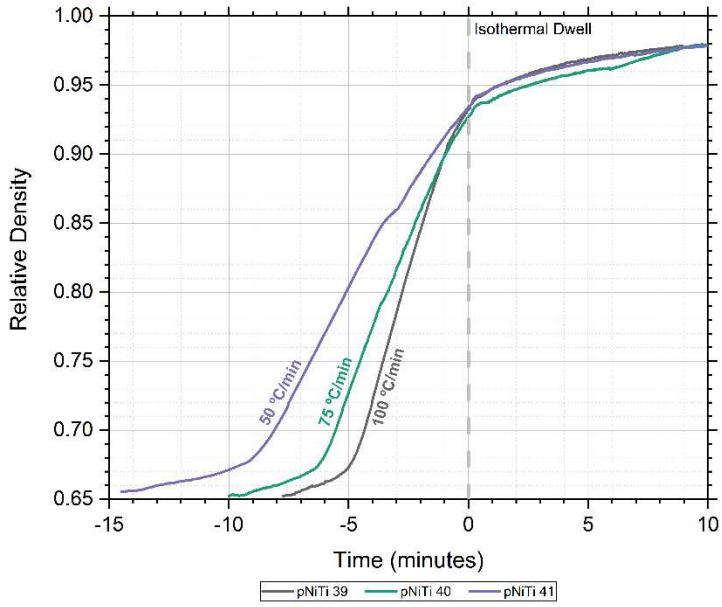

Figure 5.15. Relative density plotted versus time from the isothermal sintering runs of NiTi+Cu specimens 39 (100 °C/min), 40 (75 °C/min), and 41 (50 °C/min). Data is plotted from 225 °C through the end of the 10-minute isothermal dwell at 950 °C. The data is synchronized such that time = 0 at the start of the isothermal dwell.

Comparing the relative density profiles between NiTi (Figure 5.8) and NiTi+Cu (Figure 5.14) specimens, reveals the latter possesses a consistent upward incline during the initial sintering stage, then assumes a curve shape consistent with the NiTi specimens. The densification rate exhibited by the NiTi+Cu specimens reduces significantly during the isothermal dwell but maintains a positive value. Although the three NiTi+Cu specimens are sintered at different heating rates, they all exhibit similar relative density values at the beginning of the isothermal dwell. The profiles do not assume a typical sigmoid shape, but a more irregular shape with a few perturbations likely caused by artifacts during the background subtraction.

Based on the insights gained from the creation of the NiTi MSC, an eighth-degree polynomial curve was fitted to the *relative density-log theta* data set generated from Figure 5.14 across a range of possible activation energies. The resultant RMSE versus activation energy, plotted in Figure 5.16, indicated a minimum RMSE value (aka. best curve fit) at an apparent activation energy of 201 kJ/mol. Based on this apparent activation energy, the MSC was generated using the parameters determined during the polynomial curve fit analysis; The MSC is plotted on top of the constant heating rate experimental data in Figure 5.17. The eighth-degree polynomial fits the experimental data well with a coefficient of determination (R^2) of 0.9994.

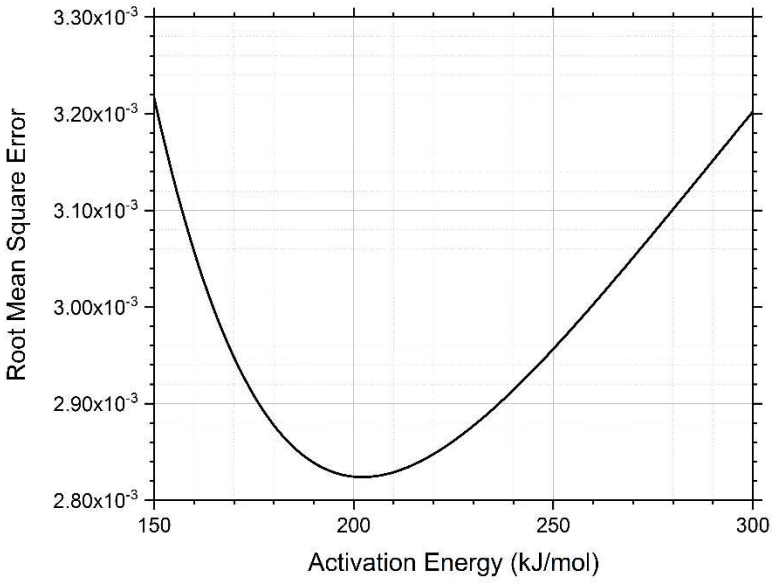

Figure 5.16. RMSE versus activation energy (Q) plotted from the eighth-degree polynomial curve fitment to the NiTi+Cu experimental data collected from the three isothermal rate sintering runs. The RMSE minimum occurs at an apparent activation energy of 201 kJ/mol.

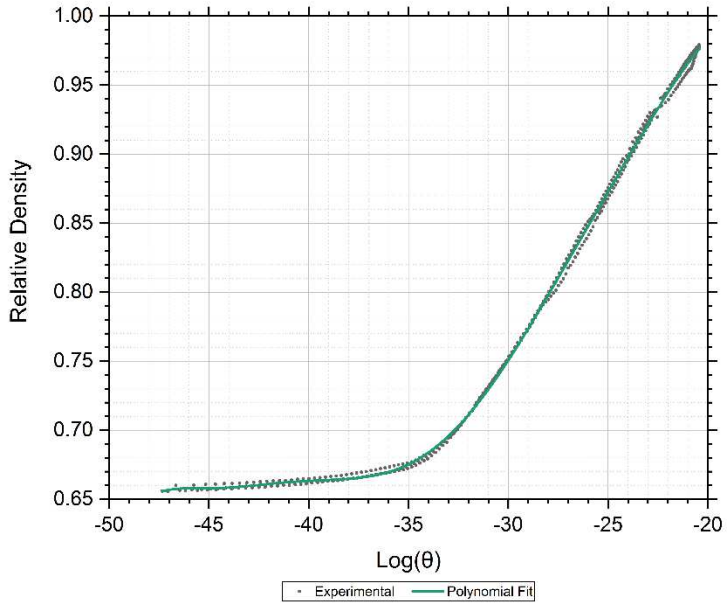

Figure 5.17. MSC for NiTi+Cu experimental data collected from the three isothermal sintering runs fitted with an eighth-degree polynomial curve.

Furthermore, a two-dimensional, cross-sectional SEM image of a NiTi open-cell foam was captured and the relative areal density was determined to be 0.975 by post-process analysis. Using the apparent activation energy of 201 kJ/mol for NiTi+Cu and the SPS process parameters used to sinter the NiTi open-cell foam (Table 4.2), the MSC predicted the relative density of the matrix to be 0.964, which was within 1.2% of the areal density extracted from the SEM cross-section image.

5.3 Discussion

5.3.1 NiTi

To the authors' knowledge, no research has been published on the application of the master sintering curve concept to NiTi. Previously published results put the activation energy for the sintering of NiTi at 201 kJ/mol [506] and 113 kJ/mol [507], a marked difference from the

apparent activation energy of 576 kJ/mol determined by the current research. The first study calculated activation energy by plotting an Arrhenius equation constructed using dilatometry data from the densification of elemental NiTi powder [506]. The second study calculated activation energy by plotting Kissinger's equation constructed using differential scanning calorimetry (DSC) data from the densification of pre-alloyed NiTi nanopowder [507]. Recent studies on the densification of alumina (Al_2O_3) provide some context for the difficulties in comparing activation energies across different analytical techniques.

The densification of alumina has been studied both by dilatometry [317, 453, 461, 471, 474, 475] and in situ by SPS [317, 480, 484] techniques. Activation energies of alumina determined through dilatometry range from 490 kJ/mol [453] to 1163 kJ/mol [461], while the apparent activation energies from SPS range from 290 kJ/mol [480] to 600 kJ/mol [484]. It has been established that the various starting raw materials, preparation procedures (green pressing techniques), and sintering techniques can significantly alter the calculated activation energy of alumina by generating differences in particle size, particle-size distribution, initial pore-size distribution, packing properties, and green density [453].

One study investigated the effects of various dopants on the densification of alumina through both dilatometry and SPS using the same starting materials; however, the SPS used constant heating rate experiments up to 1200 °C and a constantly applied 50 MPa pressure, whereas the pressureless dilatometry experiments used a green powder compacted under 50 MPa and isothermal dwells at 1500 °C for 1 hour [317]. The results of the dopant study are presented in Table 5.10, which clearly demonstrate that the activation energies for the same

starting powder can vary considerably across different preparation methods and sintering techniques.

Table 5.10. Apparent activation energies extracted from the MSCs for the sintering of alumina doped with various additives. Two MSCs were generated separately by conventional dilatometry and by SPS (note: SPS MSC for each additive combination was split into multiple segments to incorporate changes in the predominate densification mechanism during sintering) [317].

Specimen	Dilatometry Activation Energy (kJ/mol)	SPS Activation Energy (kJ/mol)
Al2O3 + Mg	590	260-350-470
Al2O3 + Y	670	250-690
Al2O3 + La	780	200-480-630
Al2O3 + Mg + Y + La	715	330-580-830

Although the sigmoid curve has been established to be a best practice for extracting an MSC equation from the *relative density-log theta* data [458, 459], the best-fit sigmoid curve shown in Figure 5.10 exhibits several deviations from the experimental data. It has been suggested that exaggerated grain growth could be responsible for discrepancies at higher densities [453], which would logically result in the MSC over-estimating the relative density as grain growth occurs at the expense of densification during final stage sintering; however, the MSC plotted in Figure 5.10 under-estimates the relative density. The more likely explanation for the deviation above 0.95 relative density relates to the applied pressure during SPS sintering. Other studies using applied pressure during SPS [480, 483] or hot-pressing techniques [478, 479] have observed the experimental data does not asymptotically approach full density as typically observed for pressureless sintering. This behavior indicates the densification rate has been maintained into the final sintering stage due to the application of

pressure, which would sustain the sintering stress even as the surface curvature is eliminated. In contrast, the final stage of pressureless sintering is characterized by pore isolation and eventual separation from the grain boundary leading to exaggerated grain growth at the expense of densification. It appears that a polynomial function is well suited to model the densification behavior of pressure-assisted sintering, while the sigmoid function primary serves pressureless sintering densification.

5.3.2 NiTi+Cu

Examination of the relative matrix density profiles for the NiTi+Cu specimens (Figure 5.14 and Figure 5.15) reveals two notable differences compared with the NiTi specimens (Figure 5.8) in addition to the difference caused by the isothermal hold.

The first difference is the occurrence of subtle perturbations in the relative matrix density profiles for the NiTi+Cu specimens, which relate to the readily observed anomalies in the displacement versus time plots (Figure 8.15, Figure 8.16, and Figure 8.17). These anomalies occur during both the sintering and background runs as step changes and brief dwells, respectively. Considering the displacement progression to be continuous, the step changes and brief dwells are unexpected. Most of the anomalies can be explained by imposing the applied power data upon the displacement versus time plots (Figure 8.18, Figure 8.19, and Figure 8.20) and observing the correlation with the sudden drops in applied power. To accommodate prescribed changes in the programmed thermal profile heating rates at 900 °C (100/75/50 → 50 °C/min) and 950 °C (50 → 0 °C/min) (Table 5.3), the SPS thermal controller precipitously reduces applied power, which causes a brief, but appreciable drop in the temperature of the graphite punches. While this reduction in temperature is not detectable by the thermocouple

embedded in the graphite die, it does cause the graphite punches to contract. In response, the SPS load controller, attempting to maintain a constant applied load of 25 kN established by the user, moves the electrode platens together in a positive direction to offset the thermal contraction of the graphite punches. This positive displacement of the electrode platens is manifested as the step changes in the sintering run data which superimposes on top of the continuing displacement due to powder densification. During the background run, where displacement is only the result of thermal expansions of the system and fully dense specimen, the positive displacement of the electrode platens appears to offset the negative displacement due to the thermal expansions resulting in brief dwells having near zero slope. There is an additional anomaly in the displacement data during the background runs for specimens pNiTi 40 (Figure 8.16) and pNiTi 41 (Figure 8.17) prior to the change in thermal profile heating rate which does not correlate with any observable event in the SPS output data file and cannot currently be explained.

The second difference relates to the initial shape of the relative matrix density profile, best illustrated by plotting the normalized relative matrix density data from specimens NiTi 112 and pNiTi 41 (Figure 8.21). Both specimens were heated at 50 °C/min from 200 to 950 °C, at which point pNiTi 41 began a 10-minute isothermal dwell and NiTi 112 continued its constant heating rate ramp to 1100 °C. A clear deviation in the normalized relative matrix density can be observed from 300 to 500 °C between the specimens; subsequently, the two profiles coincide until the isothermal dwell begins at 950 °C. Investigation into the possible root cause of this deviation requires examination of the displacement profiles during the sintering and background runs for both specimens. As shown in Figure 8.22, the sintering displacement from

NiTi 112 initially follows the trajectory of the background displacement indicating thermal expansion of the system is occurring without densification; however, the sintering displacement from pNiTi 41 exhibits a zero-slope trajectory which causes the background subtracted displacement profile of pNiTi 41 (Figure 5.14) to have a distinctly positively-sloped linear segment, a characteristic shared across all three NiTi+Cu specimens. The background displacement from pNiTi 41 is consistent with that from NiTi 112, as expected. Both specimens exhibit the same general trajectory, with pNiTi 41 having a slightly larger thermal expansion effect due to its increased specimen height. The initial deviation in the relative matrix density of pNiTi 41 appears to be isolated to the sintering run.

To further investigate the possible root cause, the chamber pressure during the sintering and background runs of specimens NiTi 112 and pNiTi 41 were plotted (Figure 8.23). The data indicates that two spikes in the chamber pressure occur during the sintering run of pNiTi 41, centered at approximately 245 °C and 458 °C; however, the subsequent background run of pNiTi 41, as well as both runs of NiTi 112, do not exhibit any sharp increases in the chamber pressure. As illustrated in Figure 8.24, the dual spikes in chamber pressure roughly correlate to the discrepancy in the sintering displacement data between 300 and 500 °C for specimen pNiTi 41. This correspondence indicates a possible outgassing event from the vaporization of the super glue used to assemble the individual copper porogen layers causing the SPS load controller to adjust the displacement of the electrode platens to maintain a constant applied load across the specimen. The potential reduction in internal volume within the graphite die due to the escapement of the vaporized super glue, pumped by the vacuum environment within the SPS chamber, would cause the SPS load controller to move the

electrode platens together in a positive direction to compress the powder sample to maintain the required load established by the user. This positive motion of the electrode platens would cause the negatively trending displacement profile to become less so, such as was observed.

To consider other potential root causes of the deviation in the relative matrix density of specimen pNiTi 41, the applied power and load were plotted in Figure 8.25 and Figure 8.26, respectively. Between 300 to 500 °C, both parameters are consistent between specimens suggesting the applied power and load are not the root cause of the deviation in the relative matrix density of specimen pNiTi 41.

5.3.3 Comparison of MSCs

The master sintering curves of NiTi (Figure 5.12) and NiTi+Cu (Figure 5.17) are plotted together in Figure 5.18. The significant difference in the apparent activation energies, 576 kJ/mol for NiTi versus 201 kJ/mol for NiTi+Cu, is echoed by the large shift along the log-theta abscissa between MSCs and suggests the NiTi+Cu specimens possess a greater sinterability than the NiTi specimens. This increased sinterability might be explained by the relative thermal conductivity and electrical resistivity properties of NiTi and copper, presented in Table 5.11. The thermal conductivity of copper is 22 times *greater* than NiTi, while the electrical resistivity of copper is 48 times *less* than NiTi. This relationship of material properties implies that the copper porogens act as a preferential pathway for the flow of current, possibly causing the asynchronous Joule heating of the copper spheres; thus, large thermal gradients could be produced within the specimen, leading to localized sintering of the NiTi powder at the copper sphere interface; however, the copper porogens only occupy a 28.1% volume fraction and are completely surrounded by NiTi powder. The small volume percentage and lack of a

continuous network of porogens between the graphite punches raises doubts that the copper can have a measurable effect on the current flow through the powder sample in the current specimen configuration.

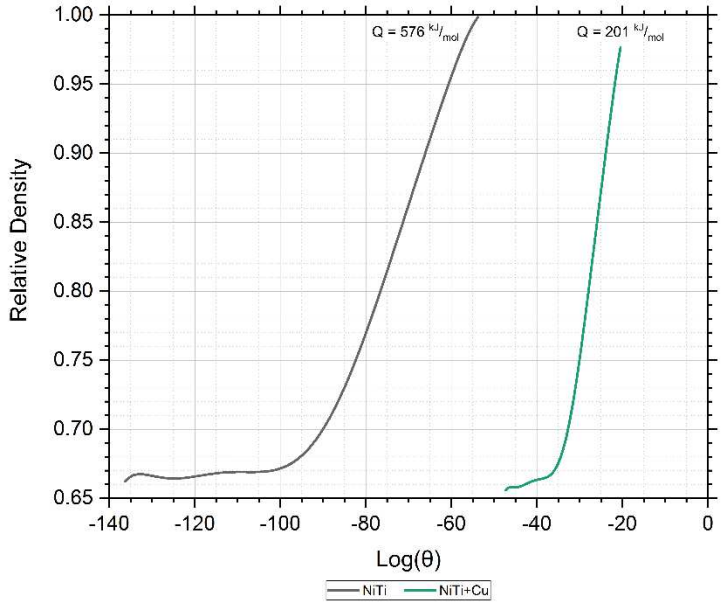

Figure 5.18. Comparison of master sintering curves for NiTi and NiTi+Cu specimens, both fitted with eighth-degree polynomial curves. Apparent activation energies are provided for comparison.

Table 5.11. Thermal conductivity and electrical resistivity room temperature material properties for NiTi and copper.

Material	Thermal Conductivity [W/(m*K)]	Electrical Resistivity [Ω*m]	Reference
NiTi (martensite)	14	960×10^{-9}	[508]
Copper (102)	391	17.1×10^{-9}	[509]

It was experimentally demonstrated that increased sinterability, indicated by a lower apparent activation energy, manifested as a higher relative density at a given temperature between two sets of alumina powders [475]. Examination of Figure 8.27, reveals that the NiTi+Cu specimens have a consistently *lower* relative matrix density than the NiTi specimens, even though they possess a significantly lower activation energy. The lower relative matrix density profiles of the NiTi+Cu specimens could be partially attributed to their higher heating rates relative to the NiTi specimens.

The similarities in relative density evolution with respect to temperature shown in Figure 8.27 implies that the copper porogens have little to no effect on the densification of NiTi powder. The apparent activation energy determined for the NiTi+Cu specimens, 201 kJ/mol, is very similar to published values for NiTi: 201 kJ/mol [506] and 113 kJ/mol [507]. In fact, if an apparent activation energy of 201 kJ/mol is used in the NiTi MSC model instead of the calculated value of 576 kJ/mol, the maximum percent difference between the experimental relative densities of the validation specimens (Table 5.8) and the MSC prediction reduces from 3.9% to 1.2%. This suggests that an apparent activation energy of 576 kJ/mol for NiTi is erroneous, likely due to convergence issues during the curve fit analysis caused by a slight variation in the green density, by selecting constant heating rates too close together, and/or by selecting one or more heating rates that were sufficiently slow to induce an influential amount of non-densifying surface diffusion.

6. CONCLUSIONS

The conclusions of the current research effort are presented below by discussing the significant findings and contributions relative to the research objectives detailed in Chapter 3, followed by the suggested future work to build upon the current research accomplishments.

6.1 Significant Findings & Contributions

The significant findings and contributions are partitioned based on the four research objectives presented in Chapter 3. Each section contains a summary of the appropriate research relevant to the objective, followed by the anticipated contributions.

6.1.1 Identification of a Porogen Material

Copper was selected as the porogen material due to its high temperature capability, its compatibility with pressure-assisted sintering, and its commercial availability in spherical form. Copper (T_{melt} = 1085 °C) extends the working range of the space holder replication technique 284 °C beyond highly utilized sodium chloride (T_{melt} = 801 °C) and 92 °C above less commonly used sodium fluoride (T_{melt} = 993 °C). The increased temperature capability of copper enabled the use of a higher sintering temperature to promote densification; The NiTi open-cell foams achieved full matrix density at 950 °C after only 5 minutes. Additionally, the porogens remain solid at the sintering temperature which provided continuous control of the pore structure as the NiTi matrix densifies, especially important during pressure-assisted sintering. The full-hard temper (H04) of the copper allowed the porogens to resist deformation during pressure-assisted densification, which in turn not only promotes densification but also provided pore control under application of load.

To the author's knowledge, this is the first reported usage of copper as a porogen material during the fabrication of metal open-cell foams. While there are porogen materials that have a higher melting temperature, such as barium fluoride (T_{melt} = 1,368 °C) [194, 195, 207] and lanthanum oxide (T_{melt} = 2,315 °C) [196], copper has demonstrated a better combination of properties for sintering open-cell foams, including cost, availability, temperature capability, strength, leachability, and (lack of) toxicity. The use of copper as a porogen material will significantly extend the working temperature range for sintering of metal powders to allow full matrix densities to be achieved at a higher temperature in less time to realize full mechanical properties of the open-cell foam.

6.1.2 Tailored Metal Open-Cell Foams

A novel approach to tailoring the pore structure of metal open-cell foams, based on a structured assembly of porogens, has been conceptually demonstrated. A manufacturing process integrating space-holder replication and electric current assisted sintering was developed to fabricate metal open-cell foams exhibiting increased control over the pore size, shape, and position. The pore structure, designed using CAD software, consisted of spherical pores arranged into a hexagonal close-packed pattern for maximum packing factor. Inspired by the space-holder replication technique, the pore structure was realized by assembling individual copper spheres into a representative sacrificial template and co-sintering with NiTi powder using electric current assisted sintering. The copper porogens were subsequently leached from machined specimens using nitric acid and the resultant NiTi open-cell foams were characterized for their spatial and mechanical properties. Geometric-based density measurements show a very low variability in the specimen porosity which exceeds the designed

value due to the deformation of the copper porogens during sintering. X-ray micro-computed tomography radiographs reveal uniform pore structure and high degree of replication of the copper porogen template throughout the specimens, while energy-dispersive x-ray spectroscopy indicates copper readily diffused up to 5 µm into the NiTi matrix. Measures of the elastic modulus and martensitic detwinning stress were consistent across all specimens, but the unexpected brittle failure during mechanical testing occurred across a range of compressive stress. The brittle failure behavior of the NiTi open-cell foams was confirmed through scanning electron microscopy to be the result of crack initiation and inter-particulate propagation through the matrix.

Space-holder replication has been extensively studied in conjunction with powder metallurgy to manufacture porous metals and metal open-cell foams, including those with NiTi matrices. The current research has demonstrated a novel manufacturing concept to tailor metal-open cell foams based on controlling the pore size, shape, and position using spherical porogens assembled by hand. This proof-of-concept will enable the next generation of open-cell foams to be tailored using advanced manufacturing techniques, such as additive manufacturing, to realize optimum pore structures for multifunctional applications, where higher performance can be achieved at lower cost and less weight.

6.1.3 Metal Powder Densification

The Master Sintering Curve concept was used to predict the densification behavior of NiTi powders sintered by Spark Plasma Sintering. The raw displacement data output by the SPS equipment was used in conjunction with the final density of the experimental specimens to calculate an apparent activation energy of 576 kJ/mol for sintering, although this value may be

erroneously high due to convergence issues. It's plausible a more accurate value is closer to 201 kJ/mol. The Master Sintering Curve was generated by fitting an eighth-degree polynomial function to the experimental data in the re*lative density-log theta* space. The polynomial function was necessary to account for the high densification rate above 95% relative density due to the applied pressure during SPS sintering, which was not modeled as well with the standard sigmoid curve. The polynomial function fitted the experimental data well, with a coefficient of determination (R^2) of 0.9997. Eight validation NiTi specimens were sintered at various time-temperature parameters and the Master Sintering Curve predicted their densities within four-percent.

The Master Sintering Curve concept can be used in conjunction with the apparent activation energy associated with the sintering of NiTi powders to predict densification behavior under arbitrary time-temperature sintering profiles assuming the powder, green-body preparation, and green density are controlled to the conditions used within the current research. Furthermore, knowledge of the apparent activation energy enables the design of tailored NiTi microstructures with functionally graded porosity.

6.1.4 Effect of Porogens on Densification

The Master Sintering Curve concept was extended to investigate the effect of copper porogens on the densification behavior of NiTi during the fabrication of open-cell foams. Following the same procedure used for the NiTi Master Sintering Curve specimens, an apparent activation energy of 201 kJ/mol for sintering of NiTi+Cu was determined. An eighth-degree polynomial function fitted the NiTi+Cu experimental data well, with a coefficient of determination (R^2) of 0.9994. The NiTi+Cu MSC was able to predict the areal matrix density of a

NiTi open-cell foam to within 1.2%. The significant reduction in apparent activation energy for NiTi powder sintering associated with the addition of copper porogens is not consistent with the relative (matrix) density versus temperature profiles. This discrepancy suggests that the copper porogens have little to no effect on the densification behavior of NiTi powders, likely due to the experimental controls put in place by the author, such as not providing a continuous conduction path of copper porogens between the graphite punches.

Although the Master Sintering Curve concept has been previously utilized for various comparative studies, the current research is the first known attempt to study the effects of porogens on the densification behavior of a powder material. The Master Sintering Curve concept can be used in conjunction with the apparent activation energy associated with the sintering of NiTi open-cell foams to predict the final matrix density under arbitrary time-temperature sintering profiles, eliminating the time consuming and costly process to measure the matrix density using imagining techniques. Additionally, the Master Sintering Curve will enable a compatible process design to avoid temperature-related limitations of the space-holder constituent materials and is extensible to numerous combinations of matrix and porogen materials.

6.2 Future Work

The future work section is the author's attempt to formulate a research path for both metal open-cell foams and for the Master Sintering Curve to build upon the research presented in this dissertation resulting in additional contributions to the knowledge base.

6.2.1 Metal Open-Cell Foams

The current research has demonstrated the possibly to create tailored metal open-cell foams using a structured porogen template, but manually assembling individual spherical porogens is time consuming and ultimately limits the tailorability. To open the design space, the follow-on effort should be focused on developing an additive manufacturing process to produce complex unit cells that can be easily assembled into a self-locating template without the use of adhesives. This process should also consider the challenges in packing metal powders around the templates, the eventual shrinkage of the matrix as the powders densify, and the deformation of the porogen template due to the applied load used during pressure-assisted sintering. Experimental verifications should employ a model material with a lower melting temperature than the porogen material, such as aluminum.

In parallel, an effort should commence to develop tools and processes capable of predicting the properties of as-designed foam structures within the digital space to facilitate iterative optimization routines. The tools and processes should eventually advance to handle multifunctional applications. Furthermore, an algorithm should be developed to process the x-ray micro-computed tomography data to determine the pore size, shape, and interconnectivity to facilitate comparisons between the as-fabricated metal open-cell foams to the as-designed model.

Once matured, the manufacturing processes and predictive design tools should be used to create metal open-cell foams for multifunctional applications, such as load bearing heat exchangers. Opportunities to branch out into other material systems that lend themselves to sintering, such as ceramics and refractory alloys, should be taken advantage of.

6.2.2 Master Sintering Curve

While the Master Sintering Curve concept can be applied to an unlimited number of material systems, the future contributions related to the current research are in continued investigations on the effect of porogens on densification behavior. The real thrust should be to explain the significant difference in apparent activation energies between the NiTi powder and NiTi powder with copper porogens.

First, a model material system, consisting of a metal powder and porogen, should be selected such that the powder has a lower melting temperature than the porogen. Special consideration should be given to minimize the reactivity between the constituents. A metal powder with a lower thermal capacity will enable the same constant heating rate experiments to be administered across both specimen groups, thus eliminating heating rate and sintering profiles (constant heat rate versus isothermal dwell) as variables. This modification would also the metal powder to be readily sintered to full density as the porogen material would no longer limit the temperature during sintering. Furthermore, exclusively using constant heating rate experiments would eliminate the undesirable perturbations in the displacement profiles caused by transitioning between heating rates required of the isothermal dwell.

Second, the possible sources of experimental error should be eliminated, focusing initially on quantifying the effects from the expected outgassing of the superglue adhesive and probable deformation of the copper spheres on displacement profiles. The thermal decomposition of the adhesive can initially be studied by thermal gravimetric analysis to understand the mass evolution with respect to temperature. Incorporation of a residual gas analyzer into the vacuum system of the sintering equipment would collect and identify the

spectra of gaseous species evolving during sintering, including those originating from the adhesive. Ultimately, the goal should be to eliminate the use of adhesive to assemble the porogen template or to devise a sintering profile to thermally decompose the adhesive prior to starting the constant heating rate experiments. Furthermore, the deformation of the copper porogens observed during the manufacture of NiTi open-cell foams has likely occurred during the Master Sintering Curve experiments. X-ray micro-computed tomography can be used to quantify the deformation of existing NiTi+Cu specimens through measurements of the copper porogen sphericity. Porogen deformation should be minimized by selecting a porogen material possessing a high degree of strength retention at the sintering temperature of the metal powder.

If the significant difference in apparent activation energy is replicated after implementing the above changes, then the next course of action is to model the system and material behavior. The modeling goal should be to study the effects of thermal and electrical conductivity differences between the powder and porogen on current density variations and thermal gradients induced during sintering. Additionally, the model should be leveraged to investigate the temperature differences between the process control point within the die and the internal temperature of the NiTi powder and porogen composite to understand what processing conditions could lead to melting of the copper spheres. Once a robust and reliable model has been established, the material constituents should be systematically replaced, such as using alumina spheres as porogens, to vary their relative thermal and electrical properties. Of course, all modelling observations should be reinforced with experimentation.

7. REFERENCES

1. Gibson, Lorna J., and Michael F. Ashby. *Cellular Solids: Structure and Properties*. 2nd ed. Cambridge University Press, 1999.
2. Sanders, W. S. “Lightweight Cellular Metals with High Structural Efficiency.” *Metallic Materials with High Structural Efficiency*, edited by O. N. Senkov et al., vol. 146, Springer, 2004, pp. 419–24.
3. Simone, Jr., Anthony E. *Porous Metals and Metallic Foams*. Massachusetts Institute of Technology, 1997.
4. Ashby, Michael F. et al. *Metal Foams: A Design Guide*. Butterworth-Heinemann, 2000.
5. Gaillard, C., J. F. Depois, and A. Mortenson. “Processing of NaCl Powders of Controlled Size and Shape for the Microstructural Tailoring of Aluminum Foams.” *Materials Science and Engineering A* 374 (2004): 250–262.
6. Evans, A. G. et al. “The Topological Design of Multifunctional Cellular Metals.” *Progress in Materials Science* 46 (2001): 309–327.
7. Evans, A. G., J. W. Hutchinson, and M. F. Ashby. “Multifunctionality of Cellular Metal Systems.” *Progress in Materials Science* 43 (1999): 171–221.
8. Sypeck, D. J., and H. N. G. Wadley. “Multifuntional Microtruss Laminates: Textile Synthesis and Properties.” *Journal of Materials Research* 16.3 (2001): 890–897.
9. Aydoğmuş, Tarık, and Şakir Bor. “Processing of Porous TiNi Alloys Using Magnesium as Space Holder.” *Journal of Alloys and Compounds* 478 (2009): 705–710.
10. Zhao, Biao, et al. “A Review on Metallic Porous Materials: Pore Formation, Mechanical Properties, and Their Applications.” *The International Journal of Advanced Manufacturing Technology*, vol. 95, 2017, pp. 2641–59.
11. Gain, Asit Kumar, et al. “Microstructure and Material Properties of Porous Hydroxyapatite-Zirconia Nanocomposites Using Polymethyl Methacrylate Powders.” *Materials and Design*, vol. 67, 2015, pp. 136–44.
12. Vogiatzis, C. A., et al. “Aluminum-Ceramic Cenospheres Syntactic Foams Produced by Powder Metallurgy Route.” *Materials and Design*, vol. 85, 2015, pp. 444–54.
13. Kennedy, Andrew. “Porous Metals and Metal Foams Made from Powders.” *Powder Metallurgy*, edited by Katsuyoshi Kondoh, InTech, 2012.
14. Lefebvre, L.-P., J. Banhart, and D. C. Dunand. “Porous Metals and Metallic Foams: Current Status and Recent Developments.” *Advanced Engineering Materials* 10.9 (2008): 775–787.
15. Banhart, John. “Manufacturing Routes for Metallic Foams.” *JOM* 52.12 (2000): 22–27.
16. Banhart, John. “Manufacture, Characterisation and Application of Cellular Metals and Metal Foams.” *Progress in Materials Science* 46 (2001): 559–632.
17. Mapelli, Carlo et al. “Viability Study of the Use of Cast Iron Open Cell Foam as Microbial Fuel Cell Electrodes.” *Advanced Engineering Materials* 15.3 (2013): 112–117.
18. Conde, Yves, et al. “Replication Processing of Highly Porous Materials.” *Advanced Engineering Materials*, vol. 8, no. 9, 2006, pp. 795–803.
19. Banhart, J. “Properties and Applications of Cast Aluminum Sponges.” *Advanced Engineering Materials*, vol. 2, no. 4, 2000, pp. 188–91.

20. Wadley, Haydn N. G. “Cellular Metals Manufacturing.” *Advanced Engineering Materials*, vol. 4, no. 10, 2002, pp. 726–33.
21. *ERG Aerospace – Materials & Aerospace*. ERG Aerospace Corporation, 2018, ergaerospace.com. Accessed 14 April 2018.
22. Evans, Anthony G., John W. Hutchinson, and Michael F. Ashby. “Cellular Metals.” *Current Opinion in Solid State and Materials Science* 3.3 (1998): 288–303.
23. Ashby, Michael F., and Tianjian Lu. “Metal Foams: A Survey.” *Science in China Series B: Chemistry* 46.6 (2003): 521–532.
24. Santosa, S., and T. Wierzbicki. “Crash Behavior of Box Columns Filled with Aluminum Honeycomb or Foam.” *Computers and Structures*, vol. 68, 1998, pp. 343–67.
25. Thornton, P. H., and C. L. Magee. “Deformation Characteristics of Zinc Foam.” *Metallurgical Transactions A*, vol. 6, 1975, pp. 1801–07.
26. Öchsner, Andreas, and Christian Augustin, eds. *Multifunctional Metallic Hollow Sphere Structures: Manufacturing, Properties, and Application*. Springer, 2009.
27. Pilon, Dominic, et al. “Influence of Micro-Structural Properties on the Acoustic Performances of Novel Metallic Foams.” *Canadian Acoustics*, vol. 32, no. 3, 2004, pp. 24–25.
28. Wang, Xiaolin, and Tian J. Lu. “Optimized Acoustic Properties of Cellular Solids.” *The Journal of the Acoustical Society of America*, vol. 106, 1999, pp. 756–65.
29. Chen, Shuo, Mohamed Bourham, and Afsaneh Rabiei. “Applications of Open-Cell and Closed-Cell Metal Foams for Radiation Shielding.” *Procedia Materials Science* 4 (2014): 293-298.
30. Gibson, L. J. “Mechanical Behavior of Metallic Foams.” *Annual Review of Materials Science*, vol. 30, 2000, pp. 191–227.
31. *Thermal Management*. *Ultramet*, 2018, ultramet.com. Accessed 11 April 2018.
32. Ejlali, Azadeh, et al. “Application of High Porosity Metal Foams as Air-Cooled Heat Exchangers to High Heat Load Removal Systems.” *International Communications in Heat and Mass Transfer*, vol. 36, 2009, pp. 674–79.
33. Lu, T. J., et al. “Heat Transfer in Open-Cell Metal Foams.” *Acta Materialia*, vol. 46, no. 10, 1998, pp. 3619–35.
34. Antohe, B. V., et al. “Numerical Characterization of Micro Heat Exchangers Using Experimentally Tested Porous Aluminum Layers.” *International Journal of Heat and Fluid Flow*, vol. 17, 1996, pp. 594–603.
35. Kaviany, M. “Laminar Flow Through a Porous Channel Bounded by Isothermal Parallel Plates.” *International Journal of Heat and Mass Transfer*, vol. 28, no. 4, 1985, pp. 851–58.
36. Hutter, C., et al. “Heat Transfer in Metal Foams and Designed Porous Media.” *Chemical Engineering Science*, vol. 66, 2011, pp. 3806–14.
37. *Refractory Open-Cell Foams: Carbon, Ceramic, and Metal*. *Ultramet*, 2018, ultramet.com. Accessed 9 April 2018.
38. Bhattacharya, A., and R. L. Mahajan. “Metal Foam and Finned Metal Foam Heat Sinks for Electronics Cooling in Buoyancy-Induced Convection.” *Journal of Electronic Packaging*, vol. 128, 2006, pp. 259–66.

39. Bhattacharya, A., et al. “Thermophysical Properties of High Porosity Metal Foams.” *International Journal of Heat and Mass Transfer*, vol. 45, 2002, pp. 1017–31.
40. Boomsma, K., et al. “Metal Foams as Compact High Performance Heat Exchangers.” *Mechanics of Materials*, vol. 35, 2003, pp. 1161–76.
41. Zhao, C. Y., et al. “The Temperature Dependence of Effective Thermal Conductivity of Open-Celled Steel Alloy Foams.” *Materials Science and Engineering A*, vol. 367, 2004, pp. 123–31.
42. Boomsma, K., et al. “Simulations of Flow Through Open Cell Metal Foams Using an Idealized Periodic Cell Structure.” *International Journal of Heat and Fluid Flow*, vol. 24, 2003, pp. 825–34.
43. Boomsma, K., and D. Poulikakos. “The Effects of Compression and Pore Size Variations on the Liquid Flow Characteristics in Metal Foams.” *Journal of Fluids Engineering*, vol. 124, 2002, pp. 263–72.
44. Boomsma, K., and D. Poulikakos. “On the Effective Thermal Conductivity of a Three-Dimensionally Structured Fluid-Saturated Metal Foam.” *International Journal of Heat and Mass Transfer*, vol. 44, 2001, pp. 827–36.
45. Phanikumar, M. S., and R. L. Mahajan. “Non-Darcy Natural Convection in High Porosity Metal Foams.” *International Journal of Heat and Mass Transfer*, vol. 45, 2002, pp. 3781–93.
46. Shih, W. H., et al. “Height Effect on Heat-Transfer Characteristics of Aluminum-Foam Heat Sinks.” *Journal of Heat Transfer*, vol. 128, 2006, pp. 530–37.
47. Pavel, Bogdan I., and Abdulmajeed A. Mohamad. “Experimental Investigation of the Potential of Metallic Porous Inserts in Enhancing Forced Convective Heat Transfer.” *Journal of Heat Transfer*, vol. 126, 2004, pp. 540–45.
48. Hutter, C., et al. “Large Eddy Simulation of Flow Through a Streamwise-Periodic Structure.” *Chemical Engineering Science*, vol. 66, 2011, pp. 519–29.
49. Mao, Shaolin, et al. “Correlation Studies of Hydrodynamics and Heat Transfer in Metal Foam Heat Exchangers.” *Applied Thermal Engineering*, vol. 71, 2014, pp. 104–18.
50. Walther, Gunnar, et al. “A New Class of High Temperature and Corrosion Resistant Nickel-Based Open-Cell Foams.” *Advanced Engineering Materials*, vol. 10, no. 9, 2008, pp. 803–11.
51. Matsumoto, Isao, et al. *Battery Electrode*. U.S. Patent No. 4,251,603, 1981.
52. Tabaatabaai, S. M., et al. “Lead-Acid Batteries with Foam Grids.” *Journal of Power Sources*, vol. 158, no. 2, 2006, pp. 879–84.
53. Gyenge, E., et al. “High Specific Surface Area, Reticulated Current Collectors for Lead-Acid Batteries.” *Journal of Applied Electrochemistry*, vol. 32, no. 3, 2002, pp. 287–95.
54. Dai, C. S., et al. “Preparation and Performance of Lead Foam Grid for Negative Electrode of VRLA Battery.” *Materials Chemistry and Physics*, vol. 99, 2006, pp. 431–36.
55. *Dynapore® in Fuel Cell Applications*. Martin Kurz & Company, Inc., www.mkicorp.com/a-fuelcells.asp. Accessed 14 April 2018.
56. Perego, Carlo, and Roberto Millini. “Porous Materials in Catalysis: Challenges for Mesoporous Materials.” *Chemical Society Reviews*, vol. 42, 2013, pp. 3956–76.

57. Giani, Leonardo, et al. “Heat Transfer Characterization of Metallic Foams.” *Industrial & Engineering Chemistry Research*, vol. 44, no. 24, 2005, pp. 9078–85.
58. Taguchi, Akira, and Ferdi Schüth. “Ordered Mesoporous Materials in Catalysis.” *Microporous and Mesoporous Materials*, vol. 77, 2005, pp. 1–45.
59. Giani, Leonardo, et al. “Mass-Transfer Characterization of Metallic Foams as Supports for Structured Catalysts.” *Industrial & Engineering Chemistry Research*, vol. 44, 2005, pp. 4993–5002.
60. *S-Series Passive DPF*. Nett Technologies, Inc., 2018, www.nettinc.com/products/diesel-particulate-filters-dpf/s-series-passive. Accessed 14 April 2018.
61. Liu, Yuxi, et al. “Catalytic Removal of Volatile Organic Compounds Using Ordered Porous Transition Metal Oxide and Supported Noble Metal Catalysts.” *Chinese Journal of Catalysis*, vol. 37, 2016, pp. 1193–205.
62. Mikami, Ikkou, et al. “Rapid Removal of Nitrate in Water by Hydrogenation to Ammonia with Zr-Modified Porous Ni Catalysts.” *Applied Catalysis B: Environmental*, vol. 49, 2004, pp. 173–79.
63. Cocks, Franklin Hadley. “Ultralight Reactive Metal Foams in Space: A Novel Concept.” *Journal of Spacecraft and Rockets* 21.5 (1984): 510–512.
64. Gu, S., et al. “On the Design of Two-Dimensional Cellular Metals for Combined Heat Dissipation and Structural Load Capacity.” *International Journal of Heat and Mass Transfer*, vol. 44, 2001, pp. 2163–75.
65. Lin, Hao et al. “Diffusion Bonding in Fabrication of Aluminum Foam Sandwich Panels.” *Journal of Materials Processing Technology* (2015): n. pag.
66. Banhart, John, and Hans-Wolfgang Seeliger. “Recent Trends in Aluminum Foam Sandwich Technology.” *Advanced Engineering Materials* 14.12 (2012): 1082–1087.
67. Nabavi, A., and J. Vahdati Khaki. “A Novel Method for Manufacturing of Aluminum Foam Sandwich Panels.” *Surface and Interface Analysis* 42 (2010): 275–280.
68. Banhart, J., and J. Baumeister. “Deformation Characteristics of Metal Foams.” *Journal of Materials Science*, vol. 33, 1998, pp. 1431–40.
69. Seeliger, Hans-Wolfgang. “Application Strategies for Aluminum-Foam-Sandwich Parts (AFS).” *Metal Foams and Porous Metal Structures*, edited by J. Banhart et al., MIT Verlag, 1999, pp. 29–36.
70. Pollien, Arnaud, et al. “Graded Open-Cell Aluminium Foam Core Sandwich Beams.” *Materials Science and Engineering A*, vol. 404, 2005, pp. 9–18.
71. Jing, Lin, et al. “The Dynamic Response of Sandwich Beams with Open-Cell Metal Foam Cores.” *Composites Part B*, vol. 42, no. 1, 2011, pp. 1–10.
72. Imwinkelried, Thomas. “Mechanical Properties of Open-Pore Titanium Foam.” *Journal of Biomedical Materials Research Part A* 81.4 (2007): 964–970.
73. Laptev, A., et al. “Study of Production Route for Titanium Parts Combining Very High Porosity and Complex Shape.” *Powder Metallurgy*, vol. 47, no. 1, 2004, pp. 85–92.
74. Müller, U., et al. “Do Human Osteoblasts Grow into Open-Porous Titanium?” *European Cells and Materials*, vol. 11, 2006, pp. 8–15.
75. Hollister, Scott J. “Porous Scaffold Design for Tissue Engineering.” *Natural Materials*, vol. 4, 2005, pp. 518–24.

76. Kohles, Sean S., et al. “Direct Perfusion Measurements of Cancellous Bone Anisotropic Permeability.” *Journal of Biomechanics*, vol. 34, 2001, pp. 1197–202.
77. Okuyama, Koichiro, et al. “PLIF with a Titanium Cage and Excised Facet Joint Bone for Degenerative Spondylolisthesis-In Augmentation with a Pedicle Screw.” *Clinical Spine Surgery*, vol. 20, no. 1, 2007, pp. 53–59.
78. Schiefer, H., et al. “Mechanical Examinations on Dental Implants with Porous Titanium Coating.” *Journal of Materials Science*, vol. 20, 2009, pp. 1763–70.
79. Nilles, J. L., et al. “Porous Titanium Alloy for Fixation of Knee Prostheses.” *Journal of Biomedical Materials Research*, vol. 8, no. 4, 1974, pp. 319–28.
80. Dunand, David C. “Processing of Titanium Foams.” *Advanced Engineering Materials* 6.6 (2004): 369–376.
81. Ye, Bing, and David C. Dunand. “Titanium Foams Produced by Solid-State Replication of NaCl Powders.” *Materials Science and Engineering A* 528 (2010): 691–697.
82. Torres, Y., J. J. Pavón, and Rodríguez. “Processing and Characterization of Porous Titanium for Implants by Using NaCl as Space Holder.” *Journal of Materials Processing Technology* 212 (2012): 1061–1069.
83. Simske, Steven J., et al. “Porous Materials for Bone Engineering.” *Materials Science Forum*, vol. 250, 1997, pp. 151–82.
84. McNamara, B. P., et al. “Effects of Implant Material Properties and Implant-Bone Bonding on Stress Shielding in Cementless Total Hip Arthroplasty.” *Key Engineering Materials*, vol. 99–100, 1995, pp. 309–14.
85. Geetha, M., et al. “Ti Based Biomaterials, the Ultimate Choice for Orthopaedic Implants-A Review.” *Progress in Materials Science*, vol. 54, 2009, pp. 397–425.
86. Spoerke, Erik D. “Titanium with Aligned, Elongated Pores for Orthopedic Tissue Engineering Applications.” *Journal of Biomedical Materials Research Part A*, vol. 84A, no. 2, 2008, pp. 402–12.
87. Singh, R., et al. “Characterization of the Deformation Behavior of Intermediate Porosity Interconnected Ti Foams Using Micro-Computed Tomography and Direct Finite Element Modeling.” *Acta Biomaterialia*, vol. 6, 2010, pp. 2342–51.
88. Davis, N. G., et al. “Solid-State Foaming of Titanium by Superplastic Expansion of Argon-Filled Pores.” *Journal of Materials Research*, vol. 16, no. 5, 2001, pp. 1508–19.
89. Murray, N. G. D., and D. C. Dunand. “Microstructure Evolution During Solid-State Foaming of Titanium.” *Composites Science and Technology*, vol. 63, 2003, pp. 2311–16.
90. Murray, N. G. D., and D. C. Dunand. “Effect of Thermal History on the Superplastic Expansion of Argon-Filled Pores in Titanium: Part I Kinetics and Microstructure.” *Acta Materialia*, vol. 52, 2004, pp. 2269–78.
91. Robertson, I. M., and G. B. Schaffer. “Swelling During Sintering of Titanium Alloys Based on Titanium Hydride Powder.” *Powder Metallurgy*, vol. 53, no. 1, 2010, pp. 27–33.
92. Simone, A. E., and L. J. Gibson. “The Compressive Behaviour of Porous Copper Made by the GASAR Process.” *Journal of Materials Science*, vol. 32, 1997, pp. 451–57.
93. Simone, A. E., and L. J. Gibson. “The Tensile Strength of Porous Copper Made by the GASAR Process.” *Acta Materialia*, vol. 44, no. 4, 1996, pp. 1437–47.

94. Shapovalov, V. I. “Formation of Ordered Gas-Solid Structures via Solidification in Metal-Hydrogen Systems.” *Porous and Cellular Materials for Structural Applications*, edited by Daniel S. Schwartz et al., vol. 521, Materials Research Society, 1998, pp. 281–90.
95. Apprill, J. M., et al. “GASAR Porous Metals Process Control.” *Porous and Cellular Materials for Structural Applications*, edited by Daniel S. Schwartz et al., vol. 521, Materials Research Society, 1998, pp. 291–96.
96. Paradies, C. J., et al. “The Effect of GASAR Processing Parameters on Porosity and Properties in Aluminum Alloy.” *Porous and Cellular Materials for Structural Applications*, edited by Daniel S. Schwartz et al., vol. 521, Materials Research Society, 1998, pp. 297–302.
97. Bonenberger, R. J., et al. “Characterization of Porous GASAR Aluminum.” *Porous and Cellular Materials for Structural Applications*, edited by Daniel S. Schwartz et al., vol. 521, Materials Research Society, 1998, pp. 303–14.
98. Park, Chanman, and Steven R. Nutt. “Metallographic Study of GASAR Porous Magnesium.” *Porous and Cellular Materials for Structural Applications*, edited by Daniel S. Schwartz et al., vol. 521, Materials Research Society, 1998, pp. 315–20.
99. Thieme, M., et al. “Titanium Powder Sintering for Preparation of a Porous Functionally Graded Material Destined for Orthopaedic Implants.” *Journal of Materials Science: Materials in Medicine*, vol. 12, 2001, pp. 225–31.
100. Li, Yong-hua, et al. “Pore Characteristics of Porous NiTi Alloy Fabricated by Combustion Synthesis.” *Journal of Alloys and Compounds*, vol. 325, 2001, pp. 259–62.
101. Sakamoto, Yuki, et al. “Chemical Surface Modification of High-Strength Porous Ti Compacts by Spark Plasma Sintering.” *Bio-Medical Materials and Engineering*, vol. 16, 2006, pp. 83–91.
102. Noël, P. A., et al. “Initial-Stage Hot-Pressing of SiC Fibre/Ti Monotapes.” *Composites*, vol. 25, no. 10, 1994, pp. 953–56.
103. An, Y. B., et al. “Mechanical Properties of Environmental-Electro-Discharge-Sintered Porous Ti Implants.” *Materials Letters*, vol. 59, 2005, pp. 2178–82.
104. Oh, Ik-Hyun, et al. “Mechanical Properties of Porous Titanium Compacts Prepared by Powder Sintering.” *Scripta Materialia*, vol. 49, 2003, pp. 1197–202.
105. Oh, Ik-Hyun, et al. “Microstructures and Mechanical Properties of Porous Titanium Compacts Prepared by Powder Sintering.” *Materials Transactions*, vol. 43, no. 3, 2002, pp. 443–46.
106. Chino, Yasumasa, and David C. Dunand. “Directionally Freeze-Cast Titanium Foam with Aligned, Elongated Pores.” *Acta Materialia*, vol. 56, 2008, pp. 105–13.
107. Yook, Se-Won, et al. “Porous Titanium (Ti) Scaffolds by Freezing TiH2/Camphene Slurries.” *Materials Letters*, vol. 62, 2008, pp. 4506–08.
108. Li, Jessica C., and David C. Dunand. “Mechanical Properties of Directionally Freeze-Cast Titanium Foams.” *Acta Materialia*, vol. 59, 2011, pp. 146–58.
109. Fife, J. L., et al. “Morphological Analysis of Pores in Directionally Freeze-Cast Titanium Foams.” *Journal of Materials Research*, vol. 24, no. 1, 2009, pp. 117–24.

110. Jung, Hyun-Do, et al. “Fabrication of Titanium Scaffolds with Porosity and Pore Size Gradients by Sequential Freeze Casting.” *Materials Letters*, vol. 63, no. 17, 2009, pp. 1545–47.
111. Jin, Iljoon, et al. *Method of Producing Lightweight Foamed Metal*. U.S. Patent No. 4,973,358.
112. Akiyama, Shigeru, et al. *Foamed Metal and Method of Producing Same*. U.S. Patent No. 4,713,277.
113. St-Pierre, Jean-Philippe, et al. “Three-Dimensional Growth of Differentiating MC3T3-E1 Pre-Osteoblasts on Porous Titanium Scaffolds.” *Biomaterials*, vol. 26, 2005, pp. 7319–28.
114. Jee, C. S. Y., et al. “Preparation of High Porosity Metal Foams.” *Metallurgical and Materials Transactions B*, vol. 31, 2000, pp. 1345–52.
115. Guo, Z. X., et al. “Novel Polymer-Metal Based Method for Open Cell Metal Foams Production.” *Materials Science and Technology*, vol. 16, 2000, pp. 776–80.
116. Cochran, Joe K. “Ceramic Hollow Spheres and Their Applications.” *Current Opinion in Solid State & Materials Science* 3 (1998): 474–479.
117. Sanders, Wynn Steven. “Mechanical Behavior of Closed-Cell and Hollow-Sphere Metallic Foams.” Dissertation. Massachusetts Institute of Technology, 2002.
118. Sypeck, David J., et al. “Novel Hollow Powder Porous Structures.” *Porous and Cellular Materials for Structural Applications*, edited by Daniel S. Schwartz et al., vol. 521, Materials Research Society, 1998, pp. 205–10.
119. Andersen, O., et al. “Novel Metallic Hollow Sphere Structures.” *Advanced Engineering Materials*, vol. 2, no. 4, 2000, pp. 192–95.
120. Hurysz, K. M., et al. “Steel and Titanium Hollow Sphere Foams.” *Porous and Cellular Materials for Structural Applications*, edited by Daniel S. Schwartz et al., vol. 521, Materials Research Society, 1998, pp. 191–204.
121. Queheillalt, Douglas T., Yasushi Katsumura, and Haydn N. G. Wadley. “Synthesis of Stochastic Open Cell Ni-Based Foams.” *Scripta Materialia* 50 (2004): 313–317.
122. Stiehl, James B. “Trabecular Metal in Hip Reconstructive Surgery.” *Orthopedics*, vol. 28, no. 7, 2005, pp. 662–70.
123. Zardiackas, Lyle D., et al. “Structure, Metallurgy, and Mechanical Properties of a Porous Tantalum Foam.” *Journal of Biomedical Materials Research*, vol. 58, no. 2, 2001, pp. 180–87.
124. Cachinho, Sandra C. P., and Rui N. Correia. “Titanium Scaffolds for Osteointegration: Mechanical, In Vitro and Corrosion Behaviour.” *Journal of Materials Science: Materials in Medicine*, vol. 19, 2008, pp. 451–57.
125. Lee, Jong-Hoon, et al. “Improving the Strength and Biocompatibility of Porous Titanium Scaffolds by Creating Elongated Pores Coated with a Bioactive, Nanoporous TiO2 Layer.” *Materials Letters*, vol. 64, 2010, pp. 2526–29.
126. Li, Jia Ping, et al. “Preparation and Characterization of Porous Titanium.” *Key Engineering Materials*, vol. 218–220, 2001, pp. 51–54.
127. Quadbeck, Peter, et al. “Synthesis and Properties of Open-Celled Metal Foams.” *Materials Science Forum*, vol. 534–536, 2007, pp. 1005–08.

128. Queheillalt, Douglas T., et al. “Synthesis of Open-Cell Metal Foams by Templated Directed Vapor Deposition.” *Journal of Materials Research*, vol. 16, no. 4, 2001, pp. 1028–36.
129. Badiche, X., et al. “Mechanical Properties and Non-Homogeneous Deformation of Open-Cell Nickel Foams: Application of the Mechanics of Cellular Solids and of Porous Materials.” *Materials Science and Engineering A*, vol. 289, 2000, pp. 276–88.
130. Bobyn, J. D., et al. “Characteristics of Bone Ingrowth and Interface Mechanics of a New Porous Tantalum Biomaterial.” *The Journal of Bone & Joint Surgery*, vol. 81, no. 5, 1999, pp. 907–14.
131. Wen, C. E. et al. “Novel Titanium Foam for Bone Tissue Engineering.” *Journal of Materials Research* 17.10 (2002): 2633–2639.
132. Davies, G. J., and Shu Zhen. “Metallic Foams: Their Production, Properties and Applications.” *Journal of Materials Science*, vol. 18, 1983, pp. 1899–911.
133. Körner, Carolin, and Robert F. Singer. “Processing of Metal Foams-Challenges and Opportunities.” *Advanced Engineering Materials*, vol. 2, no. 4, 2000, pp. 159–65.
134. Hintz, C., et al. “Investment Cast Near-Net-Shape Components Based on Cellular Metal Materials.” *Metal Foams and Porous Metal Structures*, edited by John Banhart et al., Verlag MIT, 1999, pp. 153–58.
135. Yamada, Y., et al. “Compressive Properties of Open-Cellular SG91A Al and AZ91 Mg.” *Materials Science and Engineering A*, vol. 272, no. 2, 1999, pp. 455–58.
136. Yamada, Y., et al. “Effects of Heat Treatment on Compressive Properties of AZ91 Mg and SG91A Al Foams with Open-Cell Structure.” *Materials Science and Engineering A*, vol. 280, no. 1, 2000, pp. 225–28.
137. Yamada, Y., et al. “Processing of an Open-Cellular AZ91 Magnesium Alloy with a Low Density of 0.05 g/cm3.” *Journal of Materials Science Letters*, vol. 18, 1999, pp. 1477–80.
138. Yamada, Y., et al. “Processing of Cellular Magnesium Materials.” *Advanced Engineering Materials*, vol. 2, no. 4, 2000, pp. 184–87.
139. Yamada, Yasuo, et al. “Compressive Deformation Characteristics of Open-Cell Mg Alloys with Controlled Cell Structure.” *Materials Transactions*, vol. 43, no. 6, 2002, pp. 1298–305.
140. Castrodeza, Enrique M. et al. “Processing and Characterization of Dual Phase Steel Foams Featured by Different Pore Distribution.” *Steel Research International* 82.8 (2011): 918–925.
141. Mapelli, C. et al. “Performance of Stainless Steel Foams Produced by Infiltration Casting Techniques.” *Journal of Materials Processing Technology* 213 (2013): 1846–1854.
142. Gruttadauria, A. et al. “Processing and Characterization of Dual Phase Steel Foam.” *Revista Matéria* 15.2 (2010): 182–188.
143. Polonsky, L., et al. “Lightweight Cellular Metal.” *Modern Castings*, vol. 39, 1961, pp. 57–71.
144. Wicklein, M., and K. Thoma. “Numerical Investigations of the Elastic and Plastic Behaviour of an Open-Cell Aluminium Foam.” *Materials Science and Engineering A*, vol. 397, 2005, pp. 391–99.
145. Zhao, Y. Y., and D. X. Sun. “A Novel Sintering-Dissolution Process for Manufacturing Al Foams.” *Scripta Materialia*, vol. 44, 2001, pp. 105–10.

146. Ibrahim, Ahmed et al. “Processing of Porous Ti and Ti5Mn Foams by Spark Plasma Sintering.” *Materials and Design* 32 (2011): 146–153.
147. Zhao, Xingke et al. “Pore Structures of High-Porosity NiTi Alloys Made From Elemental Powders with NaCl Temporary Space-Holders.” *Materials Letters* 63 (2009): 2402–2404.
148. Zhao, Yuyuan, Fusheng Han, and Thomas Fung. “Optimisation of Compaction and Liquid-State Sintering in Sintering and Dissolution Process for Manufacturing Al Foams.” *Materials Science and Engineering* A 364 (2004): 117–125.
149. Wang, Q. Z. et al. “Open-Celled Porous Cu Prepared by Replication of NaCl Space-Holders.” *Materials Science and Engineering A* 527 (2010): 1275–1278.
150. Wang, Q. Z. et al. “Compressive Behaviors and Energy-Absorption Properties of an Open-Celled Porous Cu Fabricated by Replication of NaCl Space-Holders.” *Journal of Materials Processing Technology* 211 (2011): 363–367.
151. Hakamada, Masataka et al. “Effect of Sintering Temperature on Compressive Properties of Porous Aluminum Produced by Spark Plasma Sintering.” *Materials Transactions* 46.2 (2005): 186–188.
152. Tuncer, Nihan, and Gursoy Arslan. “Designing Compressive Properties of Titanium Foams.” *Journal of Materials Science* 44 (2009): 1477–1484.
153. Savaci, Umut, Sinan Yilmaz, and Mustafa Güden. “Open Cell Lead Foams: Processing, Microstructure, and Mechanical Properties.” *Journal of Materials Science*47 (2012): 5646–5654.
154. Muñoz, S. et al. “On the Influence of Space Holder in the Development of Porous Titanium Implants: Mechanical, Computational and Biological Evaluation.” *Materials Characterization* 108 (2015): 68–78.
155. Sabzevari, Mina, Seyed Abdolkarim Sajjadi, and Ahmad Moloodi. “Physical and Mechanical Properties of Porous Copper Nanocomposite Produced by Powder Metallurgy.” *Advanced Powder Technology* (2015): n. pag.
156. Shahzeydi, Mohammad Hosein, Amir Masoud Parvanian, and Masoud Panjepour. “The Distribution and Mechanism of Pore Formation in Copper Foams Fabricated by Lost Carbonate Sintering Method.” *Materials Characterization* 111 (2016): 21–30.
157. Wenjuan, Niu et al. “Processing and Properties of Porous Titanium Using Space Holder Technique.” *Materials Science and Engineering A* 506 (2009): 148–151.
158. Kim, Sung Won et al. “Fabrication of Porous Titanium Scaffold with Controlled Porous Structure and Net-Shape Using Magnesium as Spacer.” *Materials Science and Engineering C* 33 (2013): 2808–2815.
159. Esen, Z., and Ş. Bor. “Processing of Titanium Foams Using Magnesium Spacer Particles.” *Scripta Materialia* 56 (2007): 341–344.
160. Hassani, Amir, et al. “Production of Graded Aluminum Foams via Powder Space Holder Technique.” *Materials and Design*, vol. 40, 2012, pp. 510–15.
161. Wen, C. E., et al. “Processing of Fine-Grained Aluminum Foam by Spark Plasma Sintering.” *Journal of Materials Science Letters*, vol. 22, 2003, pp. 1407–09.
162. Bram, Martin, et al. “High-Porosity Titanium, Stainless Steel, and Superalloy Parts.” *Advanced Engineering Materials*, vol. 2, no. 4, 2000, pp. 196–99.

163. Wen, C. E., et al. “Processing of Biocompatible Porous Ti and Mg.” *Scripta Materialia*, vol. 45, 2001, pp. 1147–53.
164. Wen, C. E., et al. “Processing and Mechanical Properties of Autogenous Titanium Implant Materials.” *Journal of Materials Science: Materials in Medicine*, vol. 13, 2002, pp. 397–401.
165. Laptev, A., et al. “Green Strength of Powder Compacts Provided for Production of Highly Porous Titanium Parts.” *Powder Metallurgy*, vol. 48, no. 4, 2005, pp. 358–64.
166. Kwok, P. J., et al. “Porous Titanium by Electro-Chemical Dissolution of Steel Space-Holders.” *Advanced Engineering Materials*, vol. 10, no. 9, 2008, pp. 820–25.
167. Jorgensen, Daniel J., and David C. Dunand. “Ti-6Al-4V with Micro- and Macropores Produced by Powder Sintering and Electrochemical Dissolution of Steel Wires.” *Materials Science and Engineering A*, vol. 527, no. 3, 2010, pp. 849–53.
168. Quadbeck, P., et al. “Superalloy IN625 with Cellular Microstructure - Fabrication Route and Mechanical Properties.” *Advanced Engineering Materials*, vol. 6, no. 8, 2004, pp. 635–39.
169. Golabgir, Mohammad Hossein, et al. “Fabrication and Evaluation of Oxidation Resistance Performance of Open-Celled Fe(Al) Foam by Space-Holder Technique.” *Advanced Powder Technology*, vol. 25, no. 3, 2014, pp. 960–67.
170. Jha, Nidhi, et al. “Highly Porous Open Cell Ti-Foam Using NaCl as Temporary Space Holder Through Powder Metallurgy Route.” *Materials and Design*, vol. 47, 2013, pp. 810–19.
171. Bakan, Halil I. “A Novel Water Leaching and Sintering Process for Manufacturing Highly Porous Stainless Steel.” *Scripta Materialia*, vol. 55, no. 2, 2006, pp. 203–06.
172. Bafti, Hasan, and Ali Habibolahzadeh. “Production of Aluminum Foam by Spherical Carbamide Space Holder Technique-Processing Parameters.” *Materials and Design*, vol. 31, no. 9, 2010, pp. 4122–29.
173. Michailidis, N., et al. “Compressive Response of Al-Foams Produced via a Powder Sintering Process Based on a Leachable Space-Holder Material.” *Materials Science and Engineering A*, vol. 528, no. 3, 2011, pp. 1662–67.
174. Jakubowicz, J., et al. “Micro-CT Analysis and Mechanical Properties of Ti Spherical and Polyhedral Void Composites Made with Saccharose as a Space Holder Material.” *Materials Characterization*, vol. 100, 2015, pp. 13–20.
175. Xie, Zhen Kai, et al. “Fabrication of Micro Porous Aluminum by Powder Sintering.” *Materials Science Forum*, vol. 539–543, 2007, pp. 2778–81.
176. Hsu, Hsueh-Chuan, et al. “Processing and Mechanical Properties of Porous Ti-7.5Mo Alloy.” *Materials and Design*, vol. 47, 2013, pp. 21–26.
177. Zhao, Y. Y., et al. “Lost Carbonate Sintering Process for Manufacturing Metal Foams.” *Scripta Materialia*, vol. 52, no. 4, 2005, pp. 295–98.
178. Zhang, Erlin, and Bin Wang. “On the Compressive Behaviour of Sintered Porous Coppers with Low to Medium Porosities-Part I: Experimental Study.” *International Journal of Mechanical Sciences*, vol. 47, 2005, pp. 744–56.
179. Wang, Bin, and Erlin Zhang. “On the Compressive Behavior of Sintered Porous Coppers with Low-to-Medium Porosities-Part II: Preparation and Microstructure.” *International Journal of Mechanical Sciences*, vol. 50, no. 3, 2008, pp. 550–58.

180. Jiang, B., et al. “A Novel Method for Making Open Cell Aluminum Foams by Powder Sintering Process.” *Materials Letters*, vol. 59, no. 26, 2005, pp. 3333–36.
181. Jiang, B., et al. “Processing of Open Cell Aluminum Foams with Tailored Porous Morphology.” *Scripta Materialia*, vol. 53, no. 6, 2005, pp. 781–85.
182. Aghion, E., and Y. Perez. “Effects of Porosity on Corrosion Resistance of Mg Alloy Foam Produced by Powder Metallurgy Technology.” *Materials Characterization*, vol. 96, 2014, pp. 78–83.
183. Hao, Gang Ling, et al. “Processing and Mechanical Properties of Magnesium Foams.” *Journal of Porous Materials*, vol. 16, no. 3, 2009, pp. 251–56.
184. Tuncer, Nihan, et al. “Study of Metal Injection Molding of Highly Porous Titanium by Physical Modeling and Direct Experiments.” *Journal of Materials Processing Technology*, vol. 214, no. 7, 2014, pp. 1352–60.
185. Sun, D. X., and Y. Y. Zhao. “Static and Dynamic Energy Absorption of Al Foams Produced by the Sintering and Dissolution Process.” *Metallurgical and Materials Transactions B*, vol. 34, no. 1, 2003, pp. 69–74.
186. Sun, D. X., and Y. Y. Zhao. “Phase Changes in Sintering of Al/Mg/NaCl Compacts for Manufacturing Al Foams by the Sintering and Dissolution Process.” *Materials Letters*, vol. 59, no. 1, 2005, pp. 6–10.
187. Niu, Wenjuan, et al. “Preparation and Characterization of Porous Titanium Using Space-Holder Technique.” *Rare Metals*, vol. 28, no. 4, 2009, pp. 338–42.
188. Hong, T. F., et al. “Fabrication of Porous Titanium Scaffold Materials by a Fugitive Filler Method.” *Journal of Materials Science: Materials in Medicine*, vol. 19, 2008, pp. 3489–95.
189. Despois, J. F. et al. “Influence of the Infiltration Pressure on the Structure and Properties of Replicated Aluminum Foams.” *Materials Science and Engineering A* 462 (2007): 68–75.
190. Castrodeza, Enrique M., and Carlo Mapelli. “Processing of Brass Open-Cell Foam by Silica-Gel Beads Replication.” *Journal of Materials Processing Technology* 209 (2009): 4958–4962.
191. Bertolino, G. et al. “Cyclic Pseudoelastic Behavior and Energy Dissipation in As-Cast Cu-Zn-Al Foams of Different Densities.” *Intermetallics* 19 (2011): 577–585.
192. Goodall, Russell et al. “Spherical Pore Replicated Microcellular Aluminium: Processing and Influence on Properties.” *Materials Science and Engineering A*465 (2007): 124–135.
193. Marchi, C. San, and A. Mortensen. “Deformation of Open-Cell Aluminum Foam.” *Acta Materialia* 49 (2001): 3959–3969.
194. Brothers, A. H. et al. “Processing and Structure of Open-Celled Amorphous Metal Foams.” *Scripta Materialia* 52 (2005): 335–339.
195. Brothers, A. H., and D. C. Dunand. “Plasticity and Damage in Cellular Amorphous Metals.” *Acta Materialia*, vol. 53, 2005, pp. 4427–40.
196. Wada, Takeshi, et al. “Preparation of Open-Cell Porous Zr-Based Bulk Glassy Alloy.” *Materials Transactions*, vol. 48, no. 9, 2007, pp. 2381–84.
197. Chen, Feng, and He Deping. “Preparation, Structure Control and Acoustic Properties of Porous Aluminium with Open Cells.” *Metal Foams and Porous Metal Structures*, edited by J. Banhart et al., MIT Verlag, 1999, pp. 163–66.

198. Despois, Jean-François, and Andreas Mortensen. “Permeability of Open-Pore Microcellular Materials.” *Acta Materialia*, vol. 53, no. 5, 2005, pp. 1381–88.
199. Belhadj, Abd-Elmouneïm, et al. “Elaboration and Characterization of Metallic Foams Based on Tin-Lead.” *Materials Science and Engineering A*, vol. 494, 2008, pp. 425–28.
200. Han, Fusheng, et al. “Effect of Pore Combination on the Mechanical Properties of an Open Cell Aluminum Foam.” *Scripta Materialia*, vol. 50, no. 1, 2004, pp. 13–17.
201. Despois, Jean-François. “Microstructural Tailoring of Open-Pore Microcellular Aluminium by Replication Processing.” *Materials Science Forum*, vol. 512, 2006, pp. 281–88.
202. Marchi, C. San, et al. “Uniaxial Deformation of Open-Cell Aluminum Foam: The Role of Internal Damage.” *Acta Materialia*, vol. 52, no. 10, 2004, pp. 2895–902.
203. Despois, J. F., et al. “Tensile Behaviour of Replicated Aluminium Foams.” *Advanced Engineering Materials*, vol. 6, no. 6, 2004, pp. 444–47.
204. Chou, Kan-Sen, and Ming-An Song. “A Novel Method for Making Open-Cell Aluminum Foams with Soft Ceramic Balls.” *Scripta Materialia*, vol. 46, no. 5, 2002, pp. 379–82.
205. Lu, T. J., and J. M. Ong. “Characterization of Close-Celled Cellular Aluminum Alloys.” *Journal of Materials Science*, vol. 36, no. 11, 2001, pp. 2773–86.
206. Li, J. R., et al. “Effect of Dual-Size Cell Mix on the Stiffness and Strength of Open-Cell Aluminum Foams.” *Materials Science and Engineering A*, vol. 362, 2003, pp. 240–48.
207. Brothers, A. H., and D. C. Dunand. “Ductile Bulk Metallic Glass Foams.” *Advanced Materials*, vol. 17, no. 4, 2005, pp. 484–86.
208. Daudt, Natália de Freitas. “Manufacturing of Highly Porous Titanium by Metal Injection Molding in Combination with Plasma Treatment.” *Journal of Materials Processing Technology* 239 (2017): 202–209.
209. Manonukul, A., et al. “Effects of Replacing Metal Powder with Powder Space Holder on Metal Foam Produced by Metal Injection Moulding.” *Journal of Materials Processing Technology*, vol. 210, no. 3, 2010, pp. 529–35.
210. Gülsoy, H. Özkan, and Randall M. German. “Production of Micro-Porous Austenitic Stainless Steel by Powder Injection Molding.” *Scripta Materialia*, vol. 58, no. 4, 2008, pp. 295–98.
211. Koikul, Othaiwan, et al. “Effects of Replacing Binder with Powder Space Holder on Properties of Metal Injection Moulded Foam.” *Journal of Metals, Materials and Minerals*, vol. 20, no. 1, 2010, pp. 57–62.
212. Chen, Liang-Jian, et al. “Porous Titanium Implants Fabricated by Metal Injection Molding.” *Transactions of Nonferrous Metals Society of China*, vol. 19, no. 5, 2009, pp. 1174–79.
213. Laptev, Alexander M., et al. “Increased Shape Stability and Porosity of Highly Porous Injection-Molded Titanium Parts.” *Advanced Engineering Materials*, vol. 17, no. 11, 2015, pp. 1579–87.
214. Daudt, N. F., et al. “Surface Modification of Highly Porous Titanium by Plasma Treatment.” *Materials Letters*, vol. 141, 2015, pp. 194–97.
215. Bansiddhi, A., and D. C. Dunand. “Shape-Memory NiTi Foams Produced by Replication of NaCl Space-Holders.” *Acta Biomaterialia* 4 (2008): 1996–2007.

216. Bansiddhi, Ampika, and David C. Dunand. “Shape-Memory NiTi Foams Produced by Solid-State Replication with NaF.” *Intermetallics* 15 (2007): 1612–1622.
217. Singh, R., et al. “Titanium Foams for Biomedical Applications: A Review.” *Materials Technology*, vol. 25, no. 3/4, 2010, pp. 127–36.
218. Ryan, Garrett, et al. “Fabrication Methods of Porous Metals for Use in Orthopaedic Applications.” *Biomaterials*, vol. 27, 2006, pp. 2651–70.
219. Thelen, Sarah, et al. “Mechanics Considerations for Microporous Titanium as an Orthopedic Implant Material.” *Journal of Biomedical Materials Research*, vol. 69A, no. 4, 2004, pp. 601–10.
220. Murr, Lawrence E. et al. “Metal Fabrication by Additive Manufacturing Using Laser and Electron Beam Melting Technologies.” *Journal of Materials Science and Technology* 28.1 (2012): 1–14.
221. Ramirez, D. A. et al. “Open-Cellular Copper Structures Fabricated by Additive Manufacturing Using Electron Beam Melting.” *Materials Science and Engineering A* 528 (2011): 5379–5386.
222. Murr, L. E. et al. “Next-Generation Biomedical Implants Using Additive Manufacturing of Complex, Cellular and Functional Mesh Arrays.” *Philosophical Transactions of the Royal Society A* 368 (2010): 1999–2032.
223. Murr, L. E., et al. “Characterization of Ti-6Al-4V Open Cellular Foams Fabricated by Additive Manufacturing Using Electron Beam Melting.” *Materials Science and Engineering A*, vol. 527, 2010, pp. 1861–68.
224. Murr, Lawrence, et al. “Open-Cellular Co-Base and Ni-Base Superalloys Fabricated by Electron Beam Melting.” *Materials*, vol. 4, 2011, pp. 782–90.
225. Hernandez, Jennifer. “Microstructures for Two-Phase Gamma Titanium Aluminide Fabricated by Electron Beam Melting.” *Metallography, Microstructure, and Analysis*, vol. 1, no. 1, 2012, pp. 14–27.
226. Balla, Vamsi Krishna, et al. “Understanding Compressive Deformation in Porous Titanium.” *Philosophical Magazine*, vol. 90, no. 22, 2010, pp. 3081–94.
227. Krishna, B. Vamsi, et al. “Low Stiffness Porous Ti Structures for Load-Bearing Implants.” *Acta Biomaterialia*, vol. 3, no. 6, 2007, pp. 997–1006.
228. Hayashi, T., et al. “Selective Laser Sintering Method Using Titanium Powder Sheet Toward Fabrication of Porous Bone Substitutes.” *JSME International Journal Series A-Solid Mechanics and Material Engineering*, vol. 48, no. 4, 2005, pp. 369–75.
229. Tuchinsky, L., and R. Loutfy. “Novel Process for Cellular Materials with Oriented Structure.” *Proceedings of the 1st International Conference on Metal Foams and Porous Metal Structures*, 1999, pp. 189–95.
230. Singh, Randhir. *A Novel Ceramic Precursor Route for the Direct Production of Hierarchically Structured Titanium Alloy Foams*. Imperial College London, 2009.
231. Wadley, Haydn N. G. “Multifunctional Periodic Cellular Metals.” *Philosophical Transactions of the Royal Society A*, vol. 364, 2006, pp. 31–68.
232. Wicks, Nathan, and John W. Hutchinson. “Optimal Truss Plates.” *International Journal of Solids and Structures*, vol. 38, 2001, pp. 5165–83.

233. Wadley, Haydn N. G., et al. “Fabrication and Structural Performance of Periodic Cellular Metal Sandwich Structures.” *Composites Science and Technology*, vol. 63, no. 16, 2003, pp. 2331–42.
234. Chiras, S., et al. “The Structural Performance of Near-Optimized Truss Core Panels.” *International Journal of Solids and Structures*, vol. 39, 2002, pp. 4093–115.
235. Deshpande, V. S., and N. A. Fleck. “Collapse of Truss Core Sandwich Beams in 3-Point Bending.” *International Journal of Solids and Structures*, vol. 38, 2001, pp. 6275–305.
236. Sypeck, D. J., and H. N. G. Wadley. “Cellular Metal Truss Core Sandwich Structures.” *Cellular Metals and Metal Foaming Technology*, edited by J. Banhart et al., Verlag MIT Publishing, 2001, pp. 381–86.
237. Kooistra, Gregory W., et al. “Shear Behavior of Aluminum Lattice Truss Sandwich Panel Structures.” *Materials Science and Engineering A*, vol. 472, 2008, pp. 242–50.
238. Kooistra, Gregory W., et al. “Compressive Behavior of Age Hardenable Tetrahedral Lattice Truss Structures Made From Aluminum.” *Acta Materialia*, vol. 52, no. 14, 2004, pp. 4229–37.
239. Rathbun, H. J., et al. “Measurement and Simulation of the Performance of a Lightweight Metallic Sandwich Structure with a Tetrahedral Truss Core.” *Journal of Applied Mechanics*, vol. 71, no. 3, 2004, pp. 368–74.
240. Sypeck, David J. “Wrought Aluminum Truss Core Sandwich Structures.” *Metallurgical and Materials Transactions B*, vol. 36, no. 1, 2005, pp. 125–31.
241. Zhou, J., et al. “On the Deformation of Aluminum Lattice Block Structures: From Struts to Structures.” *Mechanics of Materials*, vol. 36, 2004, pp. 723–37.
242. Wallach, J. C., and L. J. Gibson. “Mechanical Behavior of a Three-Dimensional Truss Material.” *International Journal of Solids and Structures*, vol. 38, 2001, pp. 7181–96.
243. Brittain, Scott T., et al. “Fabrication and Mechanical Performance of a Mesoscale Space-Filling Truss System.” *Journal of Microelectromechanical Systems*, vol. 10, no. 1, 2001, pp. 113–20.
244. Krause, David L., et al. “Mechanical Testing of IN718 Lattice Block Structures.” *131st Annual Meeting and Exhibition*, Minerals, Metals, and Materials Society, 2002.
245. Feng, Li-Jia, et al. “Shear and Bending Performance of New Type Enhanced Lattice Truss Structures.” *International Journal of Mechanical Sciences*, vol. 134, 2017, pp. 589–98.
246. Hebsur, Mohan G. “Processing of IN-718 Lattice Block Castings.” *131st Annual Meeting and Exhibition*, Minerals, Metals, and Materials Society, 2002, pp. 1–11.
247. Li, Qizhen, et al. “Mechanical Properties of Cast Ti-6Al-4V Lattice Block Structures.” *Metallurgical and Materials Transactions A*, vol. 39, 2008, pp. 441–49.
248. Renauld, M. L., et al. “The Effect of Parent Metal Properties on the Performance of Lattice Block Material.” *Porous and Cellular Materials for Structural Applications*, edited by Daniel S. Schwartz et al., vol. 521, Materials Research Society, 1998, pp. 109–17.
249. Queheillalt, Douglas T., and Haydn N. G. Wadley. “Pyramidal Lattice Truss Structures with Hollow Trusses.” *Materials Science and Engineering A*, vol. 397, 2005, pp. 132–37.
250. Zok, F. W., et al. “A Protocol for Characterizing the Structural Performance of Metallic Sandwich Panels: Application to Pyramidal Truss Cores.” *International Journal of Solids and Structures*, vol. 41, 2004, pp. 6249–71.

251. Wang, J., et al. “On the Performance of Truss Panels with Kagomé Cores.” *International Journal of Solids and Structures*, vol. 40, 2003, pp. 6981–88.
252. Lee, B. K., and K. J. Kang. “High Strength-per-Weight Cellular Metals Fabricated of Wires.” *Advanced Engineering Materials*, vol. 10, no. 9, 2008, pp. 835–39.
253. Lim, Ji-Hyun, and Ki-Ju Kang. “Mechanical Behavior of Sandwich Panels with Tetrahedral and Kagome Truss Cores Fabricated from Wires.” *International Journal of Solids and Structures*, vol. 43, no. 17, 2006, pp. 5228–46.
254. Lee, Byung-Kon, and Ki-Ju Kang. “A Parametric Study on Compressive Characteristics of Wire-Woven Bulk Kagome Truss Cores.” *Composite Structures*, vol. 92, no. 2, 2010, pp. 445–53.
255. Lee, Min-Geun, and Ki-Ju Kang. “Feasibility of a Wire-Woven Metal for Application as a Sandwich Core.” *International Journal of Mechanical Sciences*, vol. 80, 2014, pp. 81–92.
256. Lee, Min-Geun, and Ki-Ju Kang. “Mechanical Properties of Three Variations of a Wire-Woven Metal Subjected to Shear.” *International Journal of Solids and Structures*, vol. 51, 2014, pp. 4504–18.
257. Heinl, Peter, et al. “Selective Electron Beam Melting of Cellular Titanium: Mechanical Properties.” *Advanced Engineering Materials*, vol. 10, no. 9, 2008, pp. 882–88.
258. Heinl, Peter, et al. “Cellular Titanium by Selective Electron Beam Melting.” *Advanced Engineering Materials*, vol. 9, no. 5, 2007, pp. 360–64.
259. Queheillalt, Douglas T., and Haydn N. G. Wadley. “Cellular Metal Lattices with Hollow Trusses.” *Acta Materialia*, vol. 53, no. 2, 2005, pp. 303–13.
260. Rathbun, H. J., et al. “Structural Performance of Metallic Sandwich Beams with Hollow Truss Cores.” *Acta Materialia*, vol. 54, 2006, pp. 5509–18.
261. Deshpande, V. S., et al. “Effective Properties of the Octet-Truss Lattice Material.” *Journal of the Mechanics and Physics of Solids*, vol. 49, 2001, pp. 1747–69.
262. Kang, Ki-Ju. “Wire-Woven Cellular Metals: The Present and Future.” *Progress in Materials Science*, vol. 69, 2015, pp. 213–307.
263. Jonathan Aerospace Materials Corporation, www.jonathanaerospacecorp.com. Accessed 28 April 2018.
264. Li, Jia Ping, et al. “Porous Ti6Al4V Scaffold Directly Fabricating by Rapid Prototyping: Preparation and In Vitro Experiment.” *Biomaterials*, vol. 27, 2006, pp. 1223–35.
265. Li, Jia Ping, et al. “Bone Ingrowth in Porous Titanium Implants Produced by 3D Fiber Deposition.” *Biomaterials*, vol. 28, 2007, pp. 2810–20.
266. Li, J. P., et al. “Porous Ti6Al4V Scaffolds Directly Fabricated by 3D Fibre Deposition Technique: Effect of Nozzle Diameter.” *Journal of Materials Science*, vol. 16, 2005, pp. 1159–63.
267. Hollander, Dirk A., et al. “Structural, Mechanical and In Vitro Characterization of Individually Structured Ti-6Al-4V Produced by Direct Laser Forming.” *Biomaterials*, vol. 27, 2006, pp. 955–63.
268. Heinl, Peter et al. “Cellular Ti-6Al-4V Structures with Interconnected Macro Porosity for Bone Implants Fabricated by Selective Electron Beam Melting.” *Acta Biomaterialia* 4 (2008): 1536–1544.

269. Hasib, Hazman, Ola L. A. Harrysson, and Harvey A. West II. “Powder Removal from Ti-6Al-4V Cellular Structures Fabricated via Electron Beam Melting.” *JOM* 67.3 (2015): 639–646.
270. Parthasarathy, Jayanthi, et al. “Mechanical Evaluation of Porous Titanium (Ti6Al4V) Structures with Electron Beam Melting (EBM).” *Journal of the Mechanical Behavior of Biomedical Materials*, vol. 3, 2010, pp. 249–59.
271. Parthasarathy, Jayanthi, et al. “A Design for the Additive Manufacture of Functionally Graded Porous Structures with Tailored Mechanical Properties for Biomedical Applications.” *Journal of Manufacturing Processes*, vol. 13, no. 2, 2011, pp. 160–70.
272. Cansizoglu, O., et al. “Properties of Ti-6Al-4V Non-Stochastic Lattice Structures Fabricated via Electron Beam Melting.” *Materials Science and Engineering A*, vol. 492, 2008, pp. 468–74.
273. Harrysson, Ola L. A., et al. “Direct Metal Fabrication of Titanium Implants with Tailored Materials and Mechanical Properties Using Electron Beam Melting Technology.” *Materials Science and Engineering C*, vol. 28, no. 3, 2008, pp. 366–73.
274. Li, Xiang, et al. “Fabrication and Characterization of Porous Ti6Al4V Parts for Biomedical Applications Using Electron Beam Melting Process.” *Materials Letters*, vol. 63, 2009, pp. 403–05.
275. Gaytan, S. M., et al. “Comparison of Microstructures and Mechanical Properties for Solid and Mesh Cobalt-Base Alloy Prototypes Fabricated by Electron Beam Melting.” *Metallurgical and Materials Transactions A*, vol. 41A, 2010, pp. 3216–27.
276. Xue, Weichang, et al. “Processing and Biocompatibility Evaluation of Laser Processed Porous Titanium.” *Acta Biomaterialia*, vol. 3, 2007, pp. 1007–18.
277. Mullen, Lewis, et al. “Selective Laser Melting: A Regular Unit Cell Approach for the Manufacture of Porous, Titanium, Bone In-Growth Constructs, Suitable for Orthopedic Applications.” *Journal of Biomedical Materials Research*, vol. 89B, no. 2, 2009, pp. 325–34.
278. Stamp, R., et al. “The Development of a Scanning Strategy for the Manufacture of Porous Biomaterials by Selective Laser Melting.” *Journal of Materials Science: Materials in Medicine*, vol. 20, 2009, pp. 1839–48.
279. Lin, Chia-Ying, et al. “Structural and Mechanical Evaluations of a Topology Optimized Titanium Interbody Fusion Cage Fabricated by Selective Laser Melting Process.” *Journal of Biomedical Materials Research*, vol. 83A, no. 2, 2007, pp. 272–79.
280. Lopez-Heredia, M. A., et al. “Bone Growth in Rapid Prototyped Porous Titanium Implants.” *Journal of Biomedical Materials Research*, vol. 85A, no. 3, 2008, pp. 664–73.
281. Lopez-Heredia, Marco A., et al. “Rapid Prototyped Porous Titanium Coated with Calcium Phosphate as a Scaffold for Bone Tissue Engineering.” *Biomaterials*, vol. 29, 2008, pp. 2608–15.
282. Covaciu, M., et al. “A Method for Manufacturing Cellular Metals with Open- and Close-Type Porosities.” *Materials Letters*, vol. 65, 2011, pp. 2947–50.
283. Ryan, Garrett E., et al. “Porous Titanium Scaffolds Fabricated Using a Rapid Prototyping and Powder Metallurgy Technique.” *Biomaterials*, vol. 29, 2008, pp. 3625–35.
284. Sheydaeian, Esmat. *Systems, Materials, and Methodologies for Multi-Material Hybrid Additive Manufacturing Functionally Graded Structures*. University of Waterloo, 2017.

285. Vlasea, Mihaela, et al. “A Combined Additive Manufacturing and Micro-Syringe Deposition Technique for Realization of Bio-Ceramic Structures with Micro-Scale Channels.” *The International Journal of Advanced Manufacturing Technology*, vol. 68, 2013, pp. 2261–69.
286. Mondrinos, Mark J., et al. “Porogen-Based Solid Freeform Fabrication of Polycaprolactone-Calcium Phosphate Scaffolds for Tissue Engineering.” *Biomaterials*, vol. 27, no. 25, 2006, pp. 4399–408.
287. Sharif, Hajar. *Development of a Novel Porogen Insertion System Used in Solid Freeform Fabrication of Porous Biodegradable Scaffolds with Heterogeneous Internal Architectures*. University of Waterloo, 2009.
288. Kawamoto, Hiroyuki, and Kosuke Tsuji. “Manipulation of Small Particles Utilizing Electrostatic Force.” *Advanced Powder Technology*, vol. 22, no. 5, 2011, pp. 602–07.
289. Kawamoto, H. “Manipulation of Single Particles by Utilizing Electrostatic Force.” *Journal of Electrostatics*, vol. 67, no. 6, 2009, pp. 850–61.
290. Takahashi, Kunio, et al. “Voltage Required to Detach an Adhered Particle by Coulomb Interaction for Micromanipulation.” *Journal of Applied Physics*, vol. 90, no. 1, 2001, pp. 432–37.
291. Vandaele, Vincent, et al. “Non-Contact Handling in Microassembly: Acoustical Levitation.” *Precision Engineering*, vol. 29, no. 4, 2005, pp. 491–505.
292. Hon, K. K. B., et al. “Direct Writing Technology-Advances and Development.” *CIRP Annals*, vol. 57, no. 2, 2008, pp. 601–20.
293. Fardel, Romain, et al. “Shadowgraphy Investigation of Laser-Induced Forward Transfer: Front Side and Back Side Ablation of the Triazene Polymer Sacrificial Layer.” *Applied Surface Science*, vol. 255, no. 10, 2009, pp. 5430–34.
294. Serra, Pere, et al. “Laser-Induced Forward Transfer: A Direct-Writing Technique for Biosensors Preparation.” *Journal of Laser Micro/Nanoengineering*, vol. 1, no. 3, 2006, pp. 236–42.
295. Sheydaeian, Esmat, and Ehsan Toyserkani. “A System for Selectively Encapsulating Porogens Inside the Layers During Additive Manufacturing: From Conceptual Design to the First Prototype.” *Journal of Manufacturing Processes*, vol. 26, 2017, pp. 330–38.
296. Vlasea, Mihaela, and Ehsan Toyserkani. “Experimental Characterization and Numerical Modeling of a Micro-Syringe Deposition System for Dispensing Sacrificial Photopolymers on Particulate Ceramic Substrates.” *Journal of Materials Processing Technology*, vol. 213, no. 11, 2013, pp. 1970–77.
297. Sheydaeian, Esmat, et al. “Material Process Development for the Fabrication of Heterogeneous Titanium Structures with Selective Pore Morphology by a Hybrid Additive Manufacturing Process.” *Materials and Design*, vol. 135, 2017, pp. 142–50.
298. Schaedler, T. A. et al. “Ultralight Metallic Microlattices.” *Science* 334 (2011): 962–965.
299. Moussa, Nadine, et al. “Infiltration of a Porous Matrix by a Solidifying Liquid Metal: A Local Model.” *International Journal of Thermal Sciences*, vol. 120, 2017, pp. 481–90.
300. Bednářová, Vlasta, et al. “Characterisation of Cellular Metallic Materials Manufactured by Casting Methods.” *21st International Conference on Metallurgy and Materials*, 2012, pp. 1209–14.

301. Moussa, Nadine. *Multi Scale Modelling and Numerical Simulation of Metal Foam Manufacturing Process via Casting*. Université Paris-Saclay, 2016.
302. Bednářová, Vlasta, et al. “Cast Cellular Metals with Regular and Irregular Structures.” *Materials and Technology*, vol. 48, 2014, pp. 175–79.
303. Gaillard, Yves, and Jonathan Dairon. “Casting Parts with Metallic Foam.” *MetFoam 2009: 6th International Conference on Porous Metals and Metallic Foams*, 2009, pp. 1–12.
304. Evans, A. G. “Lightweight Materials and Structures.” *MRS Bulletin*, vol. 26, no. 10, 2001, pp. 790–97.
305. Tian, J., et al. “The Effects of Topology Upon Fluid-Flow and Heat-Transfer Within Cellular Copper Structures.” *International Journal of Heat and Mass Transfer*, vol. 47, 2004, pp. 3171–86.
306. Williams, Christopher B., Joe K. Cochran, and David W. Rosen. “Additive Manufacturing of Metallic Cellular Materials via Three-Dimensional Printing.” *International Journal of Advanced Manufacturing Technology* 53 (2011): 231–239.
307. Leong, K. F., et al. “Solid Freeform Fabrication of Three-Dimensional Scaffolds for Engineering Replacement Tissues and Organs.” *Biomaterials*, vol. 24, 2003, pp. 2363–78.
308. Yang, Li et al. “Additive Manufacturing of Metal Cellular Structures: Design and Fabrication.” *JOM* 67.3 (2015): 608–615.
309. Sheydaeian, Esmat, et al. “On the Effect of Throughout Layer Thickness Variation on Properties of Additively Manufactured Cellular Titanium Structures.” *Additive Manufacturing*, vol. 18, 2017, pp. 40–47.
310. Garay, J. E. “Current-Activated, Pressure-Assisted Densification of Materials.” *Annual Review of Materials Research* 40 (2010): 445–468.
311. German, Randall M. *Sintering Theory and Practice*. Wiley-Interscience, 1996.
312. Kang, Suk-Joong L. *Sintering: Densification, Grain Growth, & Microstructure*. Elsevier Butterworth-Heinemann, 2005.
313. Castro, Ricardo H. R., and Klaus van Benthem, eds. *Sintering: Mechanisms of Convention Nanodensification and Field Assisted Processes*. Vol. 35. Springer, 2013.
314. Fang, Zhigang Zak, editor. *Sintering of Advanced Materials*. Woodhead Publishing Limited, 2010.
315. Li, Bing-Yun et al. “An Investigation of the Synthesis of Ti-50 At. Pct Ni Alloys Through Combustion Synthesis and Conventional Powder Sintering.” *Metallurgical and Materials Transactions A* 31 (2000): 1867–1871.
316. Munir, Z. A., U. Anselmi-Tamburini, and M. Ohyanagi. “The Effect of Electric Field and Pressure on the Synthesis and Consolidation of Materials: A Review of the Spark Plasma Sintering Method.” *Journal of Materials Science* 41 (2006): 763–777.
317. Stuer, Michael, et al. “Comparison of Apparent Activation Energies for Densification of Alumina Powders by Pulsed Electric Current Sintering (Spark Plasma Sintering) and Conventional Sintering-Toward Applications for Transparent Polycrystalline Alumina.” *Journal of Materials Research*, vol. 32, no. 17, 2017, pp. 3309–18.
318. Li, Bing-Yun, et al. “Porous NiTi Alloy Prepared from Elemental Powder Sintering.” *Journal of Materials Research*, vol. 13, no. 10, 1998, pp. 2847–51.

319. Li, B. Y. et al. “Synthesis of Porous Ni–Ti Shape-Memory Alloys by Self-Propagating High-Temperature Synthesis: Reaction Mechanism and Anisotropy in Pore Structure.” *Acta Materialia* 48.15 (2000): 3895 – 3904.
320. Resnina, N. et al. “Martensitic Transformation and Mechanical Behavior of Porous Ti-50.0 at % Ni Alloy, Fabricated by Self-Propagating High Temperature Synthesis at Different Temperature.” *Physics Procedia* 10 (2010): 11–16. 3rd International Symposium on Shape Memory Materials for Smart Systems.
321. Shishkovsky, I. V., et al. “Porous Titanium and Nitinol Implants Synthesized by SHS/SLS: Microstructural and Histomorphological Analysis of Tissue Reactions.” *International Journal of Self-Propagating High-Temperature Synthesis*, vol. 19, no. 2, 2010, pp. 157–67.
322. Tosun, Gul, et al. “A Study on Microstructure and Porosity of NiTi Alloy Implants Produced by SHS.” *Journal of Alloys and Compounds*, vol. 487, 2009, pp. 605–11.
323. Zanotti, C., et al. “Porous Ni-Ti Ignition and Combustion Synthesis.” *Intermetallics*, vol. 15, 2007, pp. 404–12.
324. Li, Bing-Yun, et al. “A Recent Development in Producing Porous Ni-Ti Shape Memory Alloys.” *Intermetallics*, vol. 8, 2000, pp. 881–84.
325. Xinghong, Zhang, et al. “Self-Propagating High Temperature Combustion Synthesis of TiC/TiB2 Ceramic-Matrix Composites.” *Composites Science and Technology*, vol. 62, 2002, pp. 2037–41.
326. Bram, M. et al. “Powder Metallurgical Fabrication Processes for NiTi Shape Memory Alloy Parts.” *Materials Science and Engineering* A337 (2002): 254–263.
327. McNeese, Matthew D., Dimitris C. Lagoudas, and Thomas C. Pollock. “Processing of TiNi from Elemental Powders by Hot Isostatic Pressing.” *Materials Science and Engineering* A280 (2000): 334–348.
328. Zhang, Y. P. et al. “High Porosity and Large Pore Size Shape Memory Alloys Fabricated by Using Pore-Foaming Agent (NH_4HCO_3) and Capsule-Free Hot Isostatic Pressing.” *Journal of Materials Processing Technology* 192-193 (2007): 439–442.
329. Schüller, E. et al. “Hot Isostatic Pressing (HIP) of Elemental Powder Mixtures and Prealloyed Powder for NiTi Shape Memory Parts.” *Advanced Engineering Materials* 5.12 (2003): 918–924.
330. Farvizi, M. et al. “Microstructural Characterization of HIP Consolidated NiTi-Nao Al2O3 Composites.” *Journal of Alloys and Compounds* 606 (2014): 21–26.
331. Yuan, B. et al. “The Effect of Porosity on Phase Transformation Behavior of Porous Ti-50.8 at.% Ni Shape Memory Alloys Prepared by Capsule-Free Hot Isostatic Pressing.” *Materials Science and Engineering A* 438-440 (2006): 585–588.
332. Wu, Shuilin et al. “Pore Formation Mechanism and Characterization of Porous NiTi Shape Memory Alloys Synthesized by Capsule-Free Hot Isostatic Pressing.” *Acta Materialia* 55 (2007): 3437–3451.
333. Yuan, B., C. Y. Chung, and M. Zhu. “Microstructure and Martensitic Transformation Behavior of Porous NiTi Shape Memory Alloy Prepared by Hot Isostatic Pressing Processing.” *Materials Science and Engineering A* 382 (2004): 181–187.

334. Wu, S. L. et al. “Phase Transformation Behavior of Porous NiTi Alloys Fabricated by Capsule-Free Hot Isostatic Pressing.” *Journal of Alloys and Compounds* 449 (2008): 139–143.
335. Zhao, Ying et al. “Compression Behavior of Porous NiTi Shape Memory Alloy.” *Acta Materialia* 53 (2005): 337–343.
336. Olevsky, Eugene A., and Ludo Froyen. “Impact of Thermal Diffusion on Densification During SPS.” *Journal of the American Ceramic Society* 92.S1 (2009): S122–S132.
337. Omori, Mamoru. “Sintering, Consolidation, Reaction and Crystal Growth by the Spark Plasma System (SPS).” *Materials Science and Engineering A*287 (2000): 183–188.
338. Grasso, Salvatore, et al. “Highly Transparent α-Alumina Obtained by Low Cost High Pressure SPS.” *Ceramics International*, vol. 39, 2013, pp. 3243–48.
339. Angerer, P., et al. “Spark-Plasma-Sintering (SPS) of Nanostructured Titanium Carbonitride Powders.” *Journal of the European Ceramic Society*, vol. 25, 2005, pp. 1919–27.
340. Langer, Jochen, et al. “A Comparison Between FAST and SPS Apparatuses Based on the Sintering of Oxide Ceramics.” *International Journal of Applied Ceramic Technology*, vol. 8, no. 6, 2011, pp. 1459–67.
341. Chen, X. J., et al. “Overcoming the Effect of Contaminant in Solid Oxide Fuel Cell (SOFC) Electrolyte: Spark Plasma Sintering (SPS) of 0.5 Wt.% Silica-Doped Yttria-Stabilized Zirconia (YSZ).” *Materials Science and Engineering A*, vol. 374, 2004, pp. 64–71.
342. Su, Xinlu. “Optical Properties of SPS-Ed Y- and (Dy,Y)-α-Sialon Ceramics.” *Journal of Materials Science*, vol. 39, 2004, pp. 6257–62.
343. Drouet, C., et al. “Bioceramics: Spark Plasma Sintering (SPS) of Calcium Phosphates.” *Advances in Science and Technology*, vol. 49, 2006, pp. 45–50.
344. Pei, P., et al. “Improving Hydrogen Storage Properties of Laves Phase Related BCC Solid Solution Alloy by SPS Preparation Method.” *International Journal of Hydrogen Energy*, vol. 34, 2009, pp. 8597–602.
345. Bordeneuve, Hélène, et al. “Structure and Electrical Properties of Single-Phase Cobalt Manganese Oxide Spinels Mn3-XCoxO4 Sintered Classically and by Spark Plasma Sintering (SPS).” *Journal of Solid State Chemistry*, vol. 182, 2009, pp. 396–401.
346. Omori, Mamoru. “Basic Research and Industrial Production Using the Spark Plasma System (SPS).” *Advances in Microwave and Radio Frequency Processing*, edited by M. Willert-Porada, Springer, 2001, pp. 745–54.
347. Tokita, Masao. “Large-Size WC/Co Functionally Graded Materials Fabricated by Spark Plasma Sintering (SPS) Method.” *Materials Science Forum*, vol. 423–425, 2003, pp. 39–44.
348. Yu, P., and M. Qian. “Metal Injection Moulding of In-Situ Formed A1N Hollow Sphere Reinforced Al Matrix Syntactic Foam Parts.” *Materials Chemistry and Physics* 137 (2012): 435–438.
349. Ye, Hezhou, Xing Yang Liu, and Hanping Hong. “Fabrication of Metal Matrix Composites by Metal Injection Molding - A Review.” *Journal of Materials Processing Technology* 200 (2008): 12–24.
350. Guoxin, Hu et al. “Fabrication of High Porous NiTi Shape Memory Alloy by Metal Injection Molding.” *Journal of Materials Processing Technology*206 (2008): 395–399.

351. Weise, Jörg et al. “Syntactic Iron Foams with Integrated Microglass Bubbles Produced by Means of Metal Powder Injection Moulding.” *Advanced Engineering Materials* 12.7 (2010): 604–608.
352. Bram, M. et al. “Reproducibility Study of NiTi Parts Made by Metal Injection Molding.” *Journal of Materials Engineering and Performance* 21.12 (2012): 2701–2712.
353. Köhl, Manuel, et al. “Powder Metallurgical Near-Net-Shape Fabrication of Porous NiTi Shape Memory Alloys for Use as Long-Term Implants by the Combination of the Metal Injection Molding Process with the Space-Holder Technique.” *Advanced Engineering Materials*, vol. 11, no. 12, 2009, pp. 959–68.
354. Arnaboldi, S. et al. “Functional Characterization of Shape Memory CuZnAl Open-Cell Foams by Molten Metal Infiltration.” *Journal of Materials Engineering and Performance* 20.4-5 (2011): 544–550.
355. Aust, Eckhard, et al. “Advanced TiAl6Nb7 Bone Screw Implant Fabricated by Metal Injection Moulding.” *Advanced Engineering Materials*, vol. 8, no. 5, 2006, pp. 365–70.
356. Elahinia, Mohammad H. et al. “Manufacturing and Processing of NiTi Implants: A Review.” *Progress in Materials Science* 57.5 (2012): 911–946.
357. Orrù, Roberto et al. “Consolidation/Synthesis of Materials by Electric Current Activated/Assisted Sintering.” *Materials Science and Engineering R* 63 (2009): 127–287.
358. Kelly, James P., and Olivia A. Graeve. “Spark Plasma Sintering as an Approach to Manufacture Bulk Materials: Feasibility and Cost Savings.” *JOM* 67.1 (2015): 29–33.
359. Basu, Bikramjit. “Development of Nanocrystalline Wear-Resistant Y-TZP Ceramic.” *Journal of the American Ceramic Society*, vol. 87, no. 9, 2004, pp. 1771–74.
360. Yue, M., et al. “Chemical Stability and Microstructure of Nd-Fe-B Magnet Prepared by Spark Plasma Sintering.” *Journal of Magnetism and Magnetic Materials*, vol. 271, 2004, pp. 364–68.
361. Han, Y. H., et al. “Eutectic Al2O3-GdAlO3 Composite Consolidated by Combined Rapid Quenching and Spark Plasma Sintering Technique.” *British Ceramic Transactions*, vol. 103, no. 5, 2004, pp. 219–22.
362. Kwon, Y. S., et al. “Microstructure Changes in TiB2-Cu Nanocomposite Under Sintering.” *Journal of Materials Science*, vol. 39, 2004, pp. 5325–31.
363. Zhou, Longjie, et al. “Preparation and Properties of Lead Zirconate Stannate Titanate Sintered by Spark Plasma Sintering.” *Journal of the American Ceramic Society*, vol. 87, no. 4, 2004, pp. 606–11.
364. Shen, Zhijian, et al. “Formidable Increase in the Superplasticity of Ceramics in the Presence of an Electric Field.” *Advanced Materials*, vol. 15, no. 12, 2003, pp. 1006–09.
365. Yue, Ming, et al. “New Kind of NdFeB Magnet Prepared by Spark Plasma Sintering.” *IEEE Transactions on Magnetics*, vol. 39, no. 6, 2003, pp. 3551–53.
366. Zhao, X. B., et al. “Synthesis of Nanocomposites with Improved Thermoelectric Properties.” *Journal of Electronic Materials*, vol. 38, no. 7, 2009, pp. 1017–24.
367. Noudem, J. G., et al. “Thermoelectric Ca3Co4O9 Ceramics Consolidated by Spark Plasma Sintering.” *Journal of Electroceramics*, vol. 22, 2009, pp. 91–97.

368. Amezawa, Koji, et al. “Electrical and Mechanical Properties of Sr-Doped LaPO4 Prepared by Spark Plasma Sintering.” *Journal of the Electrochemical Society*, vol. 152, no. 6, 2005, pp. A1060–67.
369. Morita, Koji, et al. “Spark-Plasma-Sintering Condition Optimization for Producing Transparent MgAl2O4 Spinel Polycrystal.” *Journal of the American Ceramic Society*, vol. 92, no. 6, 2009, pp. 1208–16.
370. Nygren, Mats, and Zhijian Shen. “Novel Assemblies via Spark Plasma Sintering.” *Silicates Industriels*, vol. 69, no. 7–8, 2004, pp. 211–18.
371. Risbud, Subhash H., and Joanna R. Groza. “Clean Grain Boundaries in Aluminium Nitride Ceramics Densified without Additives by a Plasma-Activated Sintering Process.” *Philosophical Magazine*, vol. 69, no. 3, 1994, pp. 525–33.
372. Guillon, Olivier et al. “Field-Assisted Sintering Technology/Spark Plasma Sintering: Mechanisms, Materials, and Technology Developments.” *Advanced Engineering Materials* 16.7 (2014): 830–849.
373. Anselmi-Tamburini, U. et al. “Field Assisted Sintering Mechanisms.” *Sintering: Mechanisms of Convention Nanodensification and Field Assisted Processes*. Vol. 35. Springer, 2013.
374. Munir, Zuhair A., Dat V. Quach, and Manshi Ohyanagi. “Electric Current Activation of Sintering: A Review of the Pulsed Electric Current Sintering Process.” *Journal of the American Ceramic Society* 94.1 (2011): 1–19.
375. Grasso, Salvatore, et al. “Electric Current Activated/Assisted Sintering (ECAS): A Review of Patents 1906-2008.” *Science and Technology of Advanced Materials*, vol. 10, 2009.
376. Zou, Xuenong, et al. “Bone Ingrowth Characteristics of Porous Tantalum and Carbon Fiber Interbody Devices: An Experimental Study in Pigs.” *The Spine Journal*, vol. 4, 2004, pp. 99–105.
377. Lifland, M. I., and K. Okazaki. “Properties of Titanium Dental Implants Produced by Electro-Discharge Compaction.” *Clinical Materials*, vol. 17, 1994, pp. 203–09.
378. Wada, Masami, and Fumitoshi Yamashita. “New Method of Making Nd-Fe-Co-B Full Dense Magnet.” *IEEE Transactions on Magnetics*, vol. 26, no. 5, 1990, pp. 2601–03.
379. Yoo, Sang H., et al. *Apparatus for Bonding a Particle Material to Near Theoretical Density*. U.S. Patent No. 5,989,487, 1999.
380. McWilliams, Brandon, et al. “The Modeling of Electric-Current-Assisted Sintering to Produce Bulk Nanocrystalline Tungsten.” *JOM*, vol. 58, no. 4, 2006, pp. 67–71.
381. Hoyt, Samuel L. *Hard Metal Composition and Method of Making the Same*. U.S. Patent No. 1,843,768.
382. Kiyoshi, Inoue. *Electric-Discharge Sintering*. U.S. Patent No. 3,241,956, 1966.
383. Kiyoshi, Inoue. *Apparatus for Electrically Sintering Discrete Bodies*. U.S. Patent No. 3,250,892, 1966.
384. Kiyoshi, Inoue. *Method of Electrically Sintering Discrete Bodies*. U.S. Patent No. 3,340,052, 1967.
385. Tokita, Masao. *Multi-Head Pulse Energization Sintering System*. JP Patent No. 2001262202, 2001.

386. Tokita, Masao. *Method and System for Automatic Electrical Sintering*. U.S. Patent No. 6,383,446, 2002.
387. Nakagawa, Katsuyuki, and Masao Tokita. *Rotary Table Type Electric Heating/Pressure Sintering Apparatus*. JP Patent No. 2002206102, 2002.
388. Ishida, Shinichi, et al. *Shuttle Type Discharge Plasma Sintering System*. JP Patent No. 2004244662, 2004.
389. Kaneuchi, Atsuki, and Hiroaki Morita. *Sintered Compact, Nozzle, and Its Manufacturing Method*. JP Patent No. 2004168632, 2004.
390. Okano, Michiharu, and Hiroshi Izui. *Method and Apparatus for Manufacturing Bio-Compatible Concentric Circular Functionally Gradient Material*. WO Patent No. 2007069623, 2007.
391. Ikeda, Hiroshi. *Die for Molding Optical Element, Its Manufacturing Method and Optical Element*. JP Patent No. 2005272254, 2005.
392. Kamitsuma, Yasuo, et al. *Method of Manufacturing Sintered Aluminum Alloy Parts*. U.S. Patent No. 5,346,667, 1994.
393. Ward, Melvyn. *Method and Apparatus for Producing a Friction Element for a Disc Brake*. U.S. Patent No. 4,456,578, 1984.
394. Holland, Troy B., and Amiya Muhkerjee. "Spark Plasma Sintering." *Combustion Synthesis: Novel Routes to Novel Materials*. Bentham Science Publishers, 2010.
395. Holland, Troy B. *Bottom-Up Manufacturing of Advanced Materials: Sintering Mechanisms and Processes in High-Performance Material Systems*. 2014 AVS Rocky Mountain Chapter Symposium and Vendor Exhibit, Westminster, Colorado.
396. Gubicza, J., et al. "Microstructure and Mechanical Behavior of Ultrafine-Grained Ni Processed by Different Powder Metallurgy Methods." *Journal of Materials Research*, vol. 24, no. 1, 2009, pp. 217–26.
397. Ritasalo, R., et al. "Spark Plasma Sintering of Submicron-Sized Cu-Powder-Influence of Processing Parameters and Powder Oxidization on Microstructure and Mechanical Properties." *Materials Science and Engineering A*, vol. 527, 2010, pp. 2733–37.
398. Mizuguchi, Takashi, et al. "Transmission Electron Microscopy Characterization of Spark Plasma Sintered ZrB2 Ceramic." *Ceramics International*, vol. 36, 2010, pp. 943–46.
399. Kanamori, Kenji, et al. "Spark Plasma Sintering of Sol-Gel Derived Amorphous ZrW2O8 Nanopowder." *Journal of the American Ceramic Society*, vol. 92, no. 1, 2009, pp. 32–35.
400. Guo, Shu-Qi. "Spark Plasma Sintering of Zirconium Diborides." *Journal of the American Ceramic Society*, vol. 91, no. 9, 2008, pp. 2848–55.
401. Groza, Joanna R., and Vladimir Kodash. *Methods for Production of FGM Net Shaped Body for Various Applications*. U.S. Patent No. 7,393,559, 2008.
402. Fujii, Yasuyoshi, and Masao Tokita. *Method for Producing Functionally Gradient Material and Piston Produced by Using the Same.* JP Patent No. 2002047504, 2009.
403. Zhang, L., et al. *Densification Method for Gradient Material with Continuously Varying Constituent*. CN Patent No. 1544187, 2006.
404. Kiyoshi, Inoue. *Method of and Apparatus for Controlling the Porosity of Electrically Sintered Bodies*. U.S. Patent No. 3,317,705, 1967.

405. Eriksson, Mirva, et al. “Low Temperature Consolidated Lead-Free Ferroelectric Niobate Ceramics with Improved Electrical Properties.” *Journal of Materials Research*, vol. 25, no. 2, 2010, pp. 240–47.
406. Le Gallet, S., et al. “Spark Plasma Sintering of Iodine-Bearing Apatite.” *Journal of Nuclear Materials*, vol. 400, 2010, pp. 251–56.
407. Campayo, L., et al. “Spark Plasma Sintering of Lead Phosphovanadate Pb3(VO4)1.6(PO4)0.4.” *Journal of the European Ceramic Society*, vol. 29, 2009, pp. 1477–84.
408. Kan, Yanmei, et al. “Spark Plasma Sintering of Bismuth Titanate Ceramics.” *Journal of the American Ceramic Society*, vol. 88, no. 6, 2005, pp. 1631–33.
409. Hirai, Toshio, et al. *Calcium Phosphate-Titanium-Based Composite Material for Biomaterial and Method of Manufacturing the Same*. JP Patent No. 2001259017, 2001.
410. Okamoto, Masaya, et al. “Phase Transition and Electrical Conductivity of Scandia-Stabilized Zirconia Prepared by Spark Plasma Sintering Process.” *Solid State Ionics*, vol. 176, 2005, pp. 675–80.
411. Bassano, A., et al. “Particle Size and Morphology Control of Perovskite Oxide Nanopowders for Nanostructured Materials.” *Integrated Ferroelectrics*, vol. 109, 2009, pp. 153–69.
412. Anselmi-Tamburini, Umberto, et al. *Preparation of Dense Nanostructured Functionally Oxide Materials with Fine Crystallite Size by Field Activation Sintering*. U.S. Patent No. 7,601,403, 2009.
413. Tokita, Masao, et al. *Nanoprecision Sintering System*. U.S. Patent No. 7,547,204, 2009.
414. Guo, Shu-Qi. “Densification of ZrB2-Based Composites and Their Mechanical and Physical Properties: A Review.” *Journal of the European Ceramic Society*, vol. 29, 2009, pp. 995–1011.
415. Wang, Cao, and Zhe Zhao. “Transparent MgAl2O4 Ceramic Produced by Spark Plasma Sintering.” *Scripta Materialia*, vol. 61, 2009, pp. 193–96.
416. Yoshida, Hidehiro, et al. “Densification of Nanocrystalline Yttria by Low Temperature Spark Plasma Sintering.” *Journal of the American Ceramic Society*, vol. 91, no. 5, 2008, pp. 1707–10.
417. Graeve, Olivia A. et al. “Spark Plasma Sintering of Fe-Based Structural Amorphous Metals (SAM) with Y2O3 Nanoparticle Additions.” *Materials Letters*62 (2008): 2988–2991.
418. Mizushima, Takao, et al. *Sinter and Casting Comprising Fe-Based High-Hardness Glassy Alloy*. U.S. Patent No. 6,086,651, 2000.
419. Yoshida, Shoji, et al. *Low-Loss Magnetic Powder Core, and Switching Power Supply, Active Filter, Filter, and Amplifying Device Using the Same*. U.S. Patent No. 6,897,718, 2005.
420. Okazaki, Kenji. *Method of Sintering Powder*. U.S. Patent No. 4,929,415, 1990.
421. Hotta, Mikinori, and Takashi Goto. “Densification and Microstructure of Al2O3-CBN Composites Prepared by Spark Plasma Sintering.” *Journal of the Ceramic Society of Japan*, vol. 116, no. 6, 2008, pp. 744–48.
422. Suganuma, Motohiro, and Yasunori Kitagawa. “Pulsed Electric Current Sintering of Silicon Nitride.” *Journal of the American Ceramic Society*, vol. 86, no. 3, 2003, pp. 387–94.

423. Zhou, You et al. “Effects of Heating Rate and Particle Size on Pulse Electric Current Sintering of Alumina.” *Scripta Materialia*48 (2003): 1631–1635.
424. Clark, David E., and Willard H. Sutton. “Microwave Processing of Materials.” *Annual Review of Materials Science*, vol. 26, 1996, pp. 299–331.
425. Stanciu, L. A., et al. “Effects of Heating Rate on Densification and Grain Growth during Field-Assisted Sintering of α-Al2O3 and MoSi2 Powders.” *Metallurgical and Materials Transactions A*, vol. 32, 2001, pp. 2633–38.
426. Zhao, Jinfeng, et al. “Sparking Plasma Sintering of Nanometric Tungsten Carbide.” *International Journal of Refractory Metals & Hard Materials*, vol. 27, 2009, pp. 130–39.
427. Grasso, Salvatore, et al. “Pressure Effects on Temperature Distribution during Spark Plasma Sintering with Graphite Sample.” *Materials Transactions*, vol. 50, no. 8, 2009, pp. 2111–14.
428. Zavaliangos, Antonios, et al. “Temperature Evolution during Field Activated Sintering.” *Materials Science and Engineering A*, vol. 379, 2004, pp. 218–28.
429. Vanmeensel, K., et al. “Modelling of the Temperature Distribution during Field Assisted Sintering.” *Acta Materialia*, vol. 53, 2005, pp. 4379–88.
430. Frei, James M., et al. “Current Effects on Neck Growth in the Sintering of Copper Spheres to Copper Plates by the Pulsed Electric Current Method.” *Journal of Applied Physics*, vol. 101, 2007, pp. 1–8.
431. Yanagisawa, O., et al. “Observation of Particle Behavior in Copper Powder Compact during Pulsed Electric Discharge.” *Materials Science and Engineering A*, vol. 350, 2003, pp. 184–89.
432. Song, Xiaoyan, et al. “Neck Formation and Self-Adjusting Mechanism of Neck Growth of Conducting Powders in Spark Plasma Sintering.” *Journal of the American Ceramic Society*, vol. 89, no. 2, 2006, pp. 494–500.
433. Tokita, M. “Mechanism of Spark Plasma Sintering.” *Proceeding of NEDO International Symposium on Functionally Graded Materials*, vol. 22, 1999, pp. 1–13.
434. Tokita, Masao. “Trends in Advanced Spark Plasma Sintering Systems and Technology.” *Journal of the Society of Powder Technology*, vol. 30, no. 11, 1993, pp. 790–804.
435. Misawa, T., et al. “Influence of Internal Pulsed Current on the Sintering Behavior of Pulsed Current Sintering Process.” *Materials Science Forum*, vol. 638–642, 2010, pp. 2109–14.
436. Hulbert, Dustin M., et al. “The Absence of Plasma in ‘Spark Plasma Sintering.’” *Journal of Applied Physics*, vol. 104, 2008, pp. 1–7.
437. Misawa, Tatsuya, et al. “Observation of Internal Pulsed Current Flow Through the ZnO Specimen in the Spark Plasma Sintering Method.” *Journal of Materials Science*, vol. 44, 2009, pp. 1641–51.
438. Hulbert, Dustin M., et al. “A Discussion on the Absence of Plasma in Spark Plasma Sintering.” *Scripta Materialia*, vol. 60, 2009, pp. 835–38.
439. Garay, J. E., U. Anselmi-Tamburini, and Z. A. Munir. “Enhanced Growth of Intermetallic Phases in the Ni-Ti System by Current Effects.” *Acta Materialia* 51 (2003): 4487–4495.

440. Chen, W. et al. “Fundamental Investigations on the Spark Plasma Sintering/Synthesis Process I. Effect of DC Pulsing on Reactivity.” *Materials Science and Engineering A* 394 (2005): 132–138.
441. Anselmi-Tamburini, U. et al. “Fundamental Investigations on the Spark Plasma Sintering/Synthesis Process II. Modeling of Current and Temperature Distributions.” *Materials Science and Engineering A* 394 (2005): 139–148.
442. Jeong, Jin-Wook, Joo-Hwan Han, and Doh-Yeon Kim. “Effect of Electric Field on Migration of Grain Boundaries in Alumina.” *Journal of the American Ceramic Society* 83.4 (2000): 915–918.
443. Cologna, Marco, et al. “Flash Sintering of Nanograin Zirconia in < 5 s at 850°C.” *Journal of the American Ceramic Society*, vol. 93, no. 11, 2010, pp. 3556–59.
444. Yang, Di, and Hans Conrad. “Enhanced Sintering Rate and Finer Grain Size in Yttria-Stablized Zirconia (3Y-TZP) with Combined DC Electric Field and Increased Heating Rate.” *Materials Science and Engineering A*, vol. 528, 2011, pp. 1221–25.
445. Bertolino, N., et al. “Electromigration Effects in Al-Au Multilayers.” *Scripta Materialia*, vol. 44, 2001, pp. 737–42.
446. Asoka-Kumar, P., et al. “Increased Elemental Specificity of Positron Annihilation Spectra.” *Physical Review Letters*, vol. 77, no. 10, 1996, pp. 2097–100.
447. Garay, Javier E., et al. “Electric Current Enhanced Defect Mobility in Ni3Ti Intermetallics.” *Applied Physics Letters*, vol. 85, no. 4, 2004, pp. 573–75.
448. Conrad, Hans. “Effects of Electric Current on Solid State Phase Transformations in Metals.” *Materials Science and Engineering A*, vol. 287, 2000, pp. 227–37.
449. Asoka-Kumar, P., et al. “Detection of Current-Induced Vacancies in Thin Aluminum-Copper Lines Using Positrons.” *Applied Physics Letters*, vol. 68, no. 3, 1996, pp. 406–08.
450. Jayaseelan, D. Doni, et al. “Differential Sintering by Improper Selection of Sintering Parameters during Pulse Electric Current Sintering.” *Journal of the American Ceramic Society*, vol. 87, no. 1, 2004, pp. 159–61.
451. Sun, Jingjing, et al. “Synthesis of Dense NiZn Ferrites by Spark Plasma Sintering.” *Ceramics International*, vol. 28, 2002, pp. 855–58.
452. Hansen, James D. “Combined-Stage Sintering Model.” *Journal of the American Ceramic Society*, vol. 75, no. 5, 1992, pp. 1129–1135.
453. Su, Hunghai, and D. Lynn Johnson. “Master Sintering Curve: A Practical Approach to Sintering.” *Journal of American the Ceramic Society* 79.12 (1996): 3211–3217.
454. Park, S. J. et al. “Master Sintering Curve for Densification Derived from a Constitutive Equation with Consideration of Grain Growth: Application to Tungsten Heavy Alloys.” *Metallurgical and Materials Transactions A*39A (2008): 2941–2948.
455. Gupta, T. K. “Possible Correlation Between Density and Grain Size During Sintering.” *Journal of the American Ceramic Society*, vol. 55, no. 5, 1972, pp. 276–77.
456. Rahaman, Mohamed N., et al. “Effect of Green Density on Densification and Creep During Sintering.” *Journal of the American Ceramic Society*, vol. 74, no. 3, 1991, pp. 514–19.
457. Robertson, I. M., and G. B. Schaffer. “Review of Densification of Titanium Based Powder Systems in Press and Sinter Processing.” *Powder Metallurgy*, vol. 53, no. 2, 2010, pp. 146–162.

458. Blaine, D. C., et al. “Master Sintering Curve for a Two-Phase Material.” *Proceedings of the 4th International Conference on Science, Technology and Applications of Sintering*, 2005, pp. 264–67.
459. Teng, Mao-Hua, et al. “A Computer Program of Master Sintering Curve Model to Accurately Predict Sintering Results.” *Western Pacific Earth Sciences*, vol. 2, no. 2, 2002, pp. 171–80.
460. Kutty, T. R. G., et al. “Determination of Activation Energy of Sintering of ThO2-U3O8 Pellets Using the Master Sintering Curve Approach.” *Science of Sintering*, vol. 35, 2003, pp. 125–32.
461. Shao, W. Q., et al. “Prediction of Densification and Microstructure Evolution for α-Al2O3 During Pressureless Sintering at Low Heating Rates Based on the Master Sintering Curve Theory.” *Science of Sintering*, vol. 40, 2008, pp. 251–61.
462. Blaine, Deborah C., et al. “Linearization of Master Sintering Curve.” *Journal of the American Ceramic Society*, vol. 92, no. 7, 2009, pp. 1403–1409.
463. Ouyang, C. X. et al. “Master Sintering Curve of Nanocomposite WC-MgO Powder Compacts.” *Journal of Alloys and Compounds*518 (2012): 27–31.
464. Blaine, Deborah C. et al. “Application of Work-of-Sintering Concepts in Powder Metals.” *Metallurgical and Materials Transactions A* 37A (2006): 2827–2835.
465. Jung, Im Doo, et al. “Two-Phase Master Sintering Curve for 17-4 PH Stainless Steel.” *Metallurgical and Materials Transactions A*, vol. 47, 2016, pp. 5548–5556.
466. Kutty, T. R. G., et al. “Development of a Master Sintering Curve for ThO2.” *Journal of Nuclear Materials*, vol. 327, 2004, pp. 211–219.
467. Li, D., et al. “Construction and Validation of Master Sintering Curve for TiO2 for Pressureless Sintering.” *Advances in Applied Ceramics*, vol. 107, no. 1, 2008, pp. 52–56.
468. Ewsuk, Kevin G., et al. “Analysis of Nanocrystalline and Microcrystalline ZnO Sintering Using Master Sintering Curves.” *Journal of the American Ceramic Society*, vol. 89, no. 6, 2006, pp. 2003–2009.
469. Li, Da, et al. “Densification Evolution of TiO2 Ceramics During Sintering Based on the Master Sintering Curve Theory.” *Materials Letters*, vol. 62, 2008, pp. 849–51.
470. Caruso, Ricardo, et al. “Densification Kinetics of ZrO2-Based Ceramics Using a Master Sintering Curve.” *Journal of Alloys and Compounds*, vol. 495, 2010, pp. 570–73.
471. Aminzare, M., et al. “Sintering Behavior of Nano Alumina Powder Shaped by Pressure Filtration.” *Ceramics International*, vol. 37, 2011, pp. 9–14.
472. Kinemuchi, Yoshiaki, and Koji Watari. “Dilatometer Analysis of Sintering Behavior of Nano-CeO2 Particles.” *Journal of the European Ceramic Society*, vol. 28, 2008, pp. 2019–24.
473. Song, Xiaochao, et al. “Two-Stage Master Sintering Curve Approach to Sintering Kinetics of Undoped and Al2O3-Doped 8 Mol% Yttria-Stabilized Cubic Zirconia.” *Journal of the American Ceramic Society*, vol. 94, no. 4, 2011, pp. 1053–59.
474. Tatami, J., et al. “Control of Shrinkage During Sintering of Alumina Ceramics Based on Master Sintering Curve Theory.” *Key Engineering Materials*, vol. 317-318, 2006, pp. 11–14.
475. Aminzare, M., et al. “Sintering Behavior of an Ultrafine Alumina Powder Shaped by Pressure Filtration and Dry Pressing.” *Materials Science and Engineering A*, vol. 527, 2010, pp. 3807–12.

476. Nikolić, M. V., et al. “Application of the Master Sintering Curve Theory to Non-Isothermal Sintering of BaTiO3 Ceramics.” *Materials Science Forum*, vol. 494, 2005, pp. 417–22.
477. Szepesi, Christopher J. *High Yield Synthesis and Processing of Nanoscale YTZP Ceramics*. The Pennsylvania State University, 2010.
478. An, K., and M. K. Han. “Microstructural Evolution Based on the Pressure-Assisted Master Sintering Surface.” *Materials Science and Engineering A*, vol. 391, 2005, pp. 66–70.
479. An, K., and D. L. Johnson. “The Pressure-Assisted Master Sintering Surface.” *Journal of Materials Science*, vol. 37, 2002, pp. 4555–4559.
480. Guillon, Olivier, and Jochen Langer. “Master Sintering Curve Applied to the Field-Assisted Sintering Technique.” *Journal of Materials Science* 45 (2010): 5191–5195.
481. Enneti, Ravi K. et al. “Development of Master Sintering Curve for Field-Assisted Sintering of HfB2-20SiC.” *Ceramics International* 38 (2012): 4369–4372.
482. Cramer, Corson L., et al. “Continuous Functionally Graded Material to Improve the Thermoelectric Properties of ZnO.” *Journal of the European Ceramic Society*, vol. 37, 2017, pp. 4693–4700.
483. Chen, Zhichao, et al. “Master Sintering Curves for UO2 and UO2-SiC Composite Processed by Spark Plasma Sintering.” *Journal of Nuclear Materials*, vol. 454, 2014, pp. 427–33.
484. Pouchly, V., et al. “Master Sintering Surface - A Practical Approach to Its Construction and Utilization for Spark Plasma Sintering Prediction.” *Science of Sintering*, vol. 44, 2012, pp. 169–75.
485. Colasuonno, Paul S. *Method for Creating Functionally Graded Materials with Spark Plasma Sintering and a Continuous Machine for Future Scalability*. Colorado State University, 2017.
486. Xiong, Y., et al. “Microstructure and IR Transmittance of Spark Plasma Sintering Translucent A1N Ceramics with CaF2 Additive.” *Materials Science and Engineering B*, vol. 123, 2005, pp. 57–62.
487. Zhu, L. H., et al. “Preparation of Nanocrystalline WC-10Co-0.8VC by Spark Plasma Sintering.” *Journal of Materials Science Letters*, vol. 22, 2003, pp. 1631–33.
488. Mazaheri, Mehdi, et al. “Master Sintering Curves of a NanoScale 3Y-TZP Powder Compacts.” *Ceramics International*, vol. 35, 2009, pp. 547–54.
489. Blaine, Deborah C., et al. “Master Sintering Curve Concepts as Applied to the Sintering of Molybdenum.” *Metallurgical and Materials Transactions A*, vol. 37, 2006, pp. 715–720.
490. Kiani, S., et al. “A New Scheme of Finding the Master Sintering Curve.” *Journal of the American Ceramic Society*, vol. 89, no. 11, 2006, pp. 3393–3396.
491. Rahaman, Mohamed N. *Ceramic Processing and Sintering*. 1st ed., CRC Press, 2003.
492. *Silica gel Type II, 3.5 mm bead size, Suitable for desiccation*. Sigma-Aldrich, www.sigmaaldrich.com/catalog/product/sial/s7500?lang=en&region=US. Accessed 19 September 2018.
493. Castrodeza, E. M. et al. “Processing of Shape Memory CuZnAl Open-Cell Foam by Molten Metal Infiltration.” *Journal of Materials Engineering and Performance* 18.5-6 (2009): 484–489.
494. Biffi, C. A., D. Colombo, and A. Tuissi. “Laser Beam Welding of CuZn Open-Cell Foams.” *Optics and Lasers in Engineering* 62 (2014): 112–118.

495. Tuissi, Ausonio, Paola Bassani, and Carlo Alberto Biffi. “CuZnAl Shape Memory Alloys Foams.” *Advances in Science and Technology* 78 (2013): 31–39.
496. Bertolino, G. et al. “Mechanical Properties of Martensitic Cu-Zn-Al Foams in the Pseudoelastic Regime.” *Materials Letters* 64 (2010): 1448–1450.
497. Li, Hua, Bin Yuan, and Yan Gao. “Processing of CuAlMn Shape Memory Foams with Open Spherical Pores by Silica-Gel Beads Infiltration Method.” *Metallurgical and Materials Transactions B* 47 (2016): 3168–3177.
498. ASTM E1097-12(2017), Standard Guide for Determination of Various Elements by Direct Current Plasma Atomic Emission Spectrometry, ASTM International, West Conshohocken, PA, 2017, www.astm.org.
499. Cullity, B. D. *Elements of X-Ray Diffraction*. Second Edition, Addison-Wesley Publishing Company, Inc., 1978.
500. ASTM F2004-05(2010), Standard Test Method for Transformation Temperature of Nickel-Titanium Alloys by Thermal Analysis, ASTM International, West Conshohocken, PA, 2010, www.astm.org.
501. ASTM E9-09(2018), Standard Test Methods of Compression Testing of Metallic Materials at Room Temperature, ASTM International, West Conshohocken, PA, 2018, www.astm.org.
502. ASTM E111-17, Standard Test Method for Young’s Modulus, Tangent Modulus, and Chord Modulus, ASTM International, West Conshohocken, PA, 2017, www.astm.org.
503. Giuntini, Diletta, et al. “Localized Overheating Phenomena and Optimization of Spark-Plasma Sintering Tooling Design.” *Materials*, vol. 6, 2013, pp. 2612–32.
504. Dunand, D. C. et al. “NiTi and NiTi-TiC Composites: Part IV. Neutron Diffraction Study of Twinning and Shape-Memory Recovery.” *Metallurgical and Materials Transactions A* 27A (1996): 2820–2836.
505. Harris, Daniel C. *Quantitative Chemical Analysis*. Fifth Edition, W. H. Freeman and Company, 1999.
506. Panigrahi, B. B., and M. M. Godkhindi. “Dilatometric Sintering Study of Ti-50Ni Elemental Powders.” *Intermetallics*, vol. 14, 2006, pp. 130–35.
507. Fu, Yongqing, and Christopher Shearwood. “Characterization of Nanocrystalline TiNi Powder.” *Scripta Materialia*, vol. 50, 2004, pp. 319–23.
508. Faulkner, M. G., et al. “Experimental Determination of Thermal and Electrical Properties of Ni-Ti Shape Memory Wires.” *Smart Materials and Structures*, vol. 9, no. 5, 2000, pp. 632–39.
509. P. Robinson, Properties of Wrought Coppers and Copper Alloys, Properties and Selection: Nonferrous Alloys and Special-Purpose Materials, Vol 2, ASM Handbook, ASM International, 1990, p 265–345.
510. Tukey, John W. *Exploratory Data Analysis*. Addison-Wesley Publishing Company, Inc., 1977

8. APPENDICES

8.1 ARCHIMEDES' PRINCIPLE DERIVATIONS

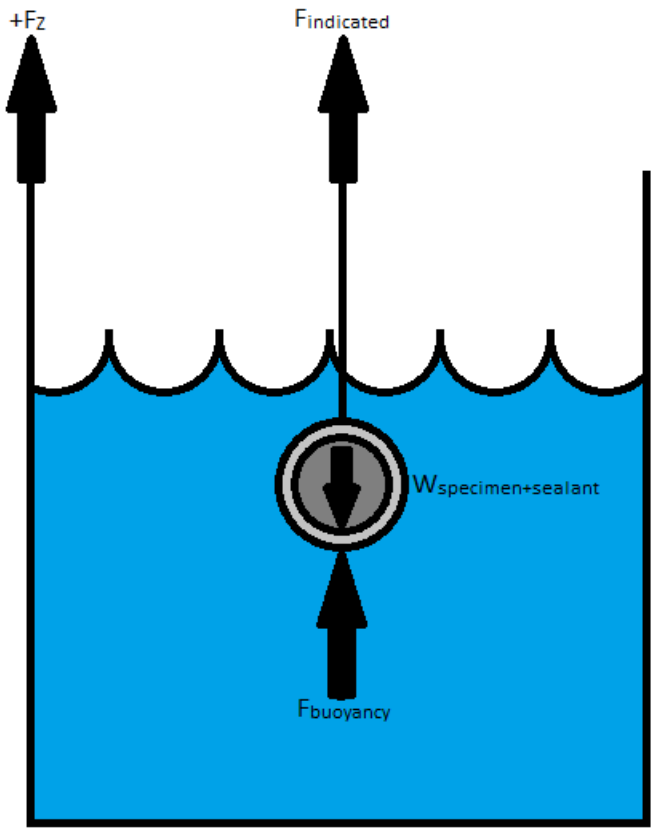

Figure 8.1. Diagram used to derive equations based on Archimedes' Principle to determine the density of both NiTi and NiTi+Cu specimens.

8.1.1 NiTi

$$\sum F_z : F_{indicated} = W_{specimen+sealant} - F_{Buoyancy}$$

$$m_{indicated}g = m_{s+s}g - \rho_{water}V_{water}g$$

$$m_{indicated}\cancel{g} = \cancel{g}(m_{s+s} - \rho_{water}V_{water})$$

$$m_{indicated} = m_{s+s} - \rho_{water}(V_{specimen} + V_{sealant})$$

$$\frac{m_{s+s} - m_{indicated}}{\rho_{water}} = V_{specimen} + V_{sealant}$$

$$\frac{m_{s+s} - m_{indicated}}{\rho_{water}} - V_{sealant} = \frac{m_{specimen}}{\rho_{specimen}}$$

$$\frac{m_{s+s} - m_{indicated} - \rho_{water} V_{sealant}}{\rho_{water} m_{specimen}} = \frac{1}{\rho_{specimen}}$$

$$\rho_{specimen} = \left(\frac{\rho_{water} m_{specimen}}{m_{s+s} - m_{indicated} - \rho_{water} V_{sealant}}\right)$$

$$where:\ V_{sealant} = \frac{m_{sealant}}{\rho_{sealant}} = \frac{m_{s+s} - m_{specimen}}{\rho_{sealant}}$$

8.1.2 NiTi+Cu

$$\sum F_z : F_{indicated} = W_{specimen+sealant} - F_{Buoyancy}$$

$$m_{indicated} g = m_{s+s} g - \rho_{water} V_{water} g$$

$$m_{indicated} \cancel{g} = \cancel{g}(m_{s+s} - \rho_{water} V_{water})$$

$$m_{indicated} = m_{s+s} - \rho_{water}\left(V_{specimen} + V_{sealant}\right)$$

$$\frac{m_{s+s} - m_{indicated}}{\rho_{water}} = V_{specimen} + V_{sealant}$$

$$V_{specimen} = \frac{m_{s+s} - m_{indicated}}{\rho_{water}} - V_{sealant}$$

$$V_{specimen} = \frac{m_{s+s} - m_{indicated}}{\rho_{water}} - \frac{m_{s+s} - m_{specimen}}{\rho_{sealant}}$$

$$\rho_{NiTi\ Matrix} = \frac{m_{specimen} - \left(N_{Cu\ spheres}\right)\left(m_{Cu\ sphere}\right)}{V_{specimen} - \left(N_{Cu\ spheres}\right)\left(V_{Cu\ sphere}\right)}$$

8.2 SUPPLEMENTAL SEM IMAGES OF NITI OPEN-CELL FOAMS

8.2.1 Post-Failure

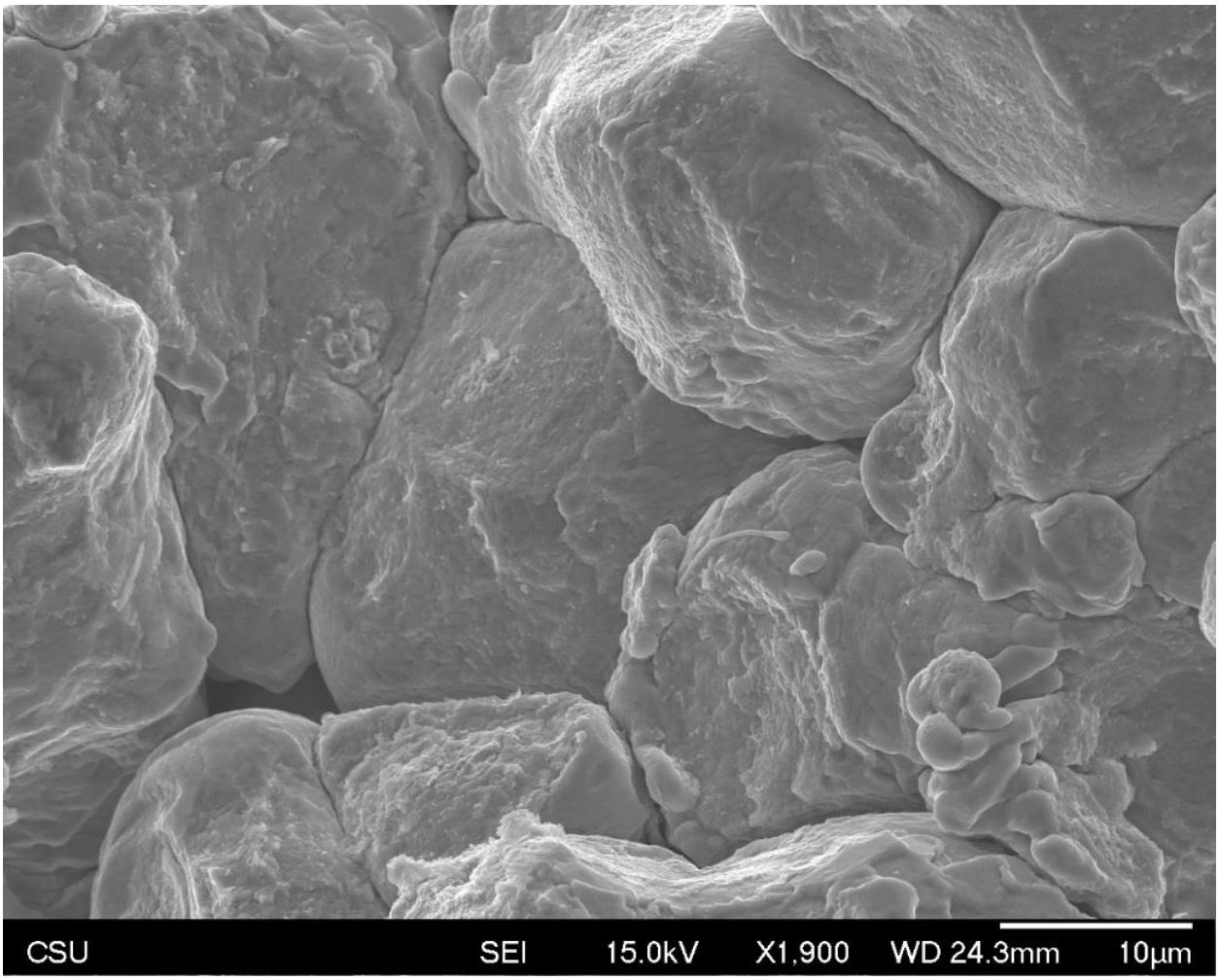

Figure 8.2. Scanning electron microscopy image from specimen pNiTi 32 of fracture surface showing high degree of sintering and inter-particle failure surface.

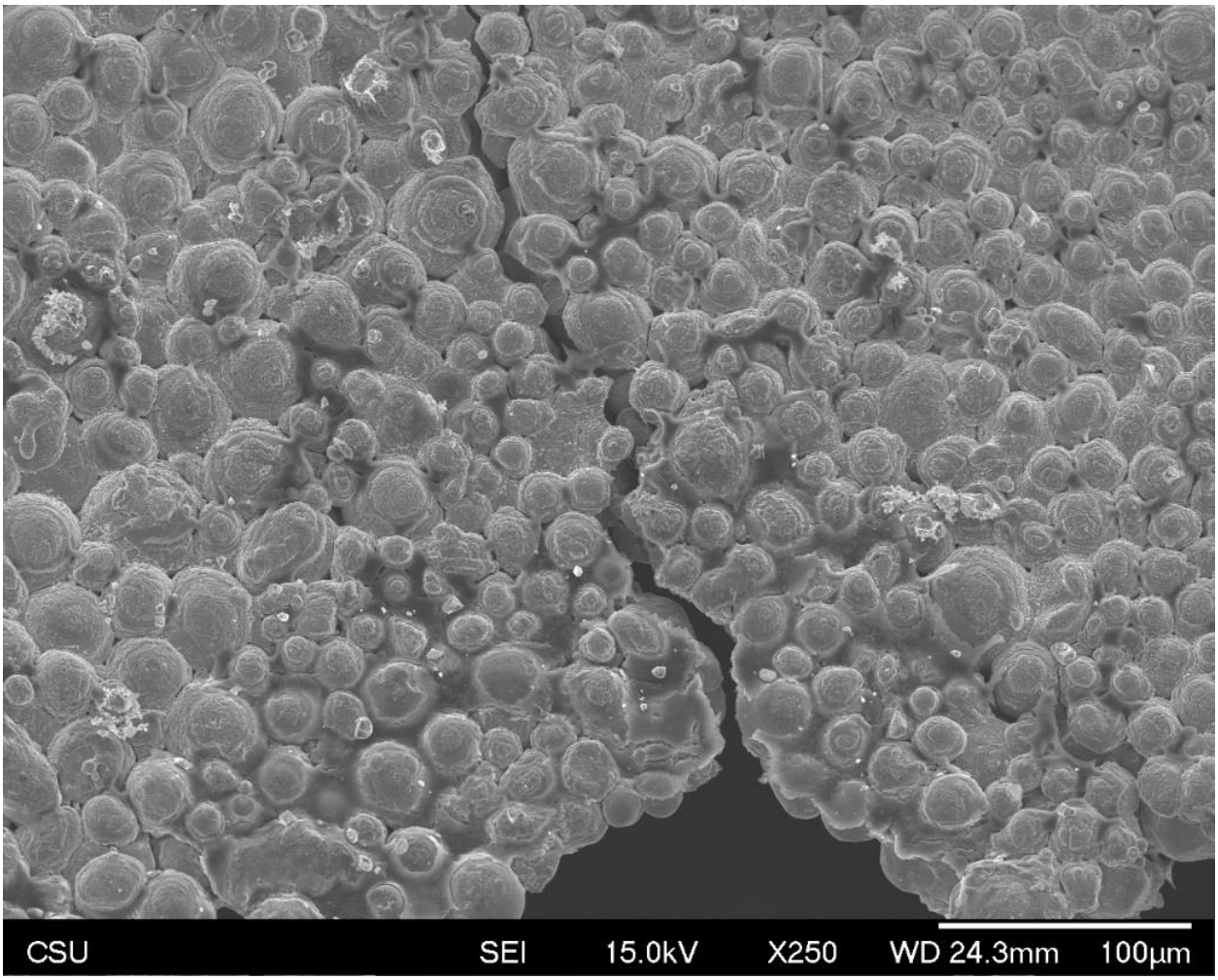

Figure 8.3. Scanning electron microscopy image from specimen pNiTi 32 of crack initiation at a stress concentration along edge of pore interconnect and inter-particle crack propagation.

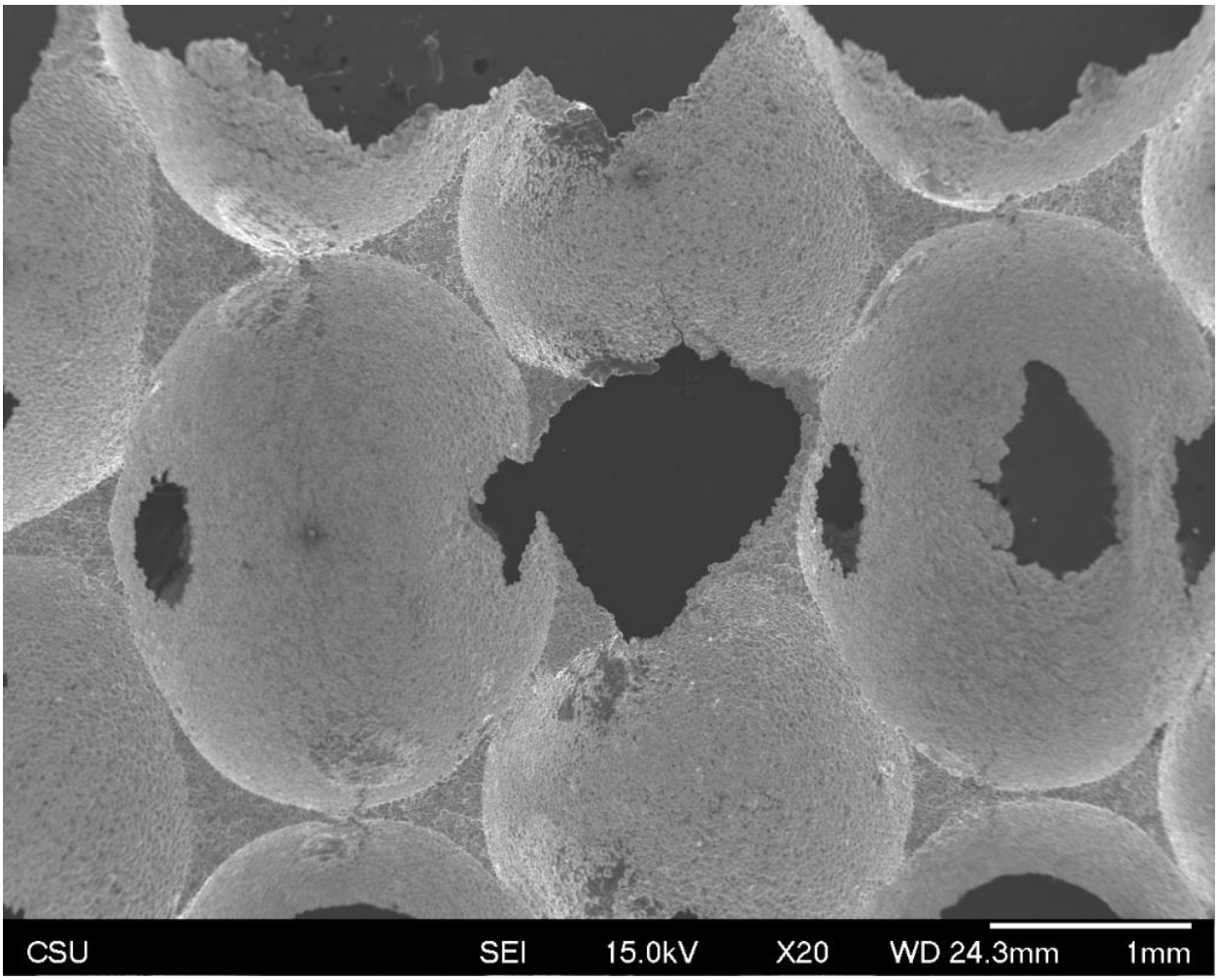

Figure 8.4. Scanning electron microscopy image from specimen pNiTi 32 of the failure surface across multiple layers of the pore structure showing deformation of spherical pore geometry.

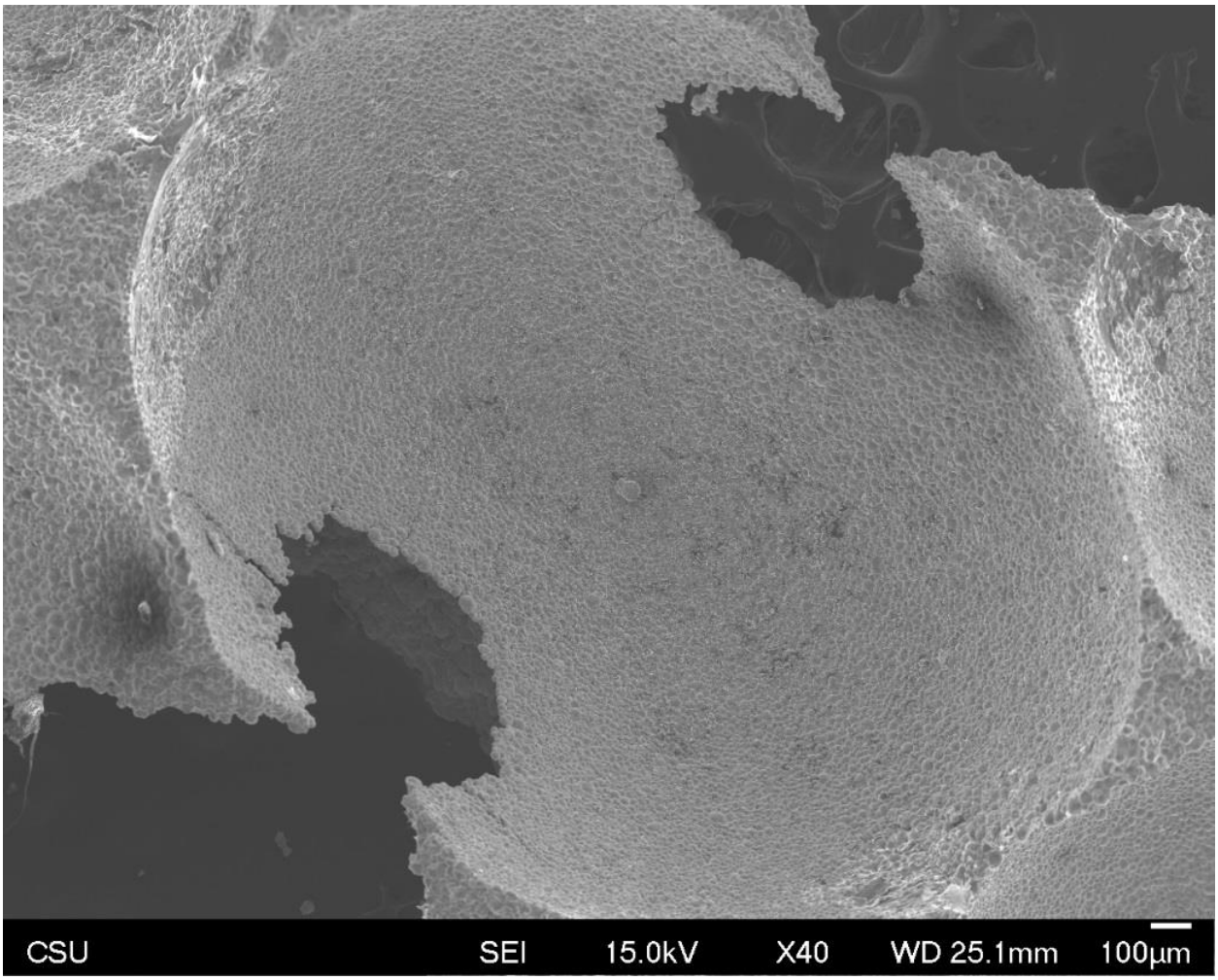

Figure 8.5. Scanning electron microscopy image from specimen pNiTi 33 of pore formed by copper porogen showing deformation of spherical geometry. Two pore interconnects are also shown exhibiting highly irregular edge profiles with stress concentrations and cracks.

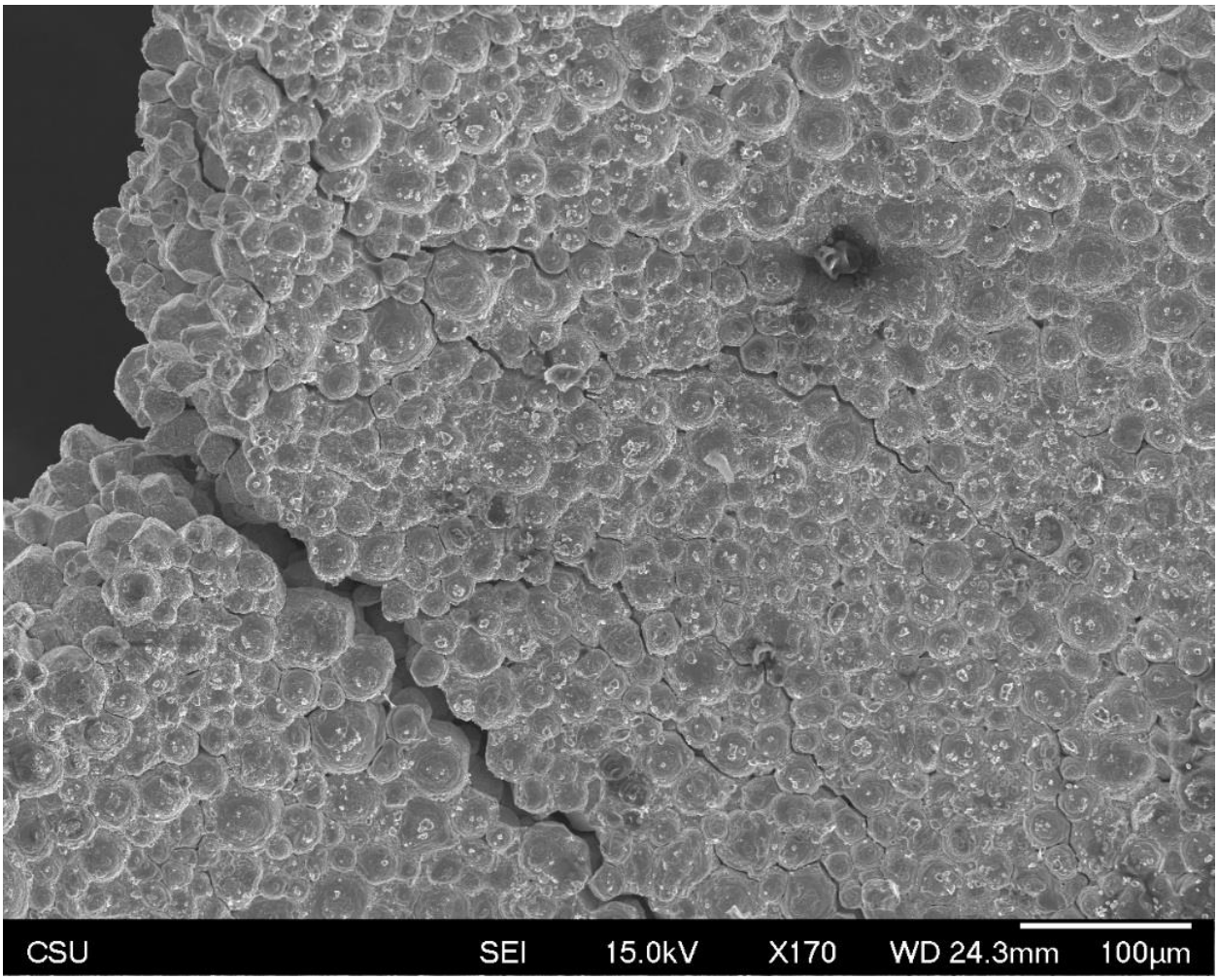

Figure 8.6. Scanning electron microscopy image from specimen pNiTi 33 of crack initiation at a stress concentration along edge of pore interconnect and inter-particle crack propagation.

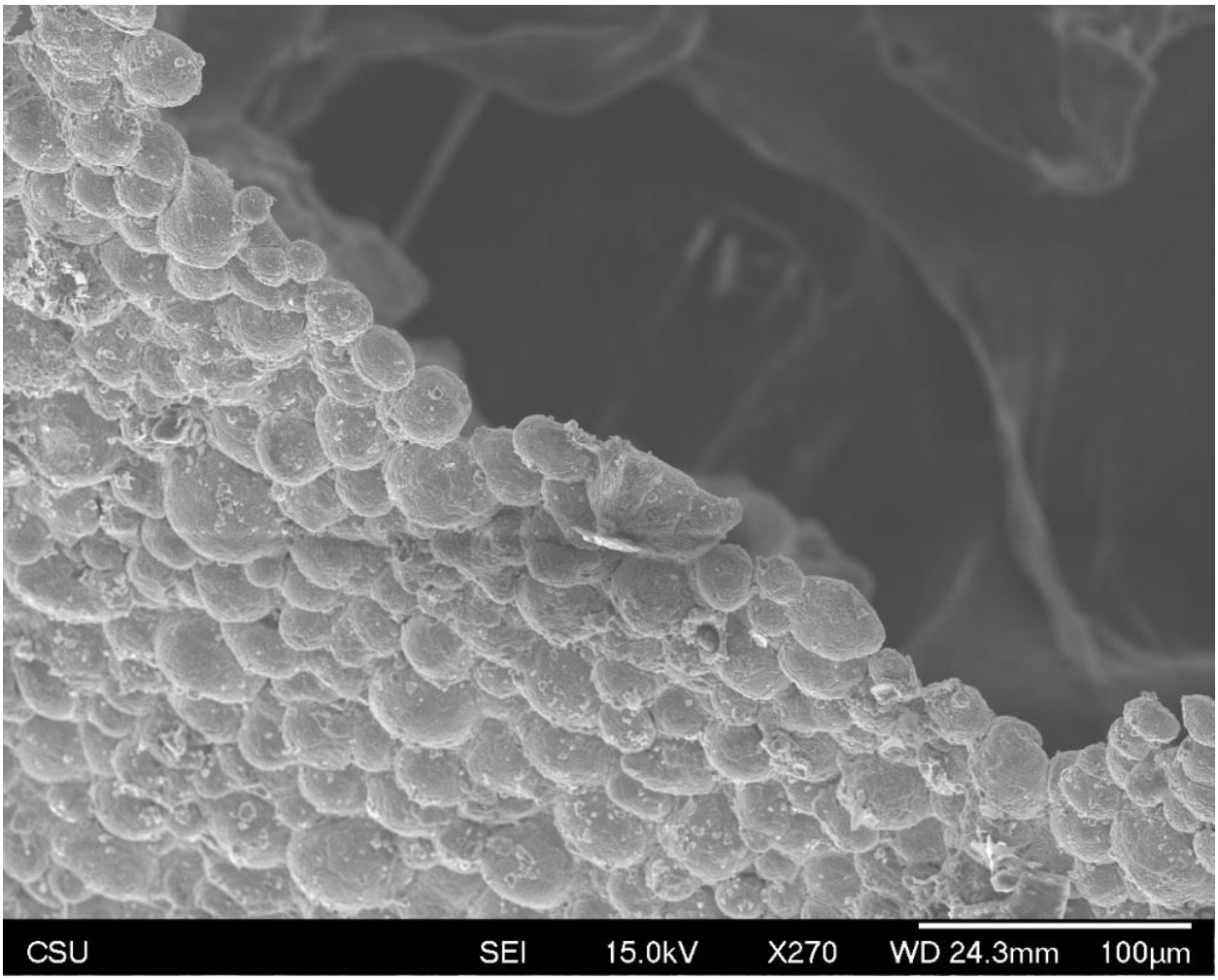

Figure 8.7. Scanning electron microscopy image from specimen pNiTi 33 of pore interconnect edge showing single powder particle thickness and irregularity.

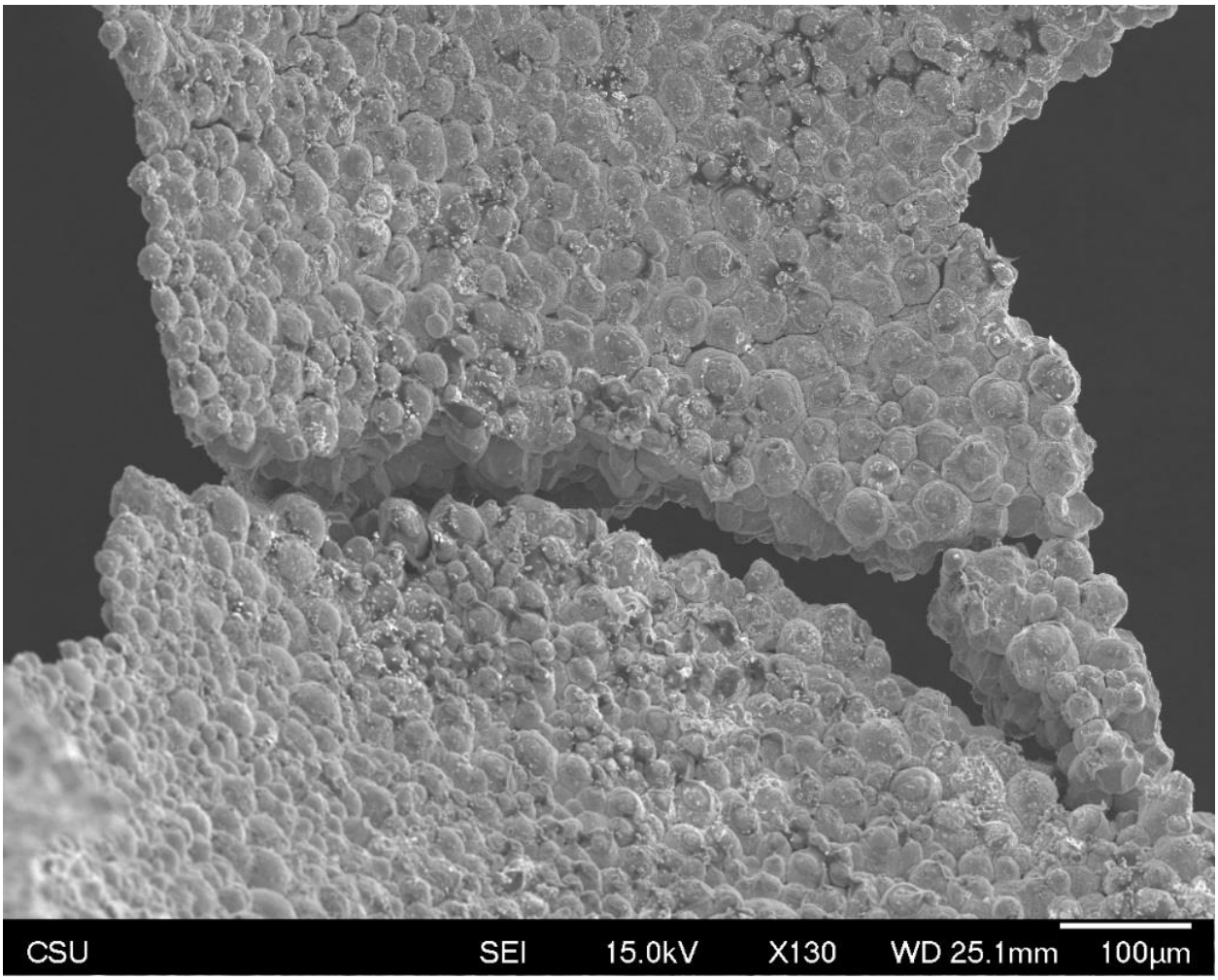

Figure 8.8. Scanning electron microscopy image from specimen pNiTi 35 of crack initiation at a stress concentration along edge of pore interconnect and inter-particle crack propagation.

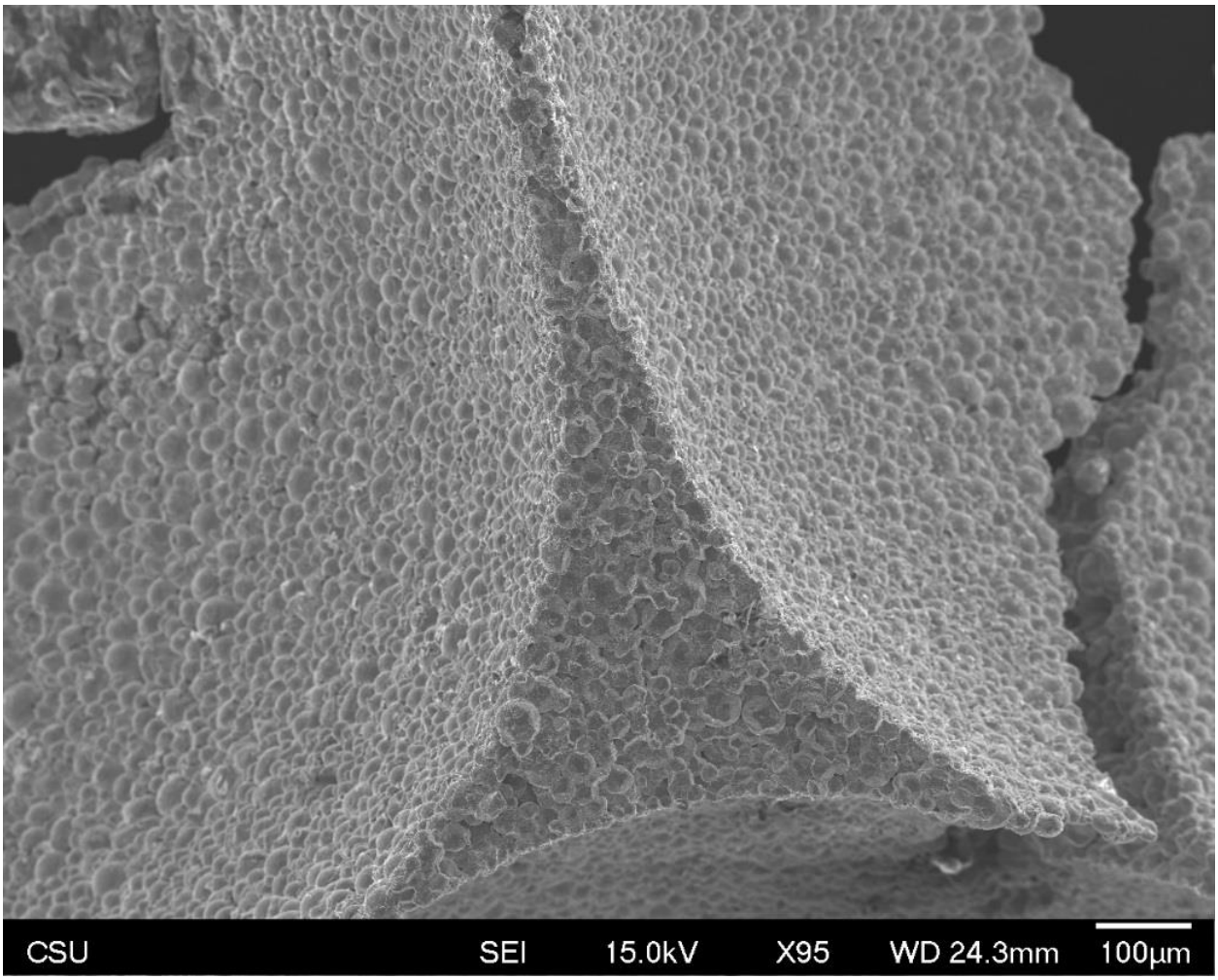

Figure 8.9. Scanning electron microscopy image from specimen pNiTi 36 of fracture surface across smallest cross-sectional area within triple junction between three pores.

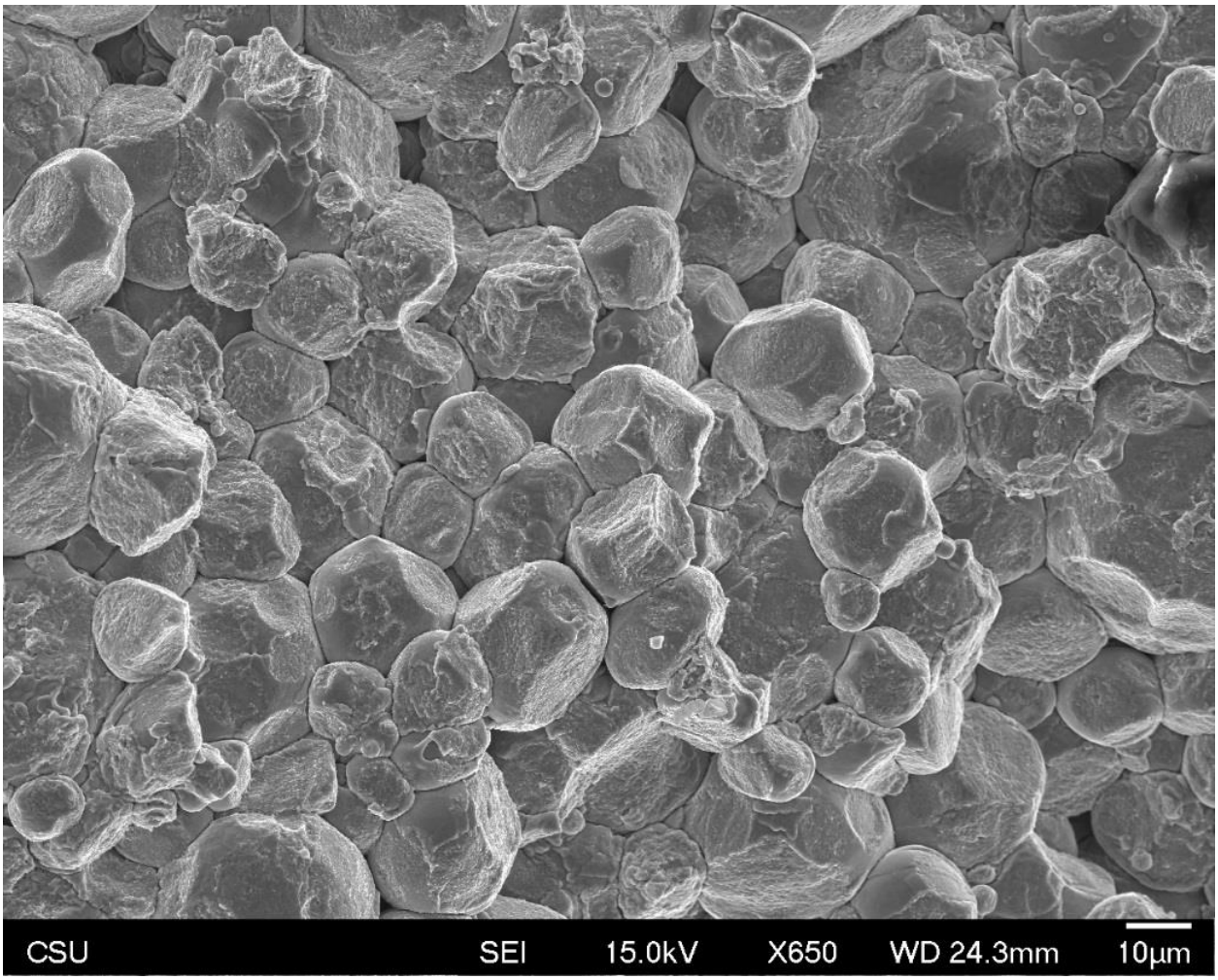

Figure 8.10. Scanning electron microscopy image from specimen pNiTi 36 of fracture surface showing high degree of sintering and inter-particle failure surface.

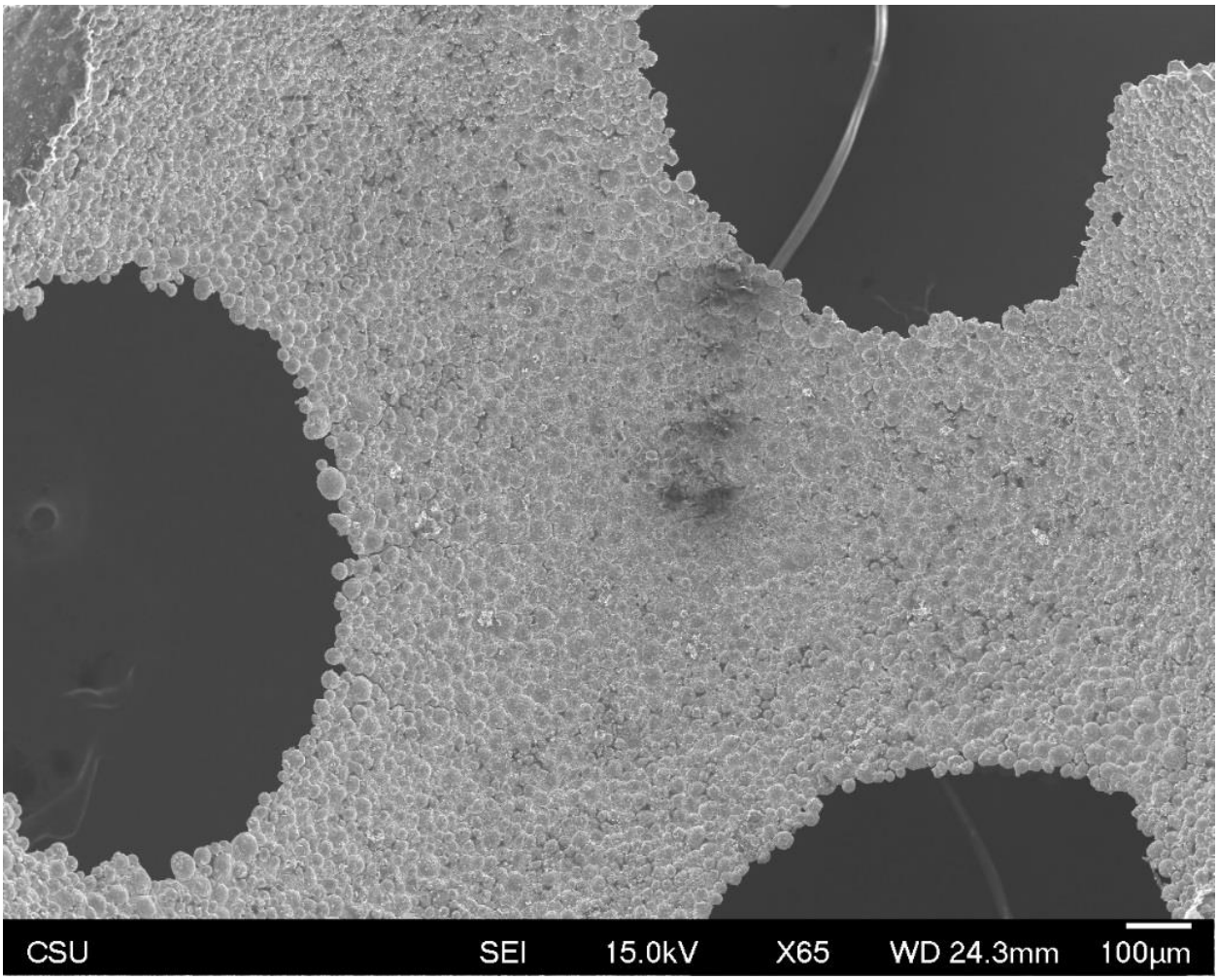

Figure 8.11. Scanning electron microscopy image from specimen pNiTi 37 of three pore interconnects exhibiting highly irregular, single powder particle edge profiles with stress concentrations and cracks.

8.3 SUPPLEMENTAL MASTER SINTERING CURVE PLOTS

8.3.1 NiTi

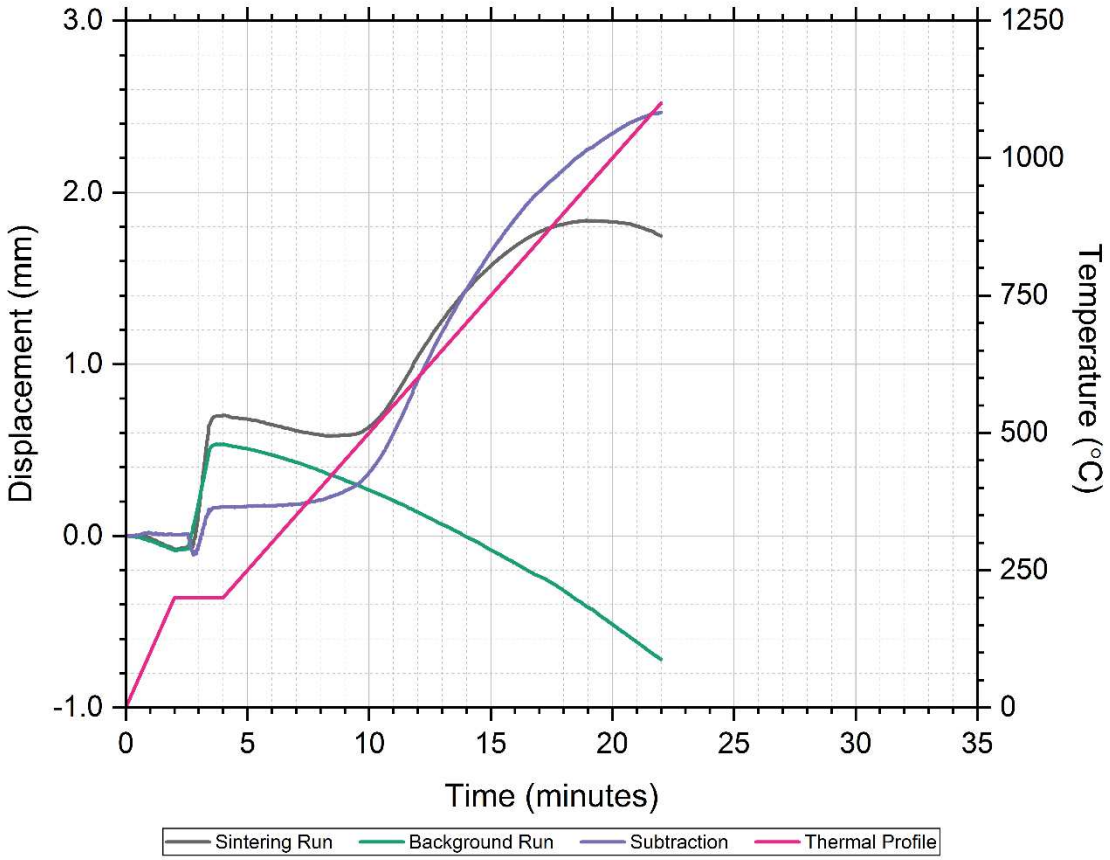

Figure 8.12. SPS electrode displacement and process temperature data plotted versus time from the sintering and background runs of NiTi specimen 112 (NiTi 112). The difference between the sintering and background runs is also plotted, indicating the densification of the powder compact.

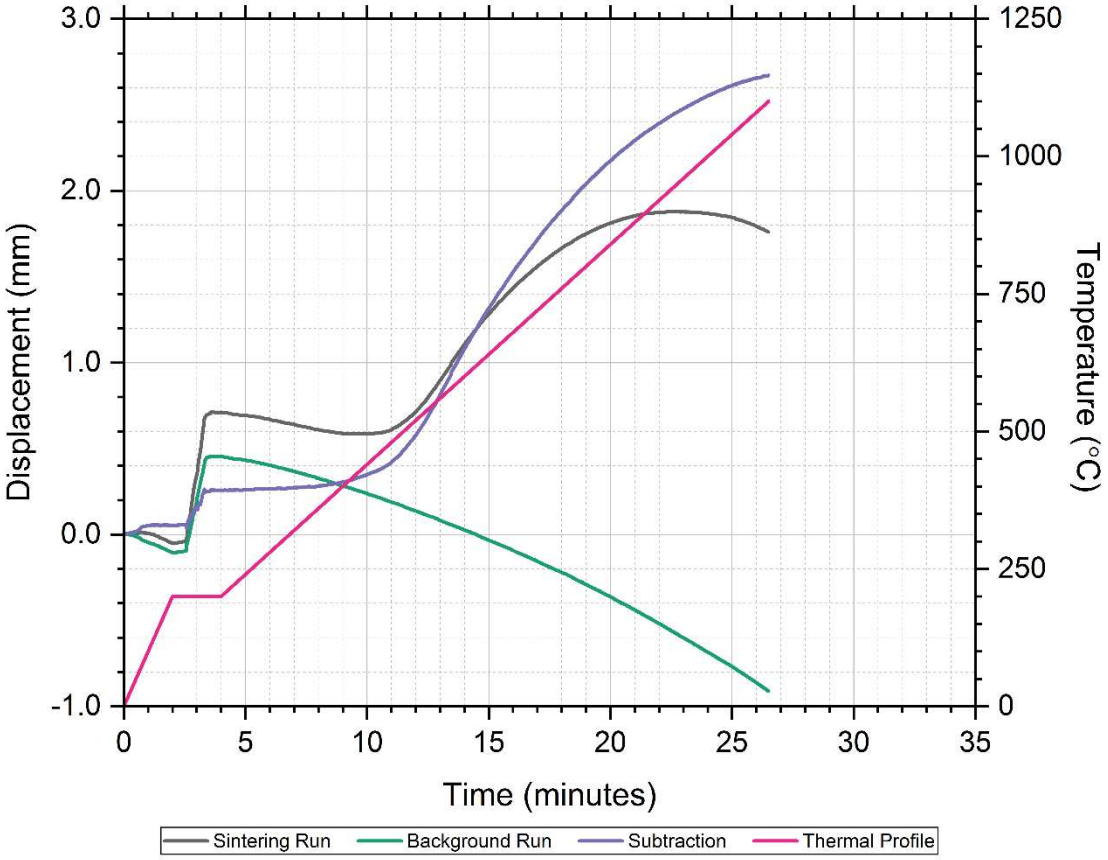

Figure 8.13. SPS electrode displacement and process temperature data plotted versus time from the sintering and background runs of NiTi specimen 113 (NiTi 113). The difference between the sintering and background runs is also plotted, indicating the densification of the powder compact.

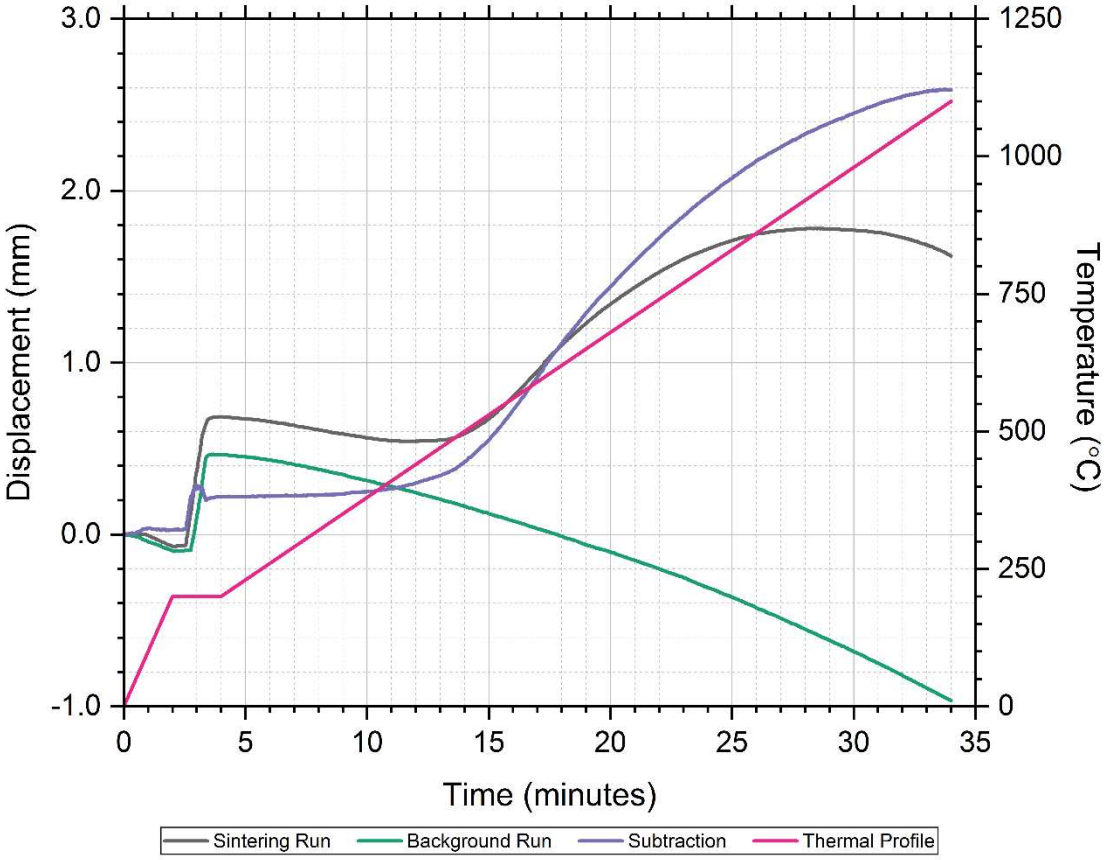

Figure 8.14. SPS electrode displacement and process temperature data plotted versus time from the sintering and background runs of NiTi specimen 114 (NiTi 114). The difference between the sintering and background runs is also plotted, indicating the densification of the powder compact.

8.3.2 NiTi+Cu

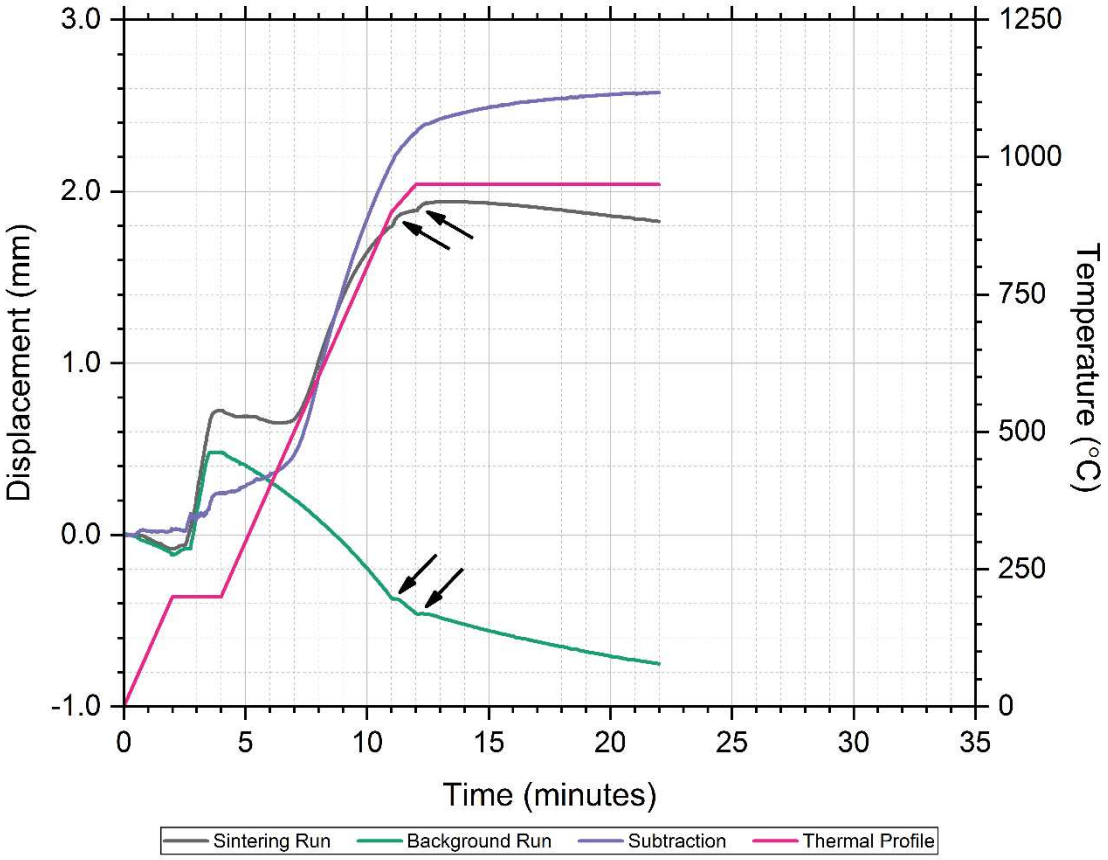

Figure 8.15. SPS electrode displacement and process temperature data plotted versus time from the sintering and background runs of NiTi+Cu specimen 39 (pNiTi 39). The difference between the sintering and background runs is also plotted, indicating the densification of the powder compact. Arrows indicate anomalies in the displacement data.

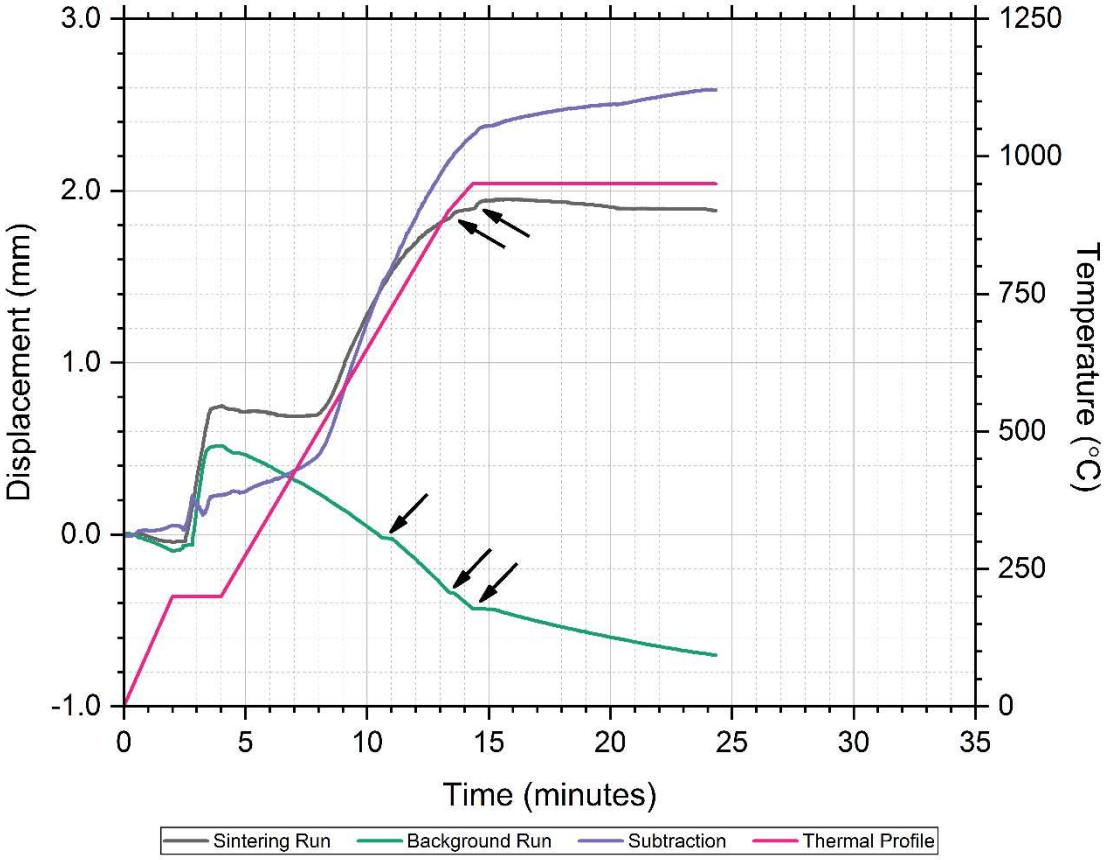

Figure 8.16. SPS electrode displacement and process temperature data plotted versus time from the sintering and background runs of NiTi+Cu specimen 40 (pNiTi 40). The difference between the sintering and background runs is also plotted, indicating the densification of the powder compact. Arrows indicate anomalies in the displacement data.

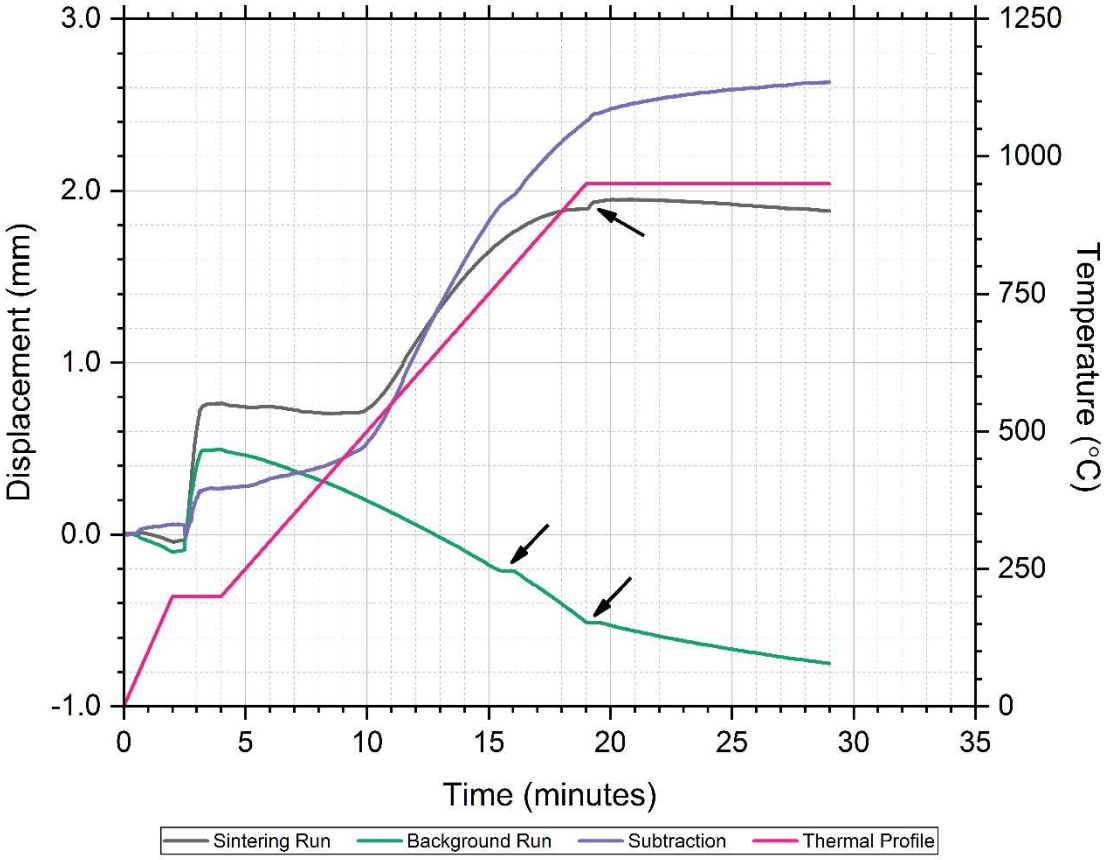

Figure 8.17. SPS electrode displacement and process temperature data plotted versus time from the sintering and background runs of NiTi+Cu specimen 41 (pNiTi 41). The difference between the sintering and background runs is also plotted, indicating the densification of the powder compact. Arrows indicate anomalies in the displacement data.

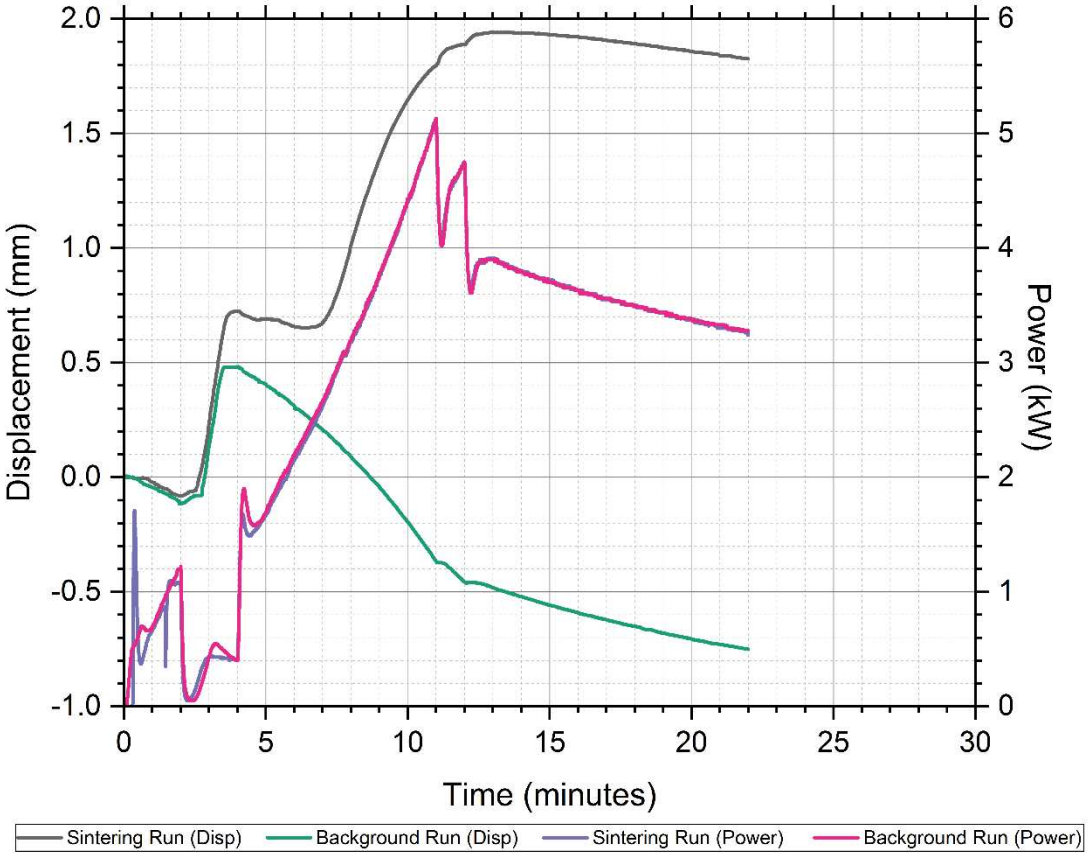

Figure 8.18. SPS electrode displacement and applied power data plotted versus time from the sintering and background runs of NiTi+Cu specimen 39 (pNiTi 39). The two anomalies in the displacement data (t = 11 min. & t = 12 min.) clearly correlate to the roughly 1 kW drops in applied power.

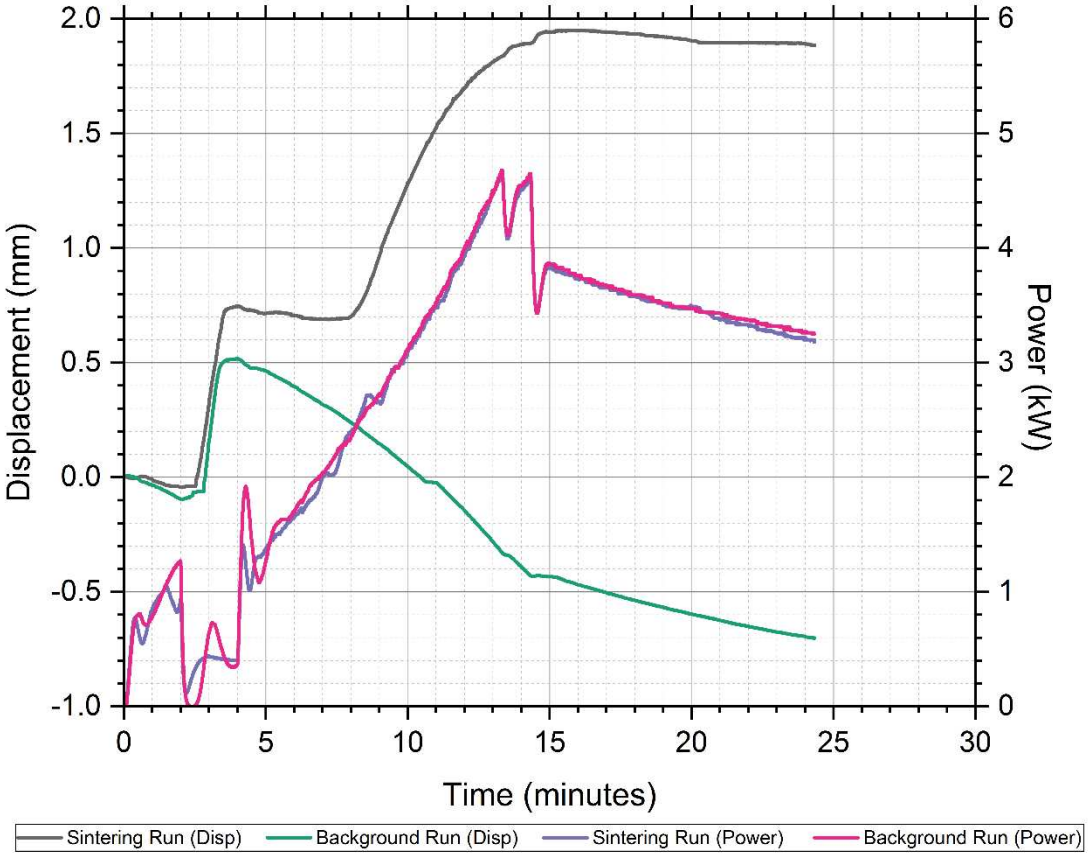

Figure 8.19. SPS electrode displacement and applied power data plotted versus time from the sintering and background runs of NiTi+Cu specimen 40 (pNiTi 40). The two anomalies in the displacement data (t = 9.3 min. & t = 10.3 min.) clearly correlate to the roughly 0.6 kW drops in applied power. The additional anomaly in the background displacement data (t ≈ 10.5 min.) does not correlate with any observable event in the SPS output data file.

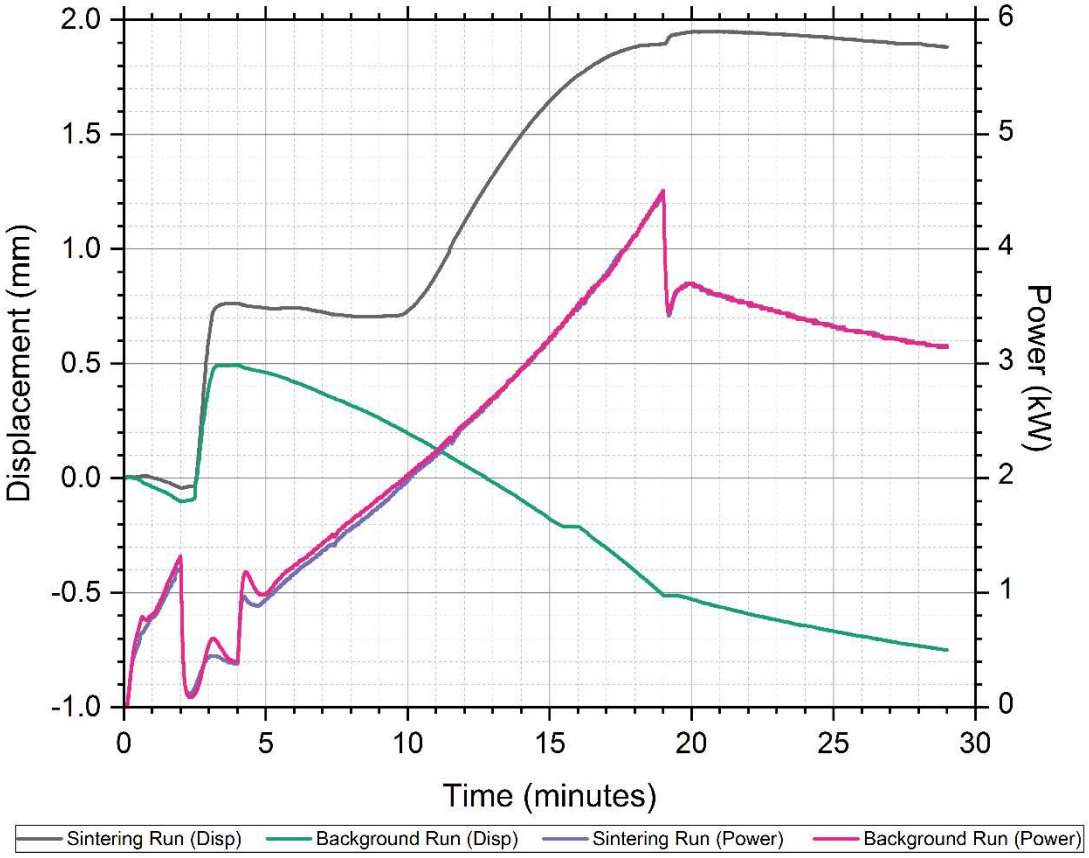

Figure 8.20. SPS electrode displacement and applied power data plotted versus time from the sintering and background runs of NiTi+Cu specimen 41 (pNiTi 41). The single anomaly in the displacement data (t = 19 min.) clearly correlates to the roughly 1 kW drop in applied power. The additional anomaly in the background displacement data (t ≈ 15.5 min.) does not correlate with any observable event in the SPS output data file.

8.3.3 NiTi 112 versus pNiTi 41

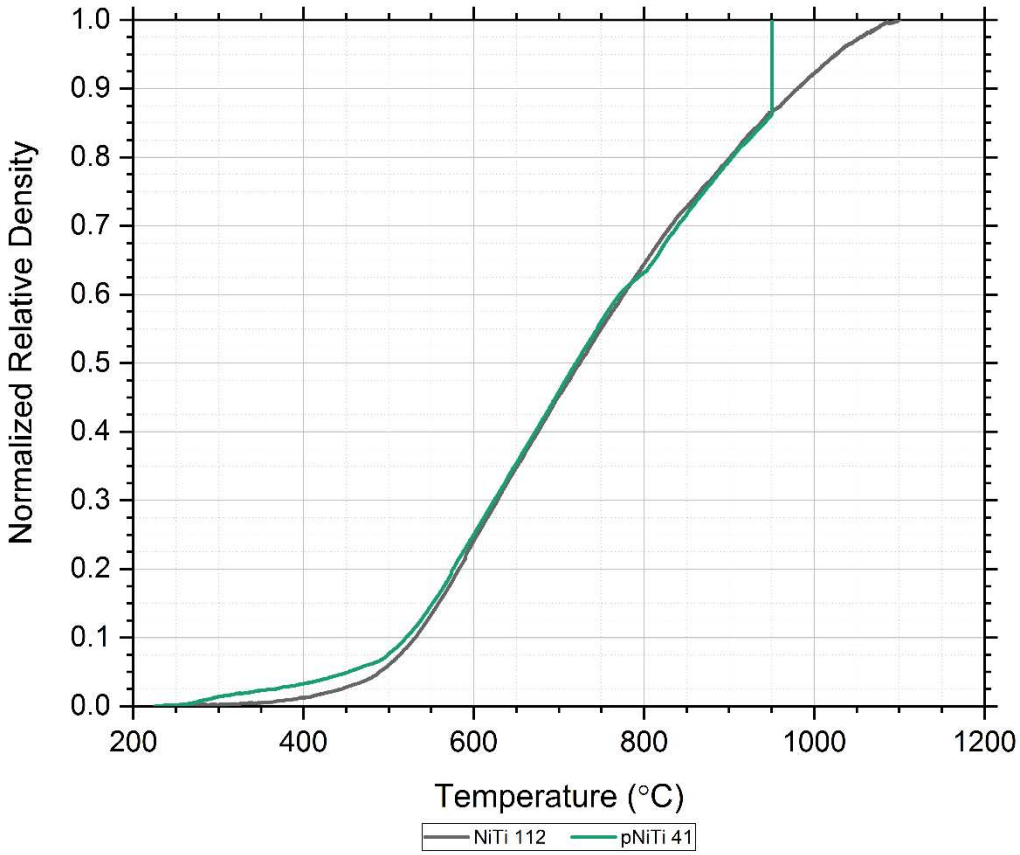

Figure 8.21. Normalized relative density data plotted versus process temperature from NiTi specimen 112 (NiTi 112) and NiTi+Cu specimen 41 (pNiTi 41). Normalization was performed by setting the minimum relative density to zero, the maximum to one, and scaling the relative density in between for each respective specimen. Notice the discrepancy in the relative density data between 300 and 500 °C, as well as the sudden change in densification rate of pNiTi 41 prior to 800 °C.

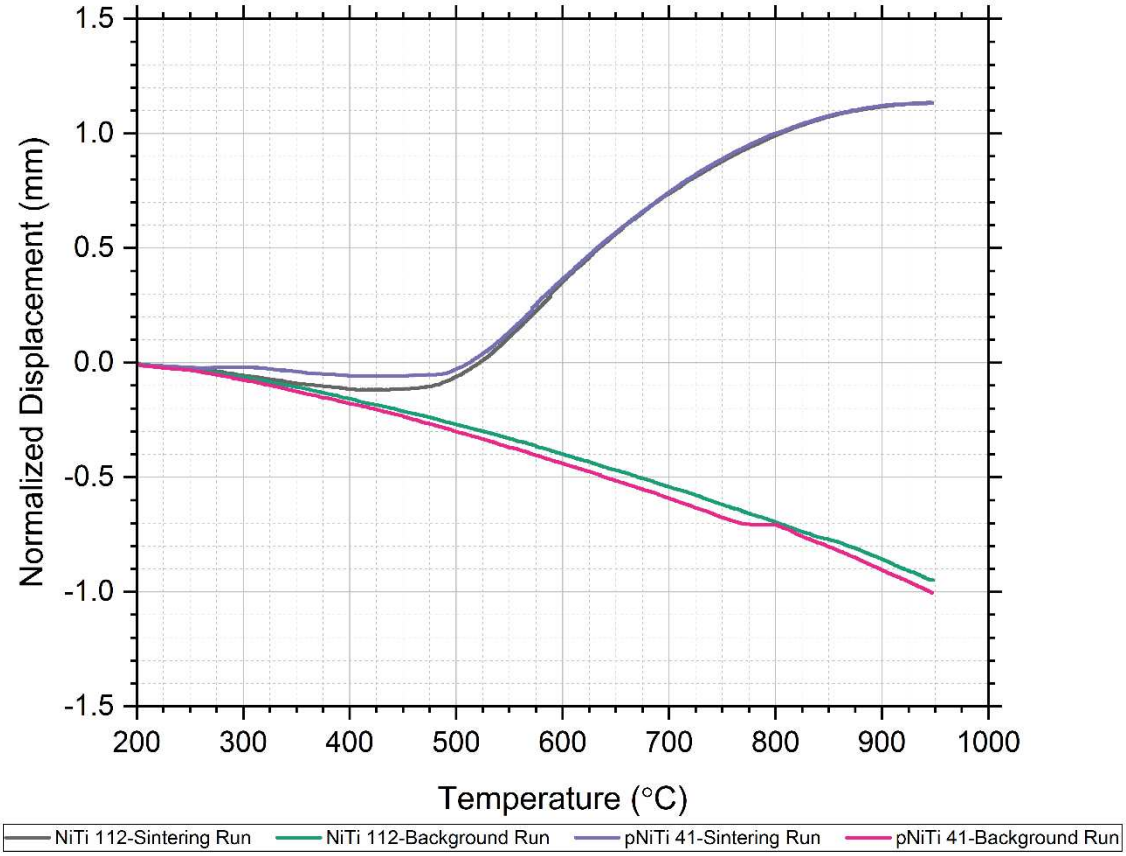

Figure 8.22. Normalized SPS electrode displacement data plotted versus process temperature from the sintering and background runs of NiTi specimen 112 (NiTi 112) and NiTi+Cu specimen 41 (pNiTi 41). Notice the discrepancy in the displacement data during the sintering runs between 300 and 500 °C.

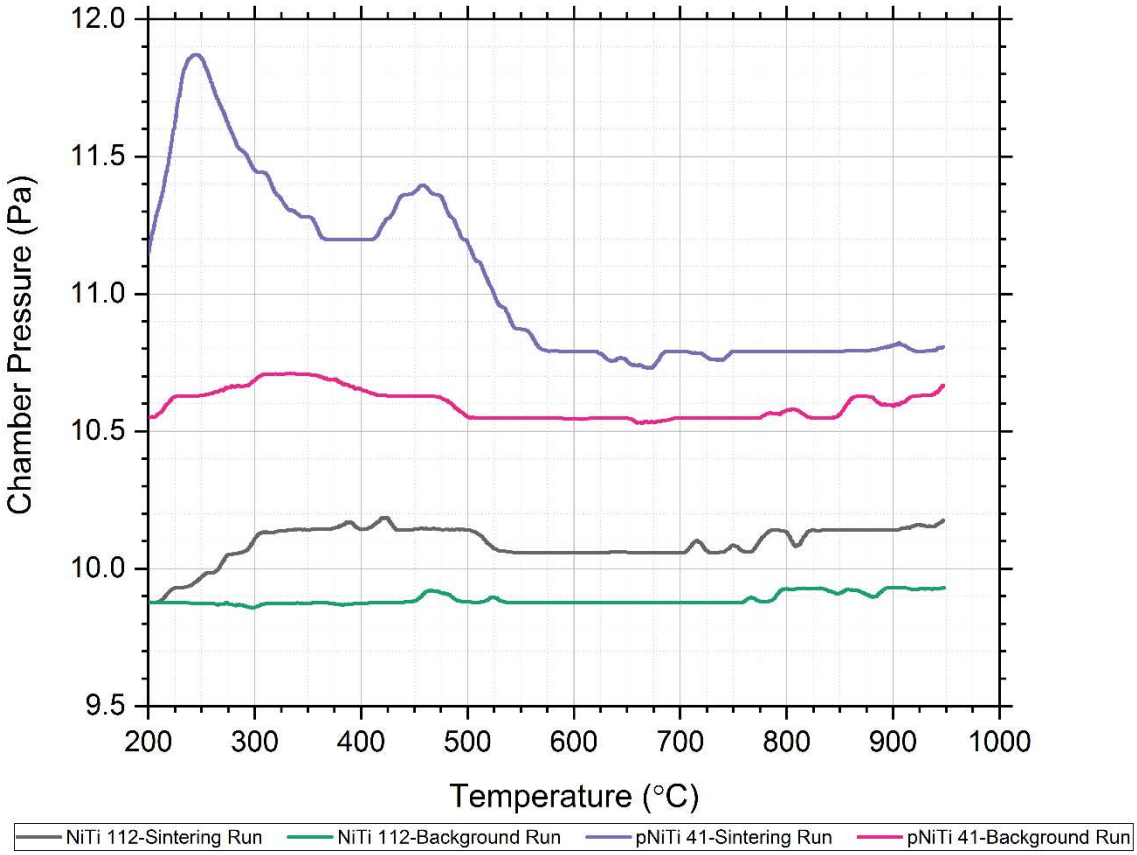

Figure 8.23. SPS chamber pressure data plotted versus process temperature from the sintering and background runs of NiTi specimen 112 (NiTi 112) and NiTi+Cu specimen 41 (pNiTi 41). Notice the unusual double peaks in the chamber pressure data during the sintering run of pNiTi 41.

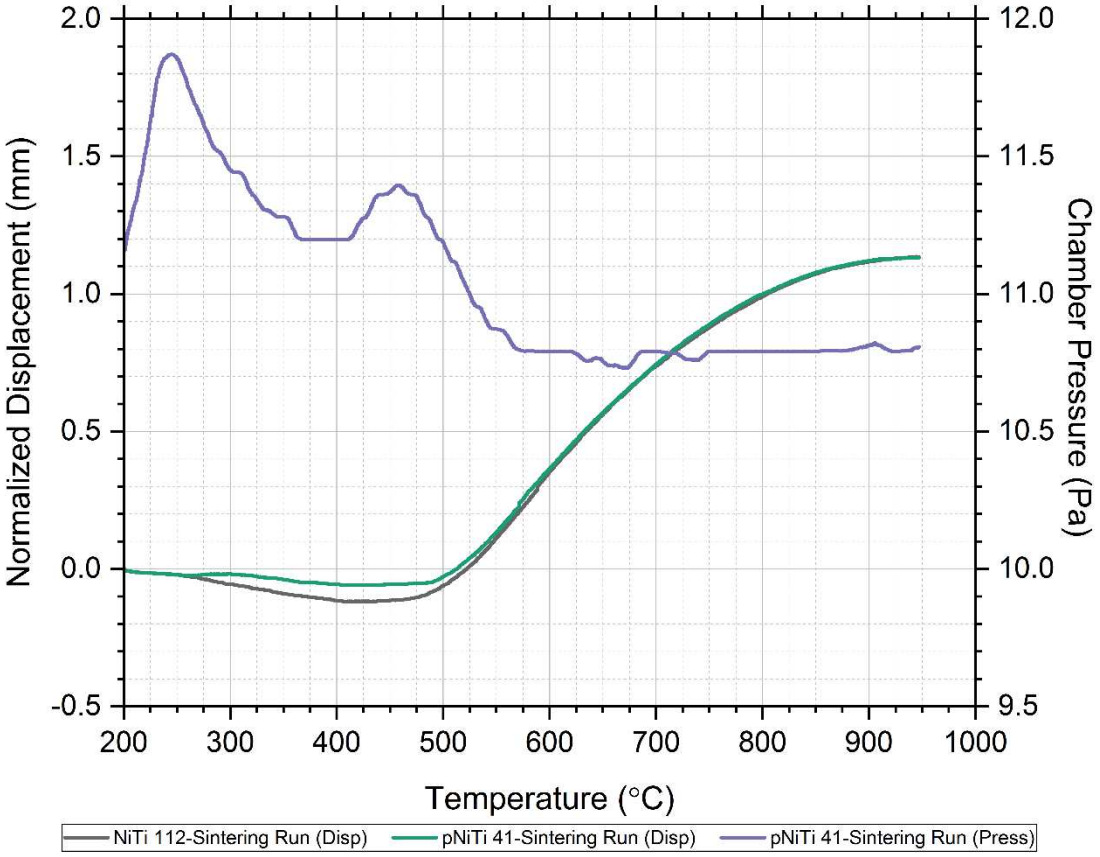

Figure 8.24. SPS electrode displacement and chamber pressure data plotted versus process temperature from the sintering runs of NiTi specimen 112 (NiTi 112) (displacement only) and NiTi+Cu specimen 41 (pNiTi 41). Notice the discrepancy in the displacement data during the sintering runs between 300 and 500 °C roughly corresponds to the unusual double peaks in the chamber pressure data during the sintering run of pNiTi 41. This potential correspondence could point to an outgassing event from the vaporization of the super glue used to construct the copper porogen templates causing a reaction from the SPS electrode displacement controller attempting to maintain a constant applied load (25 kN in this case).

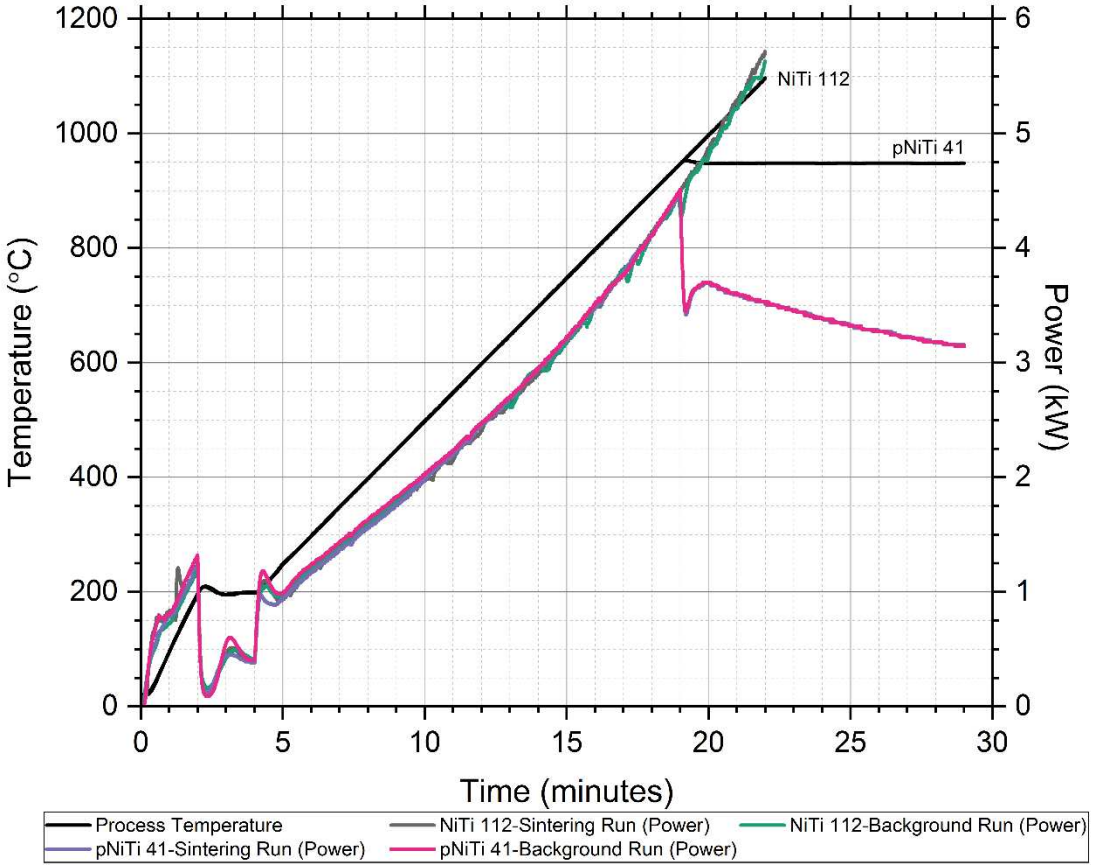

Figure 8.25. SPS process temperature and applied electrode power data plotted versus time from the sintering and background runs of NiTi specimen 112 (NiTi 112) and NiTi+Cu specimen 41 (pNiTi 41). The process temperature profile for specimen NiTi 112 was a constant heating rate, while that for specimen pNiTi 41 included an isothermal dwell at 950 °C. The applied electrode power data is all within family, suggesting the discrepancy in the displacement data between 300 and 500 °C identified in Figure 8.22 was not caused by a perturbation in the applied electrode power.

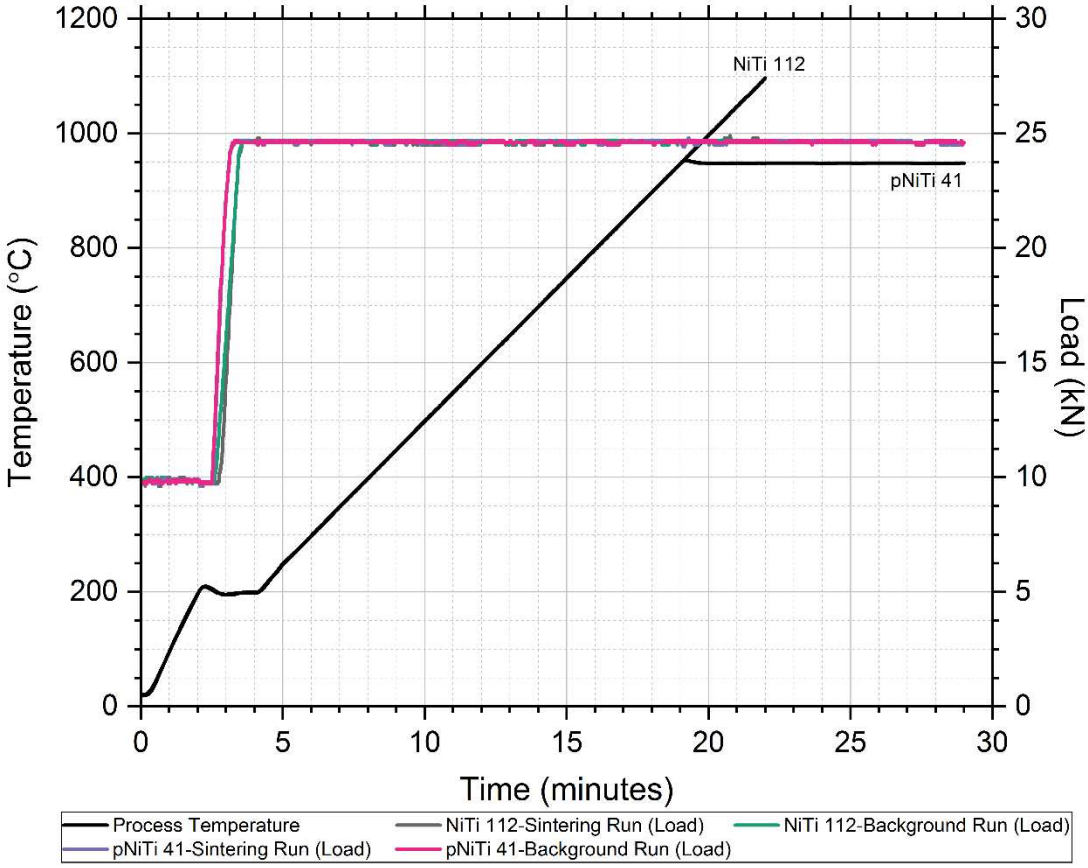

Figure 8.26. SPS process temperature and applied load data plotted versus time from the sintering and background runs of NiTi specimen 112 (NiTi 112) and NiTi+Cu specimen 41 (pNiTi 41). The process temperature profile for specimen NiTi 112 was a constant heating rate, while that for specimen pNiTi 41 included an isothermal dwell at 950 °C. The applied load data is all within family, suggesting the discrepancy in the displacement data between 300 and 500 °C identified in Figure 8.22 was not caused by a perturbation in the applied load.

8.3.4 NiTi and NiTi+Cu

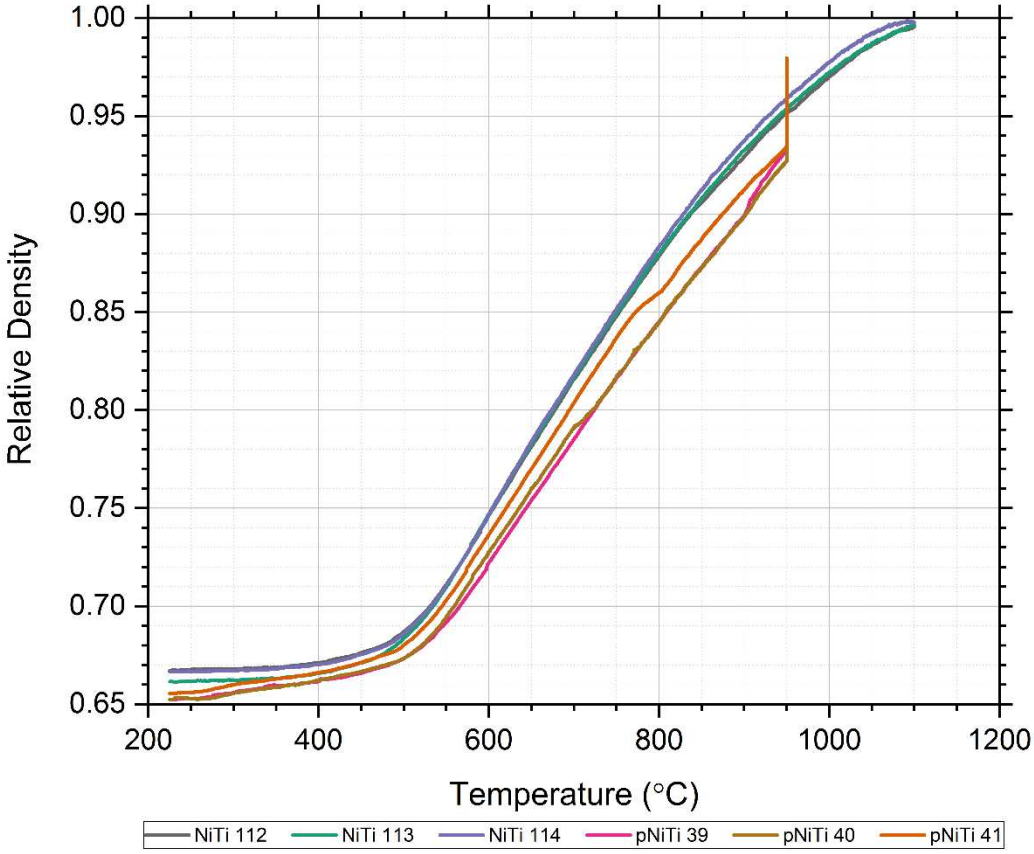

Figure 8.27. Relative density data plotted versus process temperature from all NiTi and NiTi+Cu specimens.

8.4 STATISTICAL ANALYSIS

8.4.1 Tukey Fences

Determination of Tukey Fences is a statistical method to analyze a discrete data set for potential outliers based on the following equations [510]:

$$IQR = Q_3 - Q_1$$

$$Lower\ Tukey\ Fence = Q_1 - 1.5 * IQR$$

$$Upper\ Tukey\ Fence = Q_3 + 1.5 * IQR$$

Table 8.1. The elastic modulus extracted from the stress-strain profiles (Figure 4.15) for each NiTi open-cell foam specimen. The lower (Q1) and upper (Q3) quartiles, along with the inner and outer fences, are reported as determined by the above equations based on Tukey's statistical analysis for outliers. Each value of elastic modulus falls between the Tukey Fences suggesting that no outliers are present.

Foam Specimen	Elastic Modulus (GPa)	Lower Quartile (GPa)	Upper Quartile (GPa)	Tukey Fences (GPa)
pNiTi 32	2.65	2.41	2.81	1.82 3.41
pNiTi 33	2.77			
pNiTi 35	2.86			
pNiTi 36	2.34			
pNiTi 37	2.49			

Table 8.2. The ultimate strength extracted from the stress-strain profiles (Figure 4.15) for each NiTi open-cell foam specimen. The lower (Q1) and upper (Q3) quartiles, along with the inner and outer fences, are reported as determined by the above equations based on Tukey's statistical analysis for outliers. Each value of ultimate strength falls between the Tukey Fences suggesting that no outliers are present.

Foam Specimen	Ultimate Strength (MPa)	Lower Quartile (MPa)	Upper Quartile (MPa)	Tukey Fences (MPa)
pNiTi 32	24.2	23.1	31.8	10.0 44.9
pNiTi 33	32.0			
pNiTi 35	31.7			
pNiTi 36	21.9			
pNiTi 37	25.8			

Table 8.3. The yield strength extracted from the stress-strain profiles (Figure 4.15) for each NiTi open-cell foam specimen. The lower (Q1) and upper (Q3) quartiles, along with the inner and outer fences, are reported as determined by the above equations based on Tukey's statistical analysis for outliers. Each value of yield strength falls between the Tukey Fences suggesting that no outliers are present.

Foam Specimen	Yield Strength (MPa)	Lower Quartile (MPa)	Upper Quartile (MPa)	Tukey Fences (MPa)
pNiTi 32	15.3	13.8	15.4	11.4 17.8
pNiTi 33	14.0			
pNiTi 35	14.4			
pNiTi 36	13.6			
pNiTi 37	15.5			

8.5 MATLAB CODE

8.5.1 Mechanical Compression

```
clc;
clear;
close all;

%To Dos:
%Double check indices relate to correct load values

%Import Data
%--------------------------------------------------------------------------
%Initialize Variables
Sample = 'pNiTi 32';
Filename = '01. pNiTi 32';

% Sample = 'pNiTi 33';
% Filename = '02. pNiTi 33';

% Sample = 'pNiTi 35';
% Filename = '03. pNiTi 35';

% Sample = 'pNiTi 36';
% Filename = '04. pNiTi 36';

% Sample = 'pNiTi 37';
% Filename = '05. pNiTi 37';

Path = 'G:\Peter\School\Research & Projects\06 - PhD Research (James)\Lab
Work\Analysis Data\Mechanical\2018.08.26 pNiTi Foam Crush\';
Filepath = [Path Filename '.txt'];
Delimiter = '\t';
StartRow = 2;
FormatSpec = '%f%f%f%f%f%f%f%[^\n\r]'; %Format string for each line of text

FileID = fopen(Filepath,'r'); %Open the text file
DataArray = textscan(FileID, FormatSpec, 'Delimiter', Delimiter,
'HeaderLines' ,StartRow-1, 'ReturnOnError', false); %Read columns of data
according to format string
fclose(FileID); %Close the text file

%Allocate Imported Data
Time_min = DataArray{:,1};
LaserExt_inch = DataArray{:,2};
% FrameExt_inch = DataArray{:,3};
Load_lbf = DataArray{:,4};
Diameter_inch = DataArray{:,5};
    Diameter_inch = Diameter_inch(1);
Length_inch = DataArray{:,6};
    Length_inch = Length_inch(1);
Mass_gram = DataArray{:,7};
    Mass_gram = Mass_gram(1);
```

```
A_inch2 = (pi/4)*(Diameter_inch)^2; %Cross-sectional Area (inch^2)

clearvars ans DataArray Delimiter FileID Filename Filepath FormatSpec
StartRow Path; %Clear Temporary Variables

%Determine Loading+Unload Stiffnesses
%-------------------------------------------------------------------------
%Index all starting & finishing load points
LowerLimit = 75; %(lbf)
UpperLimit1 = 125; %(lbf)
Upperlimit2 = 225; %(lbf)

Index1 = find(Load_lbf >= LowerLimit,1);

Index2 = find(Load_lbf >= UpperLimit1,1);

Index4 = Index2+find(Load_lbf(Index2:end,1) <= LowerLimit,1)-2;

[Load_max1,Indexmax1] = max(Load_lbf(Index2:Index4));
Indexmax1 = Indexmax1 + Index2;
Index3 = Indexmax1+find(Load_lbf(Indexmax1:end,1) <= UpperLimit1,1)-2;

Index6 = Index4+find(Load_lbf(Index4:end,1) >= UpperLimit1,1)-1;

[Load_min1,Indexmin1] = min(Load_lbf(Index4:Index6));
Indexmin1 = Indexmin1 + Index4-1;
Index5 = Indexmin1+find(Load_lbf(Indexmin1:end,1) >= LowerLimit,1)-1;

Index8 = Index6+find(Load_lbf(Index6:end,1) <= LowerLimit,1)-2;

[Load_max2,Indexmax2] = max(Load_lbf(Index6:Index8));
Indexmax2 = Indexmax2 + Index6;
Index7 = Indexmax2+find(Load_lbf(Indexmax2:end,1) <= Upperlimit2,1)-2;

Index10 = Index8+find(Load_lbf(Index8:end,1) >= Upperlimit2,1)-1;

[Load_min2,Indexmin2] = min(Load_lbf(Index8:Index10));
Indexmin2 = Indexmin2 + Index8;
Index9 = Indexmin2+find(Load_lbf(Indexmin2:end,1) >= LowerLimit,1)-1;

clearvars LowerLimit UpperLimit1 Upperlimit2; %Clear Temporary Variables

%Calculate stiffness between starting & finishing load points
IndexArray =
[Index1,Index2,Index3,Index4,Index5,Index6,Index7,Index8,Index9,Index10]';

coeffTime = zeros(length(IndexArray)/2,2);
R2Time = zeros(length(IndexArray)/2,1);
LoadPlotTime_lbf = zeros(length(IndexArray)/2,length(Time_min));

coeffLaserExt = zeros(length(IndexArray)/2,2);
R2LaserExt = zeros(length(IndexArray)/2,1);
LoadPlotLaserExt_lbf = zeros(length(IndexArray)/2,length(LaserExt_inch));
```

```
% %Load vs. Time
% plot(Time_min,Load_lbf);
% xlim([0 12]);
% ylim([0 500]);
% hold on

% %Load vs. Laser Extension
% plot(LaserExt_inch,Load_lbf);
% xlim([0 0.025]);
% ylim([0 500]);
% hold on
for i = 1:length(IndexArray)/2
    %Time
    X = Time_min(IndexArray(2*i-1):IndexArray(2*i));
    Y = Load_lbf(IndexArray(2*i-1):IndexArray(2*i));

    [xData,yData] = prepareCurveData(X,Y);
    ft = fittype('poly1'); %Set up fittype and options.
    [fitresult,gof] = fit(xData,yData,ft); %Fit model to data.

    coeffTime(i,:) = coeffvalues(fitresult)'; %f(x) = p1*x + p2
    R2Time(i,1) = gof.rsquare;
    LoadPlotTime_lbf(i,:) = coeffTime(i,1)*Time_min+coeffTime(i,2);

%     plot(Time_min,LoadPlotTime_lbf(i,:))

    clearvars X xData yData ft fitresult gof; %Clear Temporary Variables

    %Laser Extension
    X = LaserExt_inch(IndexArray(2*i-1):IndexArray(2*i));
    Y = Load_lbf(IndexArray(2*i-1):IndexArray(2*i));

    [xData,yData] = prepareCurveData(X,Y);
    ft = fittype('poly1'); %Set up fittype and options.
    [fitresult,gof] = fit(xData,yData,ft); %Fit model to data.

    coeffLaserExt(i,:) = coeffvalues(fitresult)'; %f(x) = p1*x + p2
    R2LaserExt(i,1) = gof.rsquare;
    LoadPlotLaserExt_lbf(i,:) =
coeffLaserExt(i,1)*LaserExt_inch+coeffLaserExt(i,2);

%     plot(LaserExt_inch,LoadPlotLaserExt_lbf(i,:))

    clearvars X Y xData yData ft fitresult gof; %Clear Temporary Variables
end

clearvars IndexArray i LoadPlotTime_lbf LoadPlotLaserExt_lbf R2Time
R2LaserExt; %Clear Temporary Variables

%Determine Elastic Strain Rate
%--------------------------------------------------------------------------
```

```
StrainRate = ((LaserExt_inch(Index6)-
LaserExt_inch(Index5))/Length_inch)/(Time_min(Index6)-Time_min(Index5));
%[(inch/inch)/min]

%Determine Elastic Modulus
%-------------------------------------------------------------------------
E_GPa = (((Load_lbf(Index6)-
Load_lbf(Index5))*4.44822/(A_inch2*0.0254^2))/((LaserExt_inch(Index6)-
LaserExt_inch(Index5))/(Length_inch)))/1e9;

%Remove Loops & Extend Linear-Elastic Portion
%-------------------------------------------------------------------------
%Remove Second Loop
Indexmax2b = find(Load_lbf > Load_max2,1); %Find Load greater or equal to
second peak on re-loading
Load_lbf(Indexmax2+1:Indexmax2b-1) = [];
Time_min(length(Time_min)-((Indexmax2b-1)-(Indexmax2+1)):end) = [];
LaserExt_inch(Indexmax2+1:Indexmax2b-1) = [];

%Extend Linear-Elastic Portion & Trim
Load_lbf(1:Index5-1) = coeffTime(3,1)*Time_min(1:Index5-1)+coeffTime(3,2);
LaserExt_inch(1:Index5-1) = (Load_lbf(1:Index5-1)-
coeffLaserExt(3,2))/coeffLaserExt(3,1);
IndexZero = find(Load_lbf >= 0,1); %Find zero Load value (aka. crosses x-
axis)
Load_lbf(1:IndexZero-1) = []; %Trim Load
LaserExt_inch(1:IndexZero-1) = []; %Trim Laser Extension
LaserExt_inch = LaserExt_inch - LaserExt_inch(1); %Shift Laser Extension to
zero starting value
Time_min(length(Time_min)-((IndexZero-1)-(1)):end) = []; %Trim Time

clearvars Indexmax1b Indexmax2b; %Clear Temporary Variables
clearvars Indexmax1 Indexmin1 Indexmax2 Indexmin2 IndexZero; %Clear Temporary
Variables
clearvars Load_max1 Load_min1 Load_max2 Load_min2; %Clear Temporary Variables
clearvars Index1 Index2 Index3 Index4 Index5 Index6 Index7 Index8 Index9
Index10; %Clear Temporary Variables
clearvars LowerLimit UpperLimit1 Upperlimit2; %Clear Temporary Variables

%Determine Yield Strength (0.2% Offset)
%-------------------------------------------------------------------------
LoadYield_lbf = coeffLaserExt(3,1)*LaserExt_inch+(-
coeffLaserExt(3,1)*0.002*Length_inch);

IndexYield = find(LoadYield_lbf >= Load_lbf,1); %Determine Yield Load Index
Fy_lbf = Load_lbf(IndexYield); %Yield Load (lbf)
Sy_MPa = ((Fy_lbf*4.44822)/(A_inch2*0.0254^2))/1e6; %Yield Strength (MPa)

clearvars LoadYield_lbf IndexYield Fy_lbf; %Clear Temporary Variables
clearvars coeffLaserExt coeffTime; %Clear Temporary Variables

%Determine Ulimate Strength
%-------------------------------------------------------------------------
Fu_lbf = max(Load_lbf); %Ultimate Load (lbf)
Su_MPa = ((Fu_lbf*4.44822)/(A_inch2*0.0254^2))/1e6; %Ultimate Strength (MPa)
```

```
clearvars Fu_lbf; %Clear Temporary Variables

%Plot Stress-Strain Profile
%--------------------------------------------------------------------------
Stress_MPa = ((Load_lbf*4.44822)/(A_inch2*0.0254^2))/1e6; %Stress (MPa)
Strain_percent = (LaserExt_inch/Length_inch)*100; %Strain (%)

plot(Strain_percent,Stress_MPa)

clearvars A_inch2 Diameter_inch Length_inch Mass_gram; %Clear Temporary
Variables
clearvars LaserExt_inch Load_lbf Time_min; %Clear Temporary Variables
clearvars Strain_percent Stress_MPa; %Clear Temporary Variables
```

8.5.2 Background Subtraction

```
clc;
clear;
close all;

%Import Data File
%------------------------------------------------------------------------
Sample = 'NiTi 112';
SampleA = 'NiTi 112a';
SampleB = 'NiTi 112b';
Path = 'G:\Peter\School\Research & Projects\06 - PhD Research (James)\Lab
Work\SPS Data\2018\2018.01.12\';
Lf_mm = 4.6736; %NiTi 112 Final height of sintered specimen as measured
across punches (mm)
rhof_gcc = 6.42086784997053; %NiTi 112 Final density of sintered specimen
(gcc) [by means of NiTi 109]

% Sample = 'NiTi 113';
% SampleA = 'NiTi 113a';
% SampleB = 'NiTi 113b';
% Path = 'G:\Peter\School\Research & Projects\06 - PhD Research (James)\Lab
Work\SPS Data\2018\2018.01.14\';
% Lf_mm = 4.7625; %NiTi 113 Final height of sintered specimen as measured
across punches (mm)
% rhof_gcc = 6.42790974962156; %NiTi 113 Final density of sintered specimen
(gcc) [by means of NiTi 110]

% Sample = 'NiTi 114';
% SampleA = 'NiTi 114a';
% SampleB = 'NiTi 114b';
% Path = 'G:\Peter\School\Research & Projects\06 - PhD Research (James)\Lab
Work\SPS Data\2018\2018.01.19\';
% Lf_mm = 4.7625; %NiTi 114 Final height of sintered specimen as measured
across punches (mm)
% rhof_gcc = 6.43540503606627; %NiTi 114 Final density of sintered specimen
(gcc) [by means of NiTi 111]

% Sample = 'pNiTi 39';
% SampleA = 'pNiTi 39a';
% SampleB = 'pNiTi 39b';
% Path = 'G:\Peter\School\Research & Projects\06 - PhD Research (James)\Lab
Work\SPS Data\2018\2018.03.16\';
% Lf_mm = 4.65467986161864; %pNiTi 39 Final height of sintered specimen as
measured across punches (mm)
% rhof_gcc = 6.31253123673234; %pNiTi 39 Final density of sintered specimen
(gcc) [by means of pNiTi 42]

% Sample = 'pNiTi 40';
% SampleA = 'pNiTi 40a';
% SampleB = 'pNiTi 40b';
% Path = 'G:\Peter\School\Research & Projects\06 - PhD Research (James)\Lab
Work\SPS Data\2018\2018.03.23\';
% Lf_mm = 4.68007986161864; %pNiTi 40 Final height of sintered specimen as
measured across punches (mm)
```

```
% rhof_gcc = 6.31463761307672; %pNiTi 40 Final density of sintered specimen
(gcc) [by means of pNiTi 43]

% Sample = 'pNiTi 41';
% SampleA = 'pNiTi 41a';
% SampleB = 'pNiTi 41b';
% Path = 'G:\Peter\School\Research & Projects\06 - PhD Research (James)\Lab
Work\SPS Data\2018\2018.03.23\';
% Lf_mm = 4.78167986161864; %pNiTi 41 Final height of sintered specimen as
measured across punches (mm)
% rhof_gcc = 6.31187440246827; %pNiTi 41 Final density of sintered specimen
(gcc) [by means of pNiTi 44]

FilenameA = [Path SampleA '.txt'];
FilenameB = [Path SampleB '.txt'];
Delimiter = '\t';
StartRow = 2;

FormatSpec = '%f%f%f%f%f%f%f%f%f%f%[^\n\r]'; %Format string for each line of
text

FileIDA = fopen(FilenameA,'r'); %Open the text file
DataArrayA = textscan(FileIDA, FormatSpec, 'Delimiter', Delimiter,
'HeaderLines' ,StartRow-1, 'ReturnOnError', false); %Read columns of data
according to format string
fclose(FileIDA); %Close the text file

FileIDB = fopen(FilenameB,'r'); %Open the text file
DataArrayB = textscan(FileIDB, FormatSpec, 'Delimiter', Delimiter,
'HeaderLines' ,StartRow-1, 'ReturnOnError', false); %Read columns of data
according to format string
fclose(FileIDB); %Close the text file

%Allocate Imported Data
% TimeA_min = DataArrayA{:, 1};
% VoltageA_V = DataArrayA{:, 2};
% AmperageA_A = DataArrayA{:, 3};
% ProcessVariableA_degC = DataArrayA{:, 4};
% LoadA_kN = DataArrayA{:, 5};
DisplacementA_mm = DataArrayA{:, 6};
% DisplacementRateA_Vs = DataArrayA{:, 7};
% ChamberPressureA_Pa = DataArrayA{:, 8};
% PowerA_kW = DataArrayA{:, 9};
SetVariableA_degC = DataArrayA{:, 10};

% TimeB_min = DataArrayB{:, 1};
% VoltageB_V = DataArrayB{:, 2};
% AmperageB_A = DataArrayB{:, 3};
% ProcessVariableB_degC = DataArrayB{:, 4};
% LoadB_kN = DataArrayB{:, 5};
DisplacementB_mm = DataArrayB{:, 6};
% DisplacementRateB_Vs = DataArrayB{:, 7};
% ChamberPressureB_Pa = DataArrayB{:, 8};
% PowerB_kW = DataArrayB{:, 9};
% SetVariableB_degC = DataArrayB{:, 10};
```

```
clearvars FilenameA FilenameB StartRow FormatSpec FileIDA FileIDB DataArrayA
DataArrayB ans; %Clear Temporary Variables

%Perform Background Subtraction & Calculate Variables
%--------------------------------------------------------------------------
%Initialize Variables
Start_SV = 225; %Starting temperature for background subtraction (degC)

rhoTheory_gcc = 6.45; %Theoretical density of NiTi (gcc)

Displacement_mm = DisplacementA_mm - DisplacementB_mm; %Subtract sintering
run from background run

%Set Starting Point for Background Subtraction
Index_SV = find(SetVariableA_degC>=Start_SV,1);
SetVariableA_degC = SetVariableA_degC(Index_SV:end);
Displacement_mm = Displacement_mm(Index_SV:end);

dL_mm = -1*(Displacement_mm - Displacement_mm(1)); %dL(T) (mm)
L_mm = dL_mm + (Lf_mm-dL_mm(end)); %L(T) (mm)

rho_gcc = ((rhof_gcc*Lf_mm)./L_mm); %rho(T) (gcc)
rho = rho_gcc/rhoTheory_gcc; %rho(T) Relative density

% clearvars dL_mm L_mm rho_gcc; %Clear Temporary Variables

% dL_mm = -1*(Displacement_mm - Displacement_mm(1)); %dL(T) (mm)
% L0_mm = Lf_mm - dL_mm(end); %Height of unsintered specimen at Start_SV
temperature (mm)
% L_mm = dL_mm + L0_mm; %L(T) (mm)
%
% rho0_gcc = (rhof_gcc*Lf_mm)/L0_mm; %Density of unsintered specimen at
Start_SV temperature (gcc)
% drho_gcc = -1*rho0_gcc*(dL_mm/Lf_mm); %drho(T) (gcc)
% rho_gcc = rho0_gcc + drho_gcc; %rho(T) (gcc)
% rho = rho_gcc/rhoTheory_gcc; %rho(T) Relative density

%Export Data
%--------------------------------------------------------------------------
T = table(SetVariableA_degC,dL_mm,L_mm,rho_gcc,rho);
writetable(T,[Path Sample '.txt'],'Delimiter', Delimiter);

% T = table(SetVariableA_degC,dL_mm,L_mm,drho_gcc,rho_gcc,rho);
% writetable(T,[Path Sample '.txt'],'Delimiter', Delimiter);
```

8.5.3 NiTi MSC

```
clc;
clear;
close all;

%Import Data
%-------------------------------------------------------------------------
%Initialize Variables
Sample = ["NiTi 112", "NiTi 113", "NiTi 114"];
Path = ["G:\Peter\School\Research & Projects\06 - PhD Research (James)\Lab
Work\SPS Data\2018\2018.01.12\",...
        "G:\Peter\School\Research & Projects\06 - PhD Research (James)\Lab
Work\SPS Data\2018\2018.01.14\",...
        "G:\Peter\School\Research & Projects\06 - PhD Research (James)\Lab
Work\SPS Data\2018\2018.01.19\"];

%Determine Maximum Data Table Height
SampleCount = size(Sample,2);
TableHeight = zeros(1,SampleCount); %Preallocate Array
for i = 1:SampleCount
    T = readtable([char(Path(i)) char(Sample(i)) '.txt']);
    TableHeight(i) = height(T);
end

%Load in Data Table Values
Temp_degC = zeros(max(TableHeight),SampleCount); %Preallocate Temperature
Matrix
rho = zeros(max(TableHeight),SampleCount); %Preallocate Relative Density
Matrix
for j = 1:SampleCount
    T = readtable([char(Path(j)) char(Sample(j)) '.txt']);
    Temp_degC(1:TableHeight(j),j) = table2array(T(:,1));
    rho(1:TableHeight(j),j) = table2array(T(:,5));
%     rho(1:TableHeight(j),j) = table2array(T(:,6));
end

Tmin = 250; %degC
Tmax = 1100; %degC
Tstep = 5; %degC
Temp_degC_Input = linspace(Tmin,Tmax,(Tmax-Tmin)/Tstep+1)';

RelDen_Input = zeros(length(Temp_degC_Input),SampleCount);
for i = 1:SampleCount
    for j = 1:length(Temp_degC_Input)
        for k = 1:TableHeight(i)
            if Temp_degC(k,i) >= Temp_degC_Input(j)
                RelDen_Input(j,i) = rho(k,i);
                break
            end
        end
    end
end

NumEntries = size(RelDen_Input,1);
```

```
%50 degC/min
time_sec_Input(:,1) = linspace(0,(max(Temp_degC_Input)-
min(Temp_degC_Input))*60/50,length(Temp_degC_Input))';

%40 degC/min
time_sec_Input(:,2) = linspace(0,(max(Temp_degC_Input)-
min(Temp_degC_Input))*60/40,length(Temp_degC_Input))';

%30 degC/min
time_sec_Input(:,3) = linspace(0,(max(Temp_degC_Input)-
min(Temp_degC_Input))*60/30,length(Temp_degC_Input))';

clearvars Sample i j k T TableHeight Tmax Tstep Temp_degC rho; %Clear
Temporary Variables

%Determine Q Value for Minimum RMSE
%--------------------------------------------------------------------------
Q =  linspace(500,700,100)'; %kJ/mol
R = 8.314; %J/(mol*K)
Temp_K = Temp_degC_Input + 273.15;

RMSE = zeros(length(Q),1);
for k = 1:length(Q)
    index = 1;
    theta = zeros((NumEntries-1),SampleCount);
    X = zeros(SampleCount*(NumEntries-1),1);
    Y = zeros(SampleCount*(NumEntries-1),1);
    for i = 1:SampleCount
        for j = 1:NumEntries
            %Calculate Theta Integrand
            Integrand(j,i) = (1/Temp_K(j,1))*exp(-
(Q(k)*1000)/(R*Temp_K(j,1))); %#ok<SAGROW>
        end

        for m = 1:NumEntries-1
            dt_sec = time_sec_Input(m+1,i)-time_sec_Input(m,i);
            if m == 1
                theta(m,i) = ((Integrand(m)+Integrand(m+1))/2)*dt_sec;
            else
                theta(m,i) =
((Integrand(m)+Integrand(m+1))/2)*dt_sec+theta(m-1,i);
            end

            %Form Curve Fitting (X,Y) Pairs
            X(index,1) = log(theta(m,i));
            Y(index,1) = RelDen_Input(m,i);
            index = index +1;
        end
    end

%     %Perform Sigmoid Curve Fit
%     [xData, yData] = prepareCurveData(X,Y);
%     ft = fittype('rho_0+((1-rho_0)/(1+exp(-(x-log_theta0)/b))^c)',...
```

```
%                   'independent', 'x', 'dependent', 'y' );
%     opts = fitoptions('Method', 'NonlinearLeastSquares');
%     opts.Algorithm = 'Levenberg-Marquardt';
%     opts.Display = 'Off';
%     opts.StartPoint = [1.0 1.0 mean(X) 0.66];
%     [fitresult, gof] = fit(xData, yData, ft, opts); %#ok<ASGLU> % Fit model
to data

    %Perform 8th-Degree Polynomial Curve Fit
    [xData, yData] = prepareCurveData(X,Y);
    ft = fittype('poly8'); % Set up fittype and options.
    [fitresult, gof] = fit(xData,yData,ft); %#ok<ASGLU> % Fit model to data.

    RMSE(k,1) = gof.rmse;

    clearvars dt_sec xData yData index theta X Y i j m Integrand; %Clear
Temporary Variables
end

plot(Q,RMSE)
[RMSE_min,index] = min(RMSE);
Q_min = Q(index);

clearvars fitresult ft gof index opts Q RMSE k Temp_degC_Input RMSE_min;
%Clear Temporary Variables

%Calculate and Plot MSC
%-------------------------------------------------------------------------
index = 1;
theta = zeros(SampleCount*(NumEntries-1),1);
X = zeros(SampleCount*(NumEntries-1),1);
Y = zeros(SampleCount*(NumEntries-1),1);
for i = 1:SampleCount
    for j = 1:NumEntries
        %Calculate Theta Integrand
        Integrand(j,i) = (1/Temp_K(j,1))*exp(-(Q_min*1000)/(R*Temp_K(j,1)));
    end

    for m = 1:NumEntries-1
        dt_sec = time_sec_Input(m+1,i)-time_sec_Input(m,i);
        if m == 1
            theta(m,i) = ((Integrand(m)+Integrand(m+1))/2)*dt_sec;
        else
            theta(m,i) = ((Integrand(m)+Integrand(m+1))/2)*dt_sec+theta(m-
1,i);
        end

        %Form Curve Fitting (X,Y) Pairs
        X(index,1) = log(theta(m,i));
        Y(index,1) = RelDen_Input(m,i);
        index = index +1;
    end
end
```

```
% %Perform Sigmoid Curve Fit
% [xData, yData] = prepareCurveData(X,Y);
% ft = fittype('rho_0+((1-rho_0)/(1+exp(-(x-log_theta0)/b))^c)',...
%               'independent', 'x', 'dependent', 'y');
% opts = fitoptions( 'Method', 'NonlinearLeastSquares');
% opts.Algorithm = 'Levenberg-Marquardt';
% opts.Display = 'Off';
% opts.StartPoint = [1.0 1.0 mean(X) 0.66];
% [fitresult, gof] = fit(xData, yData, ft, opts) % Fit model to data
%
% coeff = coeffvalues(fitresult);
% b = coeff(1);
% c = coeff(2);
% log_theta0 = coeff(3);
% rho_0 = coeff(4);

%Perform 8th-Degree Polynomial Curve Fit
[xData, yData] = prepareCurveData(X,Y);
ft = fittype( 'poly8' ); % Set up fittype and options.
[fitresult, gof] = fit(xData,yData,ft) % Fit model to data.

coeff = coeffvalues(fitresult)'; %f(x) = p1*x^8 + p2*x^7 + p3*x^6 + p4*x^5 +
p5*x^4 + p6*x^3 + p7*x^2 + p8*x + p9

% Plot curve fit with data.
figure( 'Name', 'untitled fit 1' );
h = plot( fitresult, xData, yData);
legend( h, 'Constant Heating Rate', 'Curve Fit', 'Location', 'NorthWest' );
% Label axes
xlabel X
ylabel Y
grid on

clearvars SampleCount NumEntries time_sec_Input RelDen_Input...
          dt_sec index theta X Y i j m ft gof opts...
          Temp_K Integrand; %Clear Temporary Variables

%Predictions of Sintering Time
%--------------------------------------------------------------------------

%[Sample Name | Heating Rate (degC/min) | Temp (degC) | Hold Time (min) |
% Relative Density]
Pred = ["NiTi 79", 100,  950, 5, 0.986;...
        "NiTi 80", 100,  900, 5, 0.971;...
        "NiTi 81", 100,  850, 5, 0.951;...
        "NiTi 82", 100,  800, 5, 0.926;...
        "NiTi 83", 100,  750, 5, 0.898;...
        "NiTi 84", 100,  700, 5, 0.863;...
        "NiTi 85", 100,  650, 5, 0.829;...
        "NiTi 86", 100,  600, 5, 0.796];

PredCount = size(Pred,1);
Predtfinal_sec = ((str2double(Pred(:,3))-Tmin)./str2double(Pred(:,2)))*60;
Predtstep = 100;
```

```
PredTheta = zeros(PredCount,1);
Predrho = zeros(PredCount,1);
PredTheta_Ramp = zeros(Predtstep-1,PredCount);
for i = 1:PredCount
    TempRamp_Kmin = str2double(Pred(i,2));
    Temp_K = str2double(Pred(i,3))+273.15;
    Dwell_sec = str2double(Pred(i,4))*60;

    Predt_sec = linspace(0,Predtfinal_sec(i),Predtstep)';
    PredTemp_K = ((TempRamp_Kmin/60)*Predt_sec+Tmin)+273.15;
    for j = 1:Predtstep
        Integrand(j) = (1/PredTemp_K(j,1))*exp(-
(Q_min*1000)/(R*PredTemp_K(j,1)));
    end

    for m = 1:Predtstep-1
        dt_sec = Predt_sec(m+1)-Predt_sec(m);
        PredTheta_Ramp(m,i) = ((Integrand(m)+Integrand(m+1))/2)*dt_sec;
    end

    PredTheta_Dwell = (1/Temp_K)*exp(-(Q_min*1000)/(R*Temp_K))*Dwell_sec;

    PredTheta(i,1) = sum(PredTheta_Ramp(:,i))+PredTheta_Dwell;
%     Predrho(i,1) = rho_0+((1-rho_0)/(1+exp(-(log(PredTheta(i,1))-
log_theta0)/b)^c)); %Sigmoid
    Predrho(i,1) = coeff(1)*(log(PredTheta(i,1)))^8+...
                   coeff(2)*(log(PredTheta(i,1)))^7+...
                   coeff(3)*(log(PredTheta(i,1)))^6+...
                   coeff(4)*(log(PredTheta(i,1)))^5+...
                   coeff(5)*(log(PredTheta(i,1)))^4+...
                   coeff(6)*(log(PredTheta(i,1)))^3+...
                   coeff(7)*(log(PredTheta(i,1)))^2+...
                   coeff(8)*(log(PredTheta(i,1)))^1+...
                   coeff(9); %Polynomial

    clearvars TempRamp_Kmin Temp_K Dwell_sec Predt_sec PredTemp_K Integrand;
%Clear Temporary Variables
end

% fliplr(log(PredTheta(:,1)))

hold on
% Create plot
plot(log(PredTheta(:,1)),str2double(Pred(:,5)),'DisplayName','Experimental
Data','MarkerFaceColor',[0 0 0],...
    'MarkerEdgeColor',[0 0 0],...
    'Marker','o',...
    'Color',[0 0 0]);
```

8.5.4 NiTi+Cu MSC

```
clc;
clear;
close all;

%Import Data
%-------------------------------------------------------------------------
%Initialize Variables
Sample = ["NiTi 112", "NiTi 113", "NiTi 114"];
Path = ["G:\Peter\School\Research & Projects\06 - PhD Research (James)\Lab
Work\SPS Data\2018\2018.01.12\",...
        "G:\Peter\School\Research & Projects\06 - PhD Research (James)\Lab
Work\SPS Data\2018\2018.01.14\",...
        "G:\Peter\School\Research & Projects\06 - PhD Research (James)\Lab
Work\SPS Data\2018\2018.01.19\"];

%Determine Maximum Data Table Height
SampleCount = size(Sample,2);
TableHeight = zeros(1,SampleCount); %Preallocate Array
for i = 1:SampleCount
    T = readtable([char(Path(i)) char(Sample(i)) '.txt']);
    TableHeight(i) = height(T);
end

%Load in Data Table Values
Temp_degC = zeros(max(TableHeight),SampleCount); %Preallocate Temperature
Matrix
rho = zeros(max(TableHeight),SampleCount); %Preallocate Relative Density
Matrix
for j = 1:SampleCount
    T = readtable([char(Path(j)) char(Sample(j)) '.txt']);
    Temp_degC(1:TableHeight(j),j) = table2array(T(:,1));
    rho(1:TableHeight(j),j) = table2array(T(:,5));
%     rho(1:TableHeight(j),j) = table2array(T(:,6));
end

Tmin = 250; %degC
Tmax = 1100; %degC
Tstep = 5; %degC
Temp_degC_Input = linspace(Tmin,Tmax,(Tmax-Tmin)/Tstep+1)';

RelDen_Input = zeros(length(Temp_degC_Input),SampleCount);
for i = 1:SampleCount
    for j = 1:length(Temp_degC_Input)
        for k = 1:TableHeight(i)
            if Temp_degC(k,i) >= Temp_degC_Input(j)
                RelDen_Input(j,i) = rho(k,i);
                break
            end
        end
    end
end

NumEntries = size(RelDen_Input,1);
```

```
%50 degC/min
time_sec_Input(:,1) = linspace(0,(max(Temp_degC_Input)-
min(Temp_degC_Input))*60/50,length(Temp_degC_Input))';

%40 degC/min
time_sec_Input(:,2) = linspace(0,(max(Temp_degC_Input)-
min(Temp_degC_Input))*60/40,length(Temp_degC_Input))';

%30 degC/min
time_sec_Input(:,3) = linspace(0,(max(Temp_degC_Input)-
min(Temp_degC_Input))*60/30,length(Temp_degC_Input))';

clearvars Sample i j k T TableHeight Tmax Tstep Temp_degC rho; %Clear
Temporary Variables

%Determine Q Value for Minimum RMSE
%--------------------------------------------------------------------------
Q =  linspace(500,700,100)'; %kJ/mol
R = 8.314; %J/(mol*K)
Temp_K = Temp_degC_Input + 273.15;

RMSE = zeros(length(Q),1);
for k = 1:length(Q)
    index = 1;
    theta = zeros((NumEntries-1),SampleCount);
    X = zeros(SampleCount*(NumEntries-1),1);
    Y = zeros(SampleCount*(NumEntries-1),1);
    for i = 1:SampleCount
        for j = 1:NumEntries
            %Calculate Theta Integrand
            Integrand(j,i) = (1/Temp_K(j,1))*exp(-
(Q(k)*1000)/(R*Temp_K(j,1))); %#ok<SAGROW>
        end

        for m = 1:NumEntries-1
            dt_sec = time_sec_Input(m+1,i)-time_sec_Input(m,i);
            if m == 1
                theta(m,i) = ((Integrand(m)+Integrand(m+1))/2)*dt_sec;
            else
                theta(m,i) =
((Integrand(m)+Integrand(m+1))/2)*dt_sec+theta(m-1,i);
            end

            %Form Curve Fitting (X,Y) Pairs
            X(index,1) = log(theta(m,i));
            Y(index,1) = RelDen_Input(m,i);
            index = index +1;
        end
    end

%     %Perform Sigmoid Curve Fit
%     [xData, yData] = prepareCurveData(X,Y);
%     ft = fittype('rho_0+((1-rho_0)/(1+exp(-(x-log_theta0)/b))^c)',...
```

```
%                   'independent', 'x', 'dependent', 'y' );
%     opts = fitoptions('Method', 'NonlinearLeastSquares');
%     opts.Algorithm = 'Levenberg-Marquardt';
%     opts.Display = 'Off';
%     opts.StartPoint = [1.0 1.0 mean(X) 0.66];
%     [fitresult, gof] = fit(xData, yData, ft, opts); %#ok<ASGLU> % Fit model
to data

    %Perform 8th-Degree Polynomial Curve Fit
    [xData, yData] = prepareCurveData(X,Y);
    ft = fittype('poly8'); % Set up fittype and options.
    [fitresult, gof] = fit(xData,yData,ft); %#ok<ASGLU> % Fit model to data.

    RMSE(k,1) = gof.rmse;

    clearvars dt_sec xData yData index theta X Y i j m Integrand; %Clear
Temporary Variables
end

plot(Q,RMSE)
[RMSE_min,index] = min(RMSE);
Q_min = Q(index);

clearvars fitresult ft gof index opts Q RMSE k Temp_degC_Input RMSE_min;
%Clear Temporary Variables

%Calculate and Plot MSC
%-------------------------------------------------------------------------
index = 1;
theta = zeros(SampleCount*(NumEntries-1),1);
X = zeros(SampleCount*(NumEntries-1),1);
Y = zeros(SampleCount*(NumEntries-1),1);
for i = 1:SampleCount
    for j = 1:NumEntries
        %Calculate Theta Integrand
        Integrand(j,i) = (1/Temp_K(j,1))*exp(-(Q_min*1000)/(R*Temp_K(j,1)));
    end

    for m = 1:NumEntries-1
        dt_sec = time_sec_Input(m+1,i)-time_sec_Input(m,i);
        if m == 1
            theta(m,i) = ((Integrand(m)+Integrand(m+1))/2)*dt_sec;
        else
            theta(m,i) = ((Integrand(m)+Integrand(m+1))/2)*dt_sec+theta(m-
1,i);
        end

        %Form Curve Fitting (X,Y) Pairs
        X(index,1) = log(theta(m,i));
        Y(index,1) = RelDen_Input(m,i);
        index = index +1;
    end
end
```

```
% %Perform Sigmoid Curve Fit
% [xData, yData] = prepareCurveData(X,Y);
% ft = fittype('rho_0+((1-rho_0)/(1+exp(-(x-log_theta0)/b))^c)',...
%               'independent', 'x', 'dependent', 'y');
% opts = fitoptions( 'Method', 'NonlinearLeastSquares');
% opts.Algorithm = 'Levenberg-Marquardt';
% opts.Display = 'Off';
% opts.StartPoint = [1.0 1.0 mean(X) 0.66];
% [fitresult, gof] = fit(xData, yData, ft, opts) % Fit model to data
%
% coeff = coeffvalues(fitresult);
% b = coeff(1);
% c = coeff(2);
% log_theta0 = coeff(3);
% rho_0 = coeff(4);

%Perform 8th-Degree Polynomial Curve Fit
[xData, yData] = prepareCurveData(X,Y);
ft = fittype( 'poly8' ); % Set up fittype and options.
[fitresult, gof] = fit(xData,yData,ft) % Fit model to data.

coeff = coeffvalues(fitresult)'; %f(x) = p1*x^8 + p2*x^7 + p3*x^6 + p4*x^5 +
p5*x^4 + p6*x^3 + p7*x^2 + p8*x + p9

% Plot curve fit with data.
figure( 'Name', 'untitled fit 1' );
h = plot( fitresult, xData, yData);
legend( h, 'Constant Heating Rate', 'Curve Fit', 'Location', 'NorthWest' );
% Label axes
xlabel X
ylabel Y
grid on

clearvars SampleCount NumEntries time_sec_Input RelDen_Input...
          dt_sec index theta X Y i j m ft gof opts...
          Temp_K Integrand; %Clear Temporary Variables

%Predictions of Sintering Time
%--------------------------------------------------------------------------

%[Sample Name | Heating Rate (degC/min) | Temp (degC) | Hold Time (min) |
% Relative Density]
Pred = ["NiTi 79", 100,  950, 5, 0.986;...
        "NiTi 80", 100,  900, 5, 0.971;...
        "NiTi 81", 100,  850, 5, 0.951;...
        "NiTi 82", 100,  800, 5, 0.926;...
        "NiTi 83", 100,  750, 5, 0.898;...
        "NiTi 84", 100,  700, 5, 0.863;...
        "NiTi 85", 100,  650, 5, 0.829;...
        "NiTi 86", 100,  600, 5, 0.796];

PredCount = size(Pred,1);
Predtfinal_sec = ((str2double(Pred(:,3))-Tmin)./str2double(Pred(:,2)))*60;
Predtstep = 100;
```

```
PredTheta = zeros(PredCount,1);
Predrho = zeros(PredCount,1);
PredTheta_Ramp = zeros(Predtstep-1,PredCount);
for i = 1:PredCount
    TempRamp_Kmin = str2double(Pred(i,2));
    Temp_K = str2double(Pred(i,3))+273.15;
    Dwell_sec = str2double(Pred(i,4))*60;

    Predt_sec = linspace(0,Predtfinal_sec(i),Predtstep)';
    PredTemp_K = ((TempRamp_Kmin/60)*Predt_sec+Tmin)+273.15;
    for j = 1:Predtstep
        Integrand(j) = (1/PredTemp_K(j,1))*exp(-
(Q_min*1000)/(R*PredTemp_K(j,1)));
    end

    for m = 1:Predtstep-1
        dt_sec = Predt_sec(m+1)-Predt_sec(m);
        PredTheta_Ramp(m,i) = ((Integrand(m)+Integrand(m+1))/2)*dt_sec;
    end

    PredTheta_Dwell = (1/Temp_K)*exp(-(Q_min*1000)/(R*Temp_K))*Dwell_sec;

    PredTheta(i,1) = sum(PredTheta_Ramp(:,i))+PredTheta_Dwell;
%     Predrho(i,1) = rho_0+((1-rho_0)/(1+exp(-(log(PredTheta(i,1))-
log_theta0)/b)^c)); %Sigmoid
    Predrho(i,1) = coeff(1)*(log(PredTheta(i,1)))^8+...
                   coeff(2)*(log(PredTheta(i,1)))^7+...
                   coeff(3)*(log(PredTheta(i,1)))^6+...
                   coeff(4)*(log(PredTheta(i,1)))^5+...
                   coeff(5)*(log(PredTheta(i,1)))^4+...
                   coeff(6)*(log(PredTheta(i,1)))^3+...
                   coeff(7)*(log(PredTheta(i,1)))^2+...
                   coeff(8)*(log(PredTheta(i,1)))^1+...
                   coeff(9); %Polynomial

    clearvars TempRamp_Kmin Temp_K Dwell_sec Predt_sec PredTemp_K Integrand;
%Clear Temporary Variables
end

% fliplr(log(PredTheta(:,1)))

hold on
% Create plot
plot(log(PredTheta(:,1)),str2double(Pred(:,5)),'DisplayName','Experimental
Data','MarkerFaceColor',[0 0 0],...
    'MarkerEdgeColor',[0 0 0],...
    'Marker','o',...
    'Color',[0 0 0]);
```